#7.50

①

NASA CR-152489

NASA-CR-152489

COST ITEM $7.50

COPY ON MICROFICHE

Fiche=NASA

N77-22302

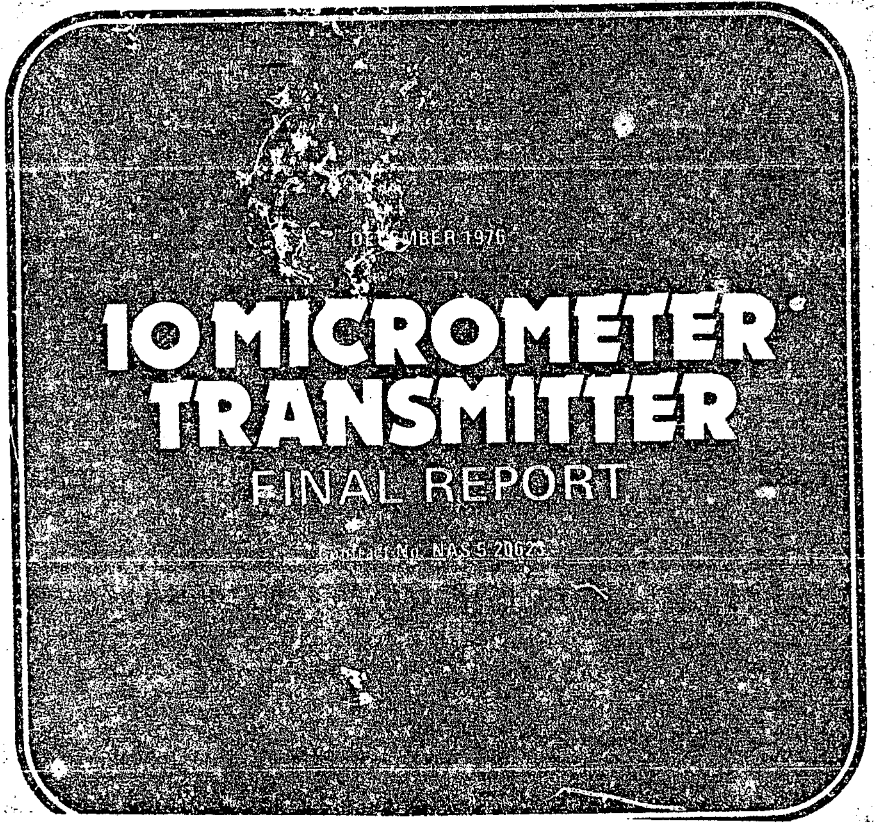

DECEMBER 1976

10 MICROMETER TRANSMITTER

FINAL REPORT

Contract No. NAS 5-20623

```
(NASA-CR-152489) THE 10 MICROMETER                    N77-22302
TRANSMITTER Final Report (Hughes Aircraft
Co.) 181 p HC A09/MF A01              CSCL 17E
                                                      Unclas
                                           G3/32     25124
```

HUGHES

HUGHES AIRCRAFT COMPANY
SPACE AND COMMUNICATIONS GROUP

MAY 1977
RECEIVED
NASA STI FACILITY
INPUT BRANCH

Hughes Ref No. D0460 • SCG 60517R

M77-16241

Page intentionally left blank

Page intentionally left blank

CONTENTS

		Page
1.	INTRODUCTION AND SUMMARY	1-1
	1.1 Introduction	1-1
	1.2 Summary	1-1
2.	10 MICROMETER TRANSMITTER LASER	2-1
	2.1 Laser Oscillator Analysis	2-1
	2.2 Parametric Data	2-3
	2.3 Laser Package Description	2-11
	2.4 Measured Performance	2-12
3.	MODULATOR PERFORMANCE	3-1
	3.1 Basic Equations	3-1
	3.2 Modulator Housing Design	3-5
	3.3 Measured Performance	3-13
4.	MODULATOR DRIVER	4-1
	4.1 Circuit Description	4-2
	4.2 Modulator Driver Package Description	4-6
	4.3 Modulator Driver Measured Performance	4-6
	4.4 Bit Error Rate Tests	4-9
	4.5 Quantized Feedback	4-15
5.	TRANSMITTER LASER PERFORMANCE	5-1
	5.1 Design Considerations	5-1
	5.2 Transmitter Package Description	5-9
	5.3 Transmitter Laser Measured Performance	5-11
	5.4 Q-Switch Tests	5-15
6.	LOCAL OSCILLATOR LASER	6-1
	6.1 Local Oscillator Laser Design Summary	6-1
	6.2 Local Oscillator Laser Description	6-3
	6.3 Laser Life Development	6-7
	6.4 Cathode Life Test Vehicles and Spectrophotometer Cells	6-9
	6.5 Life Test Results — Test Cells	6-11
	6.6 Life Test Results — Local Oscillator Lasers	6-12
7.	RECEIVER PERFORMANCE CHARACTERISTICS	7-1
	7.1 Local Oscillator Frequency Control	7-1
	7.2 Optical Mixer Characteristics	7-8
	7.3 Preamplifier Characteristics	7-8
	7.4 Comparison of Measured NEP and Theoretical Optical Mixer NEP as Function of Local Oscillator Power	7-9
	7.5 Measurement of Complete Receiver NEP	7-12

8. TRANSCEIVER DIPLEXING 8-1
- 8.1 Wire Grid Polarizer 8-1
- 8.2 Cadmium Sulfide /4 Plate 8-3
- 8.3 Diplexer Performance 8-3
- 8.4 Transceiver Integration 8-5
- 8.5 Growth to Larger Optics and Redundant Lasers 8-7

9. REFERENCES 9-1

APPENDICES

- A Experimental Data on Gain, Input Power, and Power Output for CO_2 Waveguide Laser with N_2 Fills A-1
- B Experimental Data on Gain, Input Power, and Power Output of CO_2 Waveguide Laser with CO Fills B-1
- C Modulator Thermal Gradients and Their Effects C-1
- D Waveguide Lasers with Intracavity Electro-Optic Modulators: Misalignment Loss D-1
- E Component Specification for Cadmium-Telluride Modulator Rod E-1
- F Parts Stress Derating - MSC 80041 Driver Transistors F-1
- G Specifications for Hybrid Assembly, Vari-L SA-167 G-1
- H Calculation of Average Output Power H-1
- I Hysteresis in Cavity Length Tuning of Coupling Modulated CO_2 Lasers I-1
- J Optical Coupling Modulation in Traveling Wave Cavities J-1

1. INTRODUCTION AND SUMMARY

1.1 INTRODUCTION

This document reports the completion of a program to design, fabricate, test, and evaluate engineering model components for a 10.6 μm wideband transceiver system. The effort emphasized the transmitter subsystem, including the development of the laser, the modulator and modulator driver, and included productization of both the transmitter and local oscillator lasers. The transmitter subsystem is functionally compatible with the receiver engineering model terminal developed under contract NAS 5-21859, and has undergone high data rate communication system testing against that terminal.

The transmitter subsystem is primarily intended for use in a low altitude spacecraft terminal to relay high data rate information to a synchronous or high altitude receiver terminal. The transmitter subsystem will ideally be integrated with the optomechanical subsystem developed under contract NAS 5-20018. Preliminary flight testing of the integrated transmitter terminal may then be conducted on Shuttle sorties. Operational use of the terminal would be on ERTS type missions where high resolution image formation is relayed to ground in real time via the synchronous terminal.

The transmitter subsystem is also suitable for integration into the synchronous or high altitude receiver terminal optically diplexed to form a functional high data rate transceiver. This mode of operation may be of interest to satisfy two way high data rate requirements such as may be required for a crosslink between synchronous satellites.

The completion of the present program sets the stage for engineering model development of the low altitude space transmitter terminal followed by a low risk flight experiment. It is estimated that the engineering model equipment will be suitable for a Shuttle mission with minor modifications.

1.2 SUMMARY

This report details the specific hardware design of: 1) the transmitter subsystem including the transmitter laser, modulator, and modulator driver; 2) the receiver subsystem, including the local oscillator laser and laser frequency control subsystem; and 3) the development of components and interfaces to permit diplexing the transmitter subsystem with a receiver terminal.

Substantial technical innovation was required to achieve the results reported in this document. New technology disclosures, and publication of technical papers, including a joint paper with NASA and AIL technical teams were the direct results of this program. A few of these are:

- J. A. Chakmanian, "Modulator Driver," New Technology Innovation Report No. 75205NT, 21 July 1975
- J. Wilkerson, "Stripline Modulator," New Technology Innovation Report No. 75204NT, 22 July 1975
- R. L. Abrams, H. R. Friedrich, "Waveguide Laser with Coaxial Geometry," New Technology Innovation Report No. 74283
- F. E. Goodwin, D. M. Henderson, T. A. Nussmeier, and L. S. Stokes, "Performance and Growth Potential of CO_2 Lasers in Space," Conference on Lasers and Electro-optical Systems (CLEOS), San Diego, 25 May 1976
- W. B. King, R. Kinnard, "Optical Design of CO_2 Laser Receiver," CLEOS 25 May 1976, San Diego, Calif.
- F. E. Goodwin, D. M. Henderson, J. Wilkerson, and A. Reiss, "Waveguide Electro-Optic Modulator for CO_2 Lasers," CLEOS, San Diego, 25 May 1976
- R. L. Abrams, C. K. Asawa, T. Plant, and G. Tangonan, "Application of Stark Cells to CO_2 Laser Communications," CLEOS, San Diego, 25 May 1976
- T. F. Johnson, W. B. Kolb, I. Ramsay, and C. Romero, "Waveguide CO_2 Lasers for Space," CLEOS, San Diego, 25 May 1976
- D. M. Henderson and V. A. Vilnrotter, "Optical Coupling Modulation in Traveling Wave Cavities," to be published APL.
- D. M. Henderson, "Waveguide Lasers with Intracavity Electro-optic Modulators: Misalignment Loss," Applied Optics, 15, No. 4, April 1976
- J. H. McElroy, N. McAvoy, E. H. Johnson, et al, "CO_2 Laser Communication Systems for Near Earth Space Applications," Proceedings, IEEE, February 1977.

The published material illustrates both the depth and breadth of the effort. The present report documents these technologies in even greater detail to provide a foundation for all future work related to CO_2 laser communications in space. Some of the particular areas stressed are listed below, together with the section reference:

- Laser parametric data — Saturation and gain characteristics of waveguide lasers have been measured and empirically modeled. These data also have been shown to agree with those theoretically predicted, thereby confirming use of these analyses to design laser devices (subsection 2.2, Appendices A, B)
- Coupling modulator data — Experimental performance of coupling modulator shown to agree with theoretical model (subsection 3.3, Appendix C)
- Laser modulator coupling losses — Coupling losses are now understood to be caused by thermal lensing of the modulator rod and dependence of transmitter performance on these losses has been determined (Section 5, Appendices C, D)
- Modulator procedures — Critical procedures for handling, processing, and assembling modulator have been established (subsection 3.2, Appendix E)
- Modulator driver efficiency — Using a bipolar microwave transistor in the current mode logic driver configuration, modulator driver efficiency of near 40 percent has been achieved (Section 4, Appendix F)
- Hybrid couplers — Special hybrid coupler design permits combining the outputs of four modulator driver modules to deliver nearly 120 V_{pp} to the modulator (subsection 4.1, Appendix G)
- Transistor derating — Conservative circuit design permits derating driver transistors to levels acceptable for flight qualification (subsection 4.3, Appendix F)
- Laser life development — Cathode test cells and spectrophotometer instrument permit monitoring constituent gases in lasers during life tests (subsections 6.3 through 6.6)
- Laser frequency control — Improved Stark stabilization allows programming and control of laser frequency to less than 70 kHz rms on a long term basis (subsection 7.1)
- Bit error rate (BER) tests using modulator driver — Experiments using the modulator in a complete communication system show BER close to that obtained with rf simulator, indicating only slight degradation of digital signal by modulator driver (subsection 4.4)

- Wire grid polarizer — Efficient diplexing of transmitter and receiver subsystems achieved with efficient wire grid polarizer and $\lambda/4$ plate (Section 8).

Since the main thrust of the program was aimed at the transmitter subsystem development and related technology, the overall assessment of the program can be seen by comparing the transmitter subsystem design goals with the measured performance. The desired sideband power output of 0.7 watt was approached using a 120 V_{pp} square wave driver. However, using the modulator driver with pulse rounding and hybrid losses, the measured sideband power was slightly more than 0.3 watt. It was determined that the limiting factors are modulator loss and grating coupling efficiency. Although the present transmitter subsystem yielded performance satisfactory for proving the concept and for potential Shuttle/ground experiments, further development is required to prove the technology for longer range space missions. This document clearly identifies those areas where further development is required.

The overall coordination of program tasks was achieved through the use of the PERT network shown in Figure 1-1. The pacing item in the program was the transmitter laser and modulator, delayed 6 months as a result of damage to antireflection coatings on the modulator rods. Tightening of coating specifications and rework resulted in the delay. The date code in Figure 1-1 indicates the original planned event date and the actual event date. Transmitter design parameters are given in Table 1-1.

TABLE 1-1. TRANSMITTER DESIGN PARAMETERS

Parameter		Measured Performance
Total prime power	145 W	145 W
Modulator driver power	90 W	78 W
Modulator voltage	120 p-p	110 V_{pp}
Laser prime power	55 W	64 W
Discharge length	24 cm	24 cm
Discharge voltage	3930 V	5300 V
Discharge current	3 mA	3 mA
Bore length/width	260 x 1.5 mm	260 x 1.5 mm
No. of sections	4	4
Modulator length/width	60 x 1.5 mm	60 x 1.5 mm
Gas mix/pressure	He:CO_2:CO:Xe/100-120 torr	100-120 torr
Sideband power out	0.7 W	>0.3 W
Carrier power out	0.25 W	0.1 W

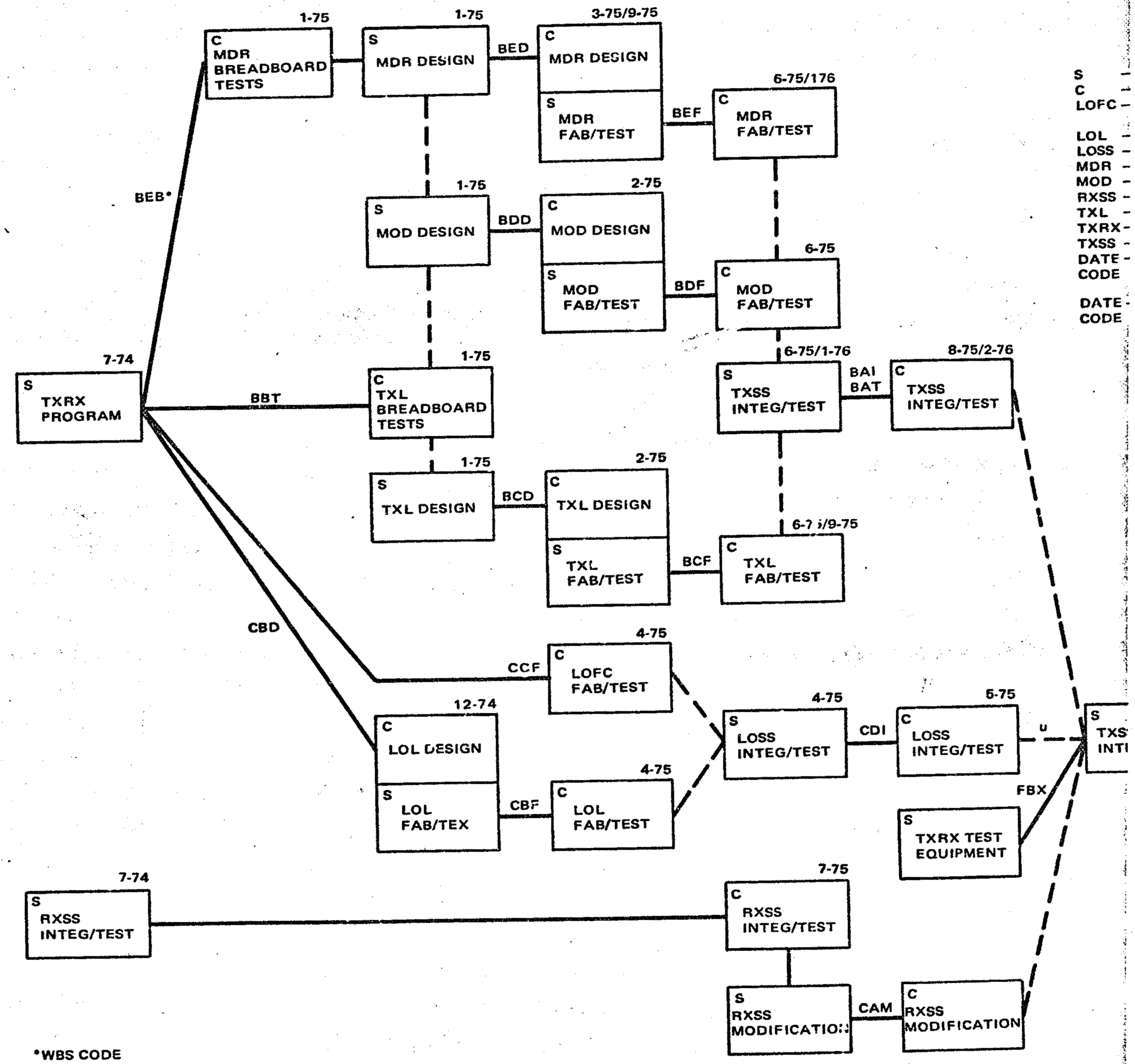

*WBS CODE

FIGURE 1-1. TOTAL PROGRAM PERT NETWORK

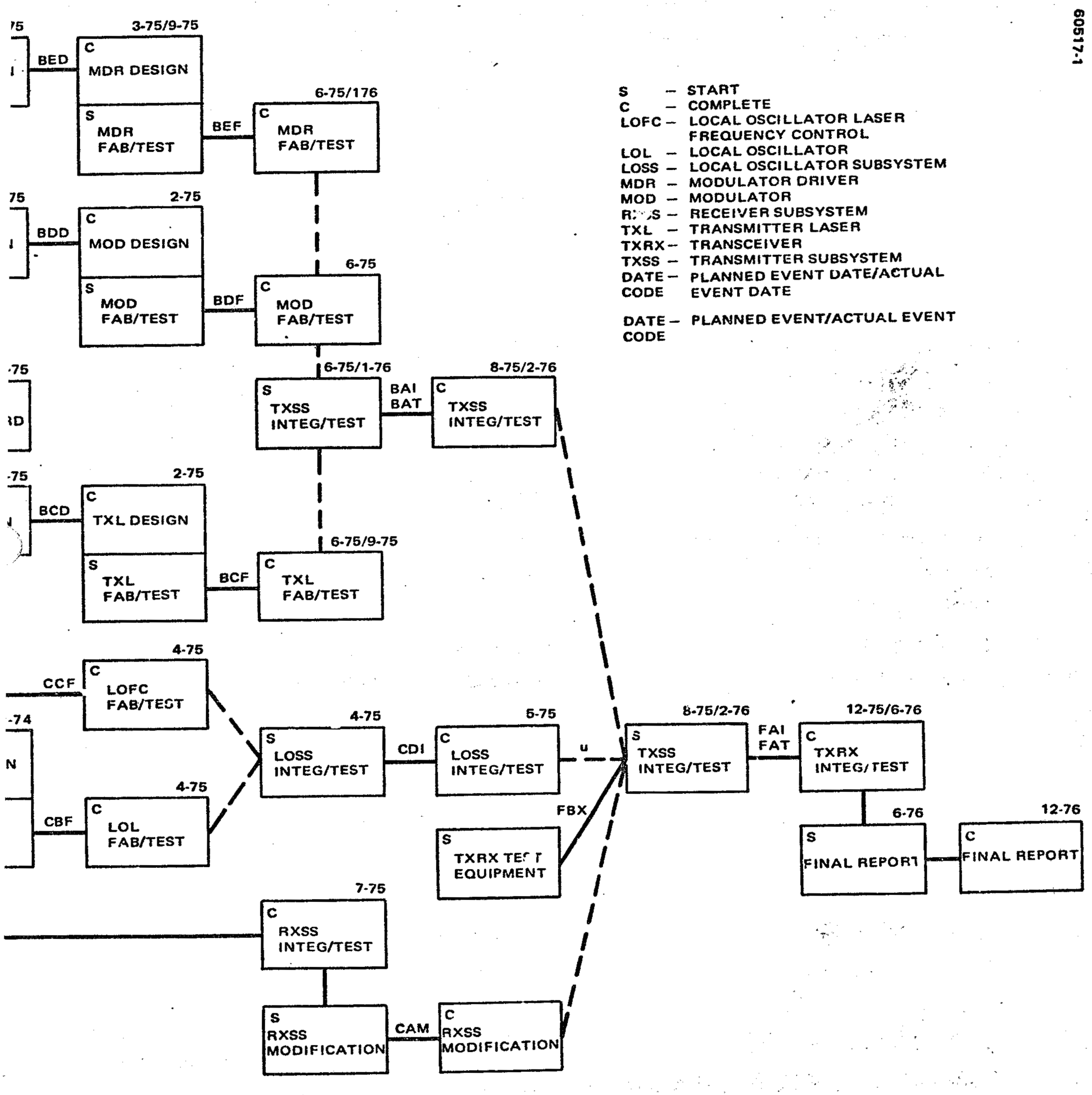

S — START
C — COMPLETE
LOFC — LOCAL OSCILLATOR LASER FREQUENCY CONTROL
LOL — LOCAL OSCILLATOR
LOSS — LOCAL OSCILLATOR SUBSYSTEM
MDR — MODULATOR DRIVER
MOD — MODULATOR
RXSS — RECEIVER SUBSYSTEM
TXL — TRANSMITTER LASER
TXRX — TRANSCEIVER
TXSS — TRANSMITTER SUBSYSTEM
DATE CODE — PLANNED EVENT DATE/ACTUAL EVENT DATE

DATE CODE — PLANNED EVENT/ACTUAL EVENT

ROGRAM PERT NETWORK

ORIGINAL PAGE IS
OF POOR QUALITY

FOLDOUT FRAME

2. 10 MICROMETER TRANSMITTER LASER

The design and testing summary of the 10 μm laser transmitter are presented in Sections 2 through 5. Performance of the individual transmitter components is first described. These components include the laser oscillator, electro-optical modulator, and 300 Mbps modulator driver. Overall performance of the completed transmitter laser subsystem, referred to as TXL, is discussed in Section 5.

2.1 LASER OSCILLATOR ANALYSIS

In the TXL design, the laser oscillator performance parameter that must be optimized is the intracavity circulating power. Practical considerations such as feasible discharge length, electrical prime power restrictions, and manageable discharge voltages impose constraints on the laser design. The numerous discharge and optical cavity parameters governing the performance are presented below.

In a laser cavity formed by elements of reflectivity r_1 and r_2, the circulating power P_{cir} at end 2 (neglecting distributed loss) is given by (Reference 1)

$$P_{cir} = \frac{P_{sat}\sqrt{r_1}}{\sqrt{r_1}+\sqrt{r_2}} \frac{g_o L + \ell n \sqrt{r_1 r_2}}{1 - \sqrt{r_1 r_2}} \tag{1}$$

where P_{sat} is a power saturation factor, g_o is the small signal gain, and L is the active laser length. Define the single pass cavity loss $\mathscr{L} = 1 - \sqrt{r_1 r_2}$. For low loss $\mathscr{L} \ll 1$ Equation 1 can be written

$$P_{cir} \simeq \frac{P_{sat}}{2} \frac{g_o L - \mathscr{L}}{\mathscr{L}} \; . \tag{2}$$

In general, the laser is formed by several independent discharge sections to maintain a satisfactory low (~5 kV) discharge voltage. For a section of length L_{sec}, the power dissipation P_{sec} has been found to be

$$P_{sec} = P_o + \frac{\partial P}{\partial L} L_{sec} \qquad (3)$$

where the quantity $\partial P/\partial L$ is interpreted as the power dissipation per unit length of the positive column and P_o is an experimentally determined quantity Note that $\partial P/\partial L = I \, \partial V/\partial L$, since the discharge current, I, is independent of length. The section length is set by the section voltage, V_{sec}, from Equation 3

$$L_{sec} = \frac{1}{\left(\frac{\partial V}{\partial L}\right)} \left(V_{sec} - \frac{P_o}{I}\right) \qquad (4)$$

The total number of sections, N, is found from the prime power, P_L, by

$$N = \eta_{hv} P_L / P_{sec} \qquad (5)$$

where an efficiency factor for the high voltage power supply has been included. The total discharge length, $L = N L_{sec}$, is simply

$$L = \frac{\eta_{hv} P_L}{P_{sec}/L_{sec}} \equiv \frac{\eta_{hv} P_L}{D_{sec}} \qquad (6)$$

The circulating power is related to the prime power by Equations 2 and 6,

$$P_{cir} = \frac{P_{sat}}{2 P_{th}} (P_L - P_{th}) \qquad (7)$$

where the factor $D_{sec} \mathscr{L}/g_o \eta_{hv}$ is identified as the power, P_{th}, required to bring the laser to the threshold of oscillation. For the nominal values,

$D_{sec} \simeq 2.6$ W/cm, $\mathscr{L} \simeq 0.06$, $g_o \simeq 0.01$ cm^{-1}, and $\eta_{hv} \simeq 0.85$, P_{th} is 18 watts. Thus, for 75 watts prime power, and using $P_{sat} \simeq 35$ watts, Equation 7 predicts that optical circulating power of 55 watts is achievable.

The laser tube is designed so it can accept either an intracavity modulator for use as a transmitter or an output mirror for use as an oscillator. A good measure of the laser oscillator performance is its efficiency (optical power out/electrical power in) when outfitted with an output mirror. The output power, P_{out}, is given by $P_{out} = t_m P_{cir}$, where t_m is the transmissivity of the mirror. Consequently, the efficiency, ϵ, becomes

$$\epsilon = \frac{P_{out}}{P_L} = \frac{t_m}{2} \frac{P_{sat}}{P_{th}} \left[1 - \frac{P_{th}}{P_L} \right] \qquad (8)$$

For a 10 percent transmitting mirror and the numerical values previously used, Equation 8 predicts an efficiency of 9 percent.

The results contained in Equations 4 through 8 constitute the major design considerations. Optimization of the circulating power requires knowledge of the discharge conditions that yield a maximum product of $g_o P_s / D_{sec}$. Parametric dependencies of these quantities, which were taken over a wide range of laser conditions, are presented in the next subsection. Discussion of the achievable values of cavity loss is contained in subsection 2.4 and Section 5.

2.2 PARAMETRIC DATA

As part of the transmitter subsystem design task, a considerable amount of data have been accumulated for small signal gain, electrical power dissipation, and output optical power from a waveguide laser. These data were taken on a BeO breadboard laser (referred to as A-31) with 1.5 mm square-bore consisting of two discharge sections, each 7.5 cm long. Nickel cathodes were used in the tube. The dependence of the above parameters on variations in laser mix ratio, pressure, current, and output mirror reflectivity was measured. A complete set of data are contained in Appendices A and B of this report. Only that material relevant to the final transmitter design is discussed in the body of the report.

Small Signal Gain

Results of small signal gain measurements taken on the A-31 breadboard laser are shown in Figure 2-1 for a standard He:CO_2 laser mix ratio of 4:1. In the past, nitrogen has been added to this mixture to provide population inversion through vibrational energy transfer during collisions between an excited state N_2 molecule and a ground state CO_2 molecule. The presence of nitrogen adversely affects laser lifetime, however, because the formation of negative ions of nitrogen causes sputtering.

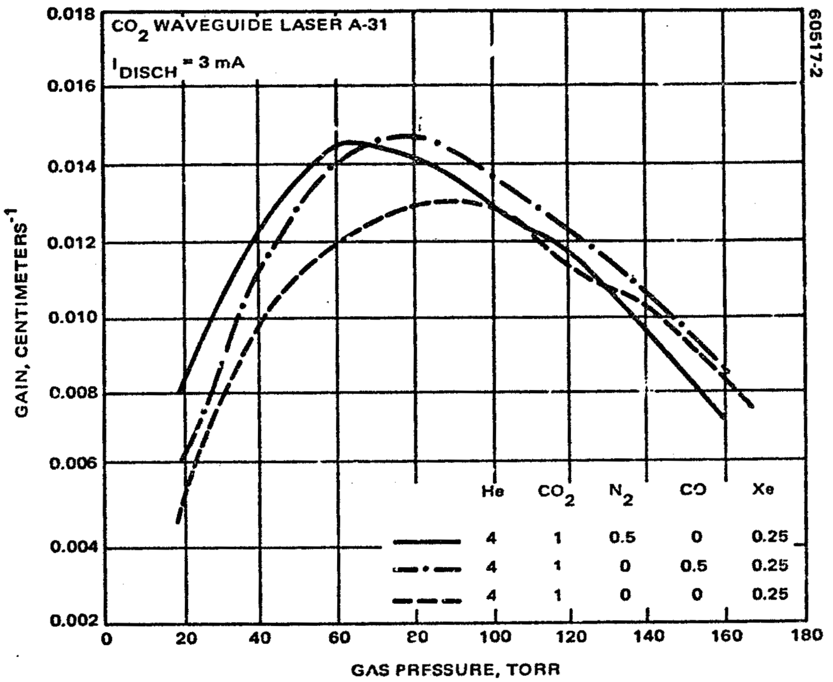

FIGURE 2-1. SMALL SIGNAL GAIN VERSUS PRESSURE

At the operating pressures of waveguide lasers, nitrogen is not required for substantial inversion as indicated by the gain data of Figure 2-1, with nitrogen totally removed. In fact, the replacement of N_2 by CO in the laser discharge results in gain very similar to the nitrogen mix, but without the sputtering problem. This latter mixture is used in filling all laser transmitters.

Saturation Power Level

The saturated gain, g_s, of the laser is given in terms of the small signal gain by (Reference 1)

$$g_s = \frac{g_o}{1 + \frac{2\mathscr{I}}{\mathscr{I}_{sat}}} \tag{9}$$

where $\mathscr{I}$ is the optical power density propagating in the bore and $\mathscr{I}_{sat}$ is the saturation intensity. For the square laser bore of sides 2a, the saturation power level, P_{sat}, is given by $P_{sat} = a^2 \mathscr{I}_{sat}$.

The saturation power level has been inferred from laser output power measurements and the known small signal gain. From Equation 1,

$$P_{sat} = \frac{\sqrt{r_1} + \sqrt{r_2}}{\sqrt{r_1}} \; \frac{1 - \sqrt{r_1 r_2}}{g_o L + \ell n \sqrt{r_1 r_2}} \; P_{cir} \tag{10}$$

In this expression, g_o L and P_{cir} (calculated from laser output power) are experimentally measured quantities. The effective reflectivities, r_1 and r_2, are not precisely known, however, as diffraction loss and absorption in the CdTe windows terminating the discharge reduce the effective reflectivity by unknown amounts. To circumvent this difficulty, the output power is measured with two different mirrors, keeping all other cavity parameters and discharge conditions fixed. As a result, the above unknown contributions are eliminated as the difference in reflectivity becomes the important parameter. This difference is due entirely to the reflectivities of the two output mirrors, which have been accurately measured.

The power saturation is calculated as follows. The reflectivity r_1 is taken to be 97 percent, the known loss of the Littrow grating used in this work. A trial value of r_2 is chosen and the saturation power P_{sat} is calculated from Equation 10 using the circulating power measured with the higher reflectivity mirror in place. Next, the effective value r_2 selected above is changed by the known difference in mirrors, and P_{cir} is calculated for the lower reflectivity mirror from Equation 1 using the value of P_{sat} found above.

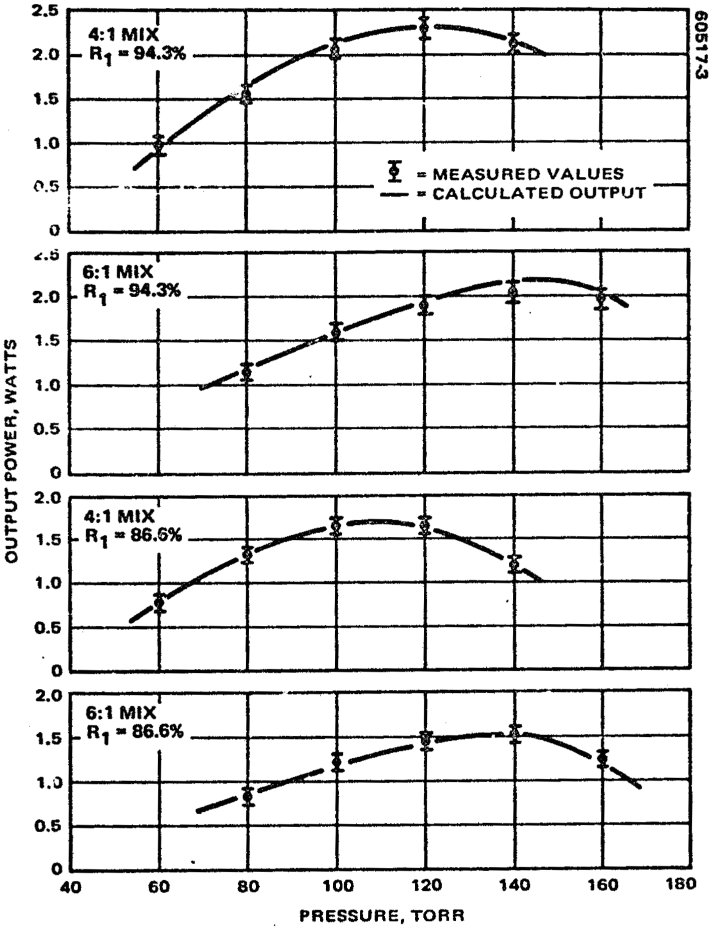

FIGURE 2-2. OUPUT POWER VERSUS PRESSURE

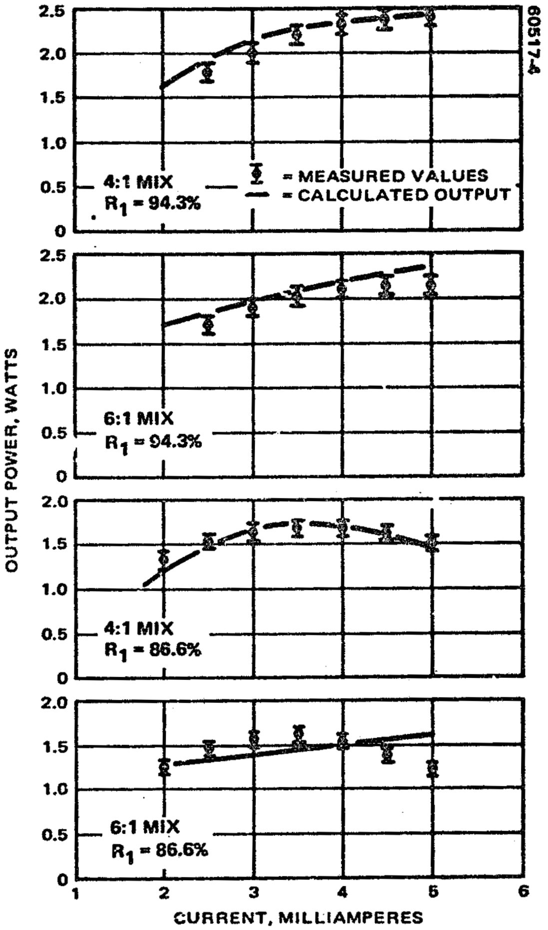

FIGURE 2-3. OUTPUT POWER VERSUS CURRENT

The actual value of circulating power is then compared with that computed from the trial r_2. The value of r_2, which minimizes the difference, is taken to be the best estimate of loss. The best value of loss over the range of pressure, current, and mixture data presented in Appendix A is $\mathscr{L} = 1 - \sqrt{r_1 r_2} = 4.44 \pm 0.38$ percent with the higher reflectivity mirror in place. This procedure is insensitive to the value of r_1 assigned.

The power saturation can now be calculated since the cavity loss has been determined. It is found that the best fit to the pressure data of the 4:1:1/2:1/4 nitrogen mixture is given by

$$P_{sat} \text{ (watts)} = -16.6 + 0.49 \times p \text{ (Torr)}; \; i = 4 \text{ mA} \qquad (11)$$

while for the current dependence

$$P_{sat} \text{ (watts)} = 13.56 + 6.99I \text{ (mA)}; \; p = 120 \text{ Torr} \qquad (12)$$

Similarly, for the 6:1:1/2:1/4 mixture

$$P_{sat} \text{ (watts)} = -8.71 + 0.36 \times p \text{ (Torr)}; \; i = 4 \text{ mA} \qquad (13)$$

$$P_{sat} \text{ (watts)} = 17.51 + 6.06 * I \text{ (mA)}; \; i = 140 \text{ Torr} \qquad (14)$$

The quality of this procedure can be judged by comparing with measurement the calculated circulating powers using the saturation powers given in Equations 11 through 14 and the estimated loss of 4.44 percent. It is seen in Figures 2-2 and 2-3 that quite reasonable agreement has been obtained over the range of the measured parameters.

Output power is shown in Figure 2-4 for the transmitter He:CO_2 ratio of 4:1 as a function of pressure and current. It is seen that the replacement of N_2 by CO gives quite similar performance. As output power as well as the small signal gain of the CO mix closely follow that of the N_2, it is felt that, within the accuracy of the method described above, Equations 11 through 14 adequately describe the power saturation level in CO fills as well as in N_2 fills.

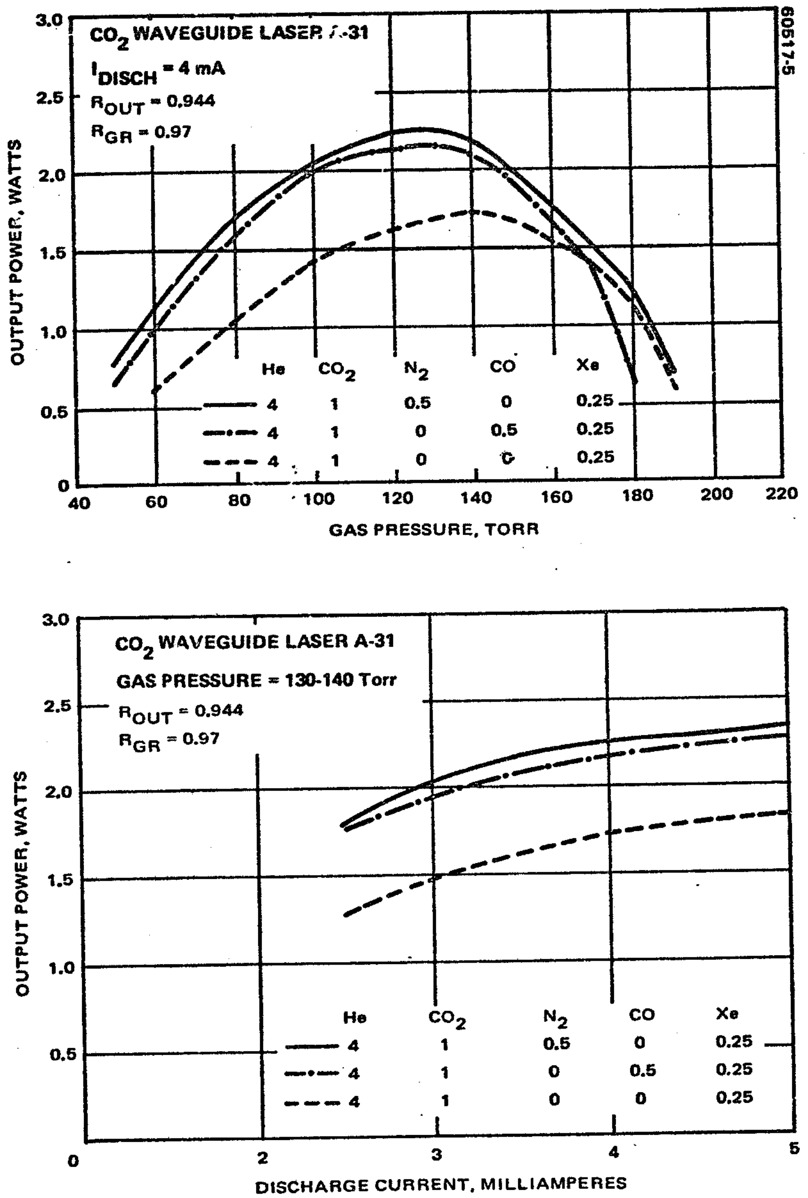

FIGURE 2-4. OUTPUT POWER FOR N_2 AND CO MIXTURES

Power Dissipation

The power dissipation data presented in Appendices A and B are given in the differential form — watts/centimeter. This factor has been computed by dividing the measured power dissipation for a single section by the bore length of that section. Care must be taken in extending these results to lasers of differing section length, differing cathode materials, and geometries. The data presented here should be viewed as appropriate to the particular Ni cathode design used. It will be seen from the results in subsection 2.4, the copper cathode discharge tube has a larger differential power dissipation.

Representative data taken on the A-31 laser tube are shown in Figure 2-5. The input power varies from 2.0 to 2.5 W/cm for the transmitter fills. A significant feature of the data is the lower dissipation of the CO mix when compared to the more common N_2 fills.

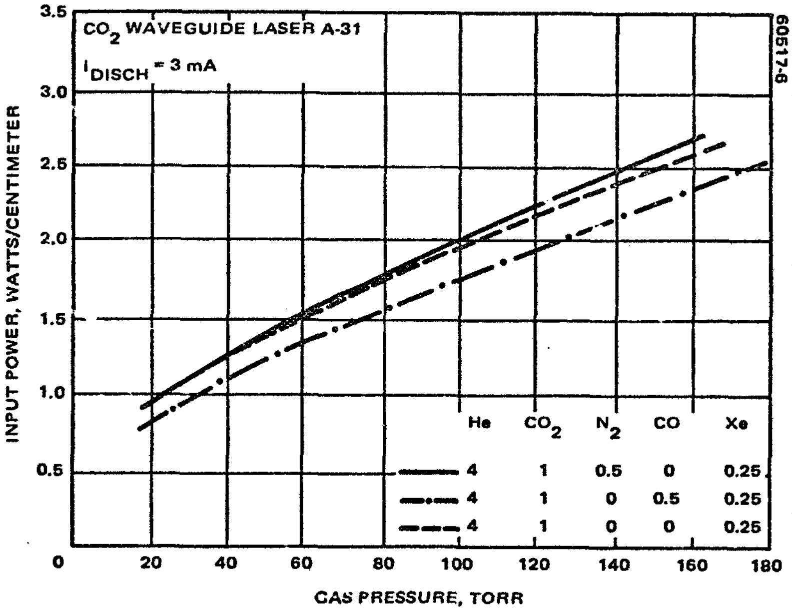

FIGURE 2-5. INPUT POWER FOR N_2 AND CO MIXTURES

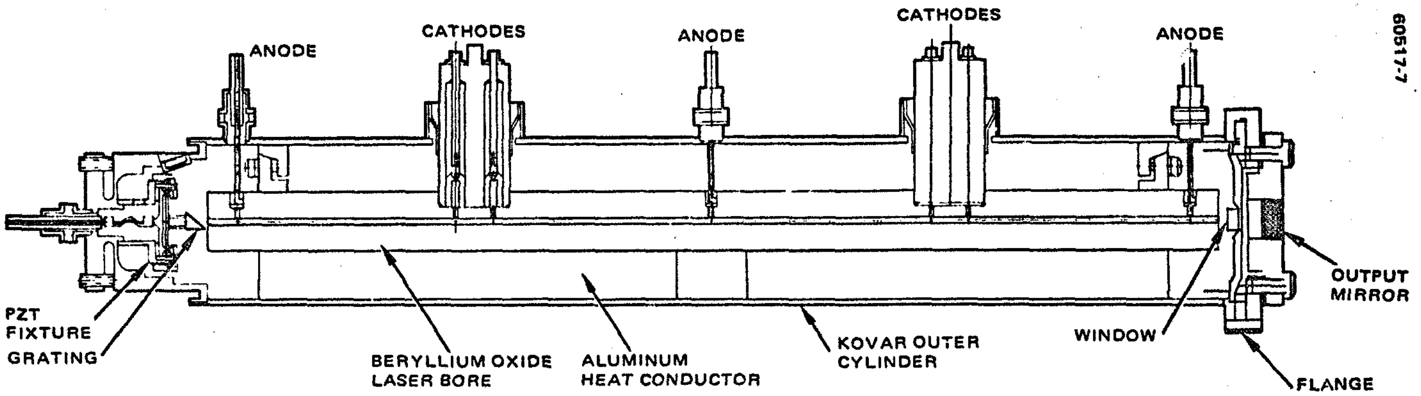

FIGURE 2-6. SECTION DRAWING OF LASER TRANSMITTER

2.3 LASER PACKAGE DESCRIPTION

A section drawing of the CO_2 waveguide laser built for the laser transmitter is shown in Figure 2-6. The tube is equipped with a mating flange that accepts either an output mirror as shown in the figure or the electro-optic modulator described in Section 3.

The laser bore is made from beryllium oxide because of the high thermal conductivity and low waveguide losses at 10 μm that this material affords (Reference 2). The discharge path is divided into four sections to reduce the high voltage requirements to practical values. Overall length of the bore is 26 cm, of which 24 cm is useful discharge length. The bore is square in cross section with 1.5 mm sides.

An aluminum block between the bore and the nickel-plated kovar outer cylinder acts to conductively cool the BeO. An indium gasket placed between the aluminum and kovar assures good thermal conductivity between the materials. The volume within the outer cylinders (~300 cm^3) is gas filled to provide ballast.

Optical components within the housing are a Littrow grating and a Zn-Se intracavity vacuum window. The grating allows line selection and also serves to couple out the cross polarized, modulated light in transmitter operation. The grating is mounted on a bender bimorph translator for cavity length control. This translator is 3/4 inch in diameter and has a measured sensitivity of 0.05 μm/V. The vacuum window isolates the modulator from the discharge and allows ready use of the tube as either an oscillator or transmitter. Figures 2-7 through 2-11 show the laser at various stages of assembly.

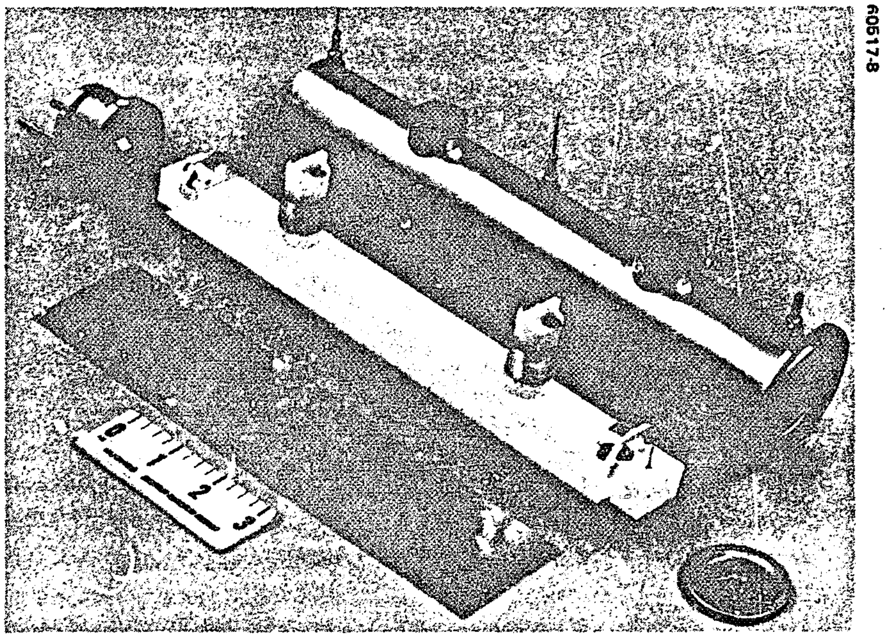

FIGURE 2-7. TRANSMITTER LASER EXPLODED VIEW (PHOTO 4R42421)

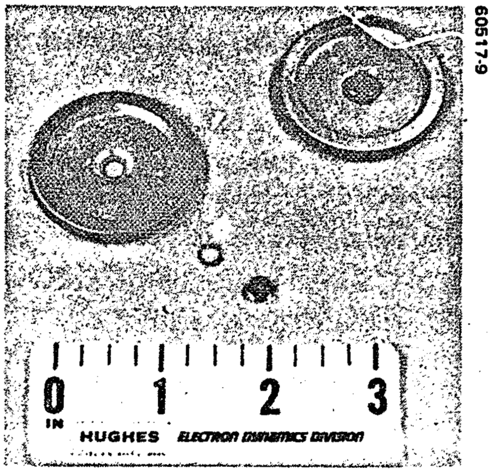

FIGURE 2-8. INTRACAVITY WINDOW ASSEMBLY (PHOTO 4R42423)

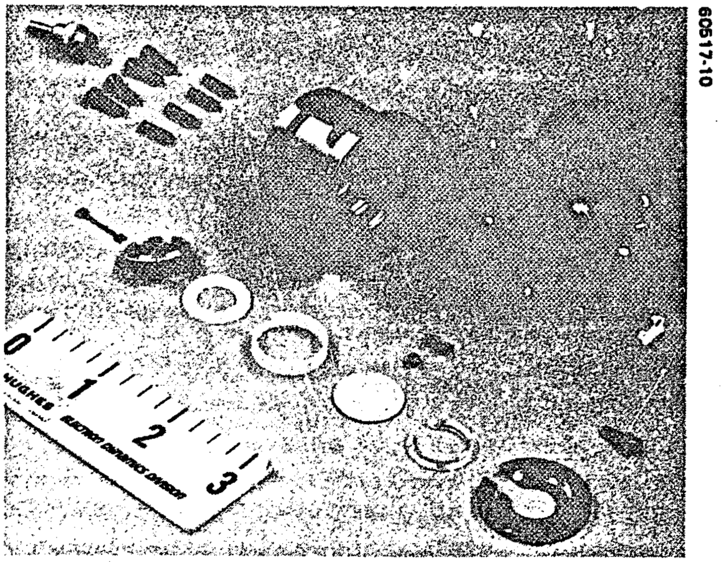

FIGURE 2-9. GRATING/PZT ASSEMBLY (PHOTO 4R42422)

Laser Starting

Starting the waveguide laser with four independent discharge sections presents a problem which has not been entirely solved. A standard Spellman 10 kV, 20 mA power supply is used to sustain the discharge. Four 1.0 megohm resistors link the four laser cathodes to the supply. When the supply is turned on and the discharge initiated, it is highly probable that less than all four sections start. The supply was modified with the starting assist circuit. A fast 10 kV pulse is added to the power supply voltage when a switch is depressed. Under the condition that the power supply voltage is just below the point where the laser wants to self-fire, all four sections come on at the same time. While this technique does work (a competent technician can start the laser within 30 seconds) the critical settings involved do not make this technique useful for a space environment. This problem will be solved in the next phase of the program.

2.4 MEASURED PERFORMANCE

The performance of the TXL operating as a laser oscillator is summarized in Table 2-1. In these measurements, an output mirror of 90 percent reflectivity has been used. The values given in the table are typical results. For example, an output power of 7.5 watts has been obtained at lower efficiency while an efficiency of 10 percent has been measured at lower output power.

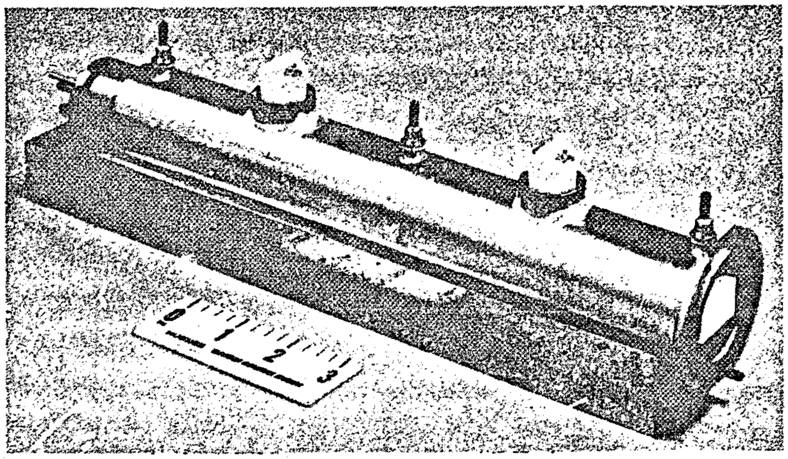

FIGURE 2-10. PARTIALLY COMPLETED TRANSMITTER LASER (PHOTO 4R42419)

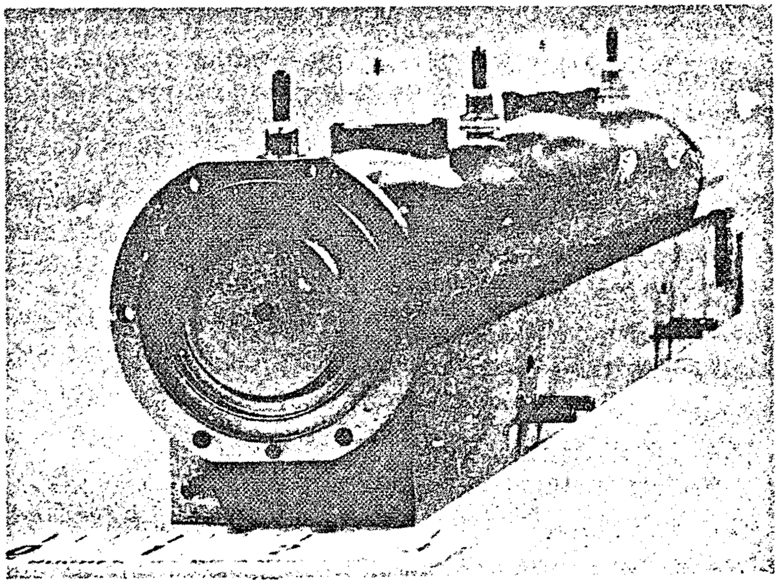

FIGURE 2-11. COMPLETED TRANSMITTER LASER (PHOTO 4R42418)

TABLE 2-1. LASER OSCILLATOR PERFORMANCE

Parameter	Measured Performance
Output power	5.8 W
Efficiency	9.1%
Discharge current	3.0 mA
Discharge voltage	5.3 kV
Input power	64 W
Transition	P-20
PZT voltage	±150 V
PZT sensitivity	0.05 μm/V
Overall length	13.5 in.
Cylinder diameter	1.75 in.
Weight	3.3 lb

Output Power

A comparison of the measured output power and efficiency with the performance calculated in subsection 2.1 is useful in evaluating these results. The output power and efficiency from Equation 8 are given in Figures 2-12 and 2-13 for the standard transmitter mixture and pressure. Small signal gain and power saturation values are taken from the breadboard laser measurements while actual input power of the TXL is used. The measured output mirror transmissivity of 9 percent has been taken. As the single pass cavity loss is not precisely known, several curves are shown for various values of loss. The comparison between the calculated and measured performance suggests a loss between 6 and 6.5 percent over the current range shown. This loss is consistent with the known grating reflectivity ($r_1 = 0.97$) and output mirror reflectivity ($r_2 = 0.90$) and indicates that negligible loss arises from the waveguide bore and intracavity window. The predicted trend of increasing output and decreasing efficiency with current is also found in the measurements.

Input Electrical Power

A significant departure from the parametric data taken on the A-31 breadboard waveguide laser is found in the discharge voltage and power dissipation of the TXL laser. These data are summarized in Figure 2-14. Note that the voltage and input power per section is greater for the TXL even though the cathode-anode spacing along the bore of the TXL (6 cm) is 25 percent less than that of the A-31 laser (7.5 cm). It has been empirically found that the power dissipation per section from 2 to 5 mA discharge current can be expressed to within 2 percent accuracy as

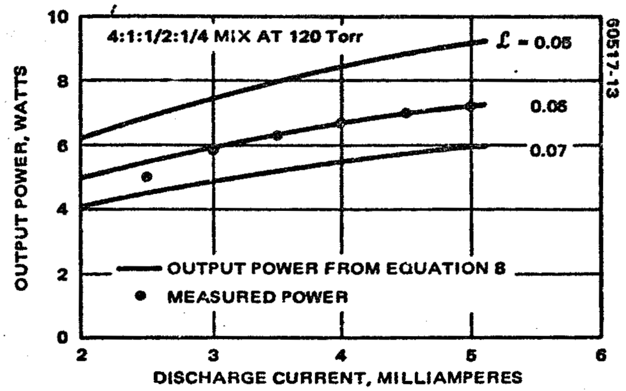

FIGURE 2-12. TRANSMITTER LASER OUTPUT POWER

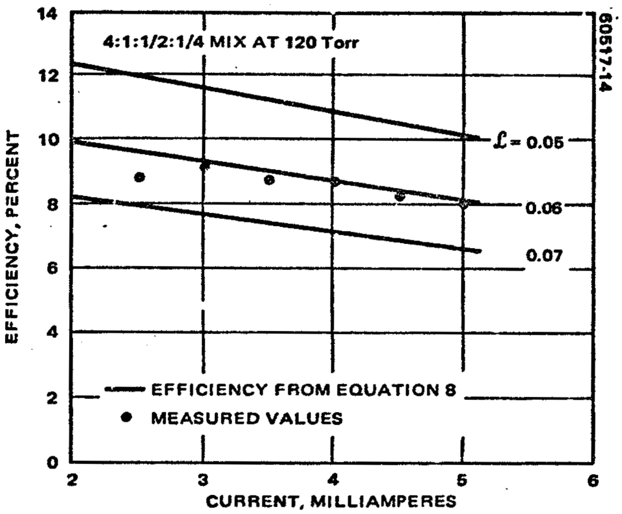

FIGURE 2-13. TRANSMITTER LASER EFFICIENCY

$$\text{TXL: } P_{sec}\text{ (watts)} = 6.44 + 0.53 * I\text{ (mA)} * L_{sec}\text{ (cm)} \qquad (15)$$

$$\text{A-31: } P_{sec}\text{ (watts)} = 3.63 + 0.50 * I\text{(mA)} * L_{sec}\text{ (cm)} \qquad (16)$$

As the two laser bores are identical in construction, the change in cathode material and geometry is responsible for the measured differences. The two cathode assemblies are shown in Figure 2-15. The higher discharge voltage in the TXL arises primarily from the length the quartz sputter shield adds and the high impedance section introduced by the 0.020 inch opening in the sputter shield. A small increase in the cathode fall potential results from the change in material.

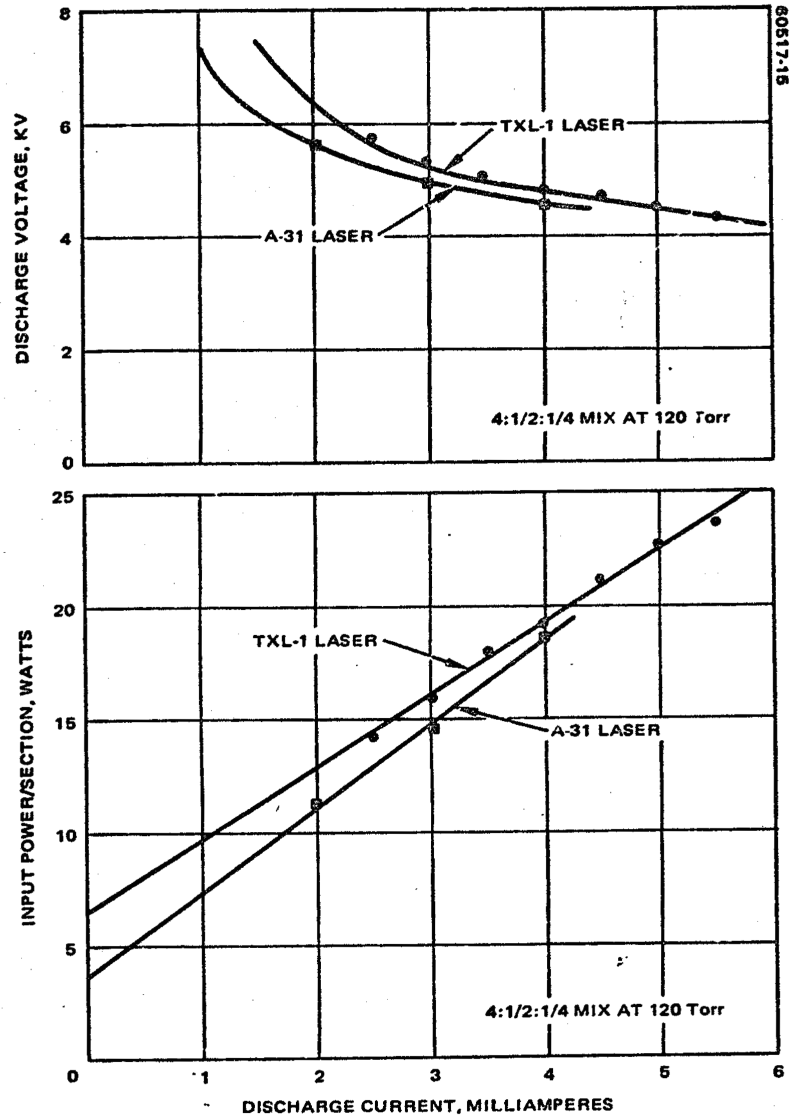

FIGURE 2-14. ELECTRICAL INPUT VOLTAGE AND POWER

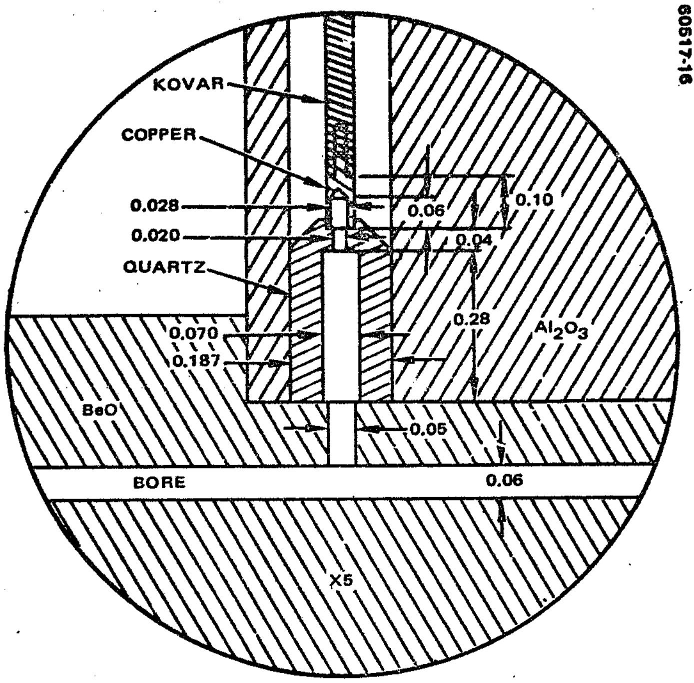

TXL LASER

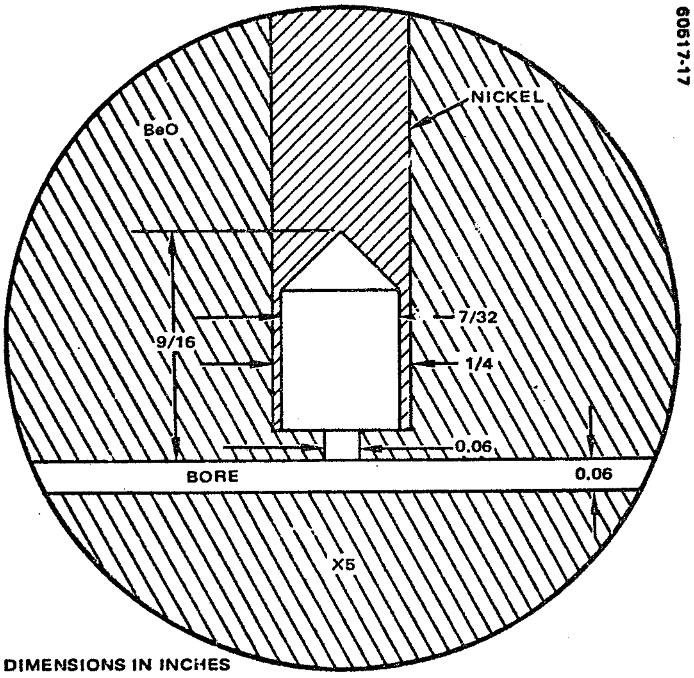

DIMENSIONS IN INCHES

A-31 LASER

FIGURE 2-15. LASER CATHODE ASSEMBLIES

3. MODULATOR PERFORMANCE

The 10 μm laser modulator utilizes intracavity coupling modulation to achieve the required sideband optical power with reasonable prime power input. In this arrangement, an electro-optic modulator is placed inside the laser cavity as the circulating power in the cavity exceeds the output power by an order of magnitude. The modulator crystal is cut so the optic axes induced by an electric field are at 45° to the laser polarization. As light passes through the crystal, its polarization is slightly rotated when voltage is applied to the modulator. In the absence of applied voltage, no rotation takes place. A polarization selective element within the cavity couples out the cross polarized optical component, which reproduces the voltage waveform applied to the crystal. The basic equations governing the modulation process are now discussed.

3.1 BASIC EQUATIONS

The orientation of the electro-optic, cadmium telluride modulator crystal used in this work is shown in Figure 3-1.

The fraction, c, of the incident optical power that exits the crystal with cross polarization after a single pass is given by (Reference 3)

$$c(t) = \sin^2 [\Gamma(t)/2] \tag{1}$$

where the time dependence has been explicitly shown. The phase shift Γ is related to the crystal properties and geometry by

$$\Gamma(t) = 2\pi \frac{\ell}{d} n_o{}^3 r_{41} \frac{V(t)}{\lambda_o} \tag{2}$$

In this expression, ℓ is the crystal length, d the electrode separation, n_o the material refractive index, r_{41} an electro-optic tensor element, V the

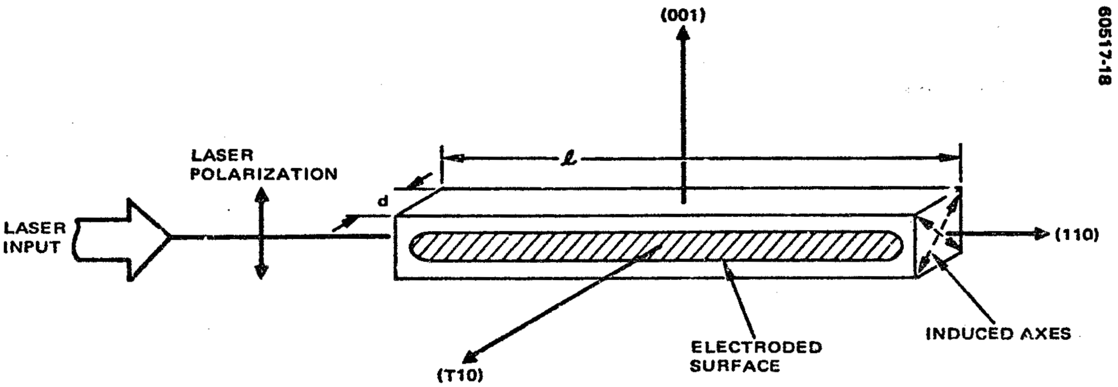

FIGURE 3-1. CADMIUM TELLURIDE MODULATOR ROD ORIENTATION

applied voltage, and λ_o the free-space wavelength. It is convenient to define the half-wave voltage V_π for which $\Gamma = \pi$. From Equation 1 it is seen that the light is completely cross polarized for this voltage. Equation 2 shows

$$V_\pi = \frac{\lambda_o}{2n_o^3 r_{41}} \frac{d}{\ell} \tag{3}$$

Thus

$$\Gamma(t) = \frac{\pi V(t)}{V_\pi} = \frac{\pi V(t) \frac{\ell}{d}}{V_\pi \frac{\ell}{d}} \tag{4}$$

The latter form of Equation 4 is useful as the quantity $V_\pi \ \ell/d$ is independent of geometry. For CdTe at 10.6 μm, the value is $V_\pi \ \ell/d \simeq 53$ kV.

Phase shifts of 0.1 radian are typical values for the laser transmitter. Consequently, the small angle approximation to Equation 1 can be used. In a single pass

$$c(t) = \Gamma^2(t)/4 \tag{5}$$

For an intracavity modulator, light passes through the modulator rod twice per cavity round trip, resulting in a phase shift twice the single pass value. Therefore, in a double pass

$$c(t) \simeq \Gamma^2(t) \tag{6}$$

The optical power coupled out of the cavity is set by the circulating power and the output coupling efficiency of the grating η_g, for the crossed polarization. Thus, the instantaneous power is simply

$$P_\perp(t) \simeq \eta_g P_{cir} \Gamma^2(t) \tag{7}$$

where the ($\perp$) symbol indicates the cross polarization. The time average power is determined by the voltage waveform, V(t), applied to the crystal. Combining Equations 4 and 7 and taking a time average (indicated by pointed brackets) gives

$$<P_\perp> = \frac{\pi^2 \eta_g P_{cir} V^2_{rms} \left(\frac{\ell}{d}\right)^2}{\left(V_\pi \frac{\ell}{d}\right)^2} \tag{8}$$

where

$$V^2_{rms} = \lim_{T \to \infty} \frac{1}{T} \int_0^T dt\, V^2(t) \tag{9}$$

The prime electrical power P_M required to drive the crystal is simply

$$P_M = \frac{1}{\eta_{md}} \frac{V^2_{rms}}{Z} \tag{10}$$

where Z is the impedance seen by the modulator driver and η_{md} is the efficiency of the modulator driver. Combining Equations 8 and 10 yields

$$<P_\perp> = \pi^2 \eta_g P_{cir} P_M/P_\pi \tag{11}$$

where P_π has been identified as the prime power required to drive the crystal at the half-wave voltage,

$$P_\pi = V^2_\pi/\eta_{md} Z$$

In the present design, V_π = 1325 volts and Z = 100 ohms, which gives $P_\pi(kW) \simeq 17.5/\eta_{md}$. Thus, for P_M = 80 watts, P_{cir} = 55 watts, η_g = 0.80, and η_{md} = 0.25. Equation 11 shows that 0.5 watt average output power will result. If the voltage waveform does not contain a dc component, all the power $<P_\perp>$ is modulated, sideband power.

3.2 MODULATOR HOUSING DESIGN

The design of a housing for the CdTe crystal must take into consideration the fact that this material, in addition to being electro-optic, is also piezo-electric, exhibits stress birefringence, and possesses a temperature dependent index of refraction. Consequently, the design must simultaneously meet certain electrical, mechanical, and thermal requirements. A description of these requirements follows.

Electrical Design

The desire to reduce the modulator driver power requirements by making the characteristic impedance of the modulator structure larger than a standard 50-ohm impedance led to a design that utilizes the CdTe rod as the dielectric for a balanced parallel strip transmission line having an RF characteristic impedance of 100 ohms; each strip is fed from a 50 ohm line. The transmission line modulator is shown schematically in Figure 3-2. One feature of the transmission line modulator is that it can be fed and terminated with coaxial lines (50 ohm unbalanced) and will allow broad bandwidth termination of the modulator driver in a matched load. Such a termination impedance is highly desirable from the standpoint of modulator driver design. The 100 ohm impedance offers a 50 percent saving in drive power.

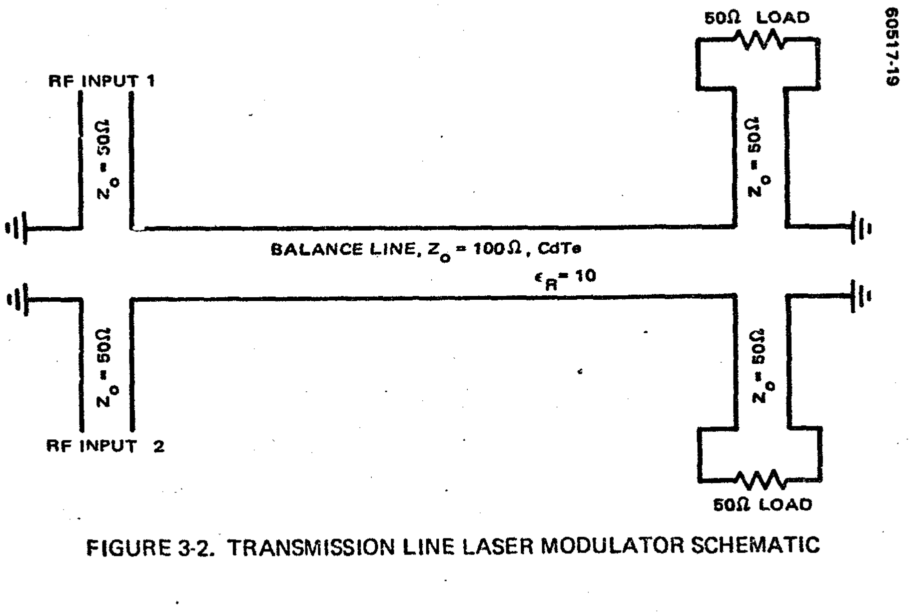

FIGURE 3-2. TRANSMISSION LINE LASER MODULATOR SCHEMATIC

Figure 3-3 shows the physical layout of the transmission line modulator as it would appear before assembly. Central to this assembly is the CdTe crystal which has evaporated film (silver) electrodes on the top and bottom faces (the 110 faces). These thick film electrodes are 0.019 inch wide and the spacing is 0.059 inch (1.5 mm), forming a 100 ohm parallel strip transmission line. The top electroded surface of the CdTe transmission line is contacted by a metalized strip (CR/AU) on the under surface of the left BeO sleeve, and the bottom electroded surface is contacted by a conducting strip on the right-hand BeO sleeve (Figure 3-3). Transition sections, coaxial to microstrip, are constructed at each of the four RF ports, thus permitting a matched transition from a 50 ohm unbalanced RF system to a 100 ohm balanced line.

Mechanical Mounting

The physical mounting of the crystal presents two seemingly conflicting requirements. The modulator rod must be clamped to suppress acoustic resonances and at the same time it is necessary to avoid straining the crystal that would introduce unwanted stress birefringence. A successful technique for modulator mounting is described below.

Acoustic resonances are generated in the crystal by the modulator driver voltage through the piezo-electric effect. Acoustic loading of the transmission line modulator is provided by two alumina or beryllia ceramic rods, one on either side of the CdTe rod shown in Figure 3-3. The acoustic

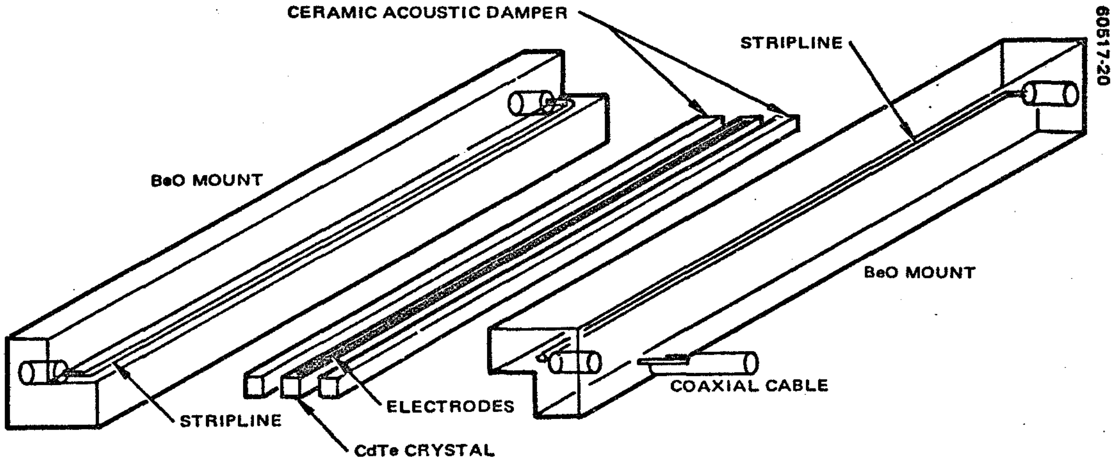

FIGURE 3-3. STRIPLINE TRANSMISSION LINE MODULATOR ASSEMBLY EXPLODED VIEW

impedance of this $A\ell_2O_3$ ceramic is 21.8 x 10^5 g/cm^2-sec which very nearly matches the 20 x 10^5 g/cm^2-sec of the CdTe rod. The wave reflection coefficient at the boundary is only 4 percent. This design requires bonding between the CdTe and acoustic damper to assure a low reflection of acoustic energy at the boundary. Ideally, the acoustic wave would pass through the boundary, propagate through the damper, and be absorbed in this material. This ideal situation is approached when the interface thickness between the CdTe and acoustic load is maintained at less than 0.01 λ_s, where λ_s is the acoustic wavelength of interest, typically $\lambda_s \approx 0.040$ inch at 1 MHz. The interface thickness thus should be less than 0.0004 inch over the length and thickness of the CdTe rod. To achieve this ideal joining of the CdTe and acoustic loading ceramic, the ceramic and crystal must have precision surfaces. In practice, it has been found that with proper surface preparation, the acoustic reflection coefficient need not be small. Successful damping has been achieved with BeO and Kovar members.

A bonding technique and bonding agent were found which eliminate the resonance peaks and which do not introduce strain birefringence in the CdTe rod. Figure 3-4 shows the special fixture used to hold the CdTe rod and electrode assembly during the bonding operation. The bonding process is done under a microscope with a bonding agent that flows at approximately 125°C. Capillary action causes a very thin film of bonding agent to flow between the CdTe/electrode interfaces at an elevated temperature. Figure 3-5 shows the frequency response of the modulator after bonding the crystal. In the data of curve B, Kerr wax was used, while in curve C, an apiezon wax was used.

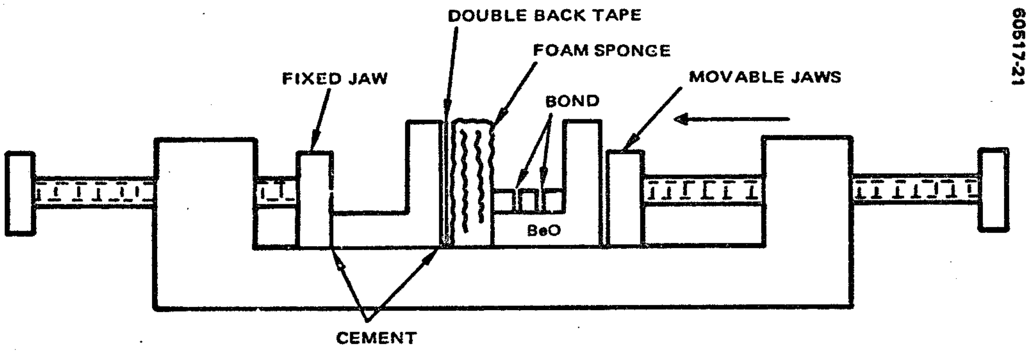

FIGURE 3-4. CRYSTAL BONDING SETUP

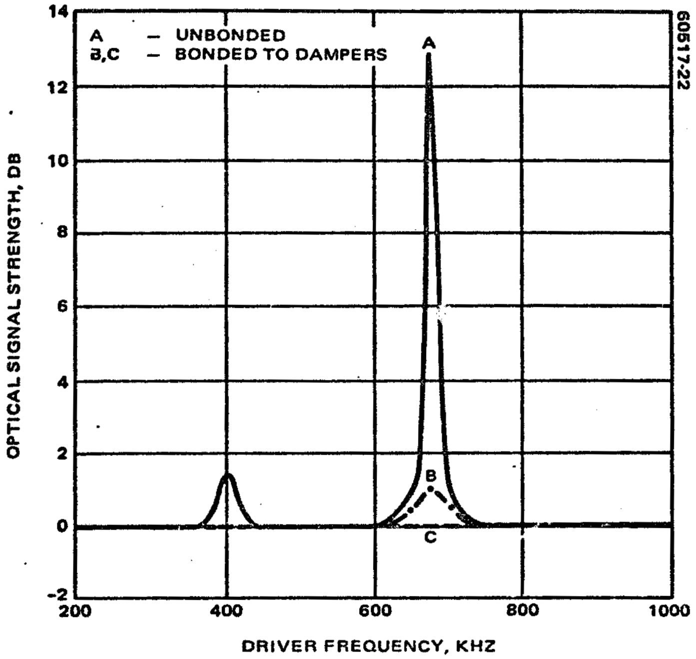

FIGURE 3-5. SWEPT FREQUENCY RESPONSE

That the bonding and mounting technique does not introduce strain birefringence can be seen in the near IR interference pattern in Figure 3-6. The photograph in the lower left-hand corner shows residual strain from crystal processing in a free-standing rod. This pattern is consistently observed in all material tested. With the mounting technique described, the crystal displays an identical pattern after assembly. The photo on the right shows strain birefringence from an improperly mounted modulator In this case, the crystal was bonded to the acoustic dampers with a thin layer of epoxy.

Thermal Considerations

The refractive index temperature coefficient of CdTe has the numerical value $1/n\ (dn/dT) = 4.4 \times 10^{-5}/{}^\circ C$. This property gives rise to a phase shift change in optical path length $\approx 0.7\ \lambda_0$ for each 1°C temperature change. Temperature stabilization is required to provide a fixed path length. The modulator internal housing is temperature controlled to approximately 60°C by a closed loop servo unit which holds the temperature to within ±0.05°C of the desired value. Figure 3-7 contains the controller circuit diagram. In addition to requiring temperature control, the temperature refractive index leads to beam bending and beam focusing in the crystal due to temperature

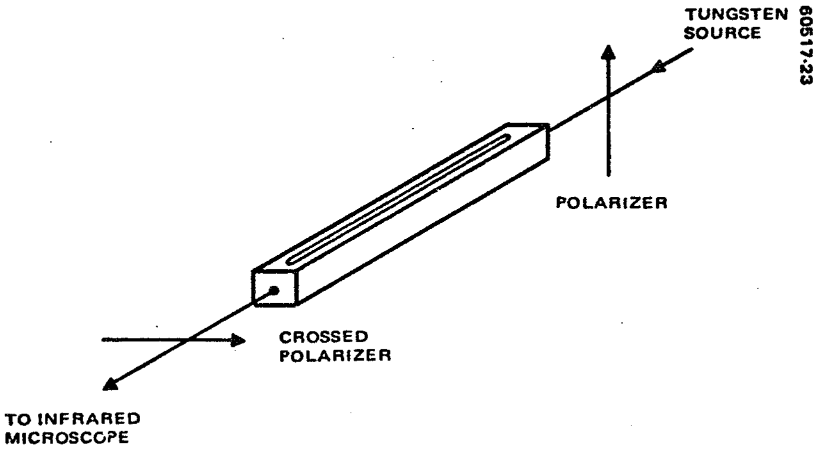

a) GEOMETRY

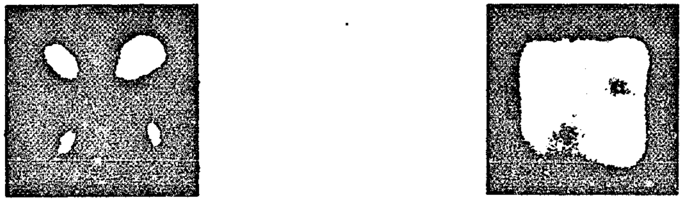

RESIDUAL STRAIN

STRAIN FROM MOUNTING

b) INTERFERENCE PATTERNS

FIGURE 3-6. NEAR IR INTERFERENCE PATTERNS

gradients. A thermal modeling of a prototype modulator housing was performed. Results are contained in Appendix C of this report. The modeling showed that it is necessary to use the high thermal conductive BeO acoustic dampers, rather than alumina, to minimize linear gradients across the rod. In addition, it showed that extreme care must be taken in avoiding air gaps around the crystal. These recommendations are utilized in the present design.

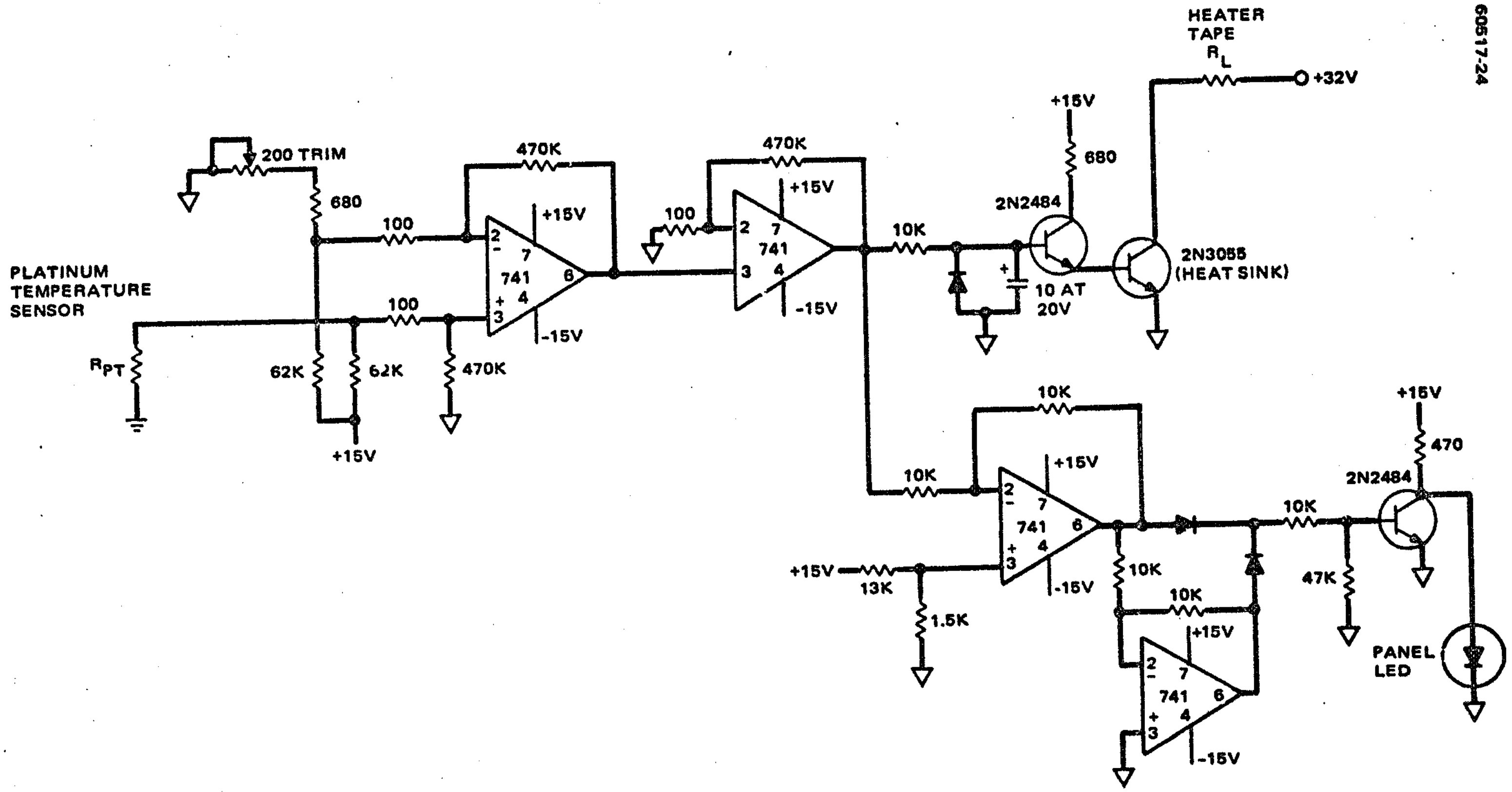

FIGURE 3-7. MODULATOR TEMPERATURE CONTROLLER USING PLATIUM RESISTOR SENSOR

Completed Assembly

An exploded view of a complete laser modulator assembly is shown in Figure 3-8. The BeO housing rides in a fiberglass inner liner. Fiberglass has been selected for its low thermal conductivity, which reduces heat loss from the temperature control heaters and thereby minimizes thermal controller power consumption. A heater tape is secured to both BeO housing members. In addition, two platinum resistors are encased in the BeO member. One sensor is used for temperature readout, while the other is in the control circuit.

The laser modulator forms an extension of the TXL optical cavity. It is necessary to accurately align the crystal to the laser bore, both in translation and rotation. Appendix D contains the alignment criteria. Consequently, the fiberglass inner liner can be mechanically aligned within the outer stainless steel outer housing to provide the necessary adjustment.

Closeup views of the modulator crystal and BeO housing are shown in Figure 3-9 and 3-10, respectively. A photograph of the assembled modulator is given in Figure 3-11. Complete specifications for the CdTe crystal are included in Appendix E.

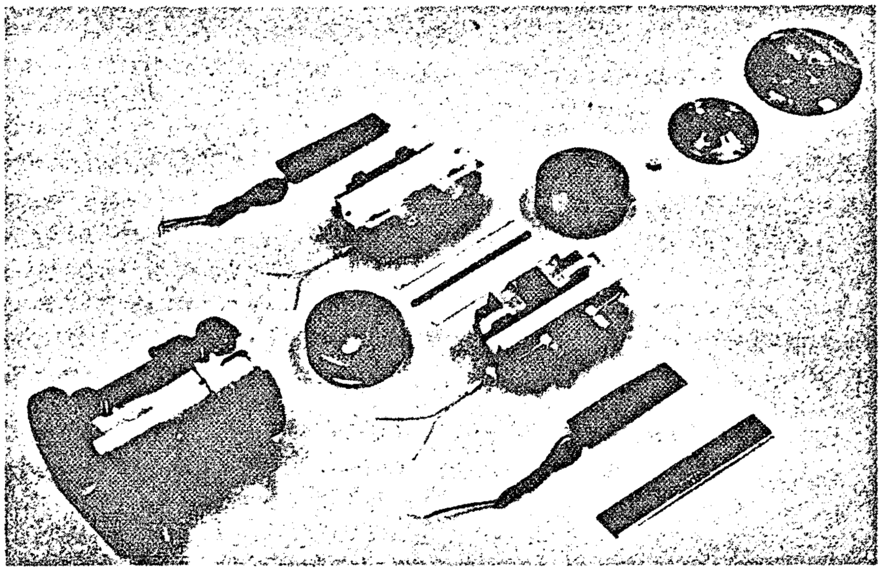

FIGURE 3-8. MODULATOR ASSEMBLY (PHOTO 75-41319)

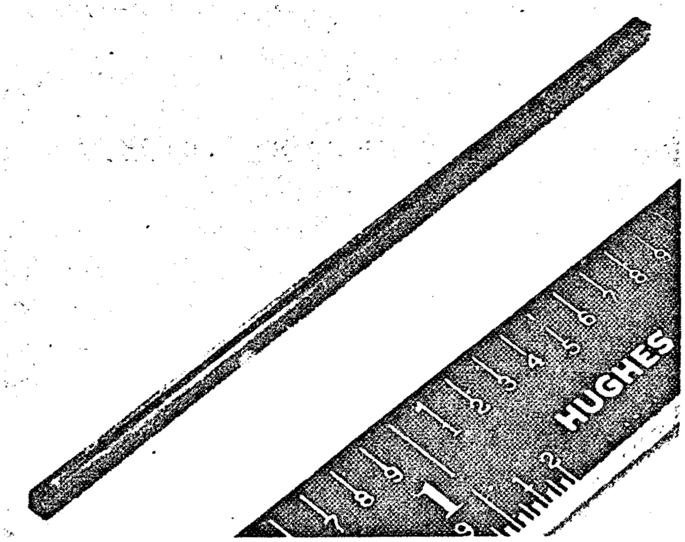

FIGURE 3-9. 1.5 x 1.5 x 60 mm CdTe SINGLE CRYSTAL
(PHOTO 75-40630)

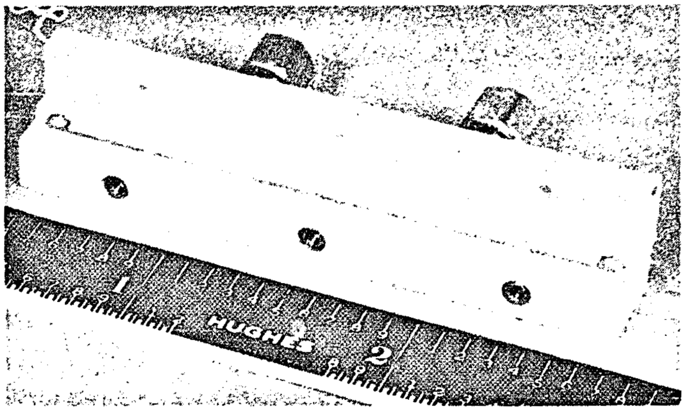

FIGURE 3-10. BeO MODULATOR HOUSING HALF SECTION
(PHOTO 75-40631)

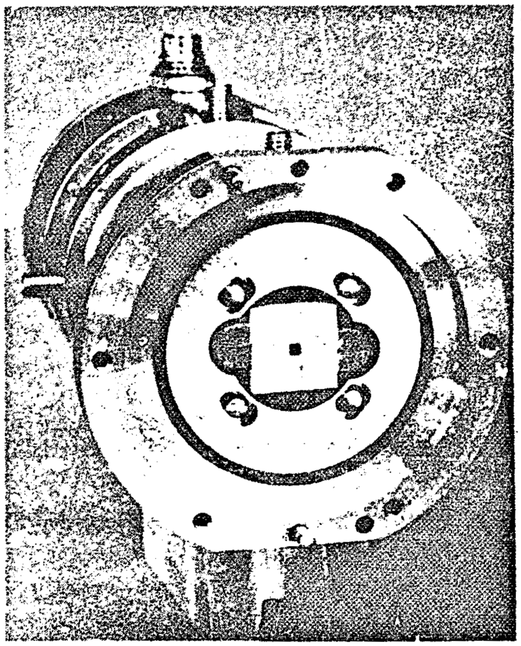

FIGURE 3-11. ASSEMBLED MODULATOR
(PHOTO 4R43486)

3.3 MEASURED PERFORMANCE

The performance of the cadmium telluride electro-optic modulator is summarized in Table 3-1.

Depth of Modulation

Depth of modulation is measured outside the cavity in a single pass configuration. A 1 watt CO_2 laser, chopped at ~100 Hz, is focused on the entrance face of the crystal. The light transmitted through the crystal then falls on a pair of wire grid polarizers. The polarizer pairs provide an extinction ratio of ~40 dB for light in the incident polarization while they present only 0.5 dB loss for the cross-polarized component. Figure 3-12 shows the direct detected waveform of modulated light, which is produced by applying a 10 kHz sine wave to the modulator.

The frequency of the modulated signal is twice that of the driver. This frequency doubling with direct dection can be easily seen from Equation 5 by letting $\Gamma(t) = \Gamma_m \sin \omega_m t$. Whence

$$c(t) = \frac{\Gamma_m^2}{8} (1 - \cos 2\omega_m t) \qquad (12)$$

The time average coupling factor is

$$<c(t)> = \Gamma_m^2/8 \qquad (13)$$

TABLE 3-1. MODULATOR PERFORMANCE

Parameter	Measured Performance
Depth of Modulation (single pass)	0.5%
Half-wave voltage	1325 V
Required drive voltage	120 V_{p-p}
Required drive power	36 W
Bulk Optical Loss	0.0015 to 0.0040 cm^1
Bandwidth	>500 MHz
VSWR	<1.3
Temperature control	0.05°C
Overall Housing Length	3.5 in.
Cylinder diameter	2.0 in.
Weight	1.3 lb

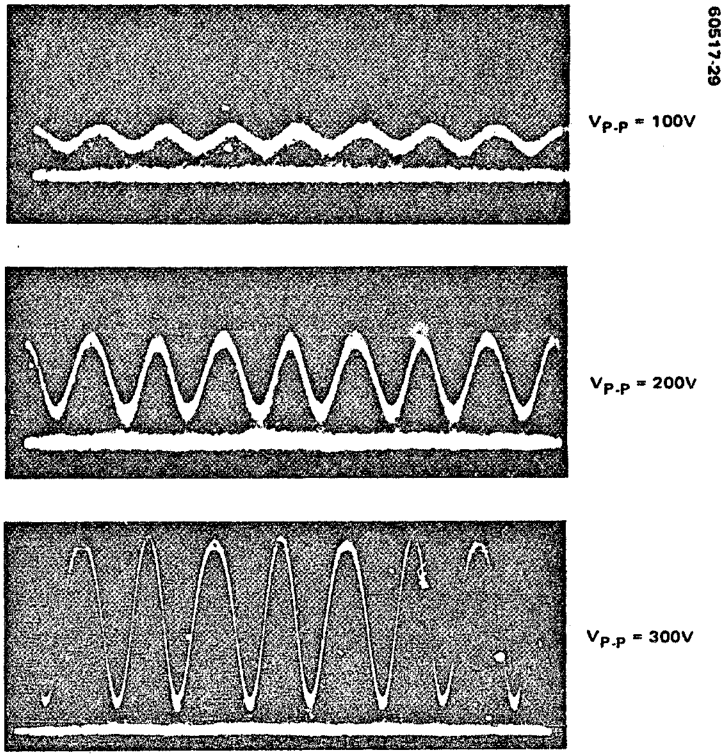

FIGURE 3 12. DIRECT DETECTION OF MODULATED 10 MICROMETER LIGHT

In Figure 3-13 the measured coupling factor is shown along with the theoretical coupling from Equation 13. The agreement between theory and experiment is good. Note that for 120 V_{p-p} drive voltage, 0.25 percent coupling is found. For a square-wave signal of the same level, the coupling becomes 0.5 percent. This value is indicated in Table 3-1. Also included in the table is the driver power required to deliver square, 120 V_{p-p} pulses to the 100 ohm modulator housing.

Optical Loss

The bulk loss of the modulator crystal is a critical parameter in transmitter performance. Therefore, an accurate knowledge of this loss is needed. As typical values are of the order 0.002 cm^{-1}, a 6 cm crystal absorbs about 1 percent of the incident light. It is difficult to measure such small absorption in a transmission measurement. Consequently, a laser calorimeter using the temperature dependence of the band gap in CdTe (Reference 4) was implemented. This technique provides a noncontacting reading of the crystal temperature when the modulator is exposed to the CO_2 laser beam. The noncontacting feature is highly desirable because of the fragile nature of CdTe.

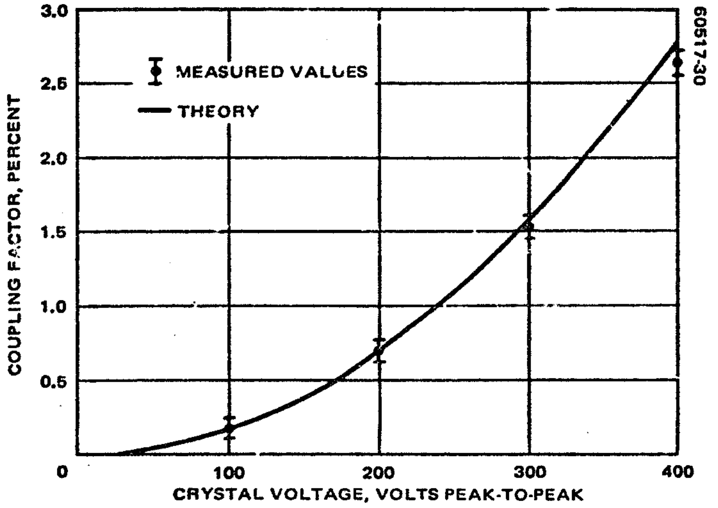

FIGURE 3-13. MODULATOR COUPLING EFFICIENCY

Narrowband (~30 Å) IR light near the band gap passes through the narrow dimension of the crystal as shown in Figure 3-14. Typically, 50 NW of power is used. The transmission is monitored with a silicon photodiode whose output is synchronously detected and recorded. When the crystal is exposed to the CO_2 laser, the crystal temperature increases due to the absorbed 10 μm energy. As a result of the temperature increase, the near IR transmission decreases. The relation between the transmission decrease and temperature change is given by

$$\Delta T = \frac{(\Delta V/V)}{\left(\frac{1}{V}\frac{dV}{d\lambda}\right)\frac{d\lambda}{dT}} \qquad (14)$$

where $\Delta V/V$ is the percent change in transmission as shown in Figure 3-15, $(1/V)\, dV/d\lambda$ is the experimentally measured steepness of the wavelength dependent transmission at the bandedge and $d\lambda/dT$ is the known shift of the bandedge with temperature.

The absorption is found from the relation

$$\alpha = \frac{\Delta T\, C_v\, d^2}{P_{inc}\, \tau} \qquad (15)$$

where C_v is the specific heat/unit volume of the modulator, d the crystal height and width, P_{inc} the heating laser power, and τ the measured thermal time constant associated with the cooling rate of the crystal which is suspended in air.

Table 3-2 is a summary of the measurements made on crystals from three separate boules. Each run represents an average of about six separate measurements. The loss value of 0.0016 ±0.0002 cm^{-1} for boule 395 is consistent with the manufacturer's standard calorimetric measurement (using thermocouples) made on the boule before rod fabrication. That method gave a value 0.001 to 0.0015 cm^{-1}. One would expect the absorption of the unprocessed boule to set the lower limit for the fabricated rods.

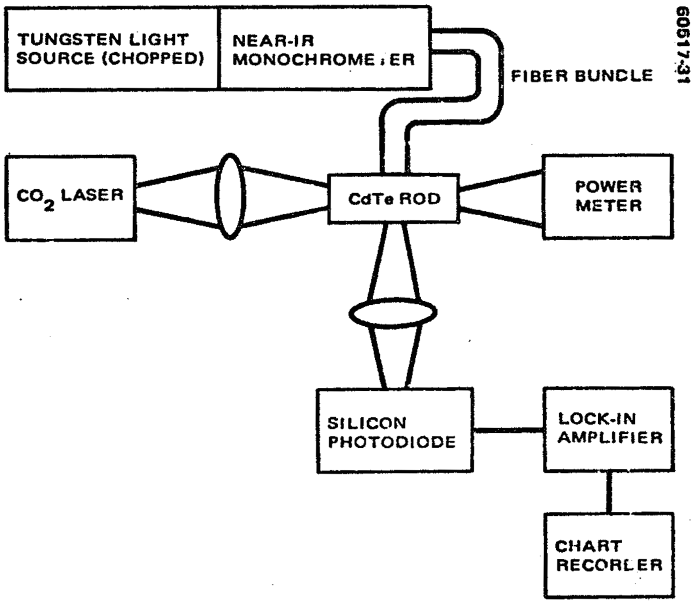

FIGURE 3-14. LASER CALORIMETER EXPERIMENTAL ARRANGEMENT

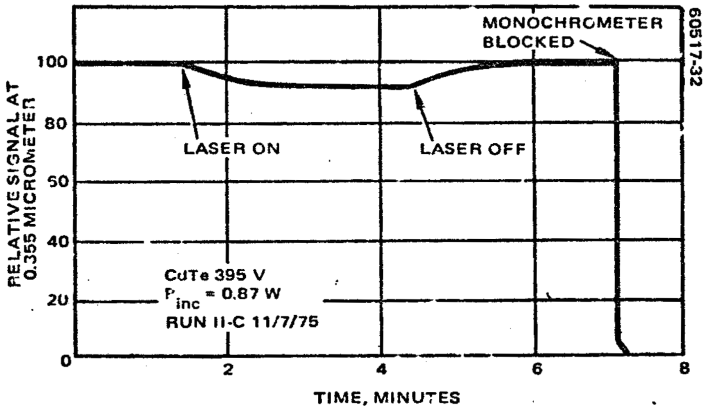

FIGURE 3-15. TYPICAL CALORIMETRIC ABSORPTION MEASUREMENT

TABLE 3-2. MODULATOR LOSS DATA

Boule No.	395	519	599
$\Delta V/V$	0.119	0.106	0.066
$(1/V)\,(dV/d\lambda)$, μ^{-1}	298	203	234
$d\lambda/dT$, $\mu/^{o}C$	2.47×10^{-4}	2.47×10^{-4}	2.47×10^{-4}
ΔT, °C	1.62	2.11	1.14
C_v, J/cm^3/°C	1.23	1.23	1.23
d, cm	0.15	0.15	0.15
P_{inc}, W	0.79	0.50	0.57
τ, sec	34.8	30.6	33.0
α, cm^{-1}	0.0016 ±0.0002	0.0038 ±0.0004	0.0017 ±0.0002

Electrical Response

Time domain reflectometer measurements of the stripline housing are shown in Figure 3-16. The balanced configuration is driven with a 180° hybrid coupler which provides the out of phase driver signals. This coupler is described in detail in Section 4. The low frequency cutoff of the hybrid results in the decaying amplitude with time just after the modulator housing. From the photographs, it is apparent that mismatch between the coaxial to stripline adapter is far worse than the modulator stripline itself. The TDR indicated a VSWR of ~1.25. Swept frequency measurements up to 500 MHz has verified this performance.

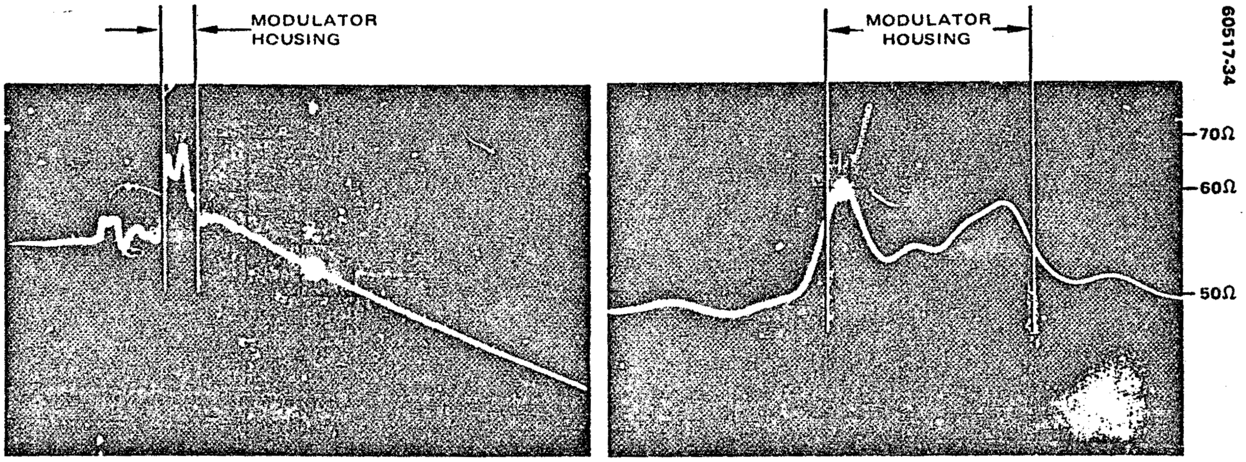

a) ρ = 0.05/DIVISION, 4 ns/DIVISION

b) ρ = 0.05/DIVISION, 0.4 ns/DIVISION

FIGURE 3-16. TDR DISPLAY OF MODULATOR HOUSING

4. MODULATOR DRIVER

Three basic types of switching circuits have been experimentally evaluated for the modulator driver: the current mode logic (CML), voltage multiplication circuit (BV_{ceo}), and linear charge-discharge circuit. The results of this evaluation show that the CML type circuit produces the fastest rise times with the greatest efficiency. Further, it was determined that the maximum gain-bandwidth product was achieved with the transistor operated well within its maximum current or voltage ratings. Switching speed of a given device is a function of the current being switched. The only advantage of selecting transistors with high collector breakdown voltage is to provide a greater derating factor. In other words, there is no advantage in selection of high BV_{ceo} transistors to increase the magnitude of the output pulse since the increase in collector current causes a degradation in the rise times.

The breadboard development effort produced a driver module that delivers nominally 30 volts peak-to-peak (p-p) into a 50 ohm load, with 300 Mbps nonreturn to zero (NRZ) data format. Efforts to achieve greater output voltage resulted in a degradation of the rise time of the module and a resultant increase in the bit-error rate. Since the requirement for the transmitter modulator is of the order of 120 volts p-p, it became obvious that a method of coupling the outputs of several driver modules would have to be developed. This was accomplished with the use of wideband hybrids that are essentially power adders; four driver modules producing 5 watts of output each will deliver 20 watts to the load. Two such combinations in a bridge configuration can supply a modulator with 120 volts p-p.

Figure 4-1 illustrates a block diagram of the complete modulator driver circuit from the emitter coupled logic (ECL) voltage levels to the output voltage to the modulator crystal. The outputs of the hybrids are matched to 50 ohm transmission lines. To prevent reflections from the modulator susceptance, which is characteristically about 8 pF, the modulator was designed to appear as a 100 ohm balanced strip line. Each 50 ohm hybrid provides a 50 ohm source impedance in a balanced configuration. A virtual ground plane exists through the center of the modulator crystal to provide an effective 50 ohm load impedance for the driver.

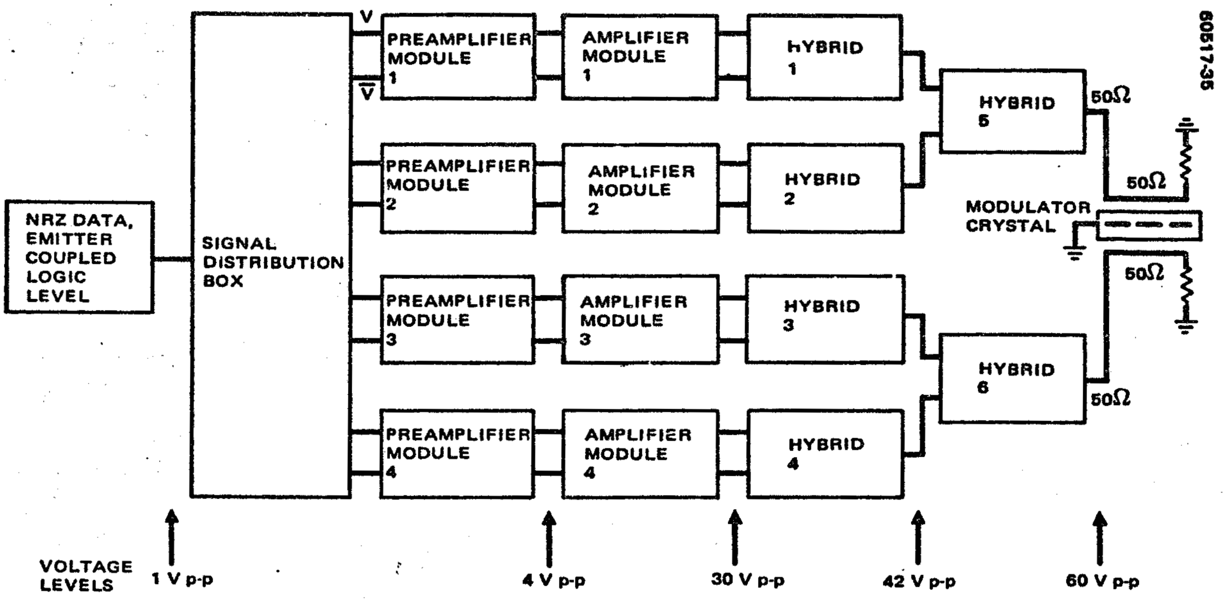

FIGURE 4-1. MODULATOR DRIVER-BLOCK DIAGRAM

4.1 CIRCUIT DESCRIPTION

Predriver Module

The input voltage to the driver circuitry is NRZ at typical ECL voltage levels and at a 300 Mbps clock rate. A preamplifier is required to amplify the logic levels up to approximately 4 volts p-p required to drive the amplifier module. A complete preamplifier module consists of two such circuits (shown in Figure 4-2). One unit amplifies the input data waveform while the other amplifies the complementary data stream derived in the signal distribution box.

Amplifier Module

The circuit shown in Figure 4-3 was selected over all circuits tested as being the fastest, most efficient, and most versatile. The circuit operates in a nonsaturated switching mode where the current is alternately directed through Q1 and Q2, producing equal amplitude, 180° phased output voltages. The following advantages of this circuit should be noted:

- Stability - Circuit performance is essentially independent of variations in transistor parameters since if $V_{EE} \gg |V_{in}|$ the circuit current is $I_{EE} \simeq V_{EE}/R_E$.
- Phase/amplitude balance - The 180° phase relationship at the output is guaranteed and the amplitude balance is a function of the equality of R_{c1} and R_{c2}.

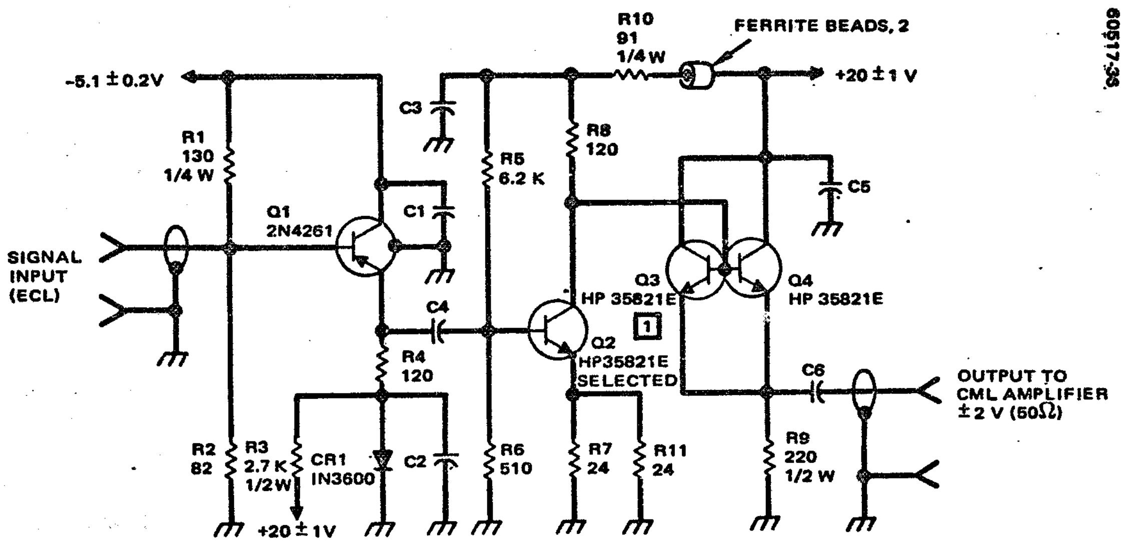

1 SELECT FOR $H_{FE} \geq 70$

ALL RESISTORS IN OHMS, 1/8 W, UNLESS OTHERWISE NOTED
ALL CAPACITORS ARE 1 μF, 50V, UNLESS OTHERWISE NOTED

FIGURE 4-2. PREAMPLIFIER SCHEMATIC

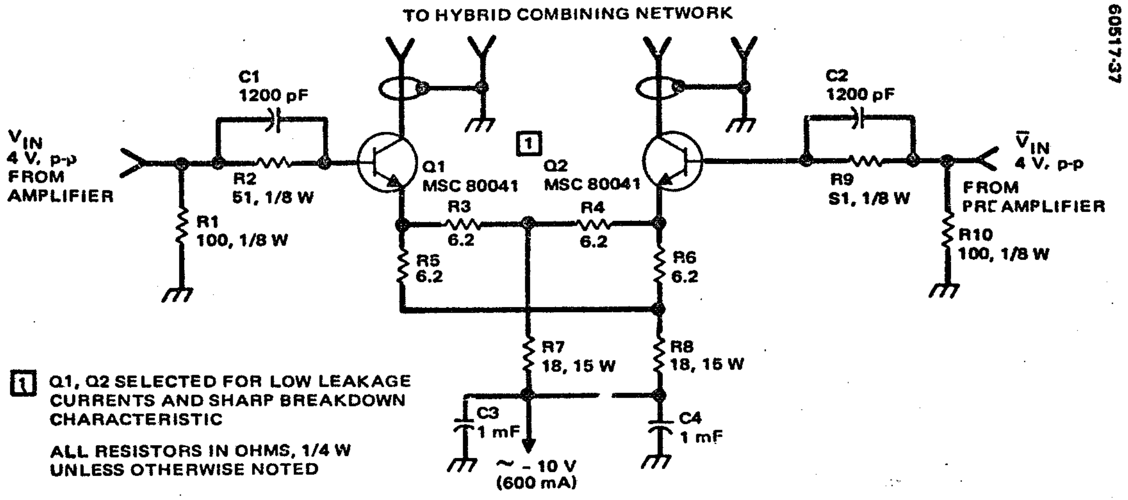

1 Q1, Q2 SELECTED FOR LOW LEAKAGE CURRENTS AND SHARP BREAKDOWN CHARACTERISTIC

ALL RESISTORS IN OHMS, 1/4 W
UNLESS OTHERWISE NOTED

FIGURE 4-3. CML AMPLIFIER SCHEMATIC

- Power supply transients - Since the circuit current is alternately switched between Q1 and Q2, the power demand from the V_{EE} and V_{cc} supplies is constant, thereby eliminating any large transient currents in the power supplies.

Parts stress derating policies for transistors used in space have been established by the Hughes Space and Communications Group Product

TABLE 4-1. MSC80041 OPERATING CONDITIONS

Category	Vc, V	i_c, A	Transistor Power Dissipation, W	$T_{junction}$ at T_{case}, °C
Maximum rated	50	1.0	11.66 minimum	200° at 25°
Maximum derated	45	0.8	6.0 minimum	115° at 25°
Operating (peak)	40	0.6	3.0	
Operating (average)	20	0.3	1.5	<115° at 25°

Effectiveness Directive (see Appendix F). The modulator driver output transistors are stressed more than other components and thus have been evaluated with respect to derating category. Table 4-1 lists the operating conditions for the MSC80041 in the driver circuit, the maximum operating conditions, and the maximum derated conditions.

The above deratings are for typical RF type applications. Since the driver application is more of a switching application, the derating methods applied to diodes may be more appropriate. In either case, the transistor lies within acceptable operating regions for space qualified operation. Figure F-1 of Appendix F shows the operating point for the RF case and the switching case.

180° Hybrid Coupler

A 3 dB, 180° hybrid coupler is a device that interfaces quite naturally with the CML amplifier. An ideal 180° hybrid coupler arrangement is shown in Figure 4-4. In this figure, if the inputs at C and D are 180° out of phase and equal in magnitude, then the output at port A is $\sqrt{2}$ times the magnitude of the input voltages. Port B is referred to as the isolated port since in this particular case no power is dissipated in the termination. The impedance level at all four ports of the hybrid is 50 ohms.

The implementation of the coupler in a CML driver module is shown in Figure 4-5. If both collector output voltages are used, the coupler can be utilized as the combining mechanism to obtain an output voltage that is $\sqrt{2}$ times the output voltage at either collector.

The practical realization of the arrangement in Figure 4-5 presents two problems; first, each port of the hybrid is a dc short circuit to the case. Second, each port is connected (dc) to all other ports internally as well as through the case (ground return). These problems are resolved by using the coupler as the collector supply via its case and internal connections. A schematic of the test circuit is shown in Figure 4-6. For this circuit, the voltage at ports C and D is 600 mA x 50 ohms = 30 volts p-p, and the expected value of $|v_{out}|$ is $30\sqrt{2}$ = 42 volts.

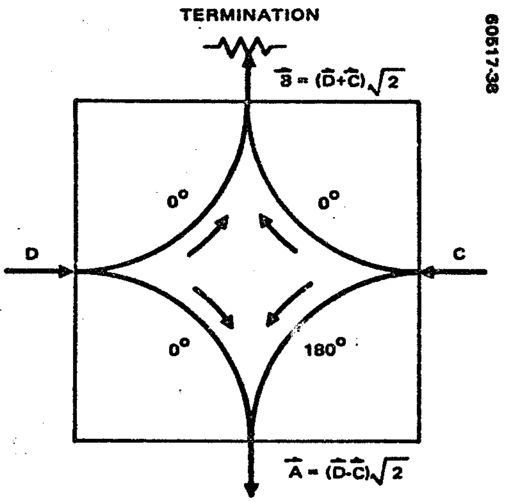

FIGURE 4-4. 0° TO 180° HYBRID COUPLER REPRESENTATION

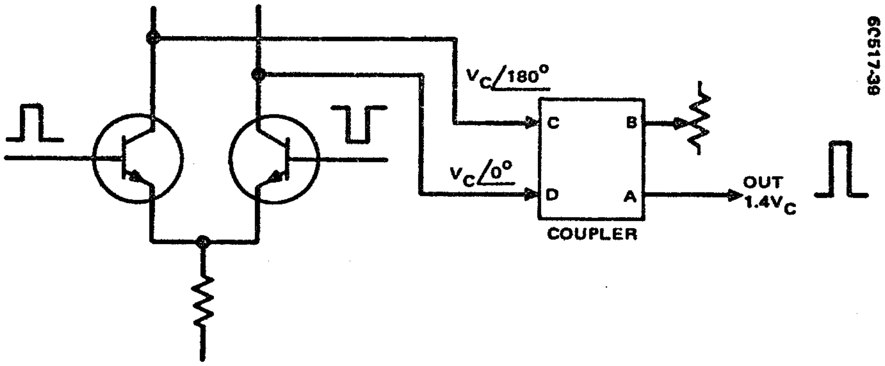

FIGURE 4-5. 180° COUPLER IN CML DRIVER CIRCUIT

Custom assemblies containing three hybrid couplers (Nos. 1, 2, and 5 in Figure 4-1) with bias ports for the CML driver modules were provided by Vari-L Inc. Specification of these units are contained in Appendix G. The overall insertion loss is 1 dB, thereby reducing the combined voltage from 60 to 53 volts.

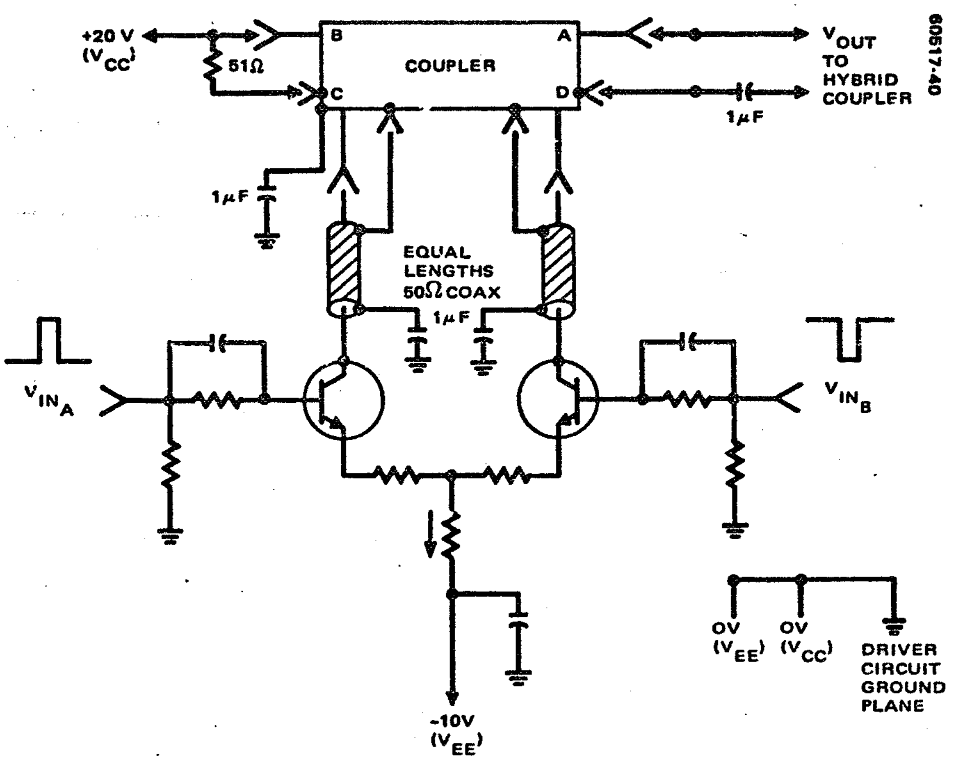

FIGURE 4-6. CML/HYBRID CIRCUIT

4.2 MODULATOR DRIVER PACKAGE DESCRIPTION

A modulator driver module consists of two preamplifiers (Figure 4-2) and the CML amplifier (Figure 4-3) which are contained in an aluminum housing 4-3/4 x 2-1/4 x 1 inches, including connectors, and weighs 7 ounces. A complete driver contains four such modules. Figure 4-7 shows a completed module.

The completed driver, which is presently housed in a standard 19 inch rack, 3 inches high by 14 inches deep, is shown in Figure 4-8. The signal distribution box measures 4-1/2 x 3 x 0.5 inches and weighs 6 ounces. (See Appendix G for the physical specifications of the hybrid assembly.)

4.3 MODULATOR DRIVER MEASURED PERFORMANCE

The modulator driver performance is summarized in Table 4-2. The output voltages indicated are those appropriate to the 100 ohm balanced modulator housing stripline design. In this subsection, the voltage waveforms shown represent one-half of the driver assembly, driving a 50-ohm unbalanced load. These voltage levels are one-half of the values shown in the table.

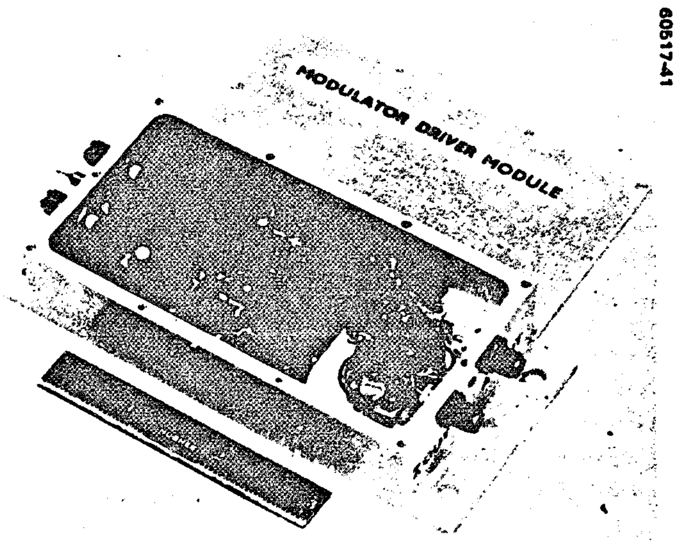

FIGURE 4-7. MODULATOR DRIVER MODULE (PHOTO 75-40954)

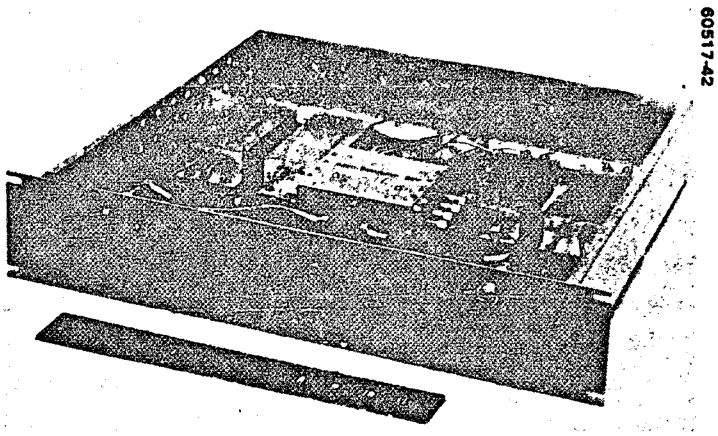

FIGURE 4-8. MODULATOR DRIVER ASSEMBLY
(PHOTO 4R42471)

Voltage Waveforms

Figure 4-9a shows the voltage waveform of the driver for a pseudo-random, NRZ word of 300 Mbps. In 4-9b the "eye pattern" of the waveform is presented. Some degree of intersymbol interference is apparent. The overall degree of degradation from this intersymbol interference was measured by driving the laser modulator, detecting the optical signal and performing a BER measurement. This measurement is described below.

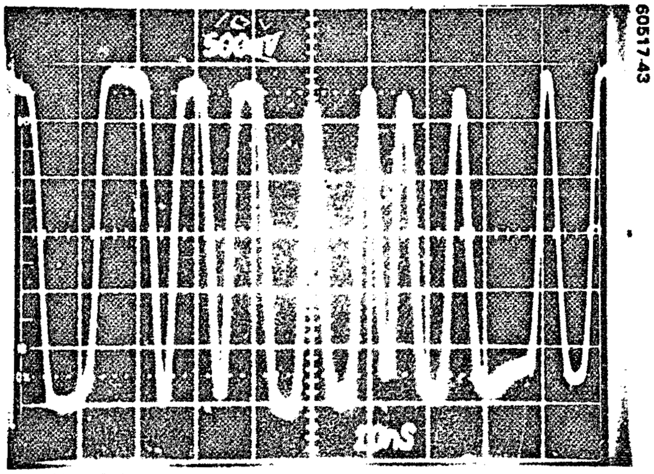

a) PSEUDORANDOM NRZ WORD

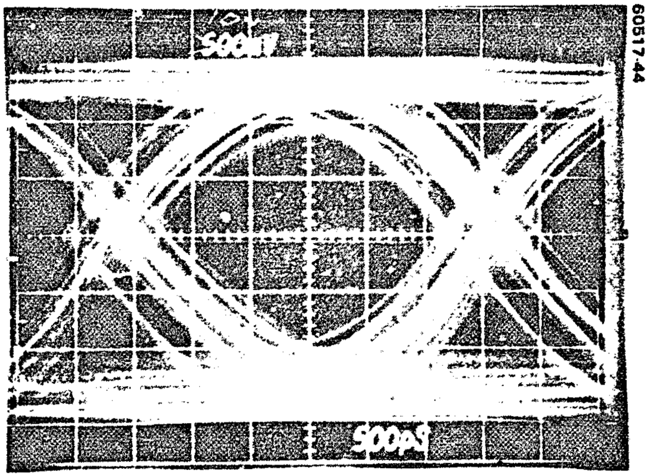

b) EYE PATTERN

FIGURE 4-9. MODULATOR DRIVER OUTPUT WAVEFORMS

TABLE 4-2. MODULATOR DRIVER PERFORMANCE

Parameter	Measured Performance
Input voltage level	ECL
Balanced output voltage	110 Vp-p at 100 ohms 44 Vrms at 100 ohms
Data rate	300 Mbps
Rise time	1.5 ns
Fall time	2.0 ns
Pulse droop	63/160, %/ns
DC input power	78 W
Efficiency	25%
Volume	150 in^3
Weight	3.7 lb

4.4 BIT ERROR RATE TESTS

The low frequency rolloff characteristics of the driver introduced by the hybrid make it necessary to use a short NRZ word for BER tests. For the tests reported here, a 127 bit pseudorandom word used, such that the word frequency was 2.34 MHz.

Figure 4-10 illustrates the 300 Mbps waveform at different points in the system. Notice that the small amount of pulse droop seen at the driver output is corrected by the level detection circuit of the receiver. The penalty for this is a greater signal-to-noise ratio requirement for a given BER.

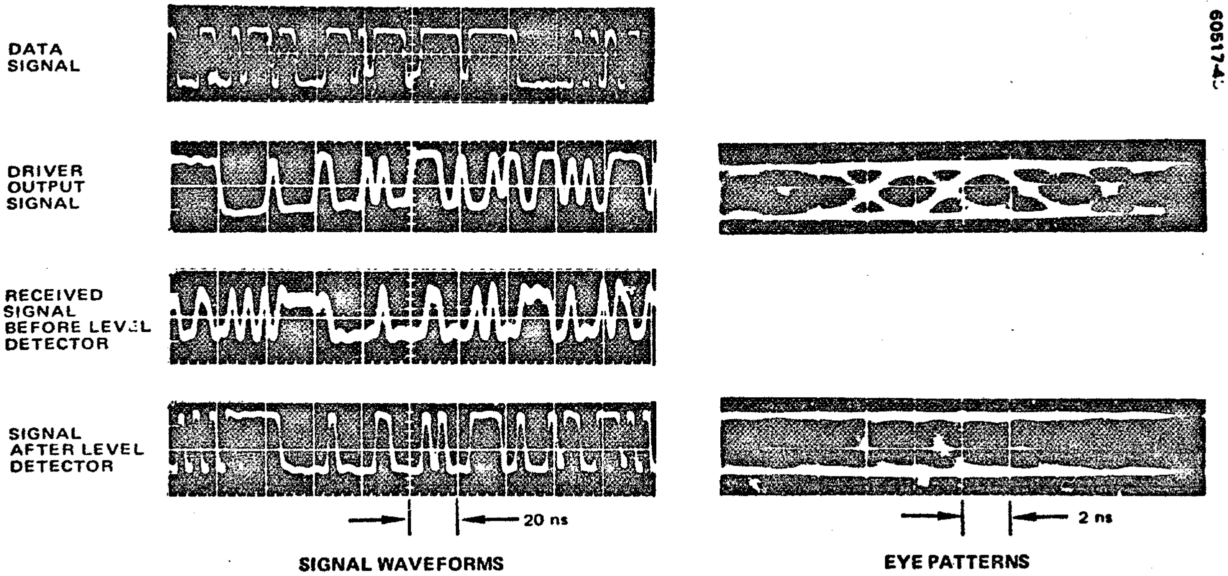

FIGURE 4-10. 30 MBPS DIGITAL SIGNAL WAVEFORMS AND EYE PATTERNS AT VARIOUS POINTS IN SYSTEM

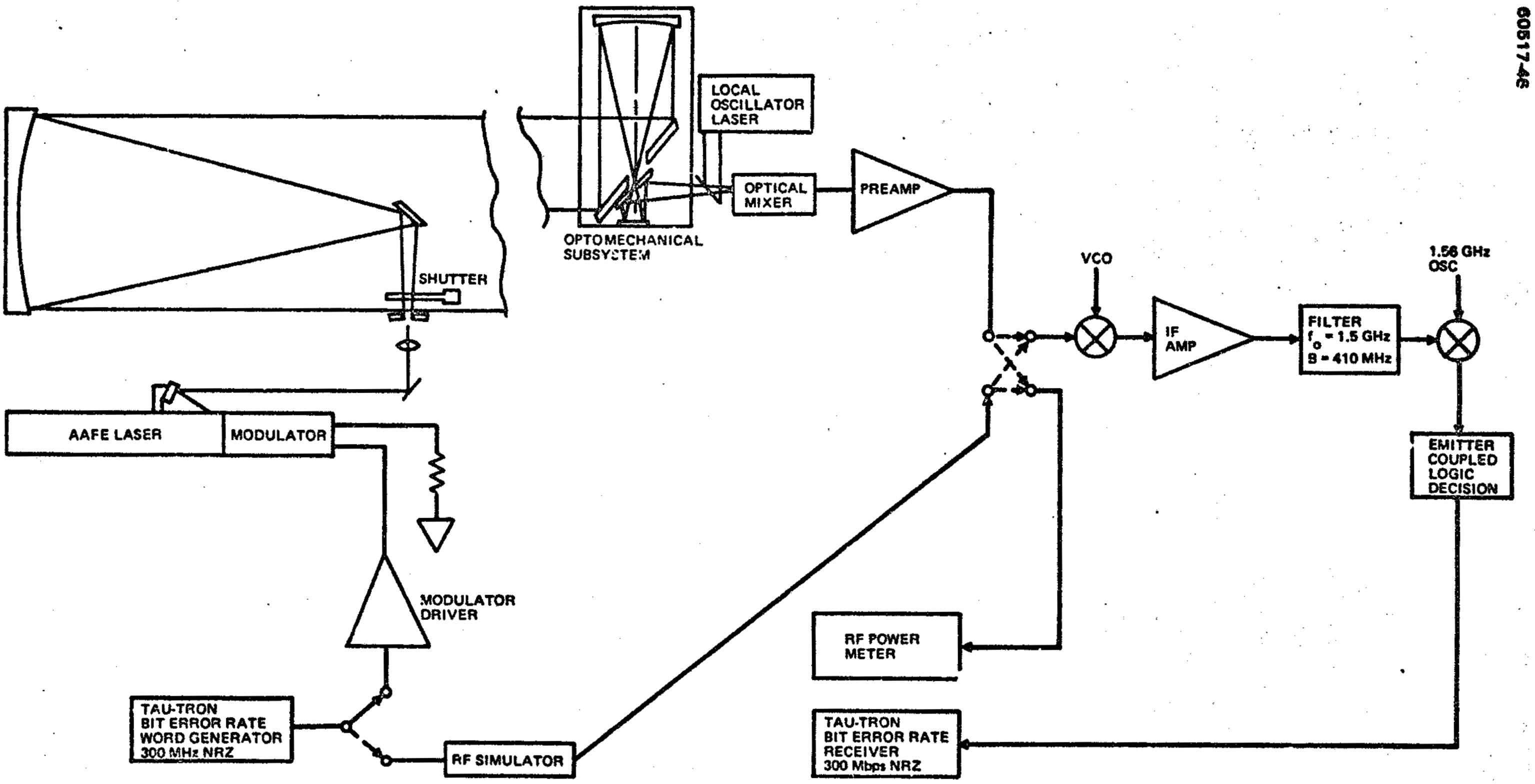

FIGURE 4-11. 300 MBPS BIT ERROR RATE MEASUREMENT TEST ARRANGEMENT FOR CO_2 LASER COMMUNICATIONS

Measurement Method

The method of measuring signal to noise is illustrated in Figure 4-11. The signal plus noise power (S+N) and the noise power (N) is measured with an RF power meter at the output of the preamplifier. The beam is completely blocked for the measurement of noise power. Thus, the measured ratio is

$$\left(\frac{S+N}{N}\right)_P$$

and

$$\left(\frac{S}{N}\right)_{IF} = \left[\left(\frac{S+N}{N}\right)_P - 1\right] \frac{B_p}{B_{IF}}$$

where B_p is the noise bandwidth at the output of the preamplifier and B_{IF} is the bandwidth of the Bessel filter in the IF. For each measurement of $(S/N)_{IF}$ a corresponding measurement of BER is made and the points are plotted. The resultant data are plotted to produce a BER curve.

Bit Error Rate Data

Data taken for BER versus SNR are plotted in Figure 4-12 for both the RF simulator and the complete laser link. The data rate was 300 Mbps and used a NRZ format. The laser used was the AAFE test transmitter with the ECL driver 1. The local oscillator offset frequency was 260 MHz.

These data can be compared with those taken on the receiver electronics with the RF simulator given in Figure 4-13. The performance of the simulator with an offset frequency of 260 MHz is far better than that at 200 MHz, since less data spectrum foldover is encountered, and is similar to previous AIL measurements taken with a 500 MHz offset.

The data taken through the laser communication system are consistently 0.5 to 1.0 dB below that achieved with the simulator. Most impressive is the laser system performance with an IF signal-to-noise ratio of 14 dB, where the difference from the simulator data is only 0.4 dB. Further data taken at higher signal-to-noise ratios were equally impressive. During one sequence, no errors were counted for 6 minutes with a signal-to-noise ratio of 25 dB, an equivalent bit error rate of $<10^{-11}$.

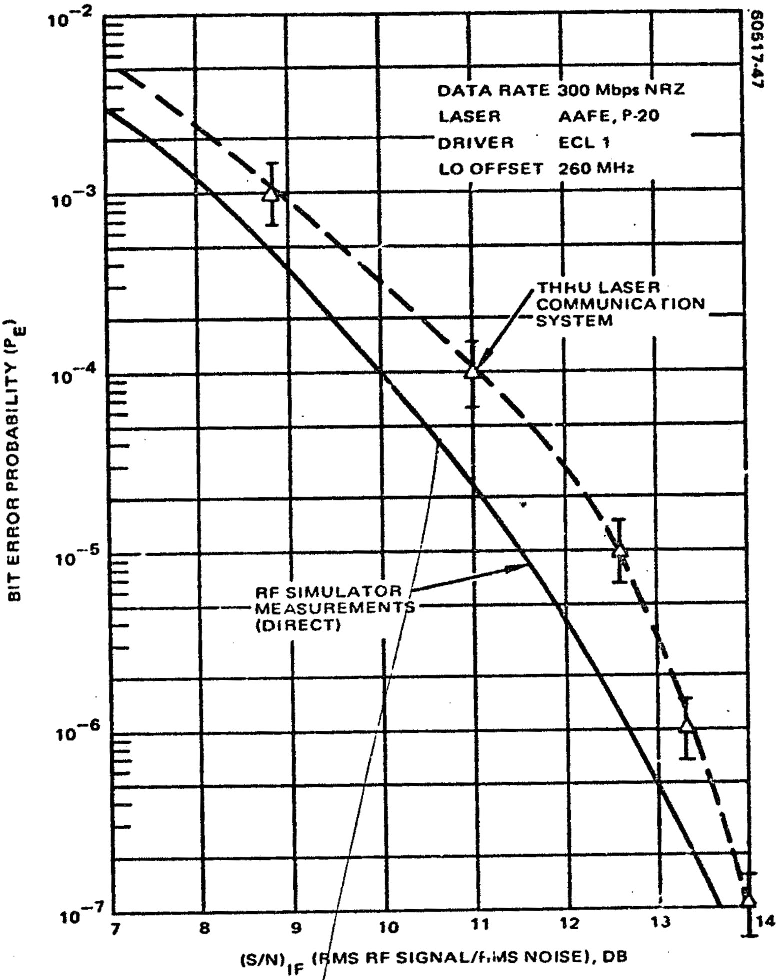

FIGURE 4-12. BIT ERROR RATE OF LASER LINK COMPARED WITH RF SIMULATOR MEASUREMENTS OF RECEIVER BACK END

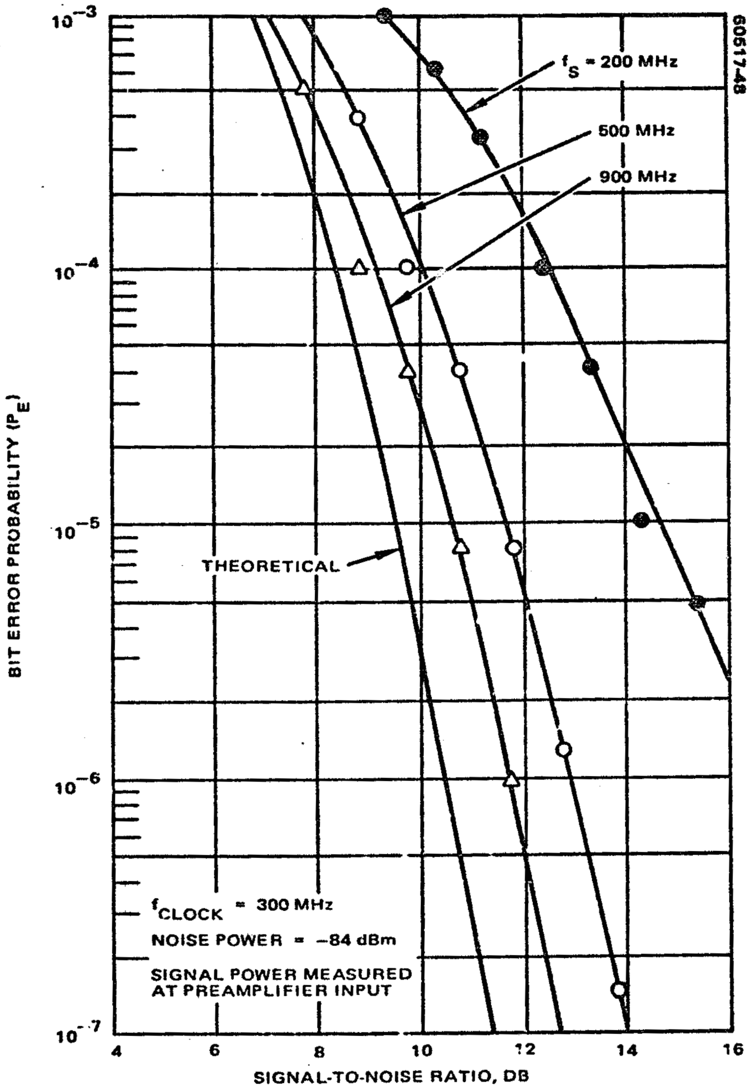

FIGURE 4-13. ORIGINAL AIL BIT ERROR RATE PERFORMANCE DATA OF RECEIVER BACK END

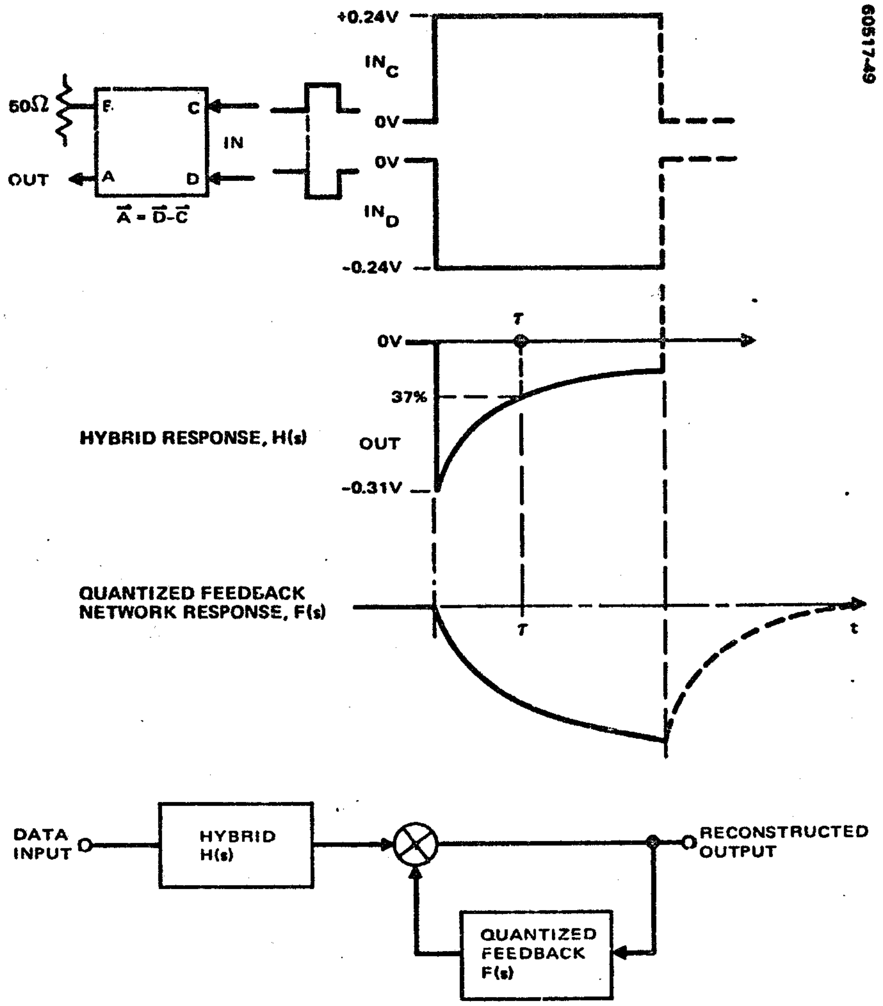

FIGURE 4-14. PULSE DROOP OF HYBRID RECONSTRUCTED WITH QUANTIZED FEEDBACK

4.5 QUANTIZED FEEDBACK

Although BER performance for the short 127 bit test word is close to theoretical, long strings of "ones" and "zeros" in a real data system are subjected to pulse droop which will deteriorate the error rate performance. A method of avoiding this problem will be required to achieve the desired performance in a field environment. The technique of quantized feedback has been investigated for this purpose (Reference 5).

The low frequency performance of the hybrid is shown in Figure 4-14. It is seen that the output fall to 1/e point in 160 ns which is equivalent to a low frequency cutoff of about 1 MHz. The principle of the quantized feedback system is to regenerate the low frequency components of the signal. The hybrid response H(s) and the quantized feedback network F(s) response are matched so that

$$H(s) + F(s) = 1$$

The difficulty of this approach is that the quantized feedback response time must be substantially shorter than one bit time. At data rates of 300 Mbps, where the bit interval is 3.3 ns, the response time of the circuit must be a fraction of a nanosecond. Such a circuit has been constructed and tested at 60 Mbps. Although the technique is extendable to 300 Mbps, extreme care in circuit design is required to achieve ideal performance.

5. TRANSMITTER LASER PERFORMANCE

Sections 2, 3, and 4 evaluated the performance of the laser, modulator, and driver as individual units. In this section, the performance of the assembled transmitter is presented. Design considerations including design tradeoffs are first discussed. This is followed by a description of the transmitter package. Finally, the measured performance is discussed.

5.1 DESIGN CONSIDERATIONS

Optimization of Output

It has been shown that the modulated output power is given by

$$\langle P_{\perp} \rangle = \pi^2 \eta_g P_{cir} P_M / P_{\pi} \qquad (1)$$

where the circulating power is

$$P_{cir} = \frac{P_{sat}}{2P_{th}} \left[P_L - P_{th} \right] \qquad (2)$$

Combining these results gives

$$\langle P_{\perp} \rangle = \frac{\pi^2}{2} \eta_g \frac{P_{sat}}{P_{th} P_{\pi}} P_M \left[P_L - P_{th} \right] \qquad (3)$$

Of prime importance for space application is the total electrical power P_T consumed by the transmitter. Note $P_T = P_L + P_M$. The available output power for a given input power is determined by the division of the total power between laser and modulator. Differentiating with respect to P_M for fixed P_T shows that the optimum division occurs for

$$P_M = \frac{1}{2}\left[P_T - P_{th}\right] \qquad (4)$$

at which point the output power is

$$\langle P_1 \rangle = \frac{\pi^2}{8}\,\eta_g\,\frac{P_{sat}}{P_{th}\,P_\pi}\left[P_T - P_{th}\right]^2 \qquad (5)$$

(This expression is only approximate since P_{th} depends to a small degree on P_M. See Appendix H for a rigorous derivation. The result in Equation 5 is accurate to within 10 percent.) Using representative values of $\eta_g \sim 0.8$, $\eta_{md} \sim 0.25$, $P_{sat} \sim 35$ watts, $P_{th} \sim 18$ watts, $P_\pi \sim 17.6$ kW/η_{md}, Equation 5 shows that 0.5 watt average output power is the maximum amount attainable for 150 watts prime electrical power.

This optimization procedure is examined in more detail in Figure 5-1, in which the output power from Equation H-1 is shown versus the ratio of modulator prime power to total power. Of the design parameters listed, only η_{hv} and r_2 are estimated values at this point. All other values are taken from measured quantities. At low values of the ratio P_M/P_T the output falls in Figure 5-1 because the resulting driver voltages are small, as indicated by the rms volts scale accompanying the figure. At large values of P_M/P_T, the output again falls as the circulating power is reduced as shown in the figure. The bold arrow shows the position on the curve of the present transmitter design. The design is near optimum, as only a 4 percent increase in power would result at the optimum division between laser and modulator power. The design favors the region of lower circulating power and higher driver voltage.

Circulating Power

The preceding discussion was based on an estimated effective modulator effectivity, r_2, of 90 percent. In Figure 5-2 the dependence of both output power and circulating power on r_2 is shown. The 1.9 dB difference between peak and average optical power results from the measured modulator driver performance

$$\left[V_{peak}/V_{rms}\right]^2 = \left[55/44\right]^2 = 1.9 \text{ dB}$$

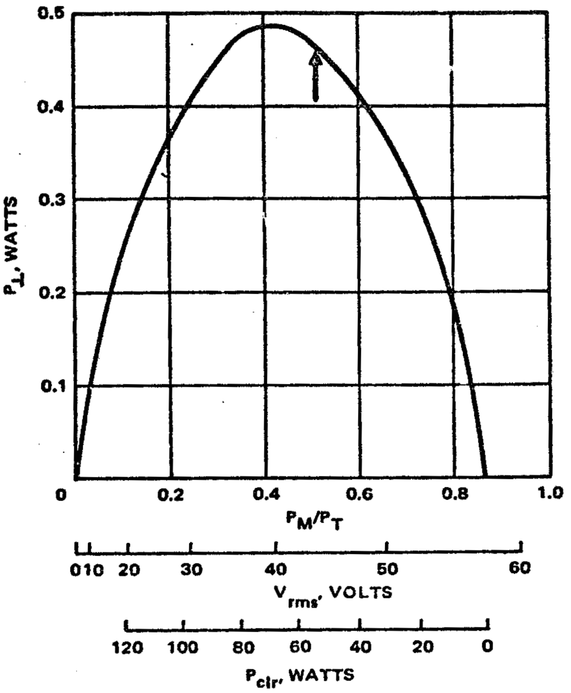

DESIGN PARAMETERS

P_T	153.2W
η_{hv}	85%
η_{md}	25%
D_{sec}	2.66 W/cm
R	100Ω
ℓ/d	40
g_o	0.012 cm^{-1}
P_s	34.5W
η_g	80%
r_1	97%
r_2	90%

FIGURE 5-1. OUTPUT POWER VERSUS RATIO OF MODULATOR PRIME POWER TO TOTAL POWER

For a design goal of 0.7 watt peak power, the figure shows that the circulating power must be 52 watts. A value of $r_2 \geq 89.6$ percent is therefore required.

Cavity Losses

The modulator loss arises from two sources, absorption and self-focusing. Thus the effective reflectivity can be written as

$$r_2' = (1 - \ell_{coating} - \ell_{bulk} - \ell_{mc})\, r_2 \qquad (6)$$

where the losses refer to the AR coatings, bulk material and mode conversion due primarily to self-focusing. The actual end-mirror reflectivity is r_2. Mode conversion is discussed first.

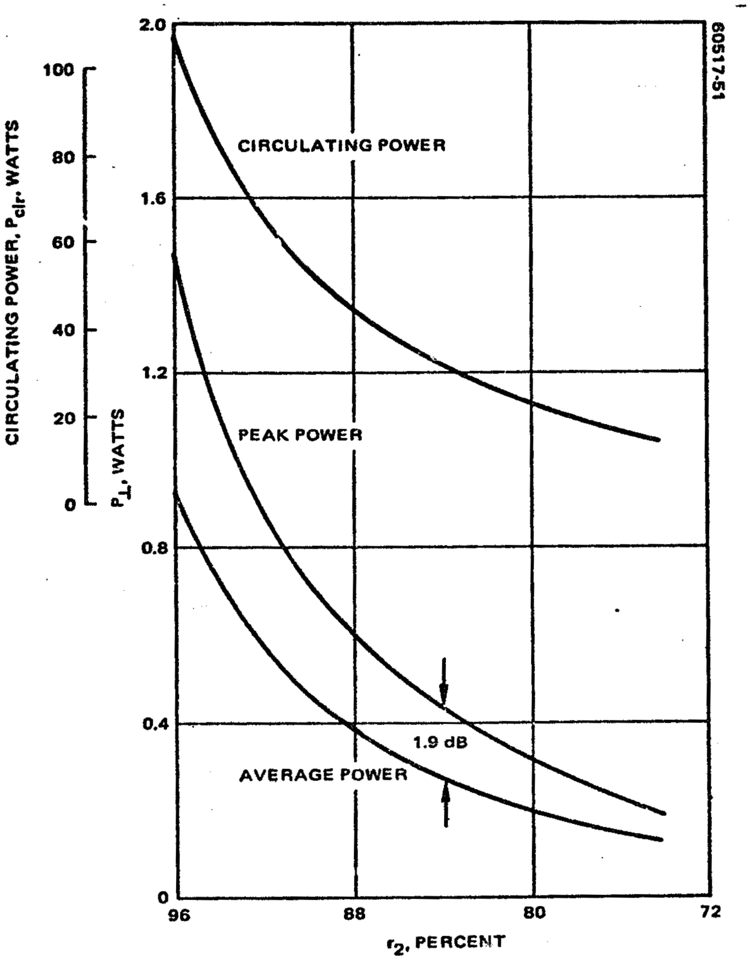

FIGURE 5-2. DEPENDANCE OF OUTPUT AND CIRCULATING POWER ON r_2

Any mechanism that converts light propagating in the fundamental waveguide mode into higher order modes will introduce loss since the higher order modes are more strongly attenuated. Such conversion can arise from surface imperfection, cavity misalignment, and thermal gradients in the modulator. Proper care in alignment in laser bore fabrication and polishing of the ceramic components result in surface conditions that exhibit apparently no mode conversion for a 1.5 mm tube.

Similarly, proper attention to alignment of the bore with the modulator rod can eliminate mode conversion resulting from misalignment. In

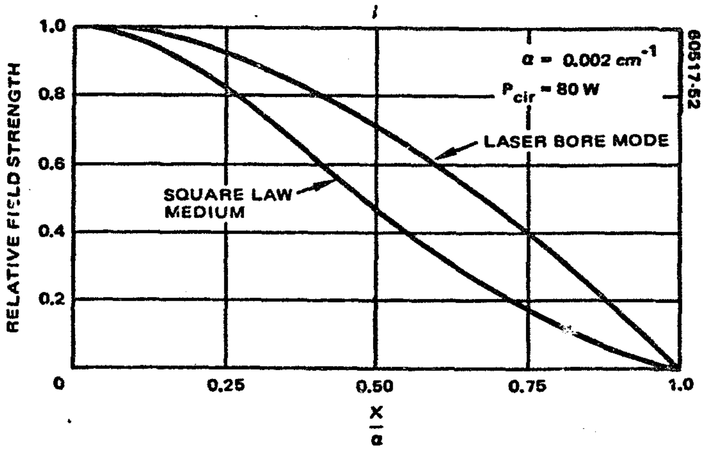

FIGURE 5-3. ELECTRIC FIELD FUNDAMENTAL MODE DISTRIBUTION

Appendix D, alignment tolerances on tilt, displacement, and separation between bore and rod are calculated. It is shown that an angular tilt of ≤100 mrad, a transverse displacement of ≤12.5 μm, and an axial separation of ≤3 mm will be required to avoid mode conversion. It is for this reason that the modulator rod is mounted in a fixture that permits such alignment.

Mode conversion arising from thermal gradients in the modulator presents a mechanism that depends on circulating power level and cannot be eliminated at high power. Its effects must be dealt with. In Appendix C the modulator thermal housing design is investigated. This study shows that, even for optimum thermal conditions, significant temperature gradients exist at high power level. For example, with 80 watt circulating power in a CdTe crystal with $\alpha = 0.002\ \text{cm}^{-1}$, a drop of 0.50°C occurs across the rod. Since CdTe possesses a positive refractive index coefficient, $(1/n)\ dn/dT = 4.4 \times 10^{-5}$°C, the light tends to become more concentrated at the center of the rod than the light in the laser bore.

The magnitude of this effect has been estimated by treating wave propagation in a square law index distribution across the rod. (See Appendix C.) This profile is chosen for mathematical convenience and is not meant to represent actual gradients. In Figure 5-3 the electric field distribution of the fundamental mode is shown for the thermal conditions above. Also shown is the mode structure for the uniform index distribution of the laser bore. Modes that vanish at the wall were used. In reality, a small tailing into the modulator electrodes and surrounding medium exists which introduces loss. Since the higher order modes have more penetration, their loss can be significantly greater. For purposes of estimating mode conversion, however, the distribution of Figure 5-3 is good.

Mode conversion results from coupling of the laser fundamental mode into the higher order modulator modes at the junction between the two. Now if all modes possessed the same loss coefficient and had the same phase velocity, then after reflection from the end mirror and upon re-entering the bore, the identical laser mode would be re-excited with no mode conversion. However, the higher order mode suffers more loss; the exact losses are not known. In addition, the difference in phase velocities is such that different modes can slip in phase several radians while passing through the rod. The approximate thermal gradients used cannot describe these velocities in sufficient detail. The model can be used to estimate an average loss by assuming that all light coupled into the higher order modes is lost. The loss has been computed in Appendix C and is shown in Figure 5-4 in the form of ℓ_{mc} (αPc).

Projected Performance

It is now possible to plot the circulating power from Equation 6 as a function of the modulator absorption coefficient, using the results of Figure 5-4 for the mode conversion contribution, taking $2\alpha\ell$ for the bulk loss

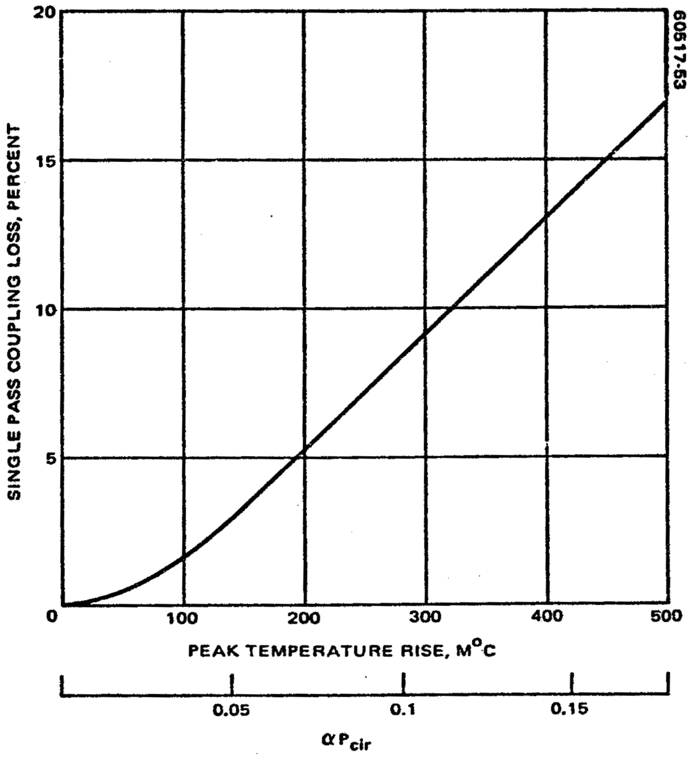

FIGURE 5-4. ESTIMATE OF MODE CONVERSION LOSS

term, and assigning a value of 1 percent loss for the coatings. In Figure 5-5 the circulating power is presented for two end-mirror situations. Curve A is plotted for a total reflector (1 percent loss) at the modulator end of the laser. Such might be the configuration in a flight transmitter. In practice to date, however, an output mirror is used to sample to circulating power in the cavity. The circulating power is shown for the mirror used: r_2 = 96.5 percent (2.7 percent transmitting). From the figure it is seen that an absorption coefficient of 0.001 cm^{-1} is required to achieve the goal of 52 watts circulating power with the total reflector. To date, the best modulator material examined which has the required aspect ratio has losses of ≥0.0015, which would indicate circulating power near 40 watts.

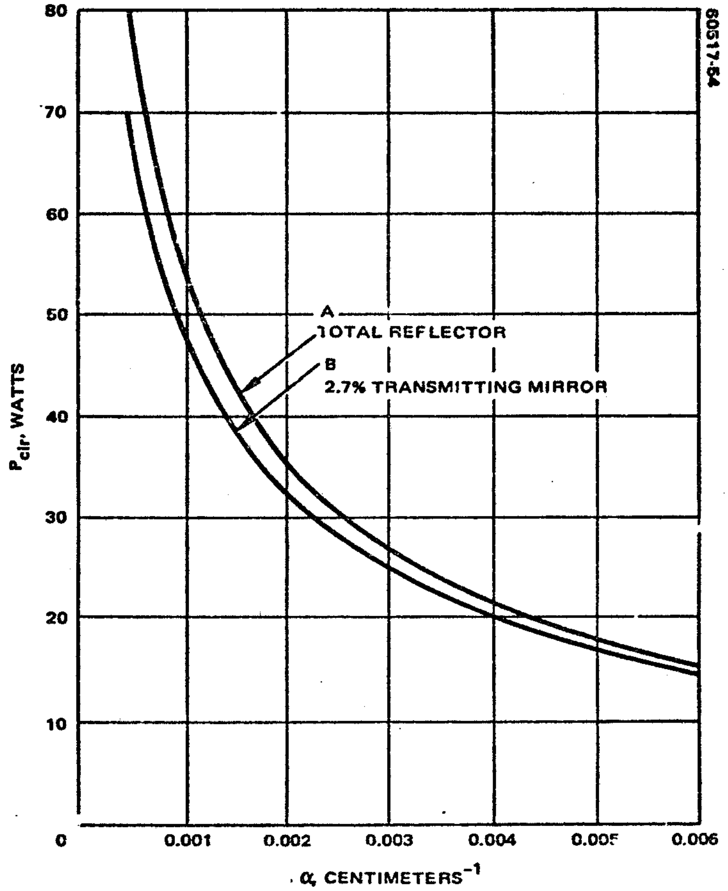

FIGURE 5-5. CIRCULATING POWER FOR TWO END MIRRORS

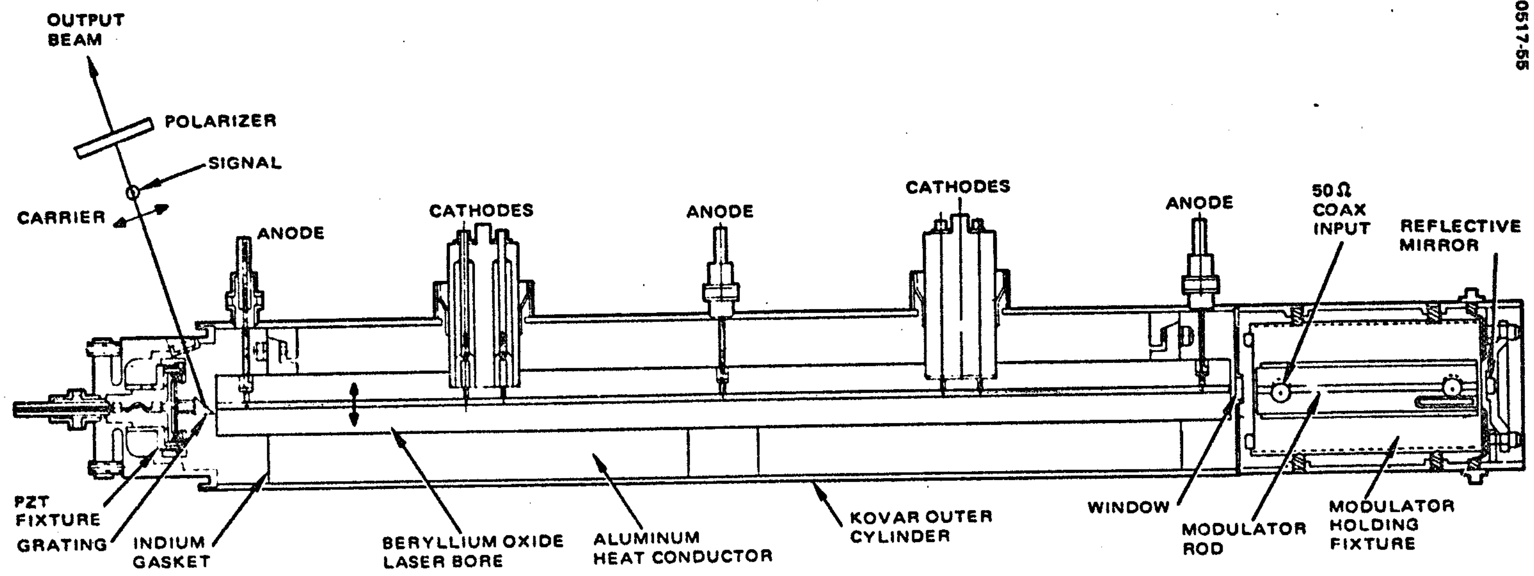

FIGURE 5-6. LASER TRANSMITTER SECTION DRAWING

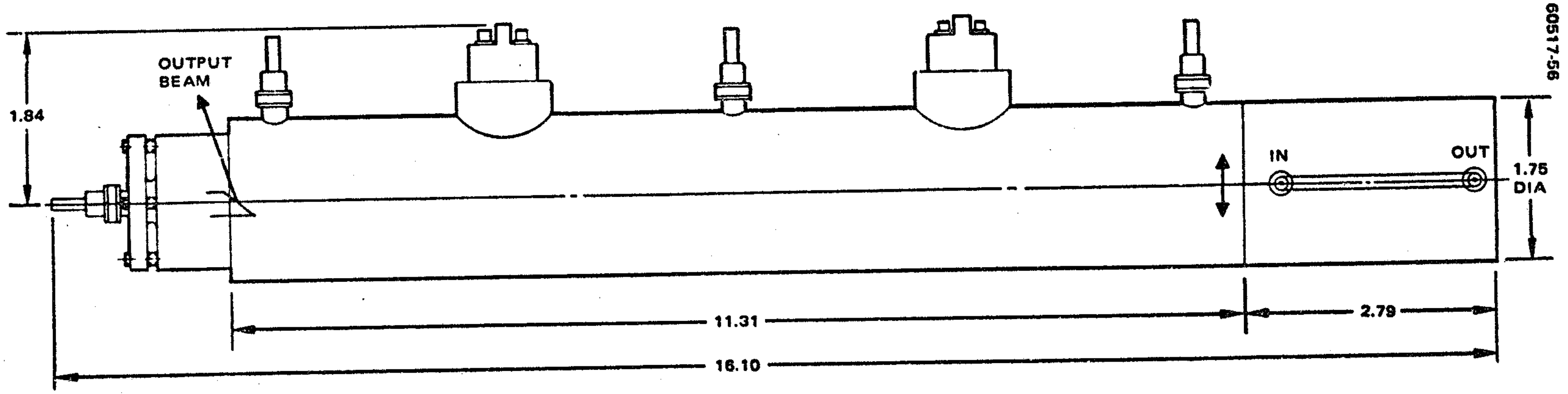

DIMENSIONS IN INCHES

FIGURE 5-7. LASER TRANSMITTER OUTLINE AND MOUNTING DRAWING

5.2 TRANSMITTER PACKAGE DESCRIPTION

A section drawing and outline drawing of the transmitter laser are shown in Figures 5-6 and 5-7. Precise alignment of the crystal axis to laser bore is required to achieve the desired performance (see Appendix D). The modulator housing is outfitted with eight alignment screws, four at each end of the modulator. The set of screws nearest the laser are located close to the end of the modulator, so they act as a pivot for angular adjustment without significant translation of the rod. The procedure for alignment is discussed below.

Alignment Procedure

Alignment of the transmitter takes place in two stages. First, a course setting permits laser oscillation to occur. Following that, fine tuning of the alignment screws optimizes the output. The course tuning is accomplished in the following steps:

1) The laser performance with 90 percent output mirror in place is peaked. This step serves to align the grating.

2) The reflective mirror in the modulator housing is aligned to the rear-end of the crystal with a HeNe alignment laser. No further adjustment of this mirror takes place.

3) The modulator is centered in the outer stainless steel housing with the adjusting screws. This step is accomplished by equalizing the gap between the outer housing and inner retainer (see Figure 3-11) around the circumference of the retainer.

When the pre-aligned housing is placed on the laser, laser oscillation invariably takes place (greater than 90 percent of the time). In those cases where the laser doesn't start, only minor adjustment is required to initiate lasing.

The output mode pattern guides the final alignment. Best performance is achieved when the modulated output beam is used. Centering this beam in the "four-leaf clover" pattern of Figure 3-6 gives the desired setting.

Completed Transmitter

Photographs of the completed transmitter are shown in Figure 5-8. Each unit is outfitted with a valve for purposes of pumping out and filling of the tube. In a space application the small copper tube exiting the output end of the laser would be pinched off. The aluminum cradle in which the laser sits is water cooled.

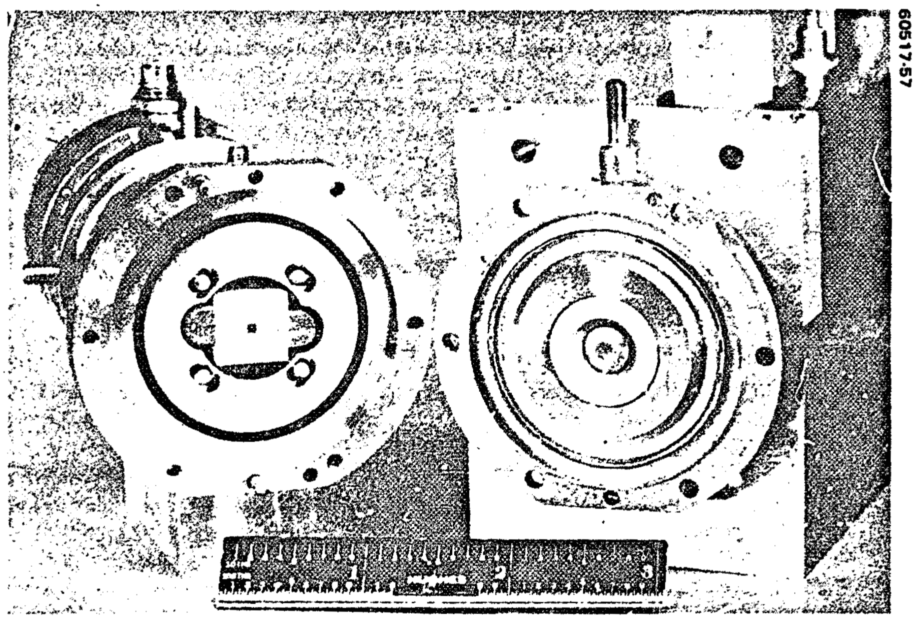

a) LASER MODULATOR INTERFACE (PHOTO 4R43486)

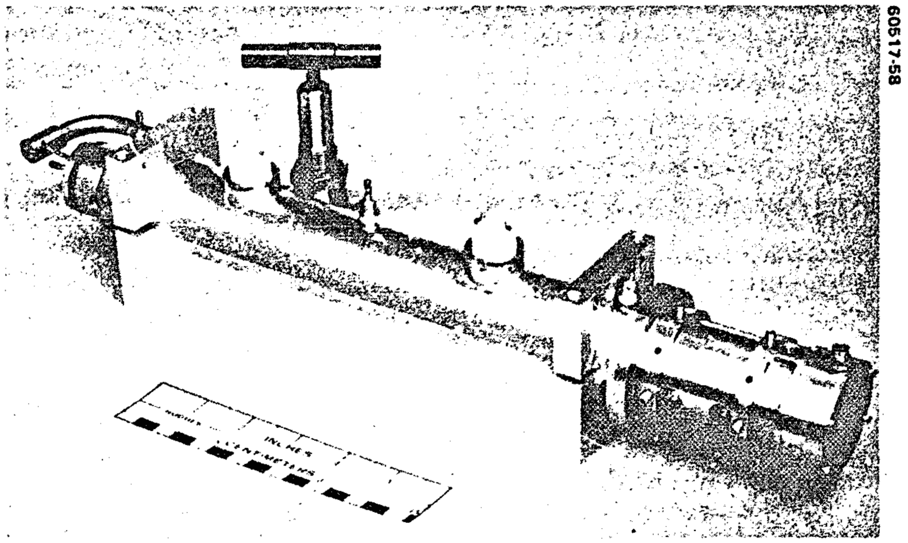

b) COMPLETED TRANSMITTER (PHOTO 4R43438)

FIGURE 5-8. 10 MICROMETER LASER TRANSMITTER

5.3 TRANSMITTER LASER MEASURED PERFORMANCE

The TXL performance tests consisted of optical power and optical bandwidth measurements. Performance results are contained in Table 5-1.

Power Measurements

There are four power measurements taken on each transmitter to specify its performance. Three measurements are taken of the light coupled off the grating. As shown in Figure 5-6, this output beam is analyzed with a wire grid polarizer. Even with no modulation signal on the crystal, leakage light leaves the cavity. Power measurements are taken on both polarizations. The third measurement is of the sideband power. This value represents the difference in readings between the power passing through the polarizer (aligned to pass the modulated component) with the modulator driver on and then turned off. Finally, the circulating power in the cavity is sampled through a 2.7 percent transmitting mirror at the modulator end of the tube.

The value of the circulating power is determined by the modulator absorption coefficient. It was found that with rods from boule 519 (see Table 3-2) that 20 watts circulating power resulted, while with crystals from boule 395, a value of 35 to 40 watts circulating power was achieved. Both these measurements are consistent with the circulating power levels of Figure 5-5. Thus, lower loss modulator material is required to achieve the desired 50 watt circulating power value. The results presented in Figure 5-5 suggest that the improvements required are not excessive. Going from the present value of 0.0016 to 0.001 cm^{-1} would give the desired performance. It is equally important to improve the yield in growing low loss crystals of the required length. Excessive delays have been encountered in procuring crystals of 6 cm length.

The sideband power performance in Table 5-1 is for a nominal circulating power value of 30 watts. Peak sideband power was actually measured by driving the crystal with a 120 volts peak to peak square wave at 10 kHz, in which case the average optical power measured is actually the peak power.

TABLE 5-1. LASER TRANSMITTER PERFORMANCE

Parameter	Measured Performance
Peak sideband power	0.45 W
Leakage power (polarized ∥ to signal)	<0.1 W
Leakage power (polarized ⊥ to signal)	~0.1 W
Bandwidth	400 MHz*
Input power	178 W
Input power (excluding ballast resistors)	144 W

*Modulated by C/2L resonances. See Figure 2-5.

When the modulator is driven with the 300 Mbps driver, the decrease in average optical power is consistent with the 1.9 dB difference in peak and average driver power discussed in association with Figure 5-3.

Leakage power in the polarization at 90 degrees to the modulated signal (the resonant polarization of the cavity) results from the 0th order coupling or specular reflection off the Littrow grating. The effective reflectivity varies from 0.33 to 0.5 percent for the gratings used. Typically, this leakage was 100 to 150 mW. It is spatially distributed in a fundamental mode or Gaussian-like spot.

Leakage power in the polarization of the modulated light results from stress birefringence in the crystal, and is strongly dependent on laser cavity alignment (Reference 6). With proper alignment, this signal is less than 100 mW. It is spatially distributed in the "four-leaf clover" pattern of Figure 3-6.

Sideband Power Beam Pattern

The power passing through the polarizer consists of the "four-leaf clover" leakage signal and a single, circular shaped modulated beam. With proper alignment, the modulated beam is centered in the cloverleaf. A burn pattern of the modulated light is shown in Figure 5-9 after alignments in two different lasers. In all cases the sideband power has a good, circular shape. The distortion that appears for larger exposure is actually leakage power. For example in TXL 2 for longer exposure, a noticeable signal shows at about the 10 o'clock direction. This component is actually the strongest of the four leaves of the leakage pattern seen in the near IR pattern of Figure 3-6.

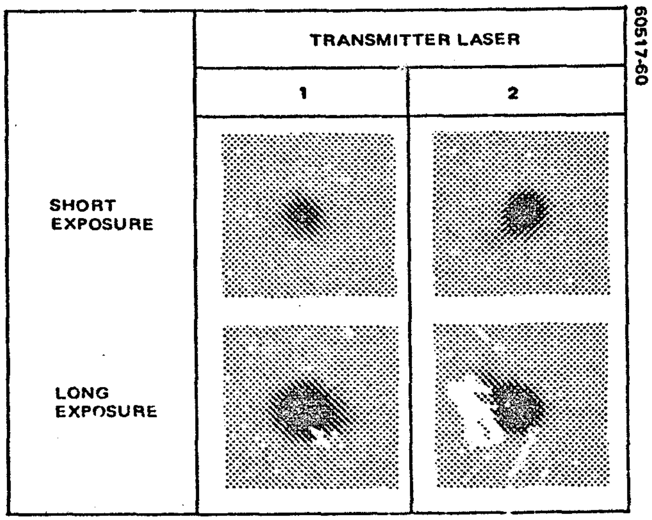

FIGURE 5-9. BURN PATTERNS FROM SIDEBAND POWER

Frequency Response

Wideband frequency response measurements of various transmitter configurations have been made with the test setup of Figure 5-10. The detector used was a nominal 50 MHz unit (S.A.T. PV748), which, surprisingly, had good response out to 1 GHz. An electrical resonance of the dewar in which the detector resides results in the notch in the following swept frequency responses.

The detected optical signal for the constant amplitude, swept frequency driver of Figure 5-10 is shown in Figure 5-11 from 0 to 1 GHz. The picket fence display results from sweep asynchronism between the sweeper and spectrum analyzer. The dominant characteristic of the spectrum is the peaked response at dc, near 330 MHz and near 680 MHz. A notch near 470 MHz results from the detector housing. Because of these unwanted resonances, the effective bandwidth in the unit is ~100 MHz.

The total distance between the cavity grating and mirror is 35 cm. When the refractive index of the modulator crystal and intracavity window is taken into account, the C/2L resonances are calculated to occur at the observed multiples of 330 MHz. It is felt that these resonances do not arise from the coupling of the oscillating line into the so-called "cold cavity modes" of the same polarization (Reference 7). Rather it has been shown that they arise because not all of the modulated light is coupled out of the cavity each pass. The modulated light that remains in the cavity resonates at the transit time or C/2L frequencies. One could term these "cross-polarized cold modes." The following set of data supports this conclusion.

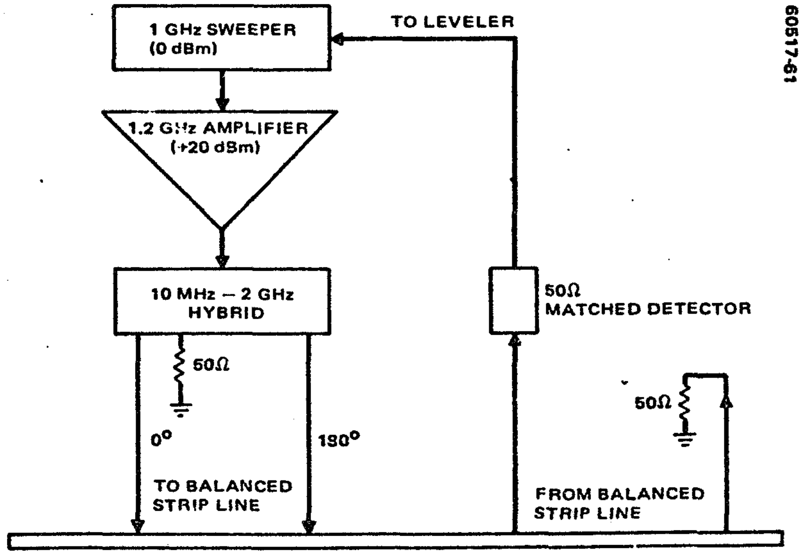

FIGURE 5-10. FREQUENCY RESPONSE TEST SETUP

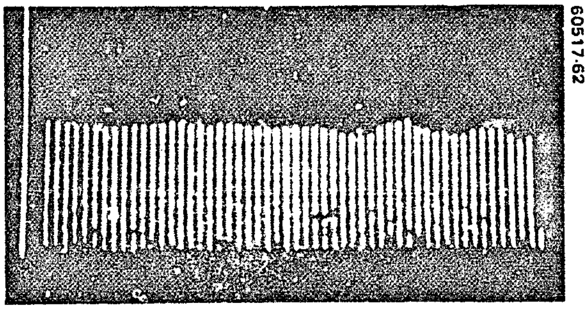

a) MODULATOR DRIVER SIGNAL

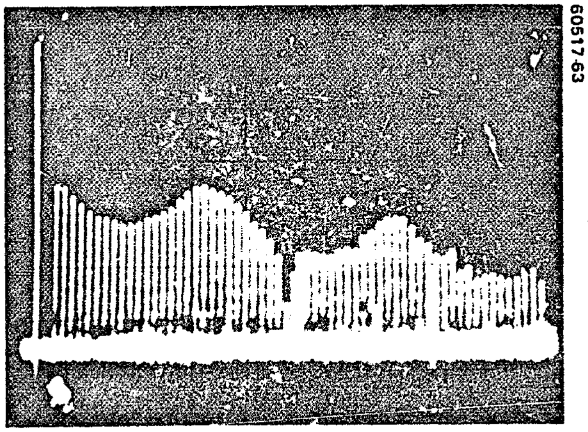

VERTICAL SCALE: 10 dB/DIVISION

b) DETECTED OPTICAL SIGNAL

FIGURE 5-11. FREQUENCY RESPONSE OF TRANSMITTER LASER FROM 0 TO 1 GHz

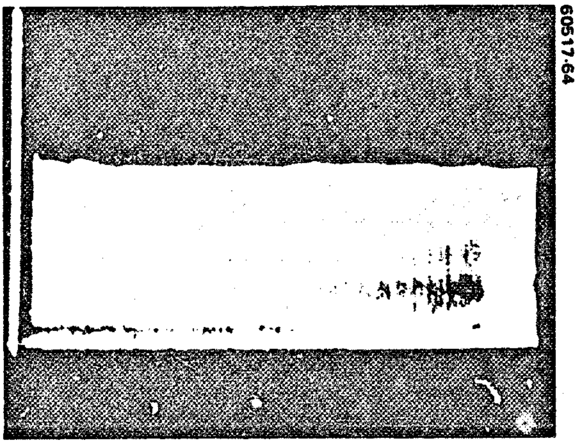

a) MODULATOR DRIVER SIGNAL

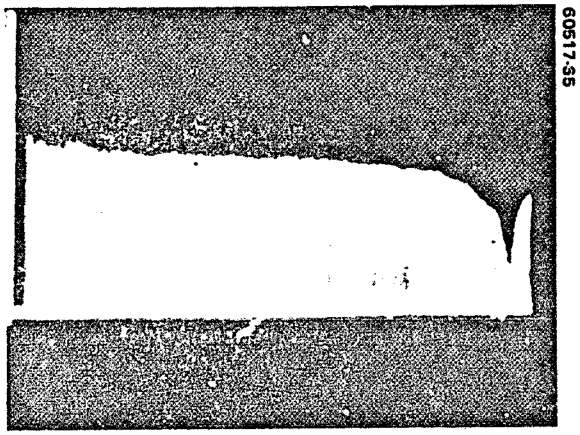

b) AAFE LASER RESPONSE

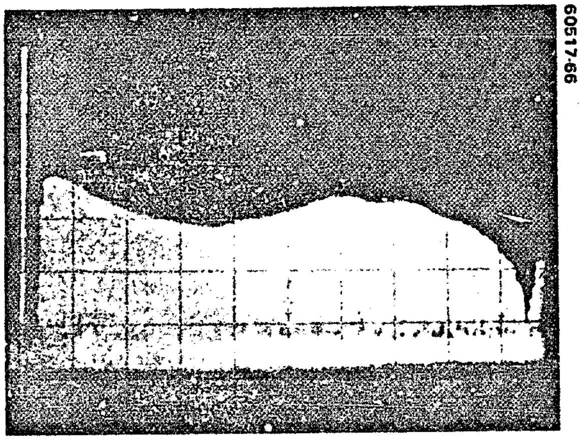

VERTICAL SCALE. 10 dB/DIVISION

c) TRANSMITTER LASER RESPONSE

FIGURE 5-12. COMPARISON OF FREQUENCY RESPONSE OF TWO TRANSMITTERS FROM 0 TO 500 MHz

The stripline modulator was operated with the AAFE transmitter laser (Reference 8). This test showed first that the modulator housing frequency response is flat and secondly that it is possible to eliminate the resonances when the modulated light is completely coupled out of the cavity. The frequency response for the AAFE configuration is shown along with that for the TXL configuration from 0 to 500 MHz in Figure 5-12. Here the 3 dB optical bandwidth (6 dB electrical) is ~350 MHz, which meets the bandwidth goal. An essential difference between the two transmitters is the polarizer used to couple out the modulated light. In the AAFE laser, the modulated light is coupled out off of a CdTe Brewster angle-window. The reflective coefficient of a single surface is 56 percent for the crossed-polarized light. However, the light encounters eight Brewster surfaces in a round trip passage of the cavity. Therefore, the unwanted modulated light that remains after the round trip is $(0.56)^8 \approx 1$ percent. This low level signal does not modify the modulation process. In contrast, the Littrow allows 20 percent of the modulated light to remain in the cavity each round trip, which will resonance at the C/2L frequencies. Identical behavior has been found in the ring modulator described in Appendix J. It is strongly felt that the ring modulator technique should be employed to avoid this problem.

5.4 Q-SWITCH TESTS

The experimental setup is shown in Figure 5-13. A dc bias voltage from 170 to 250 volts is placed across the modulator to spoil the cavity Q. Fast voltage pulses are then applied to the crystal to cancel the bias. The Q-switched optical pulse appears while the voltage pulse is present.

Two commercial drivers have been used in this work. A Tektronix Model 109 pulse generator is employed to accurately determine the optical pulse rise and fall times. With this unit, 4 ns rise time and 5 ns fall time voltage pulses are applied to the crystal. High repetition rate measurements are made with a Velonix Model 350 high power pulse generator. In this case, the rise and fall times are 12 and 42 ns, respectively. Both the driving pulse and detected optical signal are displayed on a Tektronix 7904 oscilloscope.

It has been found that the Q-switched single pulse energy is directly proportional to the continuous wave (cw) optical power that the laser puts out when the modulator is unbiased. This fact narrows the range of parameters needed to be varied in order to optimize the Q-switched laser performance, since previous parametric studies on the laser transmitter are applicable. It has been found that for the He:CO_2:CO:Xe mixtures used, optimum performance occurs for a pressure of approximately 100 Torr, a discharge current of 2 mA, and mix ratio near 2:1:1/2:1/4. Pulse output energy was optimized with an output mirror of 90 percent reflectivity.

Pulse energy of more than 15 microjoules per pulse was observed over a fairly broad range of discharge pressure and mixtures as shown in Figure 5-14. These data were taken at a 10 kHz repetition rate. The pulse energy (E_p) was found from the relation $E_p = \langle P_p \rangle / R$, where $\langle P_p \rangle$ is the average pulse power measured with a Scientech Model 361 power meter and R is the repetition rate. In Figure 5-15, the previously mentioned relationship between pulse energy and cw laser power (Pcw) is shown for the data of

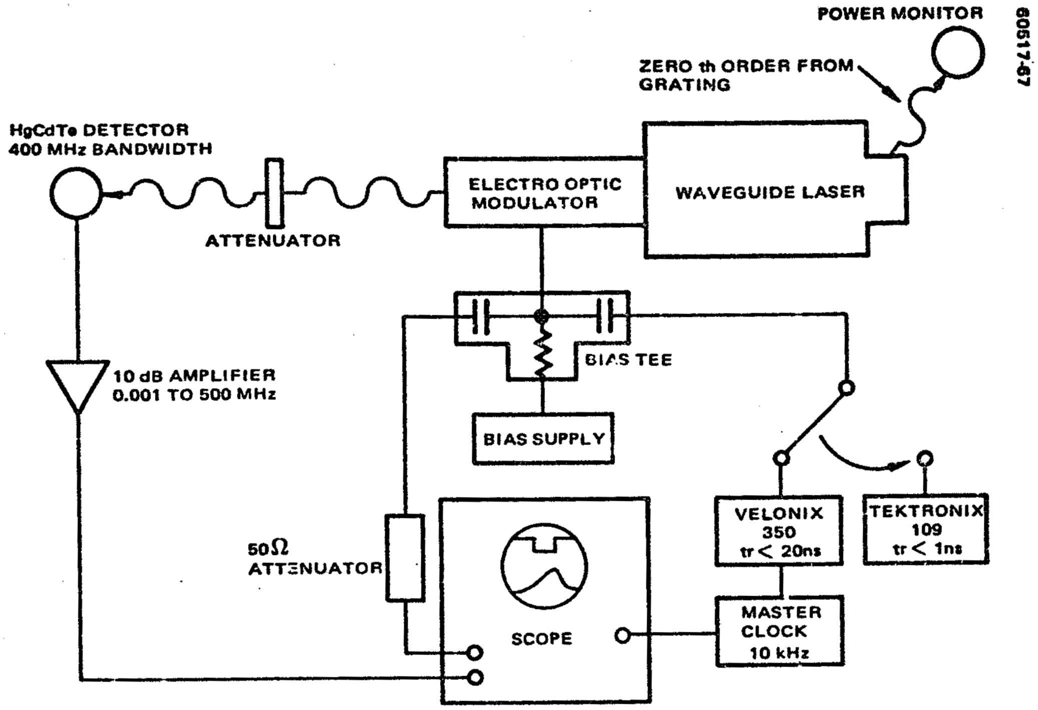

FIGURE 5-13. EXPERIMENTAL SETUP FOR Q-SWITCHED LASER TESTS

Figure 5-14. It is seen that the curve labeled $E_p(\mu J) \simeq 12.8 \times Pcw$ (watts) fits the measured points. This relationship will allow scaling of the Q-switched laser performance on the basis of known cw performance.

The bias voltage required to stop the laser oscillation ranges from 170 to 250 volts for the combination of discharge parameters used in this work. In Table 5-2 a list of conditions is shown. Also shown is the small signal gain (g_0) calculated from the threshold condition,

$$g_0 = \frac{\mathscr{L}}{L} + \frac{\ln(\cos^2\Gamma)}{2L}$$

which equates small signal gain with total cavity loss. Here L is the active discharge length, $\mathscr{L}$ represents the single pass cavity loss in the absence of bias, and the final term expresses the output coupling loss due to the biased modulator. Recall, $\Gamma = \pi V_b (\ell/d)/53$ kV for CdTe at 10.6 μm. The aspect ratio (ℓ/d) of the crystal is 40. In calculating the gain, an estimated cavity loss of $\mathscr{L}/L \simeq 0.01\ \mathrm{cm}^{-1}$ has been used. For comparison, the measured gain is also shown. Note that the calculated values fall within 20 percent of measured quantities. These results can be used to scale the required bias for modulator and cavity changes.

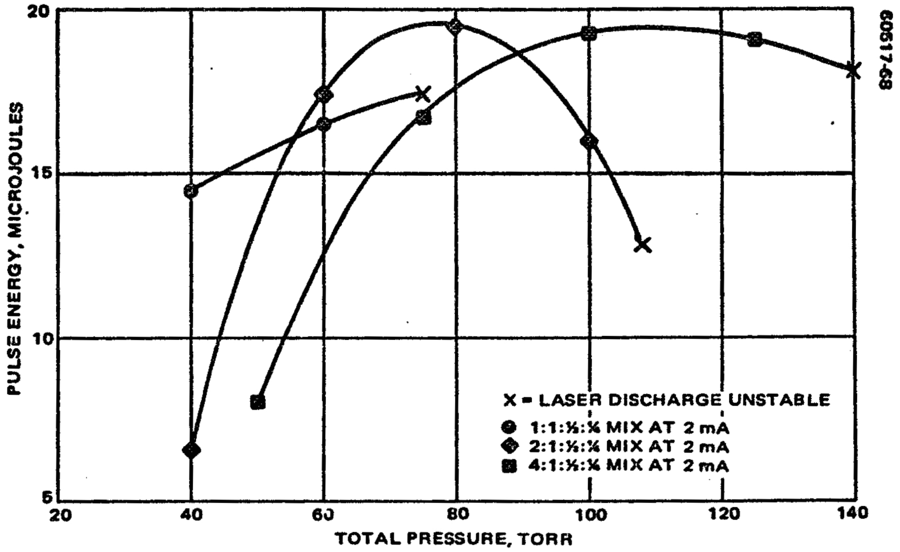

FIGURE 5-14. DEPENDENCE OF Q-SWITCHED LASER ENERGY ON DISCHARGE PARAMETERS

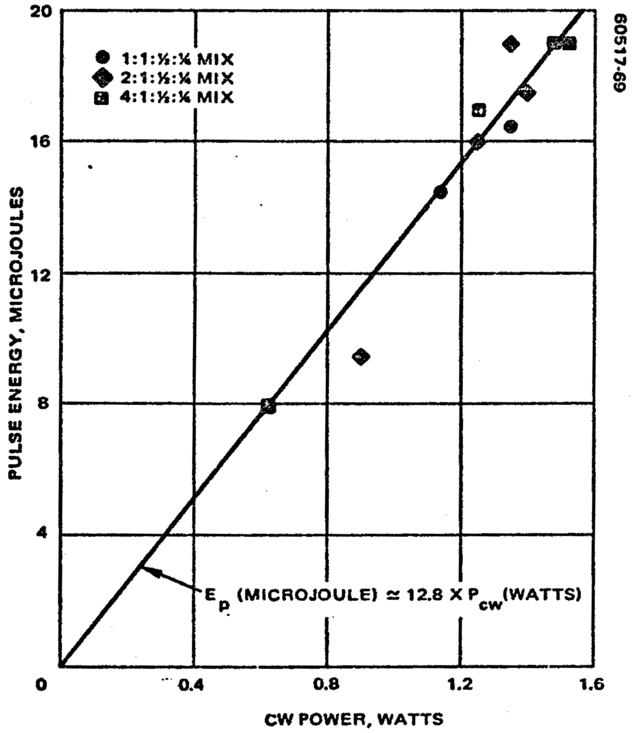

FIGURE 5-15. RELATIONSHIP BETWEEN Q-SWITCHED LASER PULSE ENERGY AND LASER OSCILLATOR OUTPUT POWER FOR VARIOUS DISCHARGE CONDITIONS

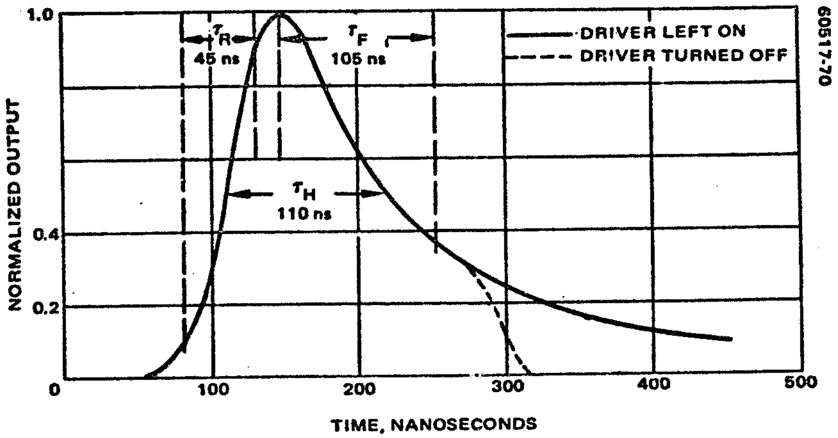

FIGURE 5-16. TYPICAL Q-SWITCHED LASER PULSE SHAPE

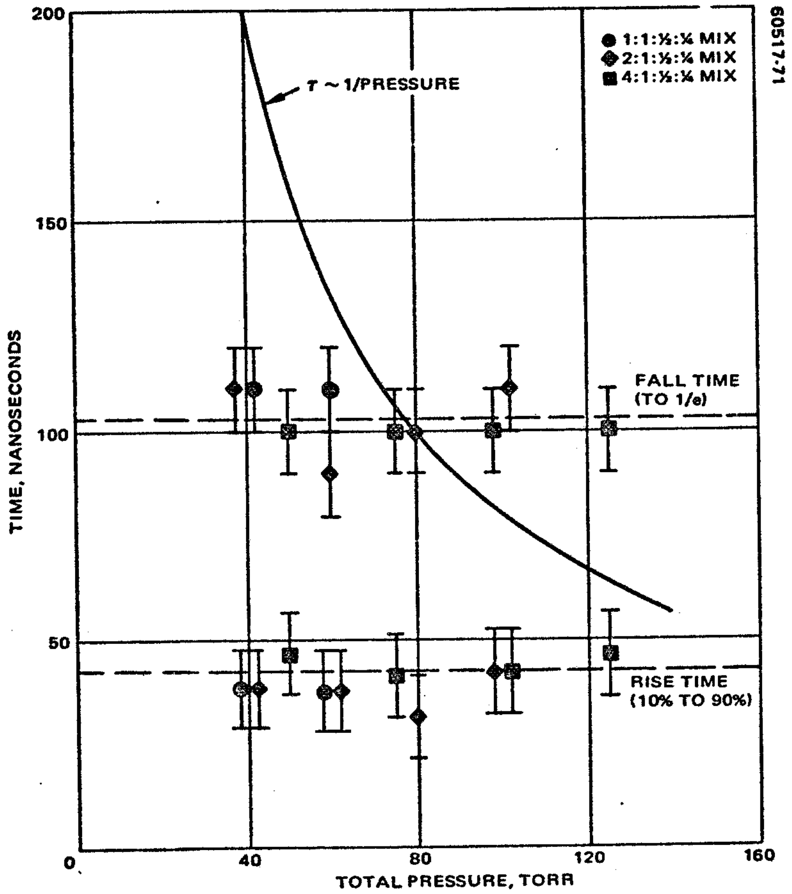

FIGURE 5-17. SUMMARY OF MEASURED RISE AND FALL TIMES OF Q-SWITCHED LASER PULSES FOR VARIOUS DISCHARGE CONDITIONS

TABLE 5-2. COMPARISON OF CALCULATED SMALL SIGNAL GAIN WITH MEASURED VALUES

Mixture ($He:CO:CO_2:Xe$)	Pressure, Torr	Current, mA	V_b, V	g_0 (calc), cm^{-1}	g_0 (meas), cm^{-1}
1:1:1/2:1/4	40	2	220	0.016	0.019
	60		200	0.015	0.018
2:1:1/2:1/4	40	2	240	0.017	0.019
	60		250	0.018	0.018
	80		230	0.017	0.017
	100		190	0.014	0.014
4:1:1/2:1/4	50	2	200	0.015	0.014
	75		180	0.014	0.014
	100		190	0.014	0.013
	125		170	0.013	0.011

Pulse Shape

A pulse shape, characteristic of the Q-switched laser, is shown in Figure 5-16. These data have been taken with the 2:1:1/2:1/4 mixture at 70 Torr and 2 mA. The measured pulse width at half height (τ_H) is 110 ns. A significant feature of the detected pulse is an exponential-like tail with e-folding time (τ_F) of approximately 105 ns. Such behavior is also found in Q-switching conventional, low pressure lasers (Reference 9). Measured time constants in that case are four to five times longer for the waveguide laser. It has been suggested that the tail arises from rotational energy transfer in both the upper and lower laser levels and therefore should scale with pressure (Reference 9). In the higher pressure waveguide laser, it has been found that this time constant is independent of pressure over the range 40 to 120 Torr (see Figure 5-17) for the measured time constants. A pressure dependent time constant would follow the indicated curve. Clearly, both rise and fall times are independent of pressure.

The peak power of the pulse, $P_p(0)$, has been found by numerically integrating the pulse shape of Figure 5-17 and normalizing the result to the measured single pulse energy. This calculation gives the expression, $P_p(0) = 0.63\ E_p/\tau_H$, which is applicable to all energy data of Figure 5-14 due to the consistency of pulse shape.

It is possible to reduce the pulse width while maintaining this peak power by terminating the drive pulse during the appearance of the Q-switched pulse as in Figure 5-17. For a 5 ns fall time drive pulse, the measured optical fall time is 24 ns in this mode of operation.

Pulse Jitter

All measurements, with the exception of pulse fall time were performed at 10 kHz pulse repetition rate.

The jitter performance is indicated in the photographs of Figure 5-18. In Figure 5-18a, extinction mode, the laser is held below threshold by the bias voltage between driving pulses. Since the optical pulse must build up from spontaneous emission, excessive jitter results. Time delays from the application of the driver pulse to appearance of the light pulse vary from 200 to 500 ns for discharge combinations studied. Jitter can be as much as 50 percent of the pulse width.

A method of eliminating this jitter while retaining the pulse energy to within 10 percent and retaining the pulse shape has been found. In Figure 5-18b, keep alive mode, the laser is not extinguished between pulses. The bias voltage is adjusted to maintain low level laser oscillation (≤20 mW) between pulses. Thus, the pulse starts from stimulated emission and not from noise, thereby eliminating the jitter. Overall jitter, including the master oscillator, modulator driver, and laser is typically ±2 ns. Approximately 30 ns delay exists between the application of the driver pulse and the appearance of the optical pulse.

Any application of Q-switched CO_2 lasers requiring low jitter must rely on a keep alive principle. Adverse effects from the attendant optical signal must be considered in potential applications.

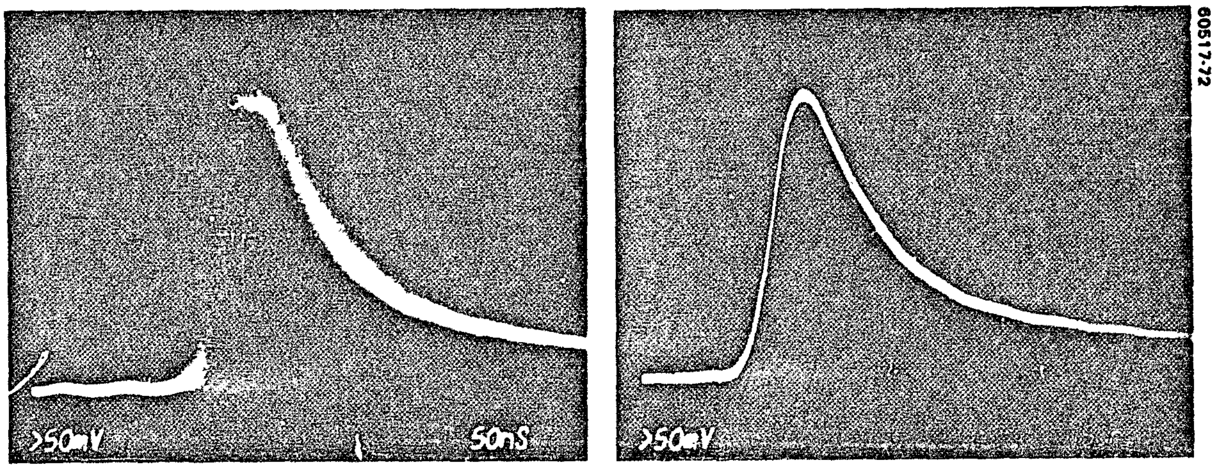

a) EXTINCTION MODE

b) KEEP ALIVE MODE

FIGURE 5-18. JITTER PERFORMANCE OF Q-SWITCHED LASER PULSES

6. LOCAL OSCILLATOR LASER

A tunable waveguide local oscillator laser developed as a task on Contract NAS5-21859 offers greater tunable range and smaller size than a conventional laser. The goal of the previous contract was to attempt to achieve sufficient tunability (±760 MHz) to accommodate doppler shifts. However, the techniques required to build lasers with tuning ranges of ±500 MHz and above include the use of square cross sectioned waveguides. This required sealing techniques that were not available at the time. For this reason, a circular bore laser was designed with a minimum tunable range of ±200 MHz, but which had a 3 dB tuning range of ±300 MHz when built and tested. A tunable range of about ±250 MHz is satisfactory for use with the 10.6 μm receiver subsystem since doppler tracking is accomplished with RF tracking electronics after detection.

The present program task is for the production of six local oscillator waveguide lasers. Performance data obtained from the receiver program model were used to set the specifications and compute design performance of the new design. The new model was produced at the Hughes Electron Dynamics Division in Torrance, California.

6.1 LOCAL OSCILLATOR LASER DESIGN SUMMARY

The design guideline for the local oscillator laser was that it was to be used as a vehicle for the study of laser life. In addition, it was to have a minimum power output of 50 mW and be undercoupled to maximize tunability.

Early in the development of NASA local oscillator laser it was decided that the He-N_2-CO_2 mixture would be abandoned in favor of the simpler He-CO_2-CO mixture. At that time >10,000 hours had been demonstrated with this mixture and Cu or AgCuO alloy cathodes in conventional 20 Torr pressure lasers. This gas mixture change was made in the waveguide laser without any sacrifice in performance. The effort at Hughes has been to investigate the Cu cathode at waveguide laser pressures in the CO mixture.

The laser has two small, hollow, copper cathodes protected by sputter shields and two platinum anodes. The inside of the envelope is nickel plated and hydrogen fired to provide a clean and inert surface. The standard gas mix used is He-CO_2-CO-Xe in the ratio 4:1:0.5:0.25 by pressure.

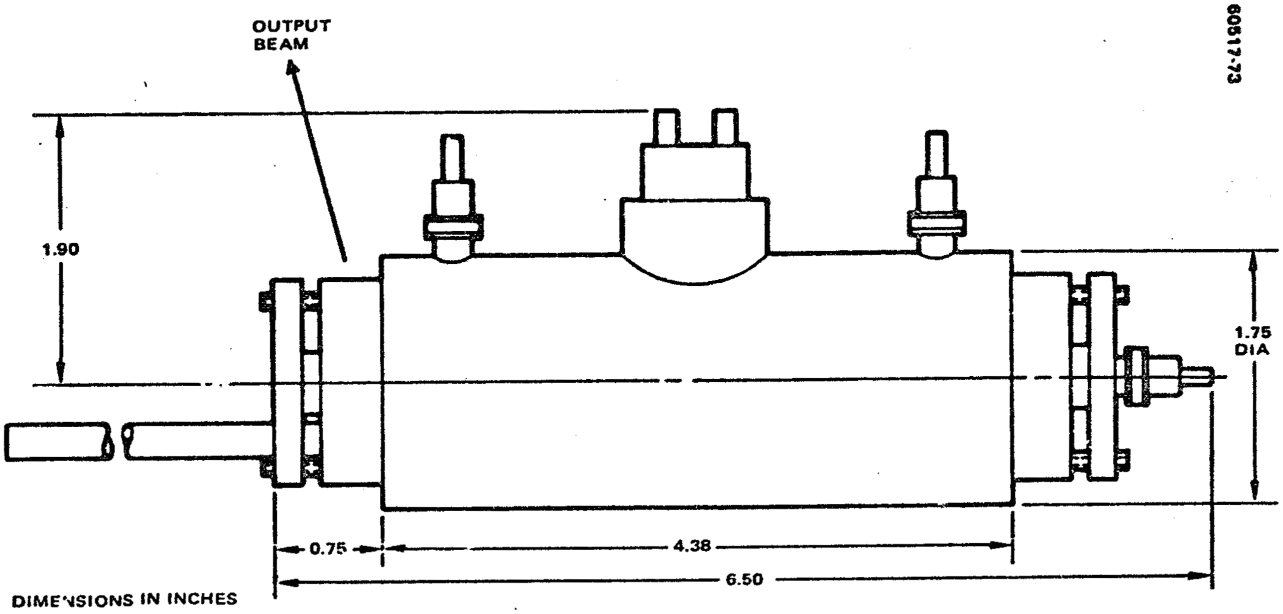

FIGURE 6-1 LOCAL OSCILLATOR LASER ENVELOPE LAYOUT

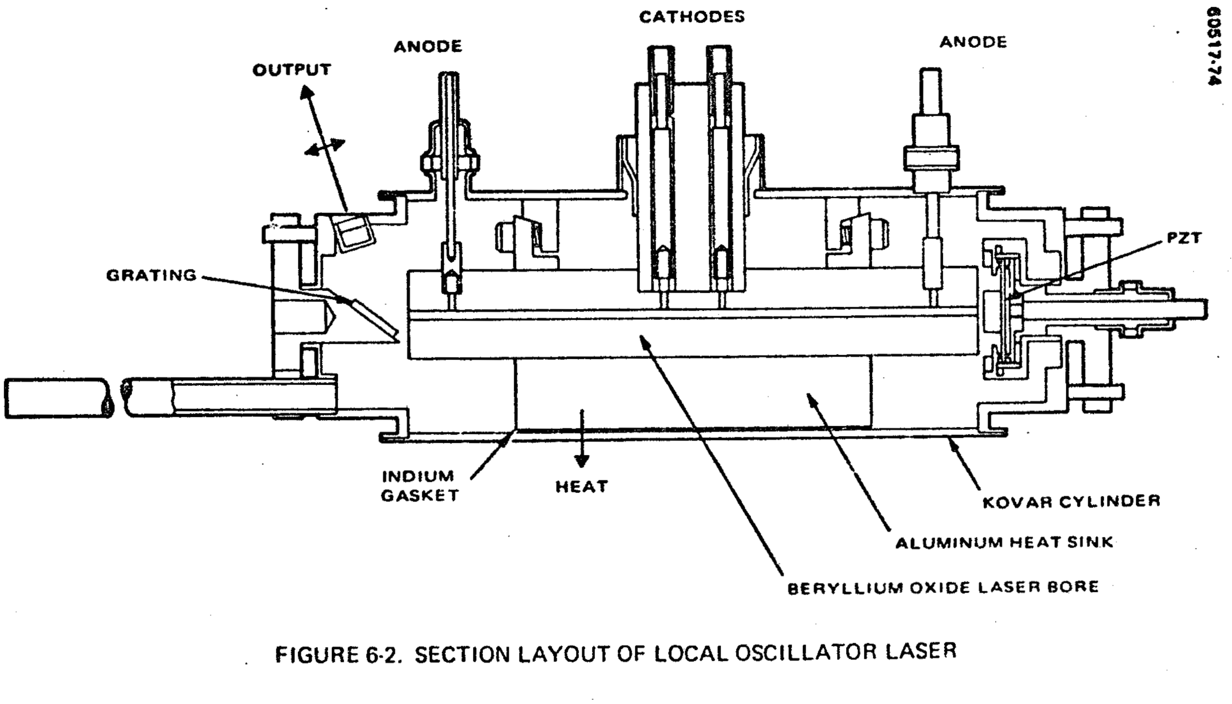

FIGURE 6-2. SECTION LAYOUT OF LOCAL OSCILLATOR LASER

The local oscillator lasers in life test are equipped with attached absorption cells. This allows the partial pressures of CO_2 and CO to be measured at intervals by IR absorption spectroscopy. Laser efficiency was also recorded. The local oscillator lasers use undercoupled internal gratings and provide an output power of 50 mW. The local oscillator laser gas volume is 130 cm^3.

6.2 LOCAL OSCILLATOR LASER DESCRIPTION

Specification and Requirements

Minimum and maximum specifications and requirements for the local oscillator laser are shown in Table 6-1. The design incorporates a rectangular bore to minimize the bore wall losses and increase the tuning range. The design also includes a concentric ballast envelope that eliminates the need for ceramic seals of the rectangular beryllium oxide bore sections. The output window is to be metal sealed to the laser outer envelope.

Performance Data

Typical performance data achieved in model local oscillator laser is shown in Table 6-1 for comparison purposes.

Description

A layout of the local oscillator laser envelope is shown in Figure 6-1 and a section layout is shown in Figure 6-2.

TABLE 6-1. SPECIFICATION AND EXPERIMENTAL PERFORMANCE OF FIRST MODEL LOCAL OSCILLATOR LASER

	Specification	Typical Performance
Power output, mW	50 minimum	65
Discharge input power, W	10 maximum	10
Tuning range (1 dB), MHz	±200 minimum	±300
PZT mechanical range, μm	20 minimum	>20
PZT voltage, V	±140 maximum	±140
Discharge length, cm	7.5 maximum	6.48
Bore size, mm	1.25 maximum	1.25
Overall length, in.	7 maximum	7.0
Weight, lb	1.25 pounds goal 1.5 maximum	1.38
Diameter of cylinder, in.	1.75	1.75
Height of beam above base mounting, in.	1.125 maximum	1.125

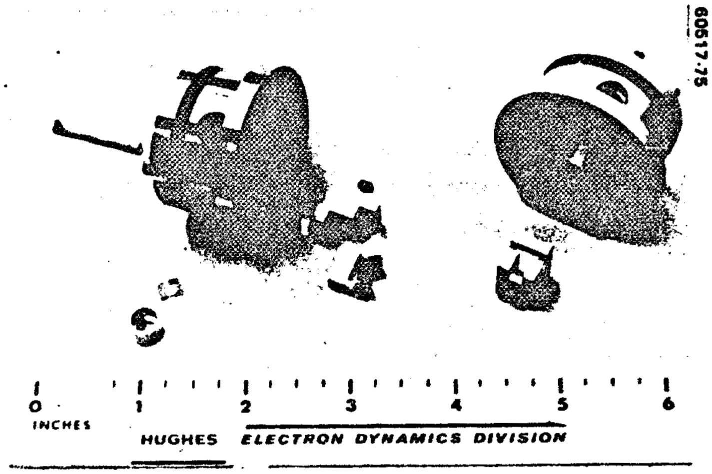

FIGURE 6-3. GRATING SUBASSEMBLY (PHOTO 4R39815)

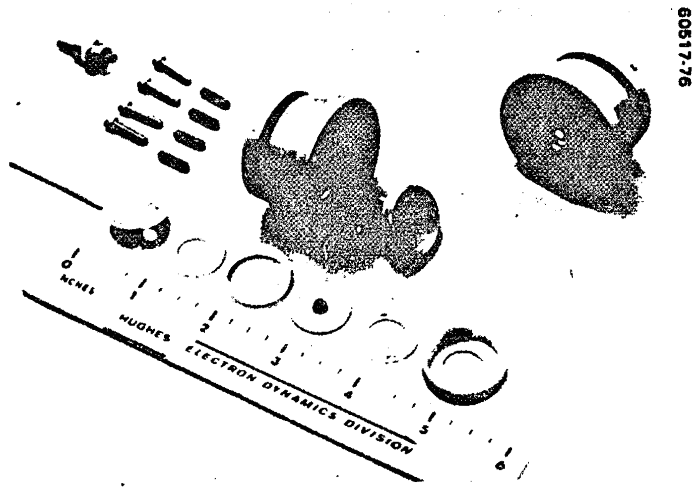

FIGURE 6-4. REFLECTIVE MIRROR SUBASSEMBLY (PHOTO 4R39812)

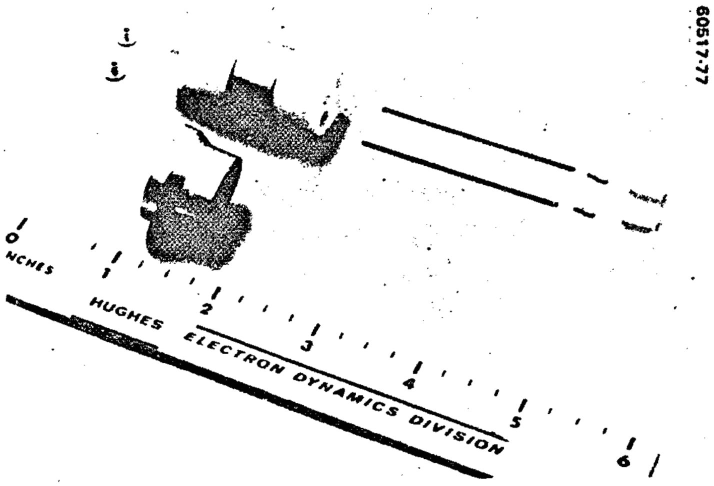

FIGURE 6-5. HIGH VOLTAGE FEEDTHROUGH SUBASSEMBLY (PHOTO 4R39813)

Grating Subassembly

The specular component of the grating in the laser polarization is about 0.5 percent. Thus, the grating acts as a coupling device to couple about 0.5 percent of the circulating power out of the laser. As seen from the section layout, the angle of the coupled energy is slightly more than 90° with reference to the axis of the bore. The grating assembly, Figure 6-3, shows a disassembled array of parts at the left, including the window, pump-out extension, and grating holder. At the right, the grating is shown in its holder as well as the complete subassembly.

Considerable variability was observed in the specular reflectivity of gratings used in the construction of the six level oscillators, which resulted in varying amounts of output power from the lasers even though their circulating powers were uniform.

High Reflectivity Mirror Subassembly

At the opposite end of the laser a high reflectivity mirror is controlled with a PZT positioning bimorph transducer. This subassembly is shown in Figure 6-4. A complete array of parts is shown on the left and a complete subassembly is shown on the right.

High Voltage Feedthrough Subassembly

Since the waveguide and electrode structure is not vacuum tight in the gas filled region, a great deal of care was taken with the design and assembly of the high voltage feedthrough to prevent arcing to the case, or through another area of the gas filled ballast region. The feedthrough subassembly consists of an alumina ceramic block with precision fit to the beryllia waveguide structure during assembly and prior to welding to the main structure. The disassembled feedthrough assembly in Figure 6-5 shows two cathodes at the right and glass sleeves for the cathodes. These glass insulators permit the cathode temperature to be elevated without significant loss of heat due to thermal conduction through the sleeves.

Final Assembly Sequence

The final assembly sequence is shown in Figures 6-6 through 6-8. The layout of subassemblies in Figure 6-6, from left to right, are the high reflectivity mirror, waveguide section, outer case, and grating subassemblies. Figure 6-7 shows the waveguide section placed inside the outer case during assembly. Figure 6-8 shows the completed local oscillator laser assembly.

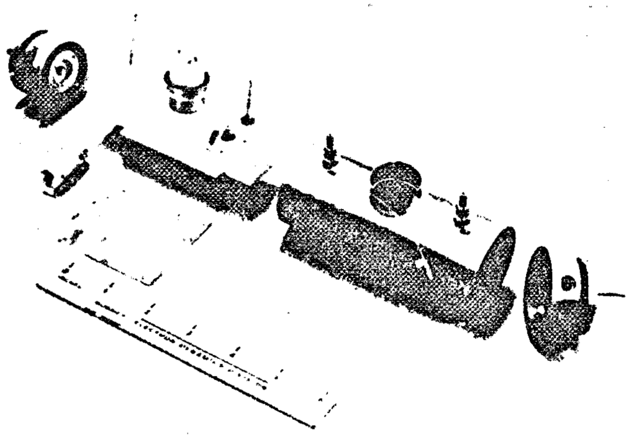
60517-78

FIGURE 6-6. SUBASSEMBLIES PRIOR TO ASSEMBLY (PHOTO 4R39814)

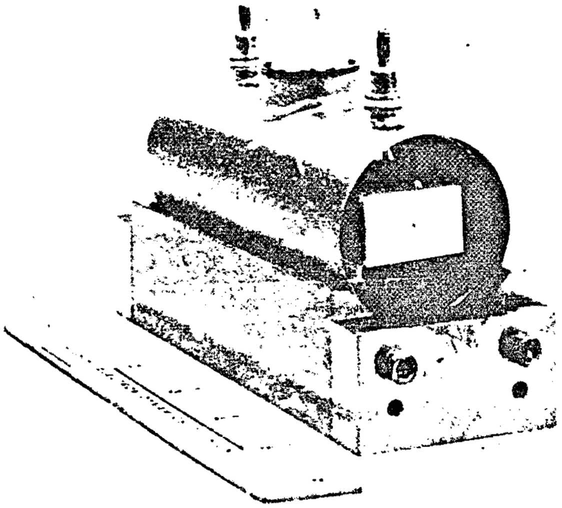
60517-79

FIGURE 6-7. WAVEGUIDE SECTION IN CASE (PHOTO 4R39817)

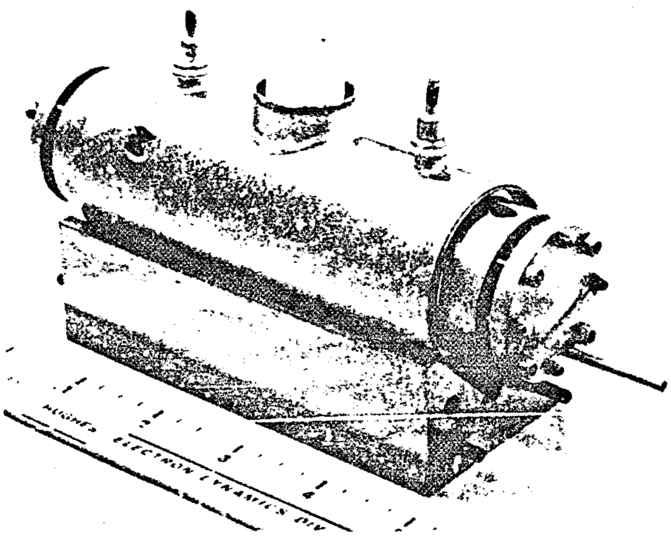

60517-80

FIGURE 6-8. COMPLETELY ASSEMBLED WAVEGUIDE LASER LOCAL OSCILLATOR (PHOTO 4R39816)

6.3 LASER LIFE DEVELOPMENT

The technical approach to achieve long life CO_2 waveguide laser is fundamentally concerned with the gas chemistry equilibrium in the laser envelope. The CO_2 laser life program initiated on this program four major parts. First, precise instrumentation was obtained to monitor the gas. The best technique appears to be the gas spectrophotometer since it has the least systematic errors. Second, quick turnaround tests, using small gas volume test cells, are being conducted. The 12 cm^3 cathode test cell, with as many as 18 in test at one time, provides continuous data with proven consistency. Third, is a correlation of the gas spectrophotometric data with laser life performance. (To achieve this, Hughes has attached spectrophotometer cells to six local oscillator lasers.) Fourth, a gas chemistry equilibrium must be established in the test cells.

Gas Chemistry Control

Past studies of sealed-off, low pressure CO_2 lasers have identified the basic requirements and approaches to be taken to achieve a stable gas chemistry in a sealed system over a long life (10^4 hours). Stability with respect to the dissociation of CO_2 molecules by electron impact, is indicated by

$$CO_2 + e^- \rightleftharpoons CO + 1/2\ O_2 + e^-$$

is achieved by catalyzing the reverse of reaction (see equation) near the electrodes by the proper choice of materials (CuO for the hollow-cathode and Pt for the anode), and in the bore by the addition of a controlled amount of H_2 (or H_2O).

The gas fill envelope must also have a passive inner wall surface so as not to consume the atomic oxygen generated in the equation by adsorption, or oxidation, which would drive reaction to the right. This is achieved, in part, by running an oxygen discharge in the tube in the initial processing which oxidizes the cathode and any reactive areas on the tube walls. In addition, the use of a laser gas mix where CO replaces the N_2 eliminates the problems of discharge instability and sputtering at the anode. The latter is associated with the negative ions readily formed in the nitrogen oxides. The CO mix also simplifies attainment of a stable chemistry by greatly reducing the number of potential molecular combinations. Deliberate addition of CO in the fill is another means of forcing reaction (see the equation) to the left. Finally, the small partial pressure of H_2 in the fill is a significant catalyzer. This is achieved by rapidly catalyzing the reverse of the equation throughout the tube volume, causing the level of atomic oxygen in the tube to be reduced and causing less oxygen to be lost in possible reactions with the tube materials.

Although the rate constants for some of the important reactions occurring in the CO_2 laser have been measured, these were generally done in N_2 mix fills and at pressures and volumes appropriate to conventional low pressure lasers. To be of maximum use, the reaction rate constants should be measured again at waveguide tube pressures with the laser discharge tube assembly being used as the reaction vessel. Then the catalyzing action of any of the materials used in the tube assembly and effects due to geometry are part of the experimental measurements and are accounted for automatically. This may be done in controlled experiments where specific reactive pairs of gases are used to fill the laser discharge tube envelope and the reaction products are monitored with an attached mass spectrograph.

The TXL and local oscillator laser model lasers are ideal vehicles for conducting a meaningful life test program. Test cells using laser cathodes have verified the basic reaction stability, but now the laser package effect must be taken into account. Epoxies used for sealants may emit hydrogen or organic materials which have an unknown effect on life. At present, it is believed that control of the hydrogen partial pressure will eliminate any dependence of laser performance on these factors.

Sealants

Both the TXL and the local oscillator laser use a polyamide epoxy to seal the output window and the transmitter intracavity window. Because this epoxy has an extremely low vapor pressure and is virtually impermeable to water vapor, it has been used successfully for many years in the manufacture of helium neon lasers. However, if the epoxy is found to have an undesirable effect on laser life, it will be necessary to provide window seals by alternate methods.

Progress has already been made in developing indium-gold seals between Kovar and substrates of CdTe, ZnSe, and GaAs. Excellent vacuum integrity has been demonstrated. For instance, window assemblies were temperature cycled 10 times from -50° to +100°C and were vacuum tight to better than 10^{-8} standard cc/min of helium. The major problem is that these seals induce optical strain in the substrates, causing a drastic reduction in output power. Further design effort is required on the window assembly and on the technique of applying the seal.

Epoxy is also presently used to bond the laser cavity mirror to a piezoelectric bender bimorph transducer. A sputter metallized indium solder bond also needs to be developed. The bimorph itself is bonded using a different polyamide epoxy. Alternate construction techniques must be investigated with a goal of eliminating this epoxy bond.

Optics

Optics degradation can be a serious life limiting factor. This was shown by one of the life tests at the Hughes Research Laboratories. The average power densities the optics must withstand in the undercoupled local oscillator laser is 2 kW/cm^2. In the transmitter laser, the circulating power is 50 watts and the average power density is 6.7 kW/cm^2. While this high average power may not be the cause of degradation, it may contribute to degradation. Mirror/window degradation could also result from ultraviolet radiation, sputter deposits, and charged particle bombardment.

6.4 CATHODE LIFE TEST VEHICLES AND SPECTROPHOTOMETER CELLS

Eighteen cathode test cells were built to provide a large number of quick turnaround tests to help establish gas chemistry equilibrium. Each test cell has only 12 cm^3 volume, including the spectrophotometer cell. The cell contains the typical CuO cathode and is operated at the laser pressure and current. Periodically, the composition of the gases, particularly CO_2 and CO, are measured using the IR spectrophotometer.

Figure 6-9 shows typical spectrophotometer cell data. The spectral lines on the chart show a partial pressure of 30 Torr of CO_2 and about 30 Torr of CO. Figure 6-10 is an example of how these data are plotted as a function of cell operating time. Note that gas equilibrium is maintained, even at 4000 hours. Since the test cell has only 12 cm^3 of volume, it is reasonable to assume that a laser having a volume of 150 cm^3 or more has a lifetime potential of more than 50,000 hours.

Figure 6-11 shows a cathode test cell. The anode is located at the lower left and the cathode at the lower right. The spectrophotometer cell is at the top of the photo.

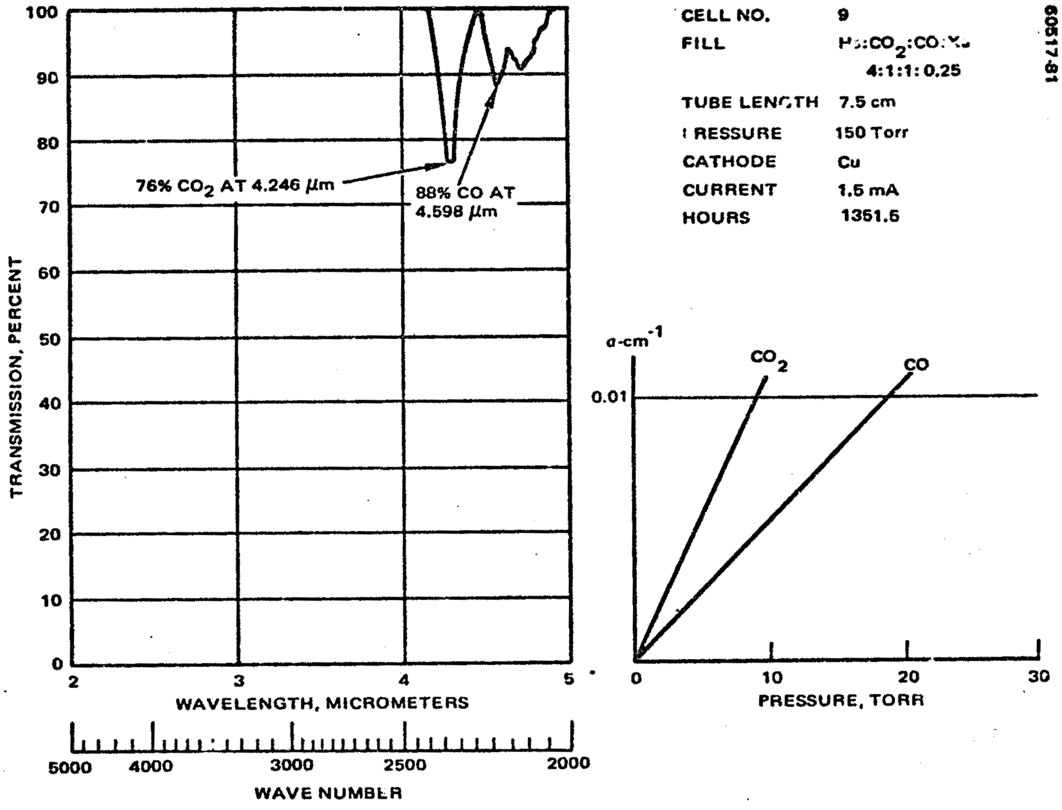

FIGURE 6-9. SPECTROPHOTOMETER CELL DATA

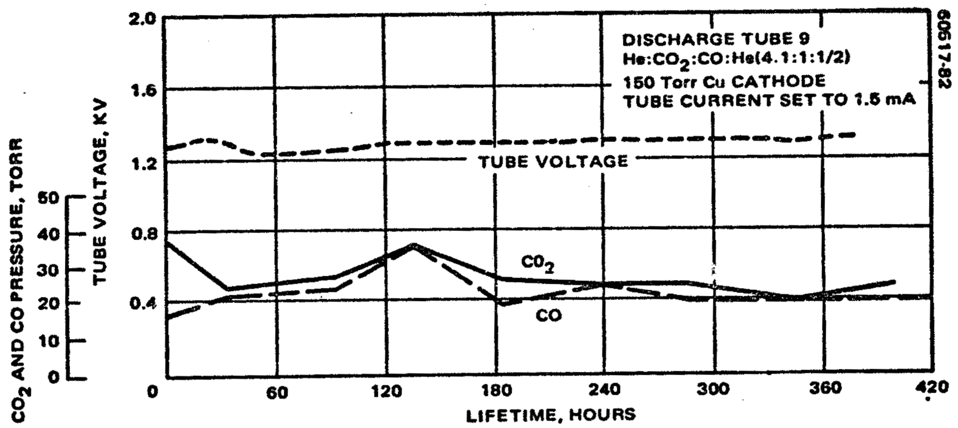

FIGURE 6-10 CO$_2$ AND CO PARTIAL PRESSURES, AND TUBE OPERATING VOLTAGE AS FUNCTION OF OPERATING TIME

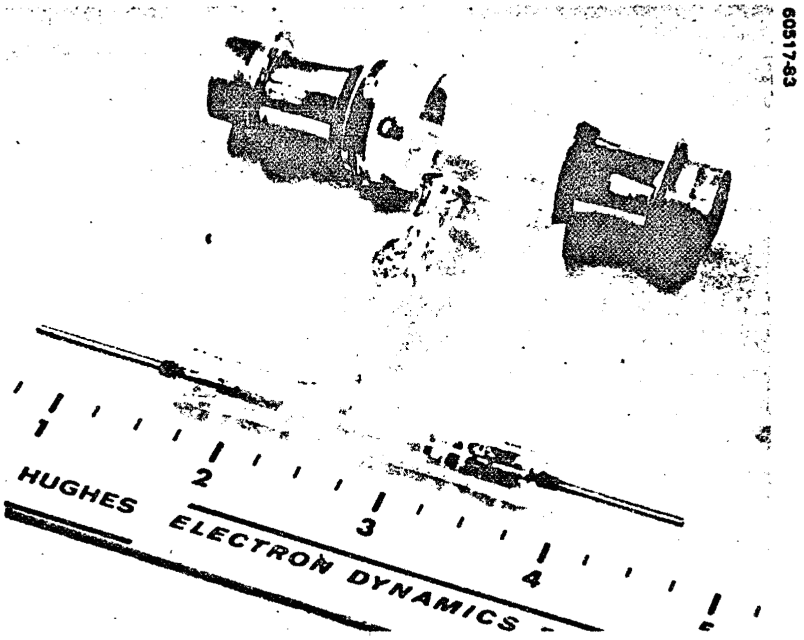

FIGURE 6-11. CATHODE TEST CELL WITH SPECTROPHOTOMETER CELL ATTACHED (PHOTO 76-35673)

6.5 LIFE TEST RESULTS – TEST CELLS

All discharge test cells and lasers were processed according to the procedure shown in Table 6-2. The purpose of the oxygen scrub is to remove excess hydrogen from the laser and cell components and to convert the copper cathode material to copper oxide. This is followed by two process fills of the specified fill gas at 150 T pressure and then by a final fill using the specified fill gas.

Table 6-3 gives the gas composition, fill pressure, and operating current for the 14 test cells that were life tested. Also shown in the table is the duration of the life test of each test cell.

TABLE 6-2. CATHODE TEST CELL AND LASER PROCESSING PROCEDURE

Step	Gas	Pressure, Torr	Current, mA	Time, min.
1	O_2	25	4	5
2	O_2	25	4	5
3	O_2	25	4	30
4	Fill gas	150	3	60
5	Fill gas	150	3	75
6	Fill gas	150	–	–

TABLE 6-3. CATHODE TEST CELL OPERATING CONDITIONS AND LIFE TEST DURATION

Cell	Cathode Material	Gas Composition			Fill Pressure, Torr	Operating Current, mA	Life Test Duration, hr
		$He:CO_2$ 4:1:1/2:1/4	CO:Xe 4:1:1:1/4	$He:CO_2:N_2:Xe$ 4:1:1/2:1/4			
1	Ni			X	190	1.5	6100
2	Cu			X	190	1.5	6100
5	Cu		X		150	1.5	4200
6	Cu	X			150	1.5	4200
7	Cu	X			150	1.5	4200
8	Cu	X			150	1.5	4200
9	Cu		X		150	1.5	4200
10	Cu		X		150	1.5	4200
11	Ni			X	150	1.5	1500
12	Ni			X	150	1.5	1500
13	Cu	X			150	1.5	900
14	Cu	X			150	1.5	900

The conclusions of the cathode cell life tests can be summarized as follows:

- Nickel cathodes show excessive sputtering and gas cleanup over the period of the life tests
- Gas mixtures using CO rather than N_2 are more stable
- All test cells using Cu cathodes and CO fills show negligible long term changes in the relative composition of CO and CO_2.

These data, and the fact that the cathode test cells are small volume units, suggest that a laser processed in such a manner should maintain stable chemistry for tens of thousands of hours.

6.6 LIFE TEST RESULTS – LOCAL OSCILLATOR LASERS

The first local oscillator laser was used exclusively for performance evaluation and shelf life tests. The second local oscillator laser was operated for 4000 hours before tests were discontinued. Tests of local oscillator laser 3 and 5 were discontinued at 500 hours when their vacuum valves were inadvertently opened. The tubes were not properly reprocessed for further life tests, although it is believed possible now that the function of the processing is better understood. Local oscillator laser 4 was operated for 1200 hours before the tests were discontinued. Local oscillator laser 6 was life tested for 10,000 hours, and this test was still in progress at the time of this report.

Table 6-4 lists the life tests conducted on each of the local oscillator laser tubes. Data of power output versus time is plotted for tubes 2, 4, and 6 in Figure 6-12. It is believed that the general characteristics of this design and processing method are best represented by these three tubes. Local oscillator laser 6 was moved twice during the life tests, which may account for the dips in power output occurring at 200 and 1500 hours. Typically, it can be expected that the power output of the local oscillator laser design will fall to the half power point at about 3000 hours. The usefulness of the laser as a local oscillator may be extended possibly to 5000 hours, since the actual power required on the detector is on the order of 1 mW, and the actual power on the detector could be controlled through through the use of an attenuator.

TABLE 6-4. LOL LIFE TEST SUMMARY

Tube No.	Type of Test	Test No.	Hours	Test Status	Tube Status
LOL-1	Shelf	1	1,400	Continuing	Operable
LOL-2	CW Operating	1	4,000	Ended	Operable
LOL-3	CW Operating	1	300	Ended	Operable
		2	500	Ended	
LOL-4	CW Operating	1	1,200	Ended	Operable
LOL-5	CW Operating	1	400	Ended	Operable
		2	100	Ended	
LOL-6	CW Operating	1	10,000	Continuing	Operable

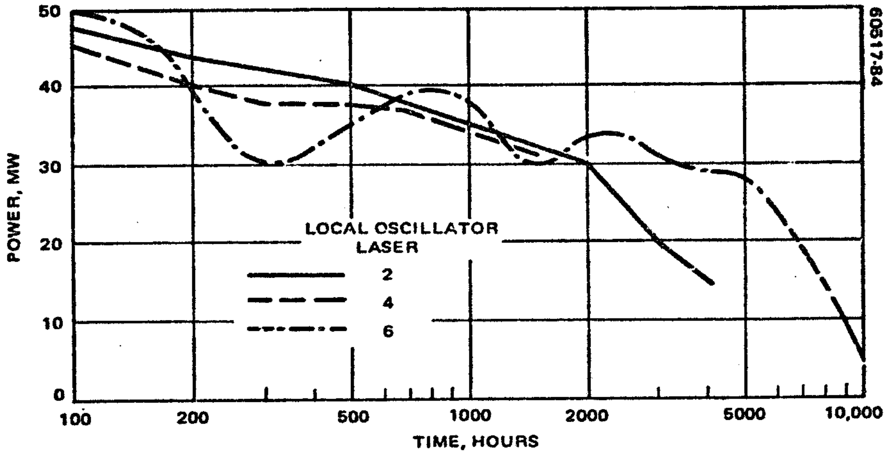

FIGURE 6-12. LOCAL OSCILLATOR LASER LIFE TEST DATA SUMMARY

7. RECEIVER PERFORMANCE CHARACTERISTICS

7.1 LOCAL OSCILLATOR FREQUENCY CONTROL

Requirements

The local oscillator frequency control utilizes a Stark cell that contains a mixture of ND_3-NH_3 which combine to form NH_2D, as well as other mixed isotopic forms of ammonia. At a total pressure of 1 Torr, the absorption coefficient is ~0.01 cm^{-1} when the Stark cell is tuned to the P(20) line center (at an electric field of 3570 V/cm). At higher pressures, the 80 MHz wide doppler broadened absorption line becomes pressure broadened and the dc breakdown voltage of the cell is reduced. If an arc develops, dissociation of the gas occurs, reducing the signal level. A convenient set of parameters which works satisfactorily for this application is:

Laser transition	P(20), 10.59 μm
Cell length	10 cm
Field gap	1.28 mm
Pressure	1 Torr
ND_3:NH_3 ratio	1:1
Resonant voltage (calculated)	456 volts
Absorption coefficient (calculated)	10 percent

A 10 percent absorption coefficient is more than adequate to provide an excellent signal-to-noise ratio for locking of the laser to the Stark cell, while the 10 cm cell length is a reasonable size for the laser package. The resonant voltage of 456 volts is a convenient value in a range where a number of precision power supplies are available.

One feature that is convenient for Stark cell applications is the ability to apply the dc potential to one of the plates, and the ac dither frequency to the opposite plate. This feature is discussed in the following subsection.

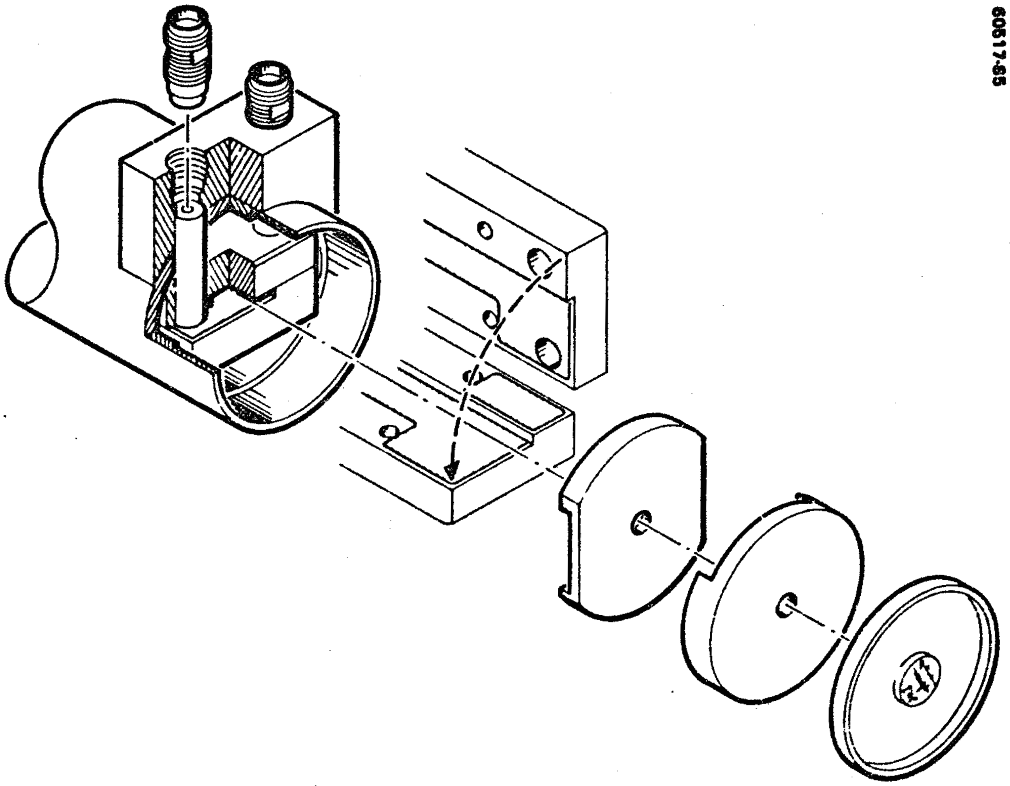

FIGURE 7-1. ASSEMBLY DETAIL AND EXPLODED VIEW OF STARK CELL

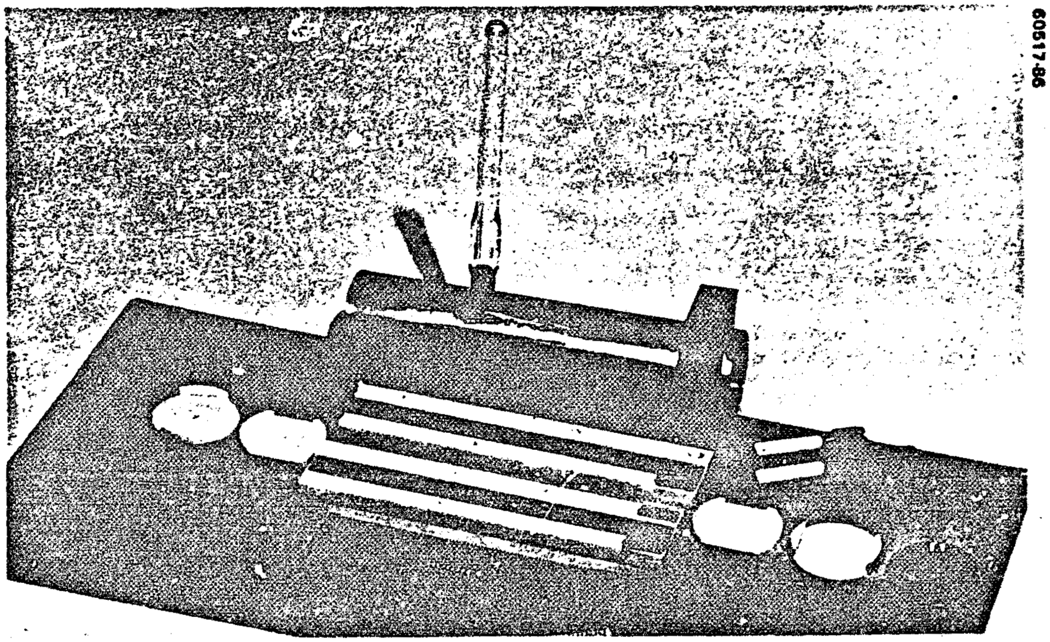

FIGURE 7-2. STARK CELL PARTS (PHOTO 60517-86)

Mechanical Design

The Stark cell consists of five main components: bore structure, end washers, end cap window assemblies, housing, and electrical feedthroughs. These components can be seen in the exploded view of Figures 7-1 and 7-2. Photos of the completed Stark cell are shown in Figures 7-3 and 7-4.

The bore structure consists of two ceramic (99.5 alumina) slabs with an evaporated gold electrode on each slab. When these slabs, whose cross section is L-shaped, are placed on each other, they form a rectangular bore of 1.28 x 6.89 x 101.7 mm. The cell voltage is applied across the 1.28 mm gap.

Each end washer is composed of two contoured ceramic disks that are also made of 99.5 alumina. When the two disks are fitted together, they form a circular washer with a rectangular recess that fits over the end of the bore structure. The washers mechanically position the bore in the center of the housing and also electrically isolate the bore electrodes from the metal end caps.

The housing and end caps, which are made of stainless steel, form the vacuum jacket for the Stark cell. The housing contains a tabulation for pumpout and processing and a flange for the electrical connectors. After the end caps are welded to the housing, the AR coated Irtran II windows are attached with epoxy.

Two electrical connections are provided, one for the electrode on each of the ceramic slabs. This allows the dc potential to be applied to one electrode and the ac dither frequency to be applied to the opposite electrode, and keeps both electrodes isolated from ground. The voltages are applied to the electrodes through OSM hermetically sealed connectors by means of a flat platinum ribbon. The ribbon is surrounded by a dual function teflon sleeve. The sleeve serves as an electrical insulator and provides a compression contact between the electrode and the ribbon, which is bent over the end face of the sleeve.

Another method of attaching the windows to the end plates is being investigated. This method involves evaporation of chrome-indium onto both the window and end plate. The two pieces are then attached by the use of an ultrasonic bonder. Future tubes will be of an all metal ceramic construction without the use of epoxies.

Cell Performance

After hard pumping and backing to 100°C, the Stark cell was filled with a 1:1 mixture to a pressure of 15 Torr and left for 48 hours. After this time, the cell pressure dropped to 8 Torr. The cell was then pumped out to 1.0 Torr where the pressure was stable. This filling procedure was found to be necessary to avoid rapid cleanup of the NH_2D onto the clean surfaces. Monitoring of the cell absorption shows that the cell is stable for more than 300 hours.

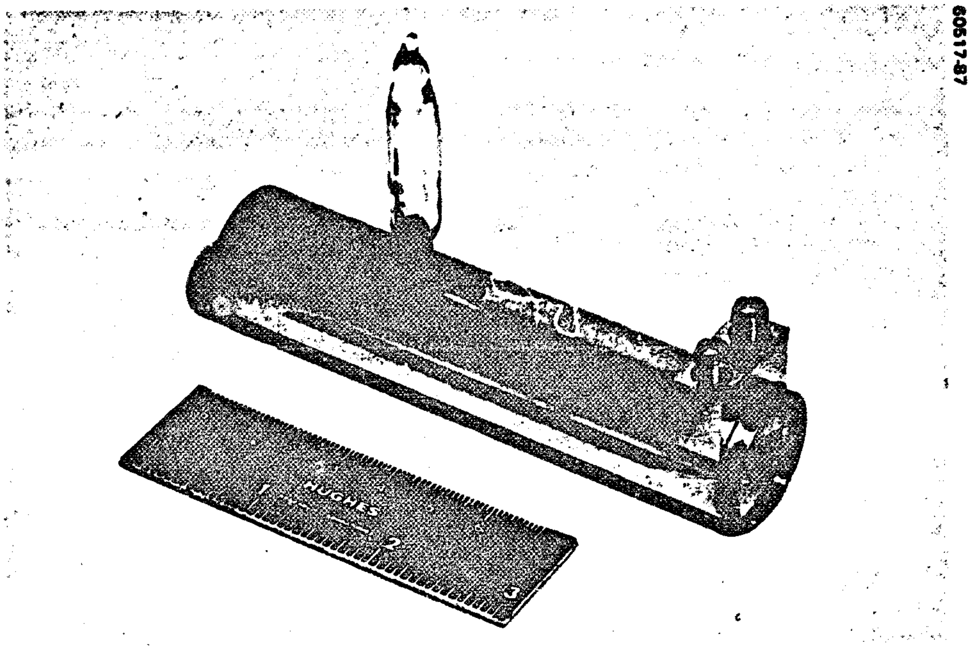

FIGURE 7-3. COMPLETED STARK CELL (PHOTO 60517-87)

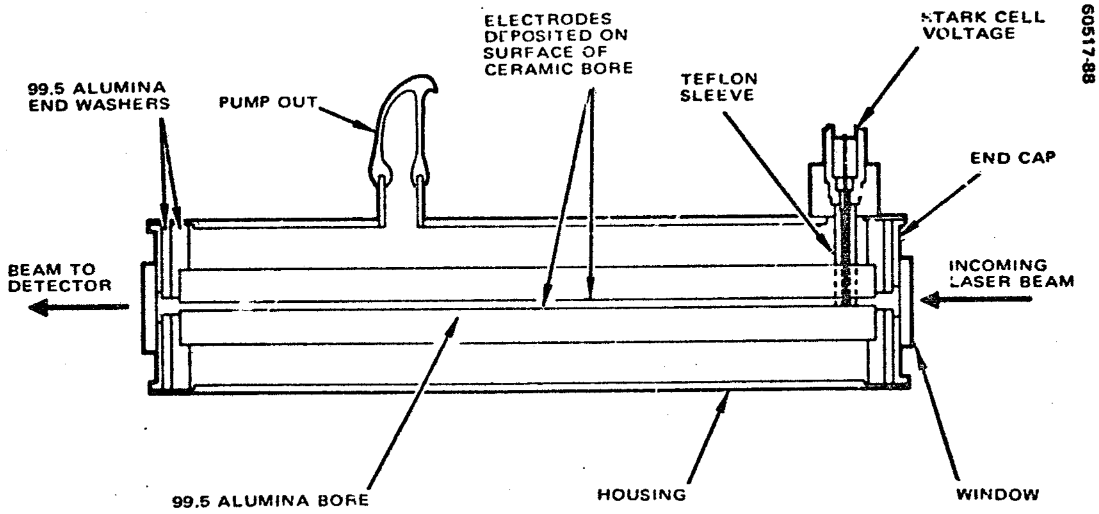

FIGURE 7-4. STARK CELL

The measured characteristics for the P(20) laser transition are as follows:

Peak absorption	9.5 percent
Resonant cell voltage	451 volts
Breakdown voltage	>1000 volts
Cell tuning sensitivity	~4.6 MHz/V

Using breadboard laboratory electronics, a CO_2 laser was locked to the cell without any difficulty. Other resonance absorptions exist in the cell to which the laser may be stabilized. The laser transitions that can be used include P(20), P(14), R(12), P(26), and R(18). The last two are associated with $N^{15}H_2D$ which is a part of the mixture used to fill the cell. Table 7-1 lists all transitions for which Stark tunable signals are observed, their measured J values, and the resonant voltages. Data were taken from oscilloscope photographs, so the voltages shown are only approximate.

Electronics

Figure 7-5 is a block diagram of the electronic system. A perturbation or dither modulation is used to generate error signals of the proper sense. These errors are filtered, amplified, and fed back to the laser to maintain the laser frequency equal to the Stark cell absorption frequency.

A precision dc power supply sets the frequency of the Stark cell absorption line. The supply is adjustable to allow laser tuning; a 4-1/2 digit

TABLE 7-1. TRANSITION SUMMARY OF STARK TUNABLE SIGNALS

Laser Line	Molecule	J	Stark Voltage	Approximate % Absorption in 10 cm
P(20)	$N^{14}H_2D$	4	442,590,880	>10
P(14)	$N^{14}H_2D$	4	570,760,1140	>10
R(12)	$N^{14}H_2D$	4	760,895	>10
R(14)	Deuterated $N^{14}H_3$		820	*
R(26)	Deuterated $N^{14}H_3$		850	*
P(26)	$N^{15}H_2D$	4	170,210,355,730	12
R(18)	$N^{15}H_2D$	6	580,700,880	8
P(10)	Deuterated $N^{15}H_3$	11	380,420,460,520 600,710,860	*
P(28)	Deuterated $N^{15}H_3$	Second order Stark effect	260	*
R(24)	Deuterated $N^{15}H_3$		910	*

*Less than 3% absorption.

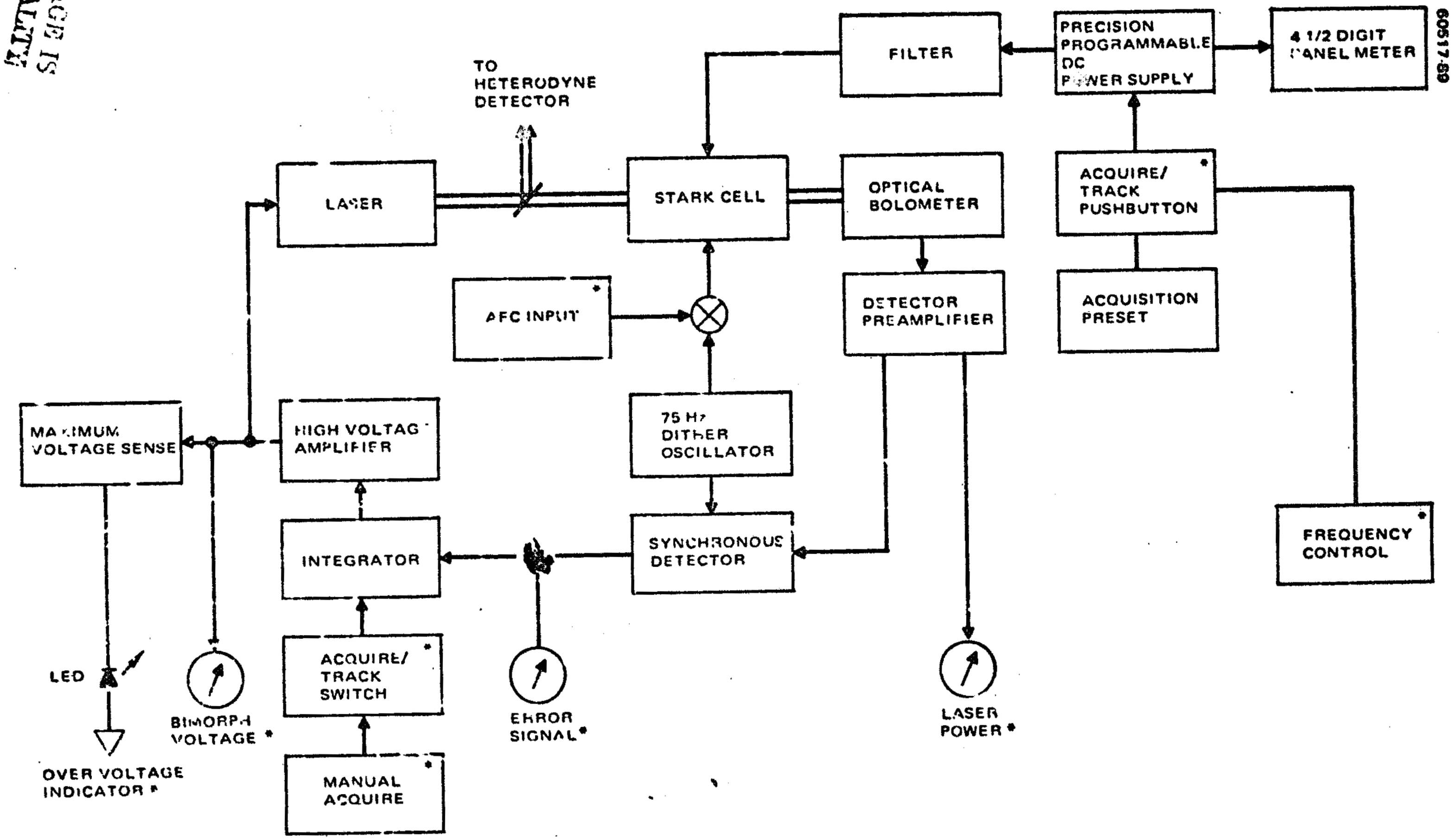

* FRONT PANEL

FIGURE 7-5. STARK CELL BREADBOARD ELECTRONICS panel meter monitors the voltage. (The supply may be remotely programmed to simulate telemetry commands at a later date if desired.) A pushbutton is incorporated for initial acquisition; the button sets the power supply to a voltage where there is no possibility of an ambiguous lock due to two Stark resonances. After acquisition, the voltage returns to the desired control voltage at a rate that the servo can track.

A 75 Hz, 20 volt peak-to-peak signal is applied to the other Stark cell electrode. Provisions are incorporated to apply a dc coupled signal to this electrode for system test or for AFC tracking without disturbing the power supply setting.

The amplitude modulation on the laser beam is detected by a dc coupled bolometer consisting of a matched pair of thin film thermistors. The dc component of this signal is used to drive a meter for an indication of laser power. The 75 Hz component is separated, amplified, and synchronously demodulated to establish an error signal. This signal is filtered and amplified, then routed to the laser bimorph for frequency correction. An integrator is incorporated in the loop filter to eliminate static tracking errors.

Stark Stabilized Laser Stability

Two Stark cell stabilized local oscillator lasers were used to determine the overall frequency stability. The laser outputs were combined on a photomixer and was observed with a linear frequency discriminator. The resulting chart record is shown in Figure 7-6. The rms stability from the chart record is approximately 0.1 MHz, while the values for each oscillator are estimated at 70 kHz. It should be noted that the limiting factor in laser frequency stability is the acoustic environment. In these tests, the environment was a typical laboratory with an acoustic noise level of about 75 dB.

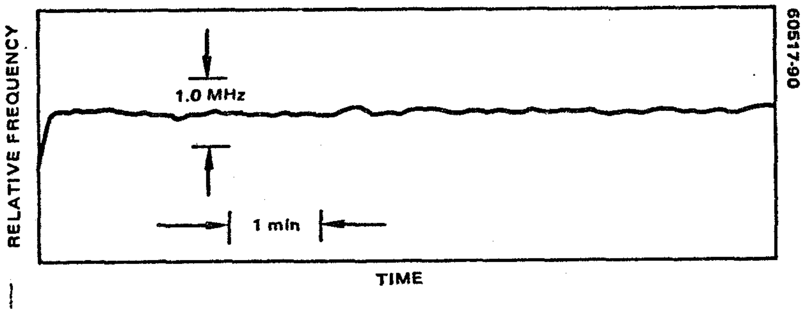

FIGURE 7-6. STARK STABILIZED LOCAL OSCILLATOR LASER STABILITY

C.2

7.2 OPTICAL MIXER CHARACTERISTICS

The type of mixer to be used in the receiver is the SAT photovoltaic HgCdTe detector operating at a temperature of about 110°K. Under these operating conditions the following characteristics of the detector are:

Diode type	HgCdTe
R_o (back resistance, ohms)	1 to 2 K
Cutoff frequency	>500 MHz
Local oscillator power	2 to 5 mW maximum 0.5 mW typical operating
Heat load, optical and electrical	2.5 mW
Operating temperature	100 to 110°K
Detector quantum efficiency	60 percent*
Operating current	0.1 to 0.4 mA

7.3 PREAMPLIFIER CHARACTERISTICS

The actual noise equivalent power (NEP) achieved in the optical heterodyne receiver is a critical function of the preamplifier characteristics. The preamplifier assumed for use in this receiver is the same used in the wideband receiver front end presently being integrated. Its characteristics are given as follows:

Preamplifier bandwidth	1.5 GHz
Noise figure	4 dB, 435°K
Dynamic range	To -40 dBm for 1 dB gain reduction
Small signal gain	50 to 55 dB
Input impedance	50 ohms
Input VSWR	2.5 to 1

---

*Recent quantum efficiencies obtained by Honeywell and Lincoln Laboratory center around 60 percent; that of the detector recently received from SAT is 59 percent. However, original wideband detector in receiver front end has η of 42 percent.

7.4 COMPARISON OF MEASURED NEP AND THEORETICAL OPTICAL MIXER NEP AS FUNCTION OF LOCAL OSCILLATOR POWER

Based on measurements reported in the AIL Final Report to Contract NA55-23119, the theoretical NEP density, of the receiver front end was calculated and compared with the measured data. NEP is composed of detector shot noise, detector thermal noise, dark current shot noise, background shot noise, and preamplifier thermal noise, and is increased by mixing loss. The general expression is

$$\mathrm{NEP}_o = L_m\left[\frac{h\nu}{\eta} + \frac{K\left(T_m + T_{IF}\right)}{G} + \frac{h\nu}{\eta}\left(\frac{I_b + I_d}{I_o}\right)\right] \qquad (1)$$

where

L_m = mixing loss, assumed as 1.54 (efficiency = 65 percent) for a focused signal and uniform local oscillator field

T_m = physical mixer temperature, 77°K

T_{If} = 435°K, NF = 4 dB

I_d = bias current, 0.3 mA at 0.6 volt back bias for the conditions of measurement

I_b = background current, not included in calculated data

I_o = local oscillator induced direct current

η = 41.8 percent, calculated from $\eta = I_o h\nu/e$ in AIL Final Report

G = conversion gain

The conversion gain G in the AIL Final Report was not used since it is derived for a load that is impedance matched to the detector output impedance. Based on a schematic supplied by NASA GSFC, it is clear that the preamplifier is not matched to the detector, but instead a standard wideband Avantek preamplifier with a nominal input impedance of 50 ohms is used. Because of this, an expression was derived for conversion gain valid for the actual circuit.

The equivalent circuit used for the derivation is shown in Figure 7-7 where

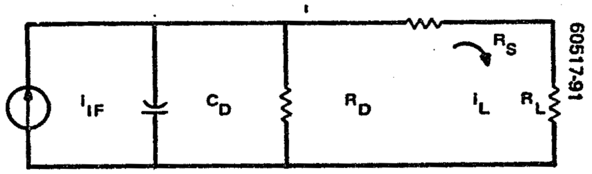

FIGURE 7-7. EQUIVALENT CIRCUIT OF SAT DETECTOR

i_{IF} = intermediate frequency current generated in detector diode

i_L = IF current flowing in load

R_D = diode reverse resistance, 1125 ohms for conditions of measurement

C_D = diode capacitance, neglected in derivation since NEP_o was measured at IF of 20 MHz

R_S = diode series contact resistance, 35 ohms

Previously, i_{IF} was given as

$$i_{IF} = \frac{\eta e}{h\nu} (P_{LO} P_S)^{1/2} \tag{2}$$

The load current flowing in R_L, i_L is

$$i_L = i_{IF} \left(\frac{R_D}{R_L + R_S + R_D} \right) \tag{3}$$

The available IF signal power or signal power delivered to R_L, P_L is

$$P_L = i_L^2 R_L \tag{4}$$

Defining conversion gain G as the ratio of signal power delivered to R_L to the input signal power P_S, and using Equations 1, 2, and 3, conversion gain G is given as

$$G = 2\left(\frac{\eta e}{h\nu}\right)^2 \left(\frac{R_D}{R_D + R_L + R_S}\right)^2 P_{LO} R_L \qquad (5)$$

NEP_o as a function of local oscillator power I_o was then calculated for several values of I_o. Results are tabulated below and are plotted in Figure 7-8.

P_{LO}, mW	I_o, mA	NEP_o, W/Hz
0.0334	0.1	5.69×10^{-19}
0.0668	0.2	3.19×10^{-19}
0.1336	0.5	1.69×10^{-19}
0.334	1.0	1.19×10^{-19}
0.668	2.0	9.39×10^{-20}
1.336	4.0	8.14×10^{-20}

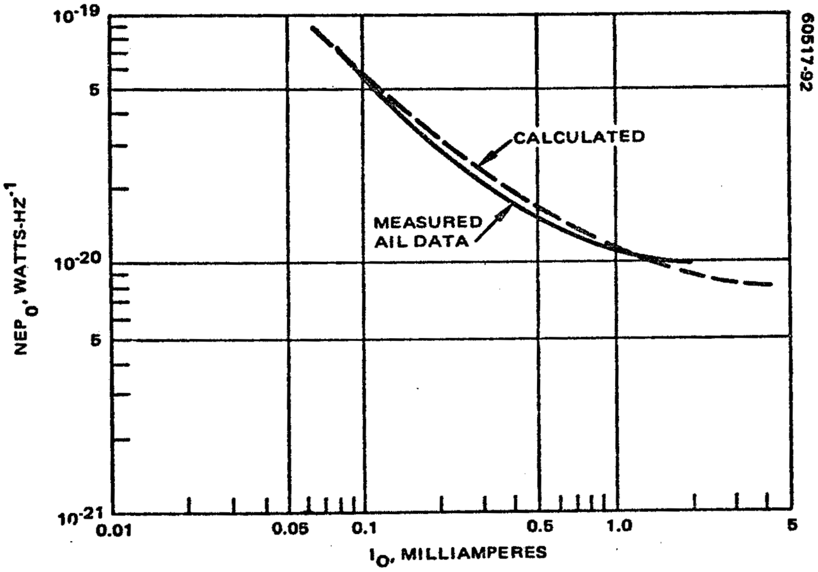

FIGURE 7-8. COMPARISON OF THEORETICAL NEP_O AND MEASURED DATA FOR AIL RECEIVER FRONT END

7.5 MEASUREMENT OF COMPLETE RECEIVER NEP

Given the sensitivity of the optical heterodyne receiver in the radiometric mode and the signal power from a thermal source, it is possible to write an expression of receiver NEP as a function of measured $(\mathrm{SNR})_{IF}$, blackbody source temperature, and radiometric integration time. From the expression of $(\mathrm{SNR})_v$

$$(\mathrm{SNR})_v = \frac{1}{8\beta}(\mathrm{SNR})_{IF}^2 \cdot (B\tau) \tag{6}$$

$(\mathrm{SNR})_{IF}$ is substituted by using

$$(\mathrm{SNR})_{IF} = \frac{P_s}{\mathrm{NEP.}\,B} = \frac{2h\nu}{\mathrm{NEP}\left\{\exp(h\nu/kT_s) - 1\right\}} \tag{7}$$

or

$$(\mathrm{SNR})_v = \frac{1}{8\beta}\,\frac{(2h\nu)^2}{(\mathrm{NEP})^2\left\{\exp(h\nu/kT_s) - 1\right\}^2} \cdot (B\tau) \tag{8}$$

Solving for NEP,

$$\mathrm{NEP} = \frac{h\nu}{\sqrt{2\beta}}\,\frac{1}{\left\{\exp(h\nu/kT_s) - 1\right\}}\left(\frac{B\tau}{(\mathrm{SNR})_v}\right)^{1/2} \tag{9}$$

The IF passband shape factor, β, is 1/2 for a single tuned circuit, $\sqrt{2}/2$ for a gaussian shaped circuit, and 1 for a rectangular passband[4]. The five-pole Bessel filter used in the receiver subsystem is closest to a gaussian shape, and the above expression becomes

---

[4] Appendix B.

$$NEP = \frac{h\nu}{\sqrt[4]{2}} \; \frac{1}{\{\exp(h\nu/kT_s) - 1\}} \left(\frac{B\tau}{(SNR)_v}\right)^{1/2} \qquad (10)$$

Figure 7-9 is a block diagram of the NEP measurement setup. The blackbody cavity source is placed near the focus of the bench collimator. An iris is placed precisely at the focus of the collimator. The source is regulated at a temperature T_s, and the chopper is located such that the output radiation is modulated at the chopping frequency, f_c. At the receiver, the output of the IF amplifier is filtered by its characteristic bandwidth B and shape factor β. The output of the amplifier is detected and drives the lock-in amplifier. The synchronously detected output or the ac output, can be monitored for signal-to-noise measurements. A true rms voltmeter is used to measure the ac output of the amplifier.

In the actual measurement, the following values were used:

$B = 100$ MHz

$\beta = \sqrt{2}/2$

$f_c = 89$ Hz

$T_s = 1000$°K

	Trial 1	Trial 2	Trial 3
τ =	0.036	0.071	0.143
$(SNR)_v^{1/2}$ =	20	27.5	42.0
NEP =	79 $h\nu$	82 $h\nu$	75 $h\nu$

Thus from Equation 10

$$NEP = (1.46 \pm 0.06) \times 10^{-18} \text{ W-Hz}^{-1}$$

The factor of 79 times the quantum limit is in accordance with what is expected from the measuring conditions. Recalling that NEP = $h\nu/\eta'$, and that $\eta' = \eta L_m L_o L_t$, the following typical values for each loss term are assigned.

$\eta = 0.3$

$L_m = 0.5$

$L_o = 0.5$

$L_t = 0.2$ (for a measured local oscillator induced current of 0.2 mA)

and calculated value of NEP is $h\nu/\eta' = 67\ h\nu$.

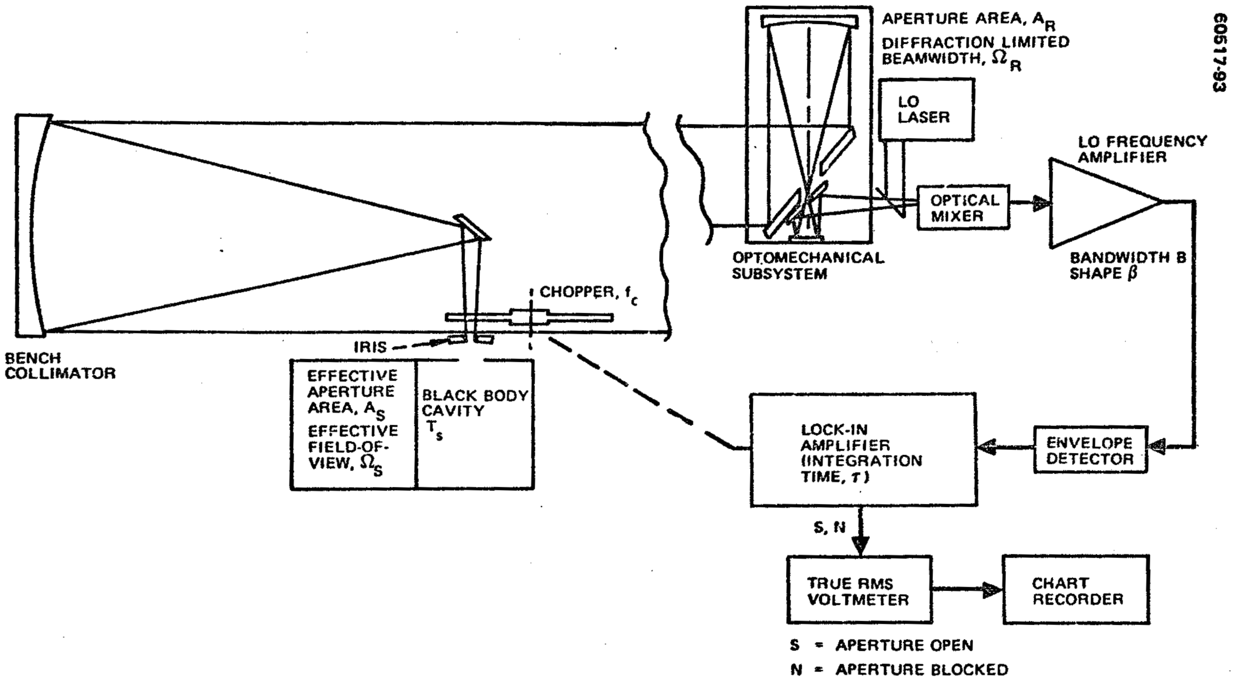

FIGURE 7-9. RECEIVER NEP MEASUREMENT BLOCK DIAGRAM

8. TRANSCEIVER DIPLEXING

Transmit and receive beams will be separated by means of polarization in the transceiver. In the optical train, the 10.6 μm energy will be linearly polarized and mutually orthogonal in the transmitter and receiver optical trains. The components used to perform the diplexing function are the wire grid polarizer and the λ/4 plate. Figure 8-1 is a schematic of the diplexer design concept.

8.1 WIRE GRID POLARIZER

A grid of closely space fine wires serve as an efficient polarizer for 10.6 μm radiation with distinct advantages over the conventional Brewster-angle polarizers. Ion-beam machining has proved to be a useful tool for precise etching of the fine wire grid patterns into the surface of a material through a deposited thin film. This technique is used to produce high quality wire grid polarizers from a gold film on a germanium or CdTe substrates. A gold film is deposited onto the AR coated window and is overcoated with photoresist masking material, exposed in converging argon laser beams to produce an interference pattern exposure, and developed. The photoresist grating pattern serves as a mask for the ion-beam machining; a broadly focused beam of argon ions is used to etch away the gold in the open areas, leaving the desired metal grid lines. Grids with 1.1 μm intervals produce extinction ratios as high as 500:1; those with 0.8 μm intervals can produce extinction ratios as high as 1000:1. Typical performance for 90° incidence is 93 percent transmission and 98 percent reflection of the orthogonal polarization.

Polarizers used as diplexers, however, must work at angles other than perpendicular incidence. The performance of the grating at an angle of 45° is degraded somewhat compared with 90°. Two polarizers were fabricated on cadmium telluride substrates and were optimized for operation at 45° incidence. The performance of these two gratings is given below:

Polarizer	Angle, °	$P_{\parallel}$ Transmittance, %	$P_{\perp}$ Reflectance, %	Aperture, cm
4-15	45	98	85.6	1 x 1.4
4-16	45	98	80.2	1 x 1.4

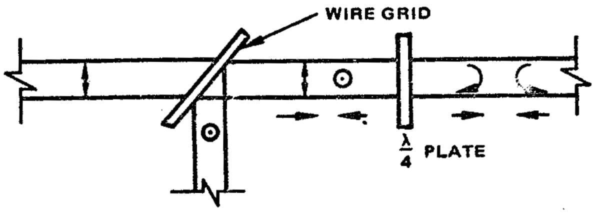

a) DIPLEXER CONCEPT

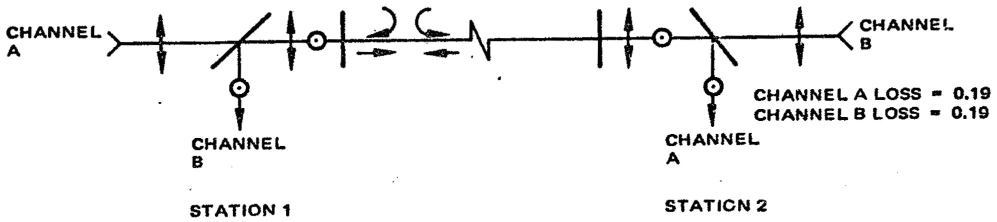

b) EQUAL LOSS CONFIGURATION

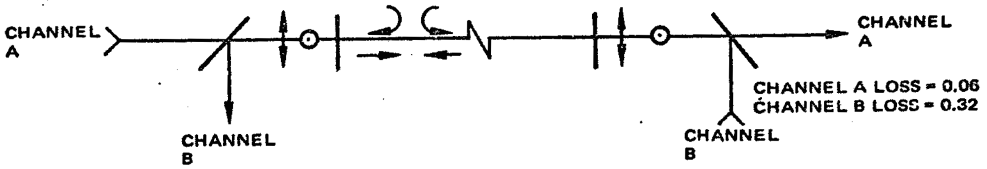

c) MINIMUM CHANNEL A LOSS CONFIGURATION

FIGURE 8-1 OPTICAL DIPLEXER

60517-94

The polarizer 4-15 has been selected for use in the transceiver because of its higher reflectance. Further development of this type of device should result in an improvement in the reflectance over what is currently being achieved.

8.2 CADMIUM SULFIDE λ/4 PLATE

The function of the quarter wave plate is to convert linear polarization into right- and left-hand circular polarization for transmission through the optical train and through space to the opposite terminal. The use of circular polarization in the medium removes the necessity of tracking the polarization. The cadmium sulfide λ/4 plate is AR coated, has a 1 by 1 cm clear aperture, and is about 1 mm thick. The plate is available commercially from II-VI, Inc., of Glenshaw, Pa. Measured transmission of 10.6 μm energy through the plate is about 99 percent.

8.3 DIPLEXER PERFORMANCE

The diplexer loss depends on which polarization is used. For two transceivers operating in a bistatic mode, it would be advantageous to use the opposite polarization at each terminal, thereby equalizing the loss of the two channels. This concept, illustrated in Figure 8-1b, allows a loss of 0.15 and 0.02 accordingly for the two polarizations through the wire grid and 0.01 loss for the λ/4 plate.

	Diplexer Loss		
Optical Channel	Terminal 1	Terminal 2	Total Diplexer Loss
A	0.15 + 0.01	0.02 + 0.01	0.17 + 0.02 = 0.19
B	0.02 + 0.01	0.15 + 0.01	0.17 + 0.02 = 0.19

An alternative method of combining polarizations may be used if it is important to minimize the loss of one channel such as may be required for a wideband data channel as compared with only a beacon require' the other channel. This alternate arrangement is shown in Figure 8-

Optical Channel	Terminal 1	Terminal 2	Total Diplexer Loss
A	0.02 + 0.01	0.02 + 0.01	0.06
B	0.15 + 0.01	0.15 + 0.01	0.32

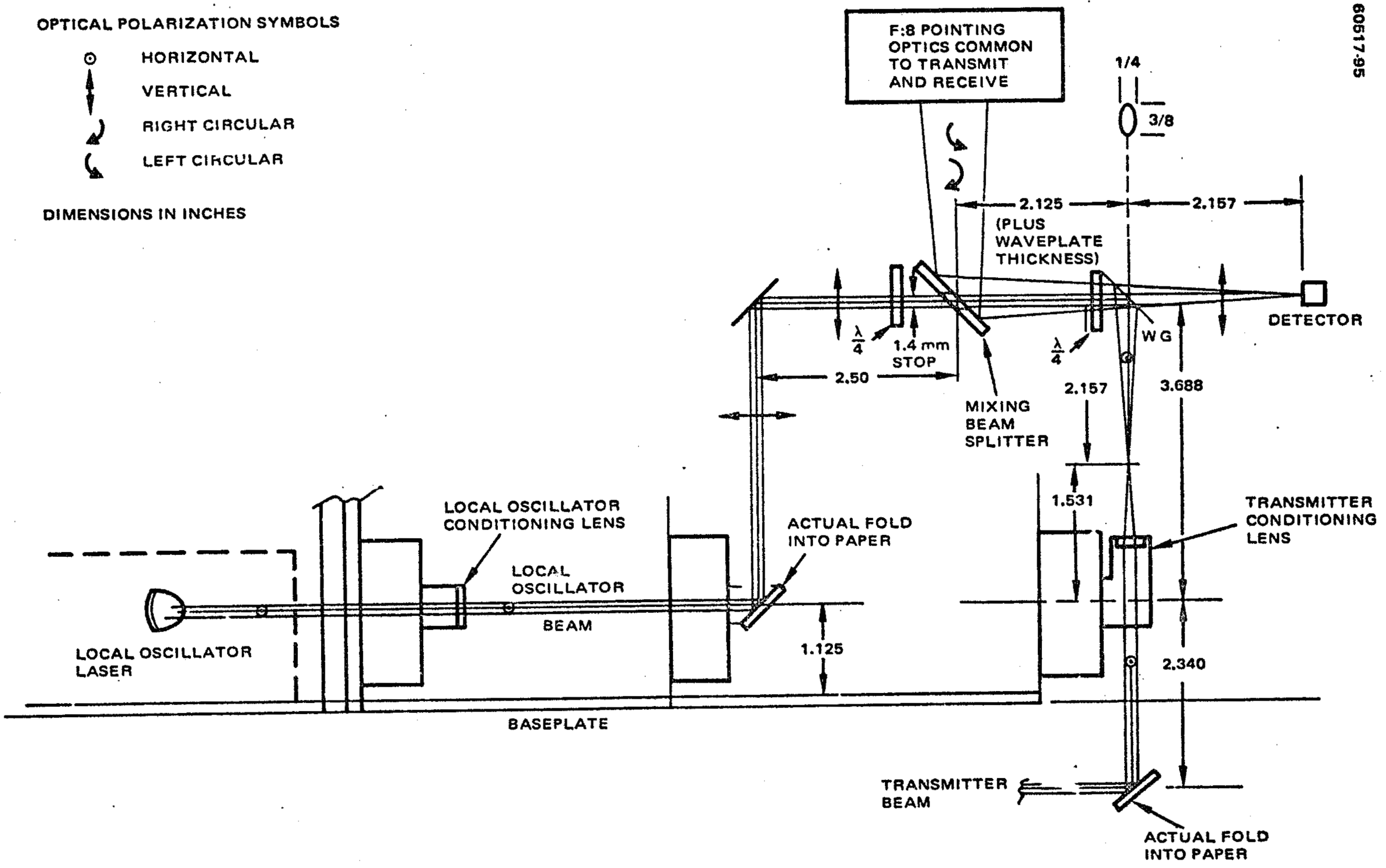

FIGURE 8-2. TRANSCEIVER OPTICAL TRAIN LAYOUT

8.4 TRANSCEIVER INTEGRATION

The transceiver concept implies wideband transmission in two directions simultaneously, although even a receiver terminal requires a beacon to facilitate acquisition and tracking between the terminals. The 10 µm receiver terminal may employ a beacon of another wavelength which could be diplexed through the use of dichroic mirrors in the subsystem. However, it is more likely that the beacon will be another 10 µm laser operating on another P-line so as not to interfere with the receiver wavelength. This discussion addresses the specific implementation of the use of diplexing of 10 µm lasers in the transmit and receive mode, whether they are data channels or merely beacon signals.

The inclusion of a wideband transmitter subsystem in the present receiver engineering model package can be accommodated by locating the transmitter laser on the back of the mounting baseplate. For later models, the transmitter laser will be located inside the structure along with local oscillator lasers and redundant transmitter lasers. These two basic optical train are discussed briefly in the following subsections.

Transceiver Optical Train (Modified Receiver Engineering Model)

The optical train for the transceiver consists of the F:8 common pointing optics, mixer beam splitter, polarization diplexer, transmitter conditioning optics, local oscillator conditioning optics, and optical mixer (detector). Figure 8-2 illustrates the complete transceiver optical train. Table 8-1 is a summary of transceiver characteristics.

The received optical signal is collected with the pointing optics, directed in an F:8 beam through the optical system, and combined with the local oscillator beam at the mixing beam splitter. Both the signal and the local oscillator beams are circularly polarized at the mixing beam splitter, but are resolved to linear polarization via the $\lambda/4$ plate located at the diplexer. The wire grid polarizer then passes both the signal and local oscillator beams through the wire grid to the detector.

The main losses in the receiver optical train are:

1) Absorption loss - Approximately 1 percent loss is incurred for each of seven reflective surfaces, a total of 6.7 percent, or 0.3 dB.

2) Diplexer loss - Approximately 3 percent loss is incurred as described in Section 4.3, or 0.13 dB.

3) Surface figure - Surface figure of the primary and secondary show overall surface quality of two fringes of 6328 Å light. The loss of peak energy is about 1.8 percent per surface, or a net loss of 0.16 dB.

TABLE 8-1. OPTOMECHANICAL CHARACTERISTICS OF TRANSCEIVER

Parameter	Optomechanical	Receiver	Transmitter
Weight, lb	24.78	4.8*	3.3**
Volume of structural frame, in^3	2349	14	38
Diagonal, in	24		
Antenna gain over 0.26° field of view, dB	93.7	91.4	91.7
Gimbal coarse pointing range, deg	±10°	Common	
Pointing accuracy, deg	0.02°		
Step size, deg	0.002°		
IMC pointing accuracy (reset), deg	0.0083°		
Beam tilt at mixer, rad	1.76×10^{-3}		
System loss (optical), dB			
Absorption		0.30	0.30
Diplexer		0.13	0.76
Surface figure		0.16	0.16
Mixing efficiency		1.67	
Illumination efficiency			0.75
Off-axis losses		0.01	
Total, dB		2.27	1.97

*Weight of local oscillator laser and radiation cooler.
**Weight of transmitter laser = 3.[illegible], not including modulator driver

4) Beam tilt - Off-axis losses are caused by beam tilt between the signal and local oscillator beams, 0.011 dB maximum.

5) Mixing efficiency - because of the F:8 signal beam and the F:40 local oscillator beam, taking into account the 0.2 central obscuration, the loss in mixing efficiency is 1.67 dB.

The total receiver optical train losses are 2.27 dB, and the total antenna gain is reduced from 93.7 dB for uniformly illuminated aperture to 91.4 dB with losses fully accounted for

The transmitter train includes the same basic F:8 pointing optics as the receiver train. The transmitter train thus includes a conditioning lens to produce an F:3 beam to illuminate the primary optical system. However, since the transmitter beam is gaussian and the primary optical system is centrally obscured, the minimum truncation and obscuration loss occurs for an aperture radius to beamwidth ratio of 1.25*. The resulting loss of

---

*B. J. Klein and J. J. Degnan, Applied Optics, Vol. 13, 9 September 1974 pp. 2134-2140.

transmitter antenna efficiency (compared to the ideal $4\pi A/\lambda^2$) is 0.75 dB. The losses, therefore, are as follows:

1) Absorption losses - Same as the receiver train: 0.3 dB
2) Diplexer loss - 0.75 dB as described in subsection 8.2
3) Surface figure losses - Same as receiver train: 0.16 dB
4) Illumination efficiency - 0.75 dB

Total transmitter train optical loss is 1.97 dB, reducing the net transmitter antenna gain to 91.7 dB.

Opto-Mechanical Layout

The optomechanical subsystem of the receiver terminal was designed to accommodate a laser having a maximum length of 10.5 inches. Both the developmental model waveguide local oscillator laser and the productized version can easily be accommodated within the 10.5 inch space constraint. However, the transmitter laser with its modulator will have a length of slightly over 16 inches and cannot be fitted inside the present receiver optomechanical package.

There are two straightforward methods of accommodating the longer laser. First, a hole could be cut into the end plate, allowing the transmitter laser to protrude about 5 or 6 inches. This method is ruled out, however, since modification of the structure will render environmental tests invalid. The second method is to mount the transmitter laser on the backside of the baseplate. Figure 8-3 shows how the layout may be accomplished with no modifications required of the basic structure. The addition of two folding mirrors external to the structure and the removal of one folding mirror inside the box (replacing it with a transmitter conditioning lens) will provide ideal accommodation for the transmitter laser. Cooling of the transmitter and the local oscillator laser can be easily handled by the beryllium baseplate. A conduction cooling device can be attached adjacent to the transmitter laser.

8.5 GROWTH TO LARGER OPTICS AND REDUNDANT LASERS

Higher data rate requirements of the future and concerns for long life and reliable operation will force optical aperture sizes to be larger than the 7-inch diameter presently in use in the receiver engineering model. It has been determined that the optics size should be about 10 inches as opposed to the present 7 inches, and the structure should be somewhat longer to accommodate the transmitter lasers. Conveniently, both of these requirements can be met by directly scaling the present optomechanical structure size.

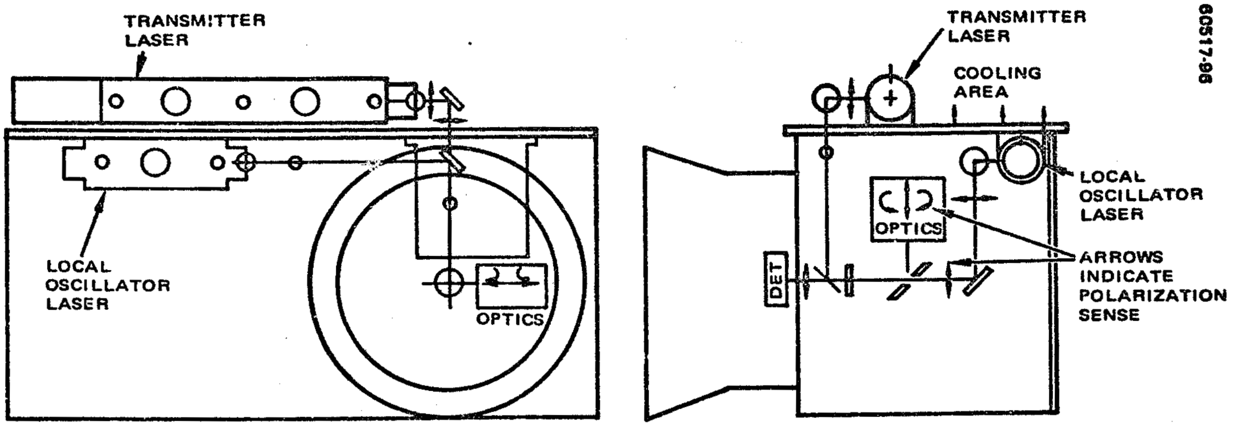

TOP VIEW

SIDE VIEW

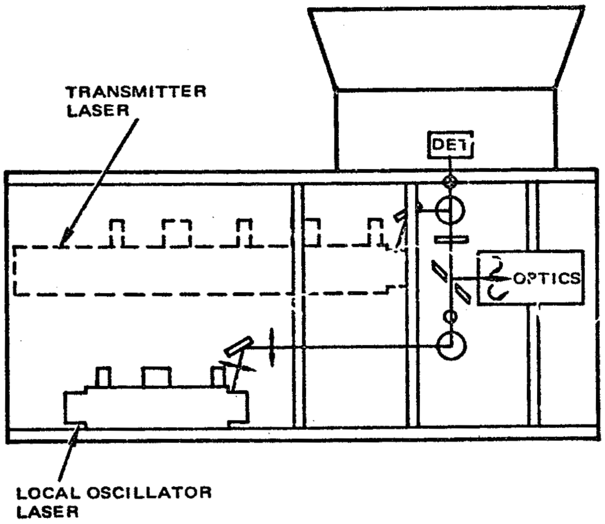

FRONT VIEW

FIGURE 8-3. TRANSCEIVER OPTOMECHANICAL LAYOUT

Figure 8-4 illustrates how two transmitter lasers and two local oscillator lasers may be accommodated on the baseplate inside the structure.

Scaling the size of the basic structure will not invalidate the thermal and structural analyses which were performed on the previous contract since thermal and mechanical loading factors also scale in a known manner with change in size. However, addition of the redundant lasers and the specific locations and heat loads will have to be included in new analytical runs.

Designing a larger structure, switching optics, and conducting new thermal and mechanical runs are tasks that should be included in the development of a prototype transceiver. Refinements of design suggested from testing of the engineering model may also be included in the prototype.

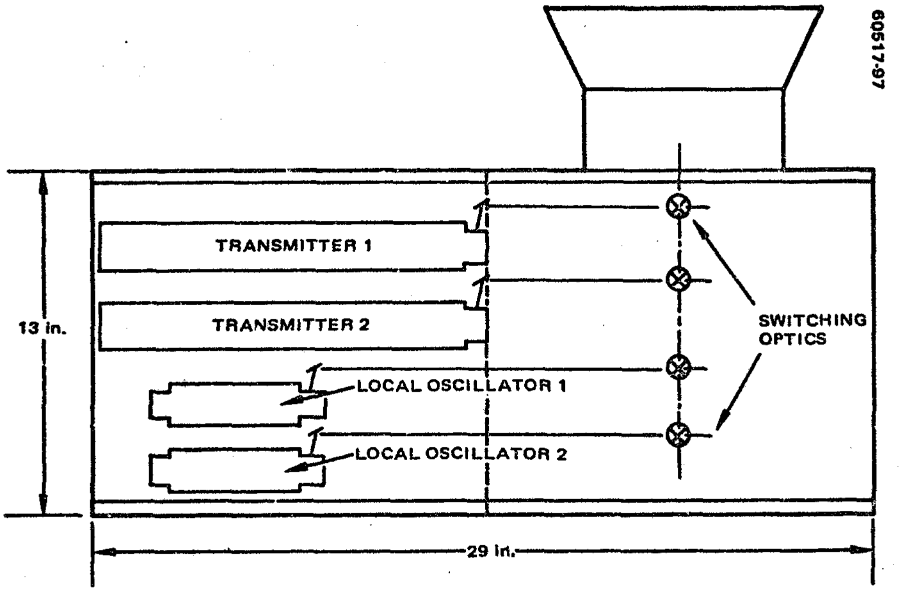

FIGURE 8-4. TRANSCEIVER OPTOMECHANICAL STRUCTURE TO ACCOMMODATE: 10 INCH DIAMETER OPTICS, REDUNDANT TRANSMITTERS AND LOCAL OSCILLATORS

9. REFERENCES

1. W.W. Rigrod, "Saturation Effects in High-Gain Lasers," Journal of Applied Physics, Vol. 36, No. 8, August 1965, pp. 2487-2490.

2. R.L. Abrams and W.B. Bridges, "Characteristics of Sealed-Off Waveguide CO_2 Lasers," IEEE Journal of Quantum Electronics, Vol. QE-9, No. 9, September 1973, pp. 940-946.

3. I.P. Kaminow and E.H. Turner, "Electrooptic Light Modulators," Applied Optics, Vol. 5, No. 10, October 1965, pp. 1612-1628.

4. A.V. Nurmikko, "A Novel Technique for Measuring Small Absorption Coefficients in Semiconductor Infrared Laser Window Materials," Applied Physics Letters, Vol. 26, No. 4, February 1975, pp. 175-178.

5. Bell Telephone Laboratories, Transmission Systems for Communications, Chapter 27, Western Electric, Inc., Winston-Salem, North Carolina, 1970.

6. A. Yariv, Introduction to Optical Electronics, Chapter 9, Holt, Rinehart and Winston, New York, 1971.

7. A.L. Schultz, "Excitation of Cold Cavity Modes in a Coupling Modulated CO_2 Laser," IEEE Journal of Quantum Electronics, Vol. QE-11, No. 9, December 1975, pp. 791-793.

8. Final report for NASA Contract NAS1-10894.

9. G.W. Day, O.L. Gaddy, and K.C. Jungling, "Electro-optic Q-Switching of the CO_2 Laser," IEEE Journal of Quantum Electronics, Vol. QE-6, September 1970, pp. 553-556.

10. R.L. Abrams, "Coupling Losses in Hollow Waveguide Laser Resonators," IEEE Journal of Quantum Electronics, Vol. QE-8, November 1972, pp. 838-843.

APPENDIX A

EXPERIMENTAL DATA ON GAIN, INPUT POWER, AND POWER OUTPUT FOR CO_2 WAVEGUIDE LASER WITH N_2 FILLS

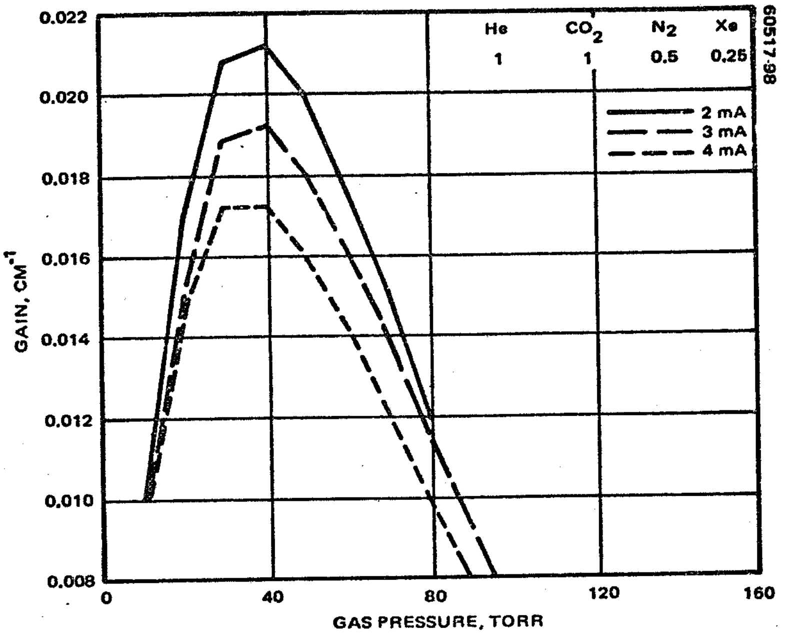
60517-98
He 1
CO2 1
N2 0.5
Xe 0.25
2 mA
3 mA
4 mA
GAIN, CM-1
0.022
0.020
0.018
0.016
0.014
0.012
0.010
0.008
0
40
80
120
160
GAS PRESSURE, TORR

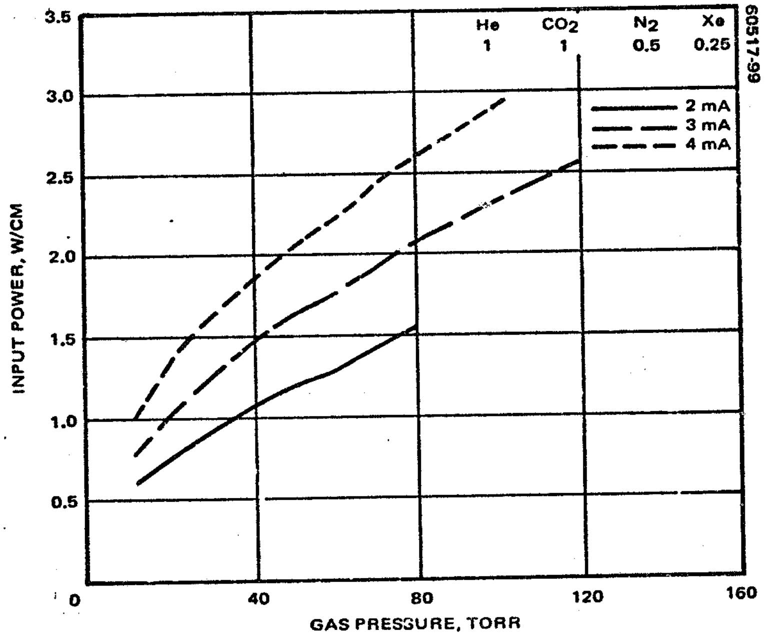
60517-99
He 1
CO2 1
N2 0.5
Xe 0.25
2 mA
3 mA
4 mA
INPUT POWER, W/CM
3.5
3.0
2.5
2.0
1.5
1.0
0.5
0
40
80
120
160
GAS PRESSURE, TORR

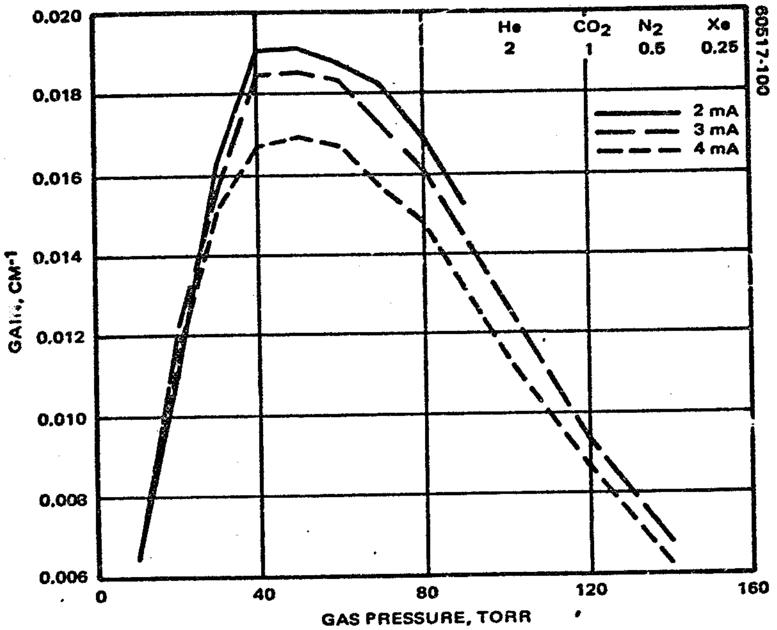

60517-100
He 2
CO2 1
N2 0.5
Xe 0.25
2 mA
3 mA
4 mA
GAIN, CM-1
0.020
0.018
0.016
0.014
0.012
0.010
0.008
0.006
0
40
80
120
160
GAS PRESSURE, TORR

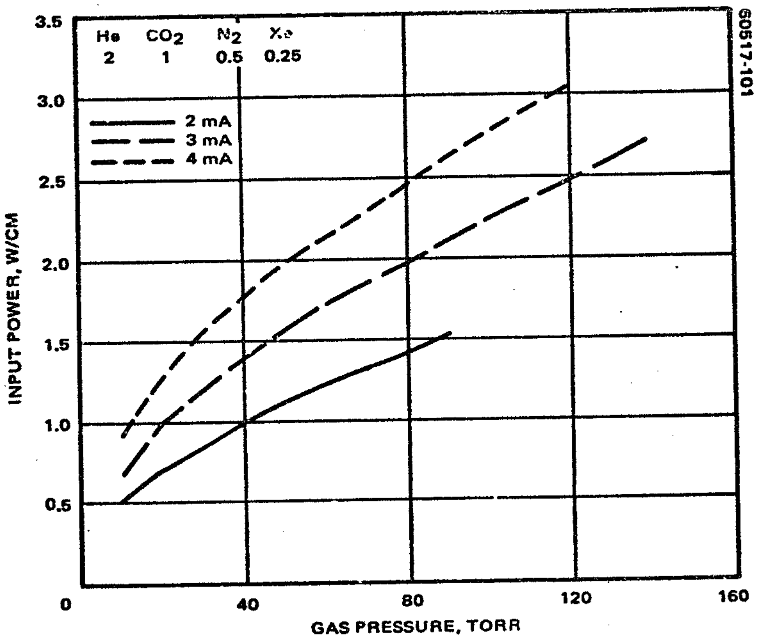

60517-101
He 2
CO2 1
N2 0.5
Xe 0.25
2 mA
3 mA
4 mA
INPUT POWER, W/CM
3.5
3.0
2.5
2.0
1.5
1.0
0.5
0
40
80
120
160
GAS PRESSURE, TORR

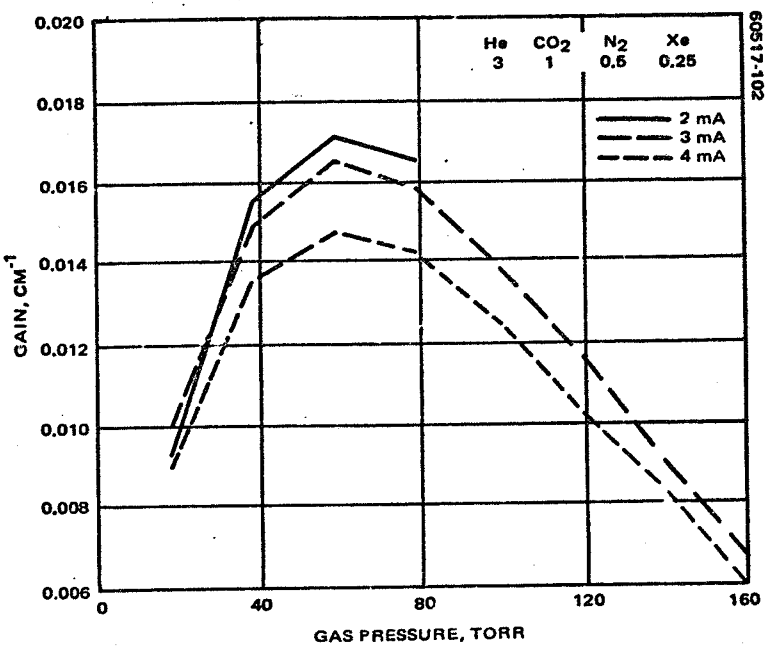

0.020
0.018
0.016
0.014
0.012
0.010
0.008
0.006
GAIN, CM^{-1}
0
40
80
120
160
GAS PRESSURE, TORR
He 3
CO$_2$ 1
N$_2$ 0.5
Xe 0.25
2 mA
3 mA
4 mA
60517-102

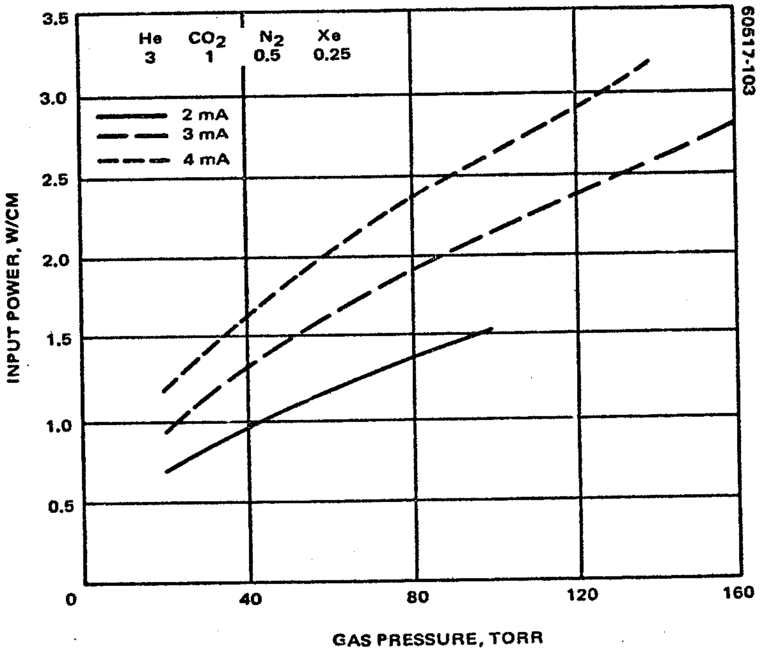

3.5
3.0
2.5
2.0
1.5
1.0
0.5
INPUT POWER, W/CM
0
40
80
120
160
GAS PRESSURE, TORR
He 3
CO$_2$ 1
N$_2$ 0.5
Xe 0.25
2 mA
3 mA
4 mA
60517-103

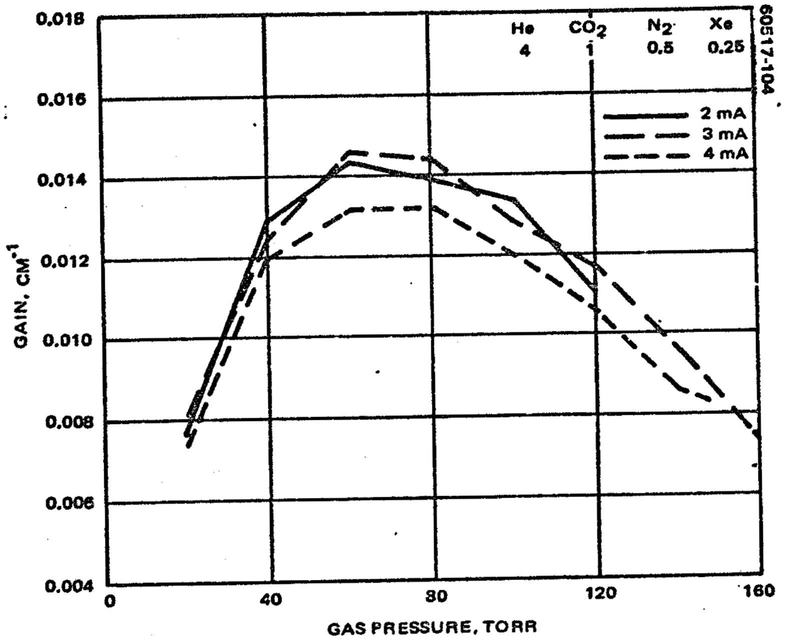
0.018
0.016
0.014
0.012
0.010
0.008
0.006
0.004
GAIN, CM^{-1}
0
40
80
120
160
GAS PRESSURE, TORR
He 4
CO$_2$ 1
N$_2$ 0.5
Xe 0.25
60517-104
2 mA
3 mA
4 mA

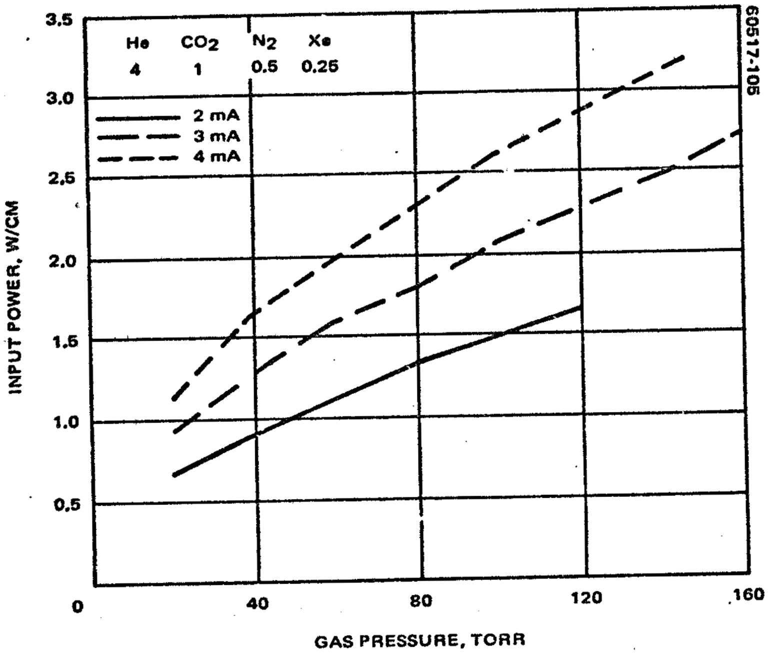
3.5
3.0
2.5
2.0
1.5
1.0
0.5
INPUT POWER, W/CM
0
40
80
120
160
GAS PRESSURE, TORR
He 4
CO$_2$ 1
N$_2$ 0.5
Xe 0.25
60517-105
2 mA
3 mA
4 mA

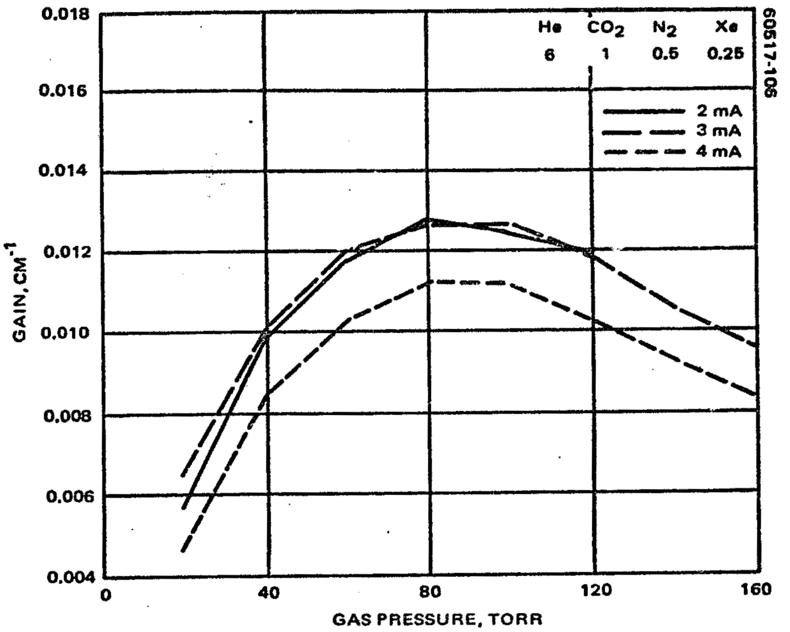
60517-106
He 6
CO2 1
N2 0.5
Xe 0.25
2 mA
3 mA
4 mA
GAIN, CM-1
0.018
0.016
0.014
0.012
0.010
0.008
0.006
0.004
0
40
80
120
160
GAS PRESSURE, TORR

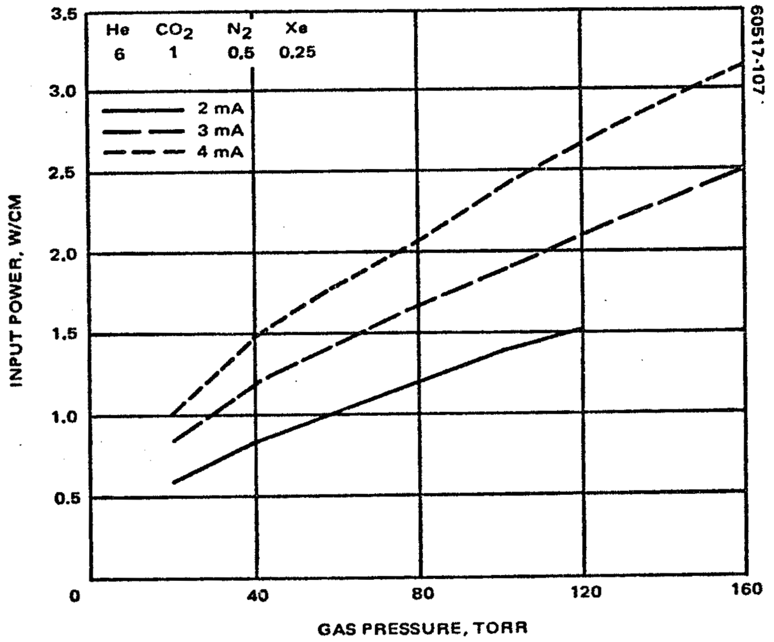
60517-107
He 6
CO2 1
N2 0.5
Xe 0.25
2 mA
3 mA
4 mA
INPUT POWER, W/CM
3.5
3.0
2.5
2.0
1.5
1.0
0.5
0
40
80
120
160
GAS PRESSURE, TORR

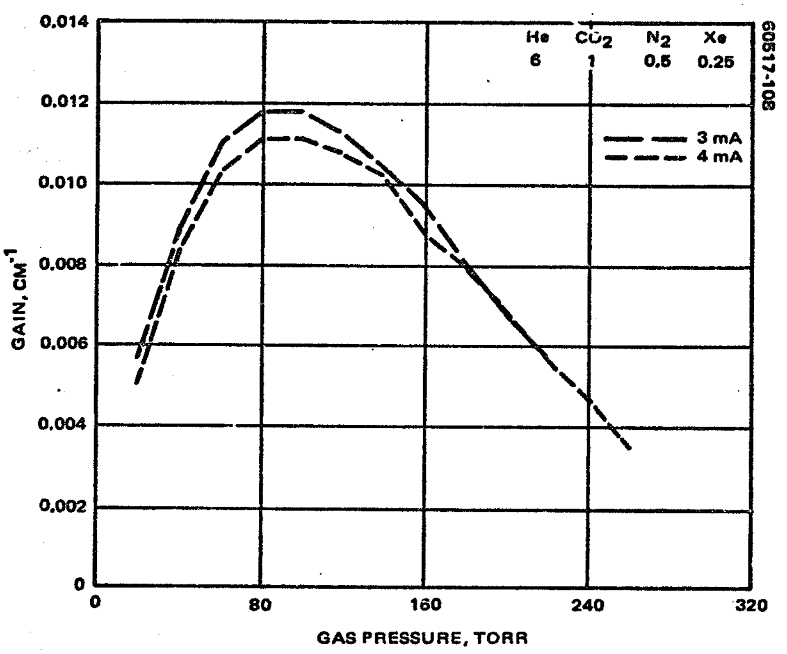
0.014
0.012
0.010
0.008
0.006
0.004
0.002
0
GAIN, CM^{-1}
0
80
160
240
320
GAS PRESSURE, TORR
He 6
CO$_2$ 1
N$_2$ 0.5
Xe 0.25
3 mA
4 mA
60517-108

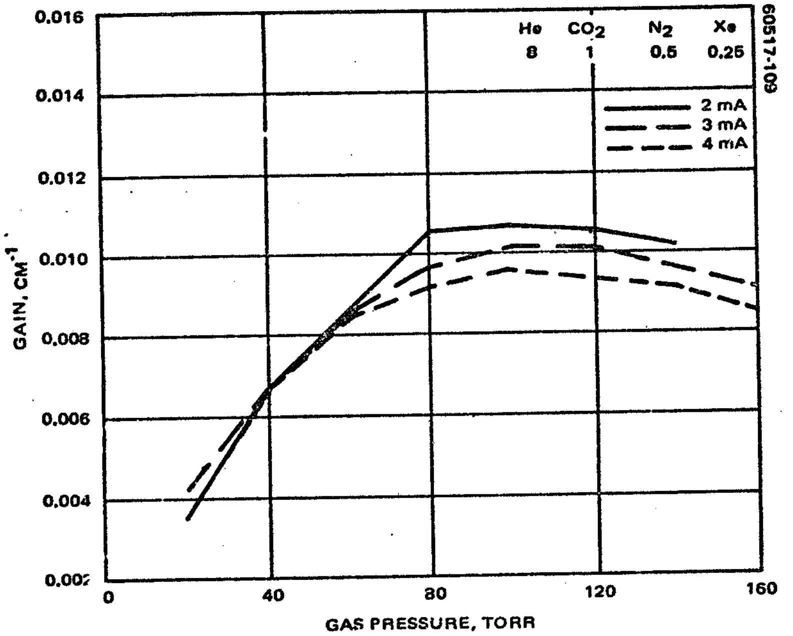
0.016
0.014
0.012
0.010
0.008
0.006
0.004
0.002
GAIN, CM^{-1}
0
40
80
120
160
GAS PRESSURE, TORR
He 8
CO$_2$ 1
N$_2$ 0.5
Xe 0.25
2 mA
3 mA
4 mA
60517-109

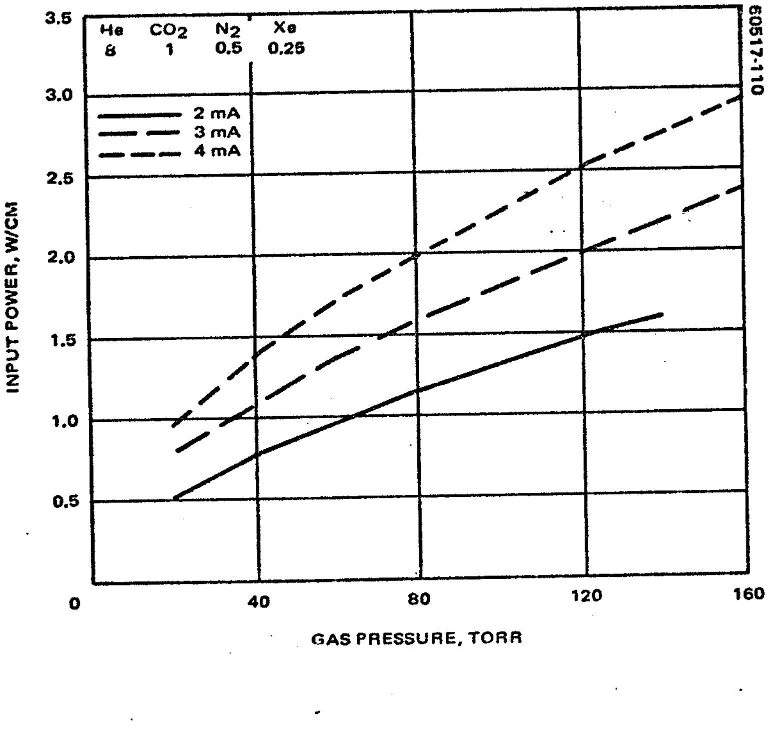
3.5
3.0
2.5
2.0
1.5
1.0
0.5
INPUT POWER, W/CM
0
40
80
120
160
GAS PRESSURE, TORR
He 8
CO$_2$ 1
N$_2$ 0.5
Xe 0.25
2 mA
3 mA
4 mA
60517-110

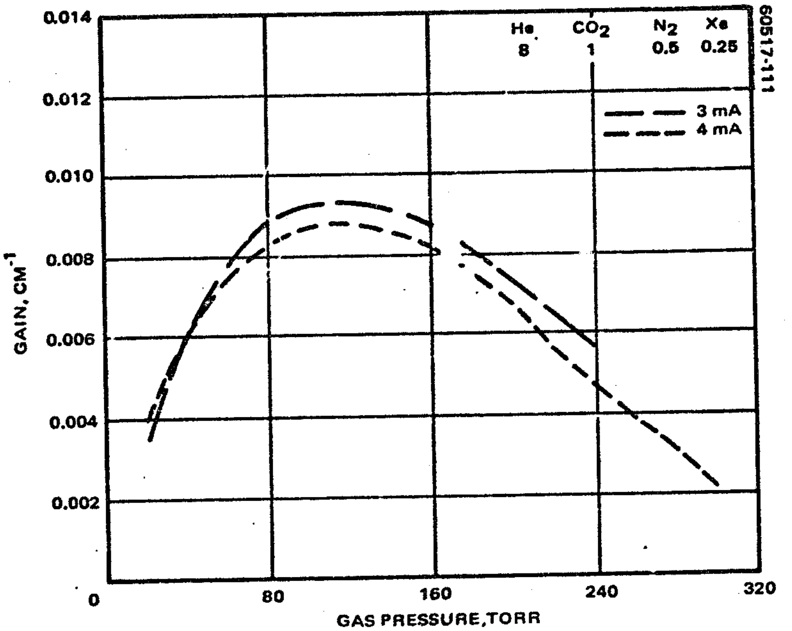
0.014
0.012
0.010
0.008
0.006
0.004
0.002
0
80
160
240
320
GAIN, CM^{-1}
GAS PRESSURE, TORR
He 8
CO$_2$ 1
N$_2$ 0.5
Xe 0.25
3 mA
4 mA
60517-111

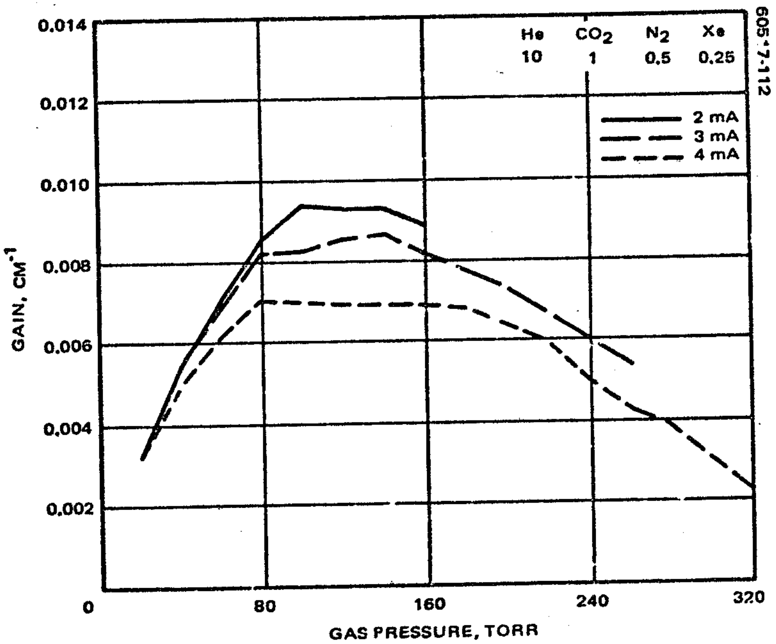
0.014
0.012
0.010
0.008
0.006
0.004
0.002
0
80
160
240
320
GAIN, CM^{-1}
GAS PRESSURE, TORR
He 10
CO$_2$ 1
N$_2$ 0.5
Xe 0.25
2 mA
3 mA
4 mA
605‘7-112

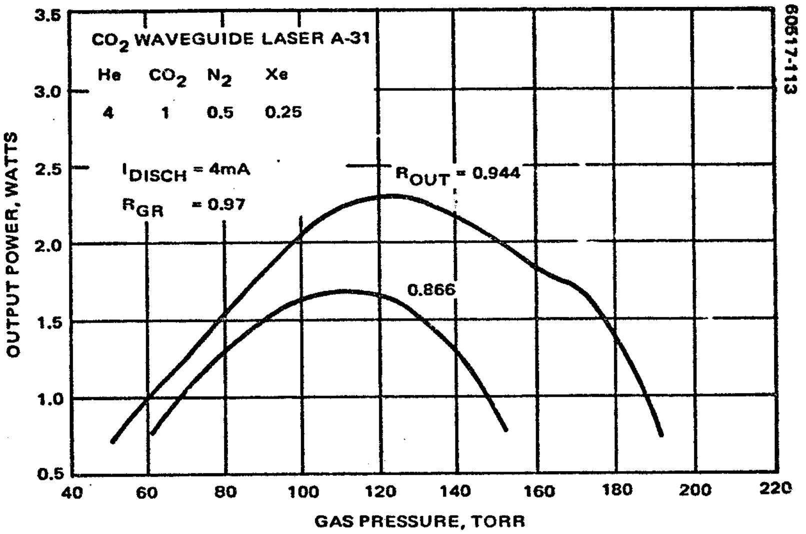
60517-113
CO2 WAVEGUIDE LASER A-31
He CO2 N2 Xe
4 1 0.5 0.25
IDISCH = 4mA
RGR = 0.97
ROUT = 0.944
0.866
OUTPUT POWER, WATTS
3.5
3.0
2.5
2.0
1.5
1.0
0.5
40
60
80
100
120
140
160
180
200
220
GAS PRESSURE, TORR

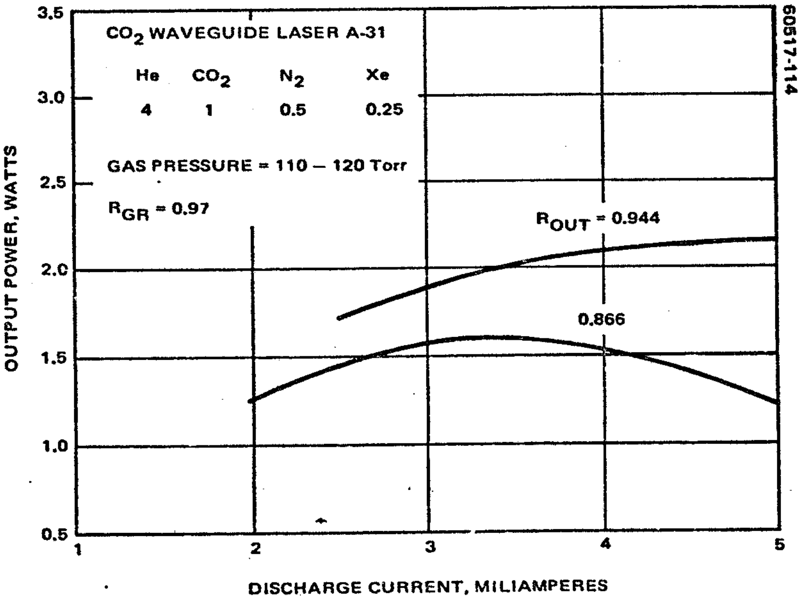
60517-114
CO2 WAVEGUIDE LASER A-31
He CO2 N2 Xe
4 1 0.5 0.25
GAS PRESSURE = 110 — 120 Torr
RGR = 0.97
ROUT = 0.944
0.866
OUTPUT POWER, WATTS
3.5
3.0
2.5
2.0
1.5
1.0
0.5
1
2
3
4
5
DISCHARGE CURRENT, MILIAMPERES

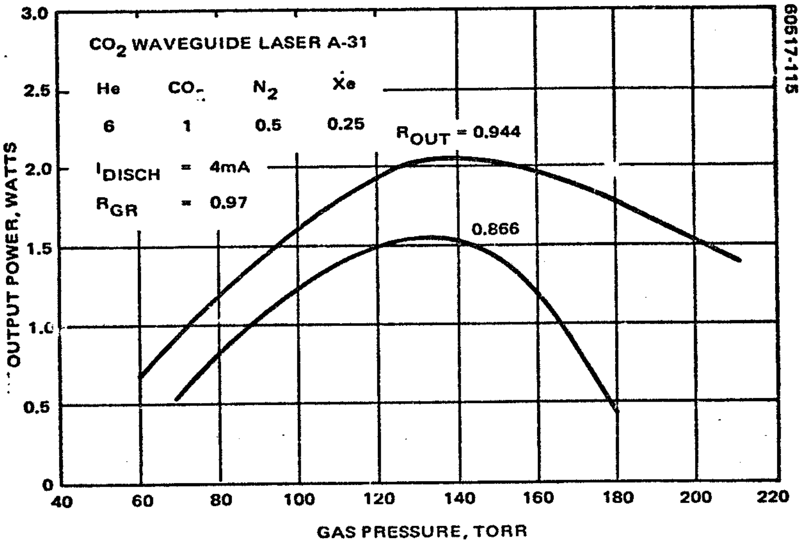

60517-115
CO2 WAVEGUIDE LASER A-31
He CO2 N2 Xe
6 1 0.5 0.25
IDISCH = 4mA
RGR = 0.97
ROUT = 0.944
0.866
OUTPUT POWER, WATTS
GAS PRESSURE, TORR
0
0.5
1.0
1.5
2.0
2.5
3.0
40
60
80
100
120
140
160
180
200
220

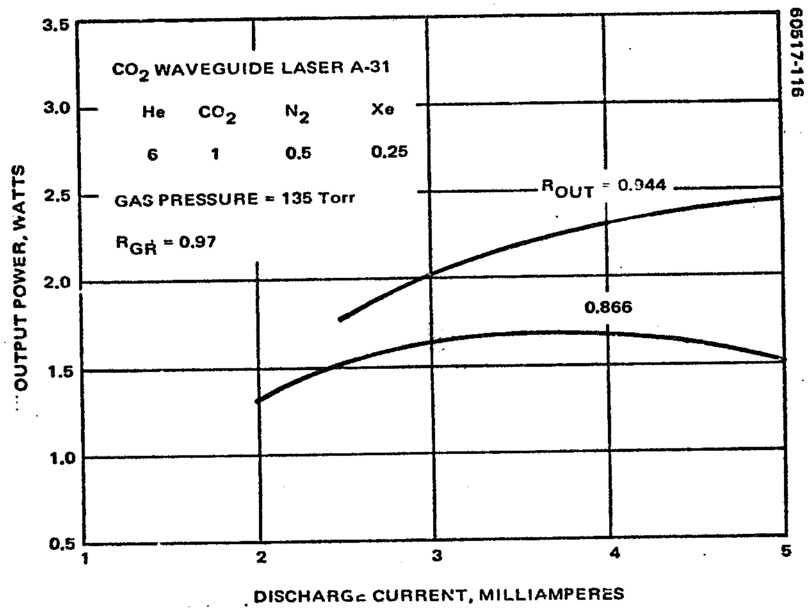

60517-116
CO2 WAVEGUIDE LASER A-31
He CO2 N2 Xe
6 1 0.5 0.25
GAS PRESSURE = 135 Torr
RGR = 0.97
ROUT = 0.944
0.866
OUTPUT POWER, WATTS
DISCHARGE CURRENT, MILLIAMPERES
0.5
1.0
1.5
2.0
2.5
3.0
3.5
1
2
3
4
5

APPENDIX B

EXPERIMENTAL DATA ON GAIN, INPUT POWER AND POWER OUTPUT OF CO_2 WAVEGUIDE LASER WITH CO FILLS

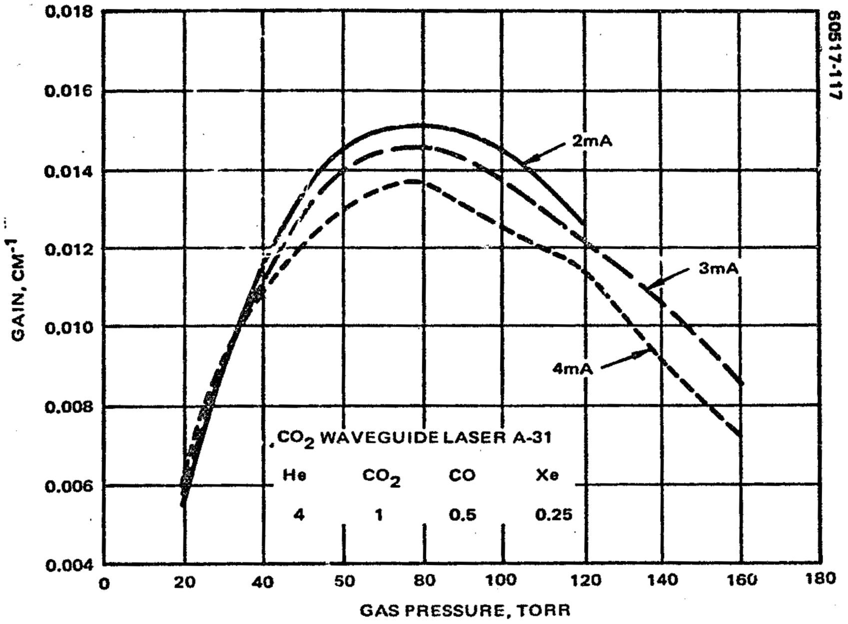

60517-117
GAIN, CM^{-1}
0.018
0.016
0.014
0.012
0.010
0.008
0.006
0.004
0
20
40
50
80
100
120
140
160
180
GAS PRESSURE, TORR
2mA
3mA
4mA
CO$_2$ WAVEGUIDE LASER A-31
He
CO$_2$
CO
Xe
4
1
0.5
0.25

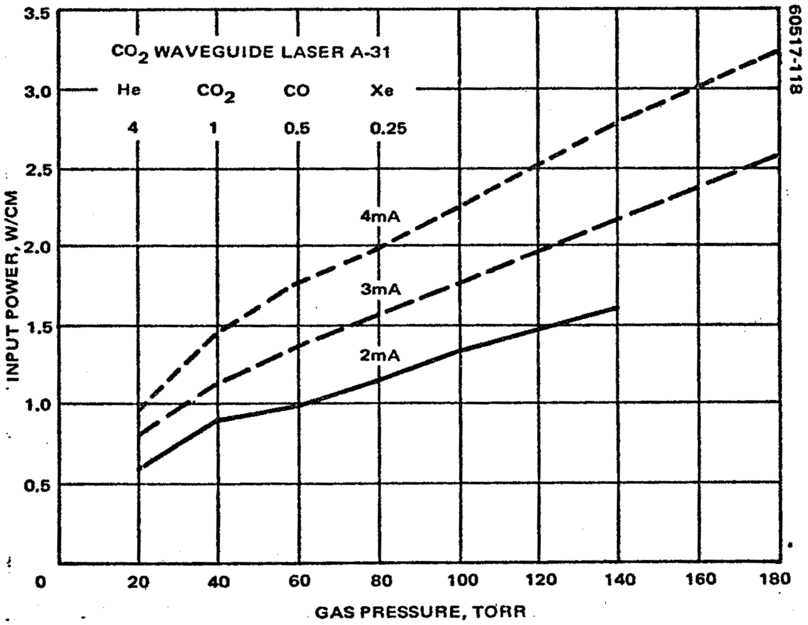

60517-118
INPUT POWER, W/CM
3.5
3.0
2.5
2.0
1.5
1.0
0.5
0
20
40
60
80
100
120
140
160
180
GAS PRESSURE, TORR
CO$_2$ WAVEGUIDE LASER A-31
He
CO$_2$
CO
Xe
4
1
0.5
0.25
4mA
3mA
2mA

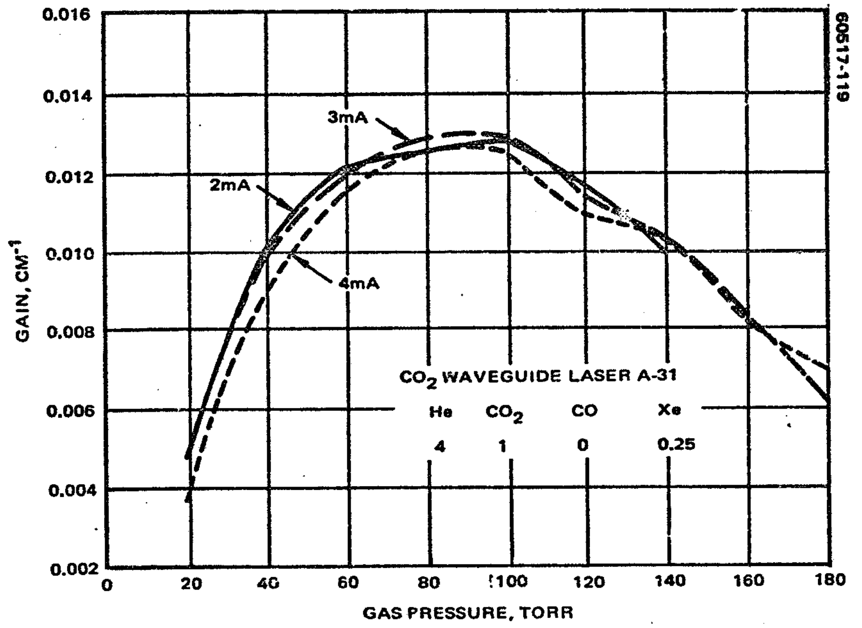
60517-119
GAIN, CM⁻¹
0.016
0.014
0.012
0.010
0.008
0.006
0.004
0.002
0
20
40
60
80
100
120
140
160
180
GAS PRESSURE, TORR
3mA
2mA
4mA
CO2 WAVEGUIDE LASER A-31
He
CO2
CO
Xe
4
1
0
0.25

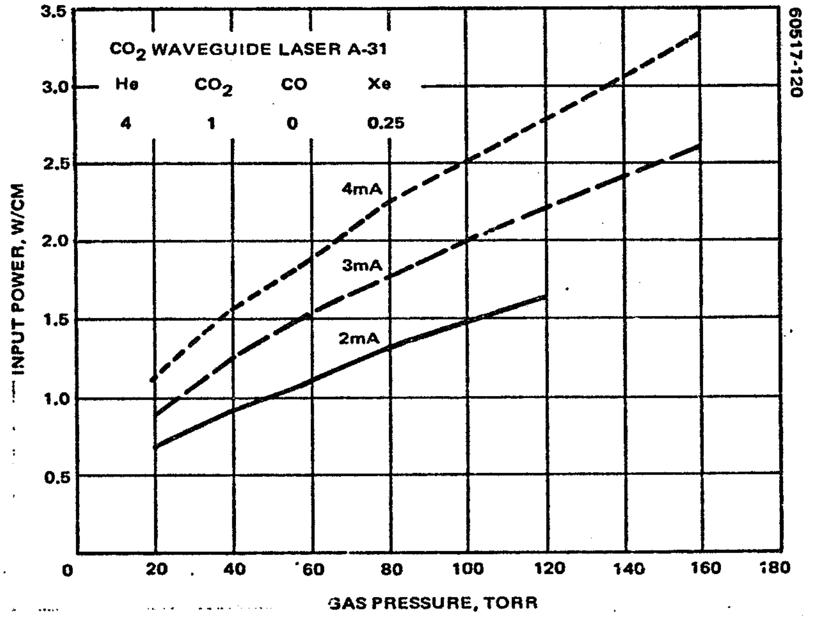
60517-120
INPUT POWER, W/CM
3.5
3.0
2.5
2.0
1.5
1.0
0.5
0
20
40
60
80
100
120
140
160
180
GAS PRESSURE, TORR
CO2 WAVEGUIDE LASER A-31
He
CO2
CO
Xe
4
1
0
0.25
4mA
3mA
2mA

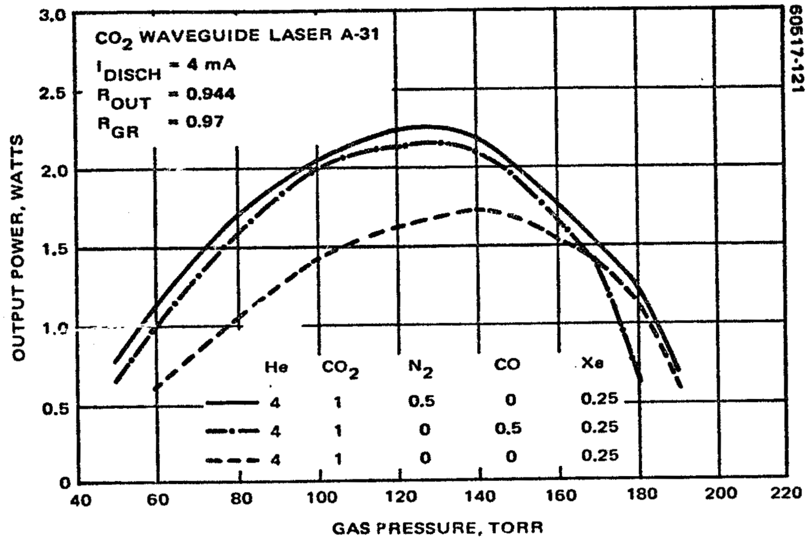
CO2 WAVEGUIDE LASER A-31
IDISCH = 4 mA
ROUT = 0.944
RGR = 0.97
60517-121
OUTPUT POWER, WATTS
GAS PRESSURE, TORR
3.0
2.5
2.0
1.5
1.0
0.5
0
40
60
80
100
120
140
160
180
200
220
He
CO2
N2
CO
Xe
4
1
0.5
0
0.25
4
1
0
0.5
0.25
4
1
0
0
0.25

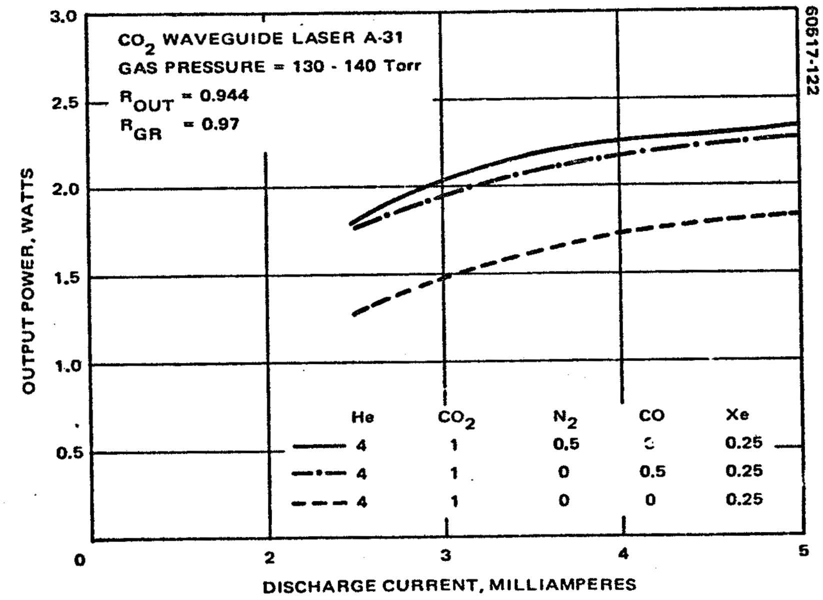
CO2 WAVEGUIDE LASER A-31
GAS PRESSURE = 130 - 140 Torr
ROUT = 0.944
RGR = 0.97
60517-122
OUTPUT POWER, WATTS
DISCHARGE CURRENT, MILLIAMPERES
3.0
2.5
2.0
1.5
1.0
0.5
0
2
3
4
5
He
CO2
N2
CO
Xe
4
1
0.5
0
0.25
4
1
0
0.5
0.25
4
1
0
0
0.25

APPENDIX C. MODULATOR THERMAL GRADIENTS AND THEIR EFFECTS

The temperature dependent index of retraction in CdTe leads to the well known effects of beam focusing and beam bending in the presence of thermal gradients. At the power levels intended for transmitter operation, these gradients become significant. Consequently, a computer modeling of the steady state temperature distribution across the modulator rod has been carried out for various crystal housings. The results provide the thermal design data required to avoid beam bending (due to a linear gradient across the rod) and indicate the degree of focusing to be expected (due to a quadratic thermal gradient). A description of the model and its results are now presented, follwed by a discussion of the effects of thermal gradients.

C.1 MODEL DESCRIPTION

A portion of the modulator housing for a prototype design is shown in Figure C-1. The rod is bonded to lapped Kovar electrodes which serve to damp acoustic resonances generated in the cyrstal as well as apply the modulating field. This unit is then placed in a BeO L-shaped piece and capped with a BeO plate. The plate is pressed on the electrode structure by an insulating compressive material. This assembly is then mated to a matching L-shaped BeO piece to form the complete model.

In the thermal modeling of the housing, ideal interfaces between rod and electrodes are assumed because of the care given in electrode surface preparation. The assembly of the unit can, however, result in small air gaps between the rod and mating BeO; consequently such gaps are included in the model. At the interface between, BeO "L" and plate, any temperature drop is neglected. A perfect insulator is assumed at the point of compressive loading. The boundary temperature is held constant at a distant location. Heat input corresponds to 80 watts circulating power in each direction for 0.002 cm^{-1} crystal absorption. Longitudinal variation of the intensity is ignored, as absorption is small. In addition to the Kovar acoustic dumping rods, results for BeO side pieces are presented as well.

The model was broken up into 144 squares (16 across by 9 high) with a node at the center of each square. Then the square in the middle of the crystal was broken up into 25 additional squares (5 across by 5 deep).

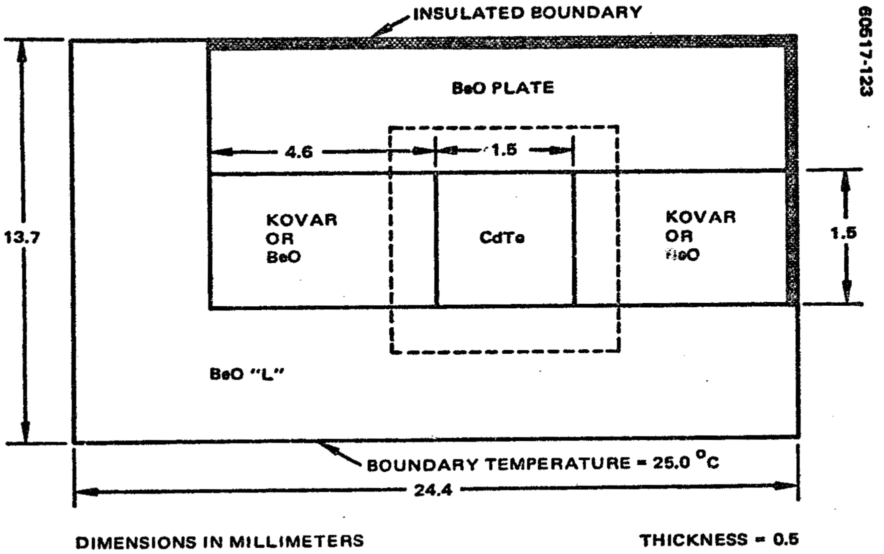

FIGURE C-1. COMPLETE MODEL OF MODULATOR CRYSTAL TEMPERATURE RISE STUDY

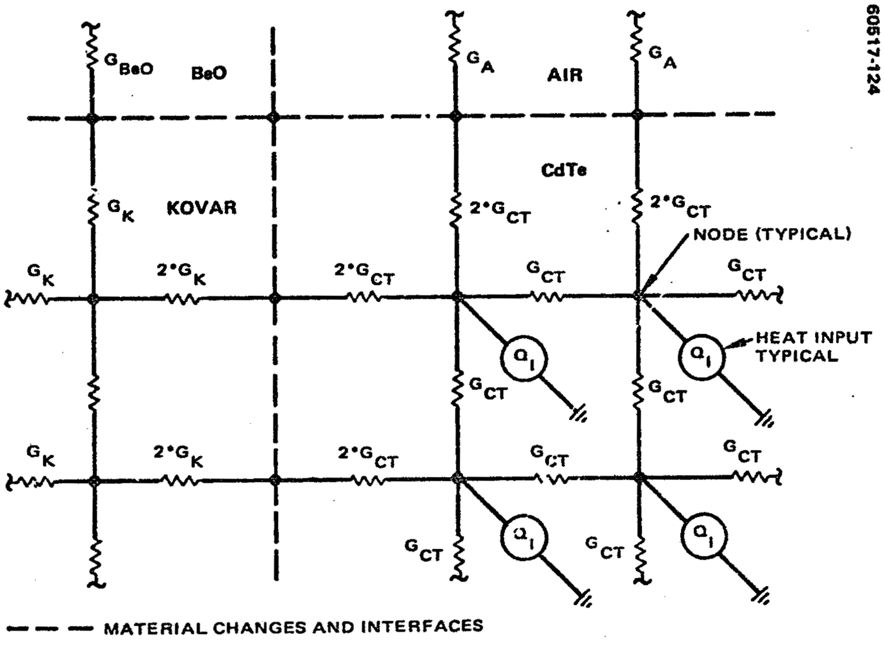

FIGURE C-2. TYPICAL THERMAL NETWORK

Additional nodes were provided at the boundary edge of each uninsulated boundary square. Also, nodes were provided at the joint between crystal and the damping member. Additional nodes were provided at the top and bottom sides of the crystal to simulate air gaps at these interfaces. This gives a total of 217 nodes. These nodes were interconnected with thermal conductances. Conductance values were computed using the thermal conductivity of the material, path length between nodes, and the path cross sectional area. There are 365 conductors in the model.

Figure C-2 shows a typical nodal interconnection set. Heat input was provided to each of the crystal nodes and distributed in a "cosine squared" fashion. The total input power was 0.01627 watt over the entire face of the crystal.

The resulting mesh was solved for the steady state nodal temperatures and branch heat flows using a version of the NASA's SINDA thermal analysis program. A given solution was terminated when 95 percent or more of the input heat flowed across the outside boundary.

C.2 RESULTS OF THERMAL MODELING

A total of 10 cases were run. These cases are defined in Table C-1.

TABLE C-1. THERMAL MODELING RESULTS FOR TEN CASES

Case	Side Material	Air Gap Bottom, μm	Air Gap Top, μm	Peak Temperature Above Ambient, m°C *
1	Kovar	0.00	0.00	637
2	Kovar	2.54	0.00	755
3	Kovar	2.54	2.54	871
4	Kovar	2.54	6.35	915
5	Kovar	2.54	12.7	950
6	BeO	0.00	0.00	558
7	BeO	2.54	0.00	628
8	BeO	2.54	2.54	703
9	BeO	2.54	6.35	729
10	BeO	2.54	12.7	742

*Millidegrees centigrade.

Figure C-3 shows a detailed portion of the model including the location of the top and bottom air gaps. The peak temperature occurs at the center of the crystal.

Figures C-4 and C-5 show the temperature rise profiles for sections A-A and B-B for both Kovar and berillyium oxide side bars as a function of the top and bottom air gap widths. As with all other temperatures reported here, the temperature is in millidegrees centigrade (m°C) rise above the boundary. Note particularly the large temperature gradients that exist across these air gaps.

Figure C-6 shows an isothermal contour map of the crystal and side bars for case 5 (Kovar, 2.54, and 12.7 μm air gaps). Contour lines are drawn in 100 m°C increments. Notice the distortion produced by the air gaps both by their presence and also the difference in their magnitude.

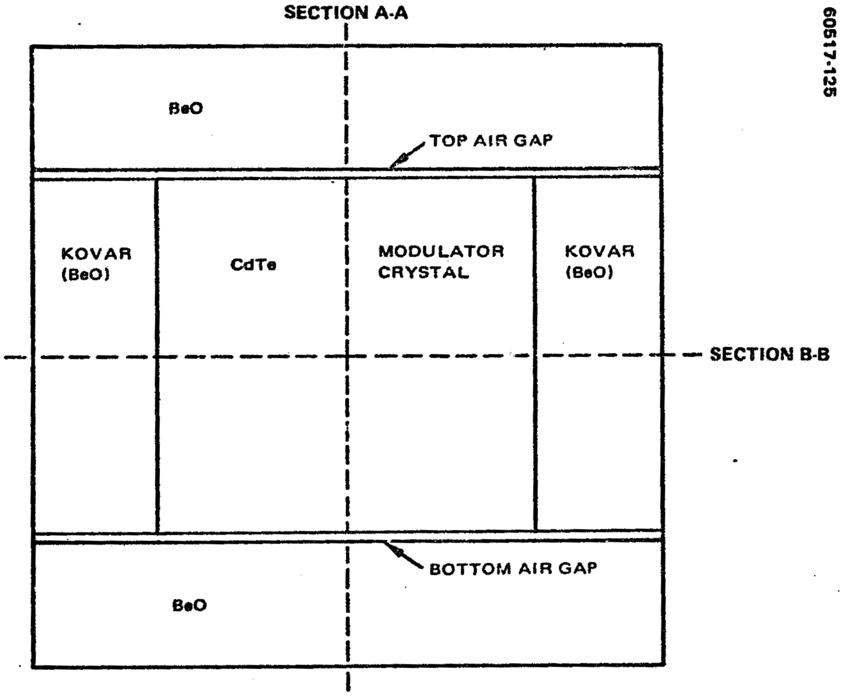

FIGURE C-3. DETAILED SECTION OF MODULATOR CRYSTAL TEMPERATURE RISE STUDY

60517-126

CURVE	TOP GAP, μm	BOTTOM GAP, μm
A	12.7	2.54
B	6.35	2.54
C	2.54	2.54
D	0.00	2.54
E	0.00	0.00

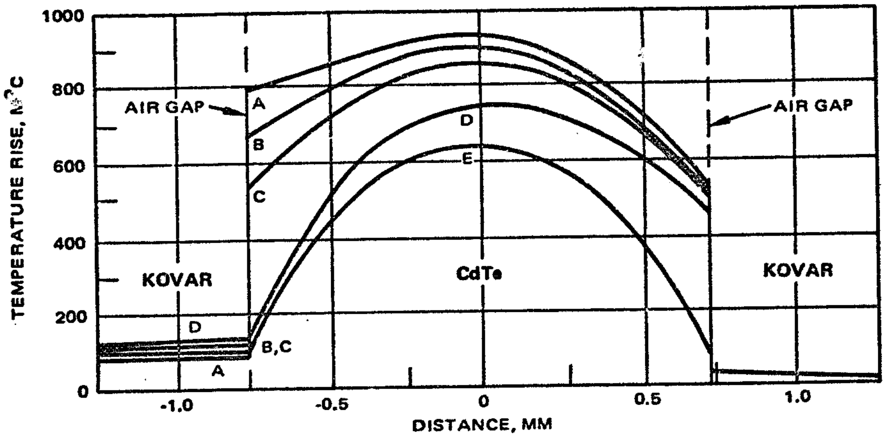

a) SECTION A-A OF FIGURE C-3

CURVE	TOP GAP, μm	BOTTOM GAP, μm
A	12.7	2.54
B	6.35	2.54
C	2.54	2.54
D	0.00	2.54
E	0.00	0.00

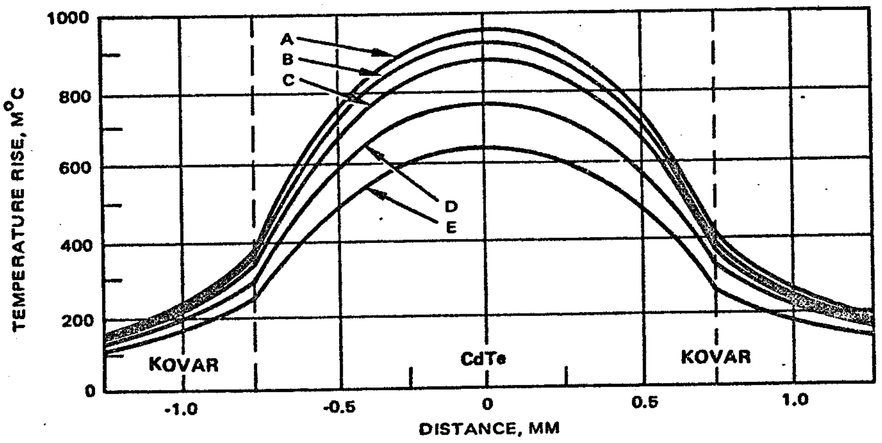

b) SECTION B-B OF FIGURE C-3

FIGURE C-4. CRYSTAL TEMPERATURE DISTRIBUTION FOR KOVAR SIDE PIECES

60517-127

CURVE	TOP GAP, μm	BOTTOM GAP, μm
A	12.7	2.54
B	6.35	2.54
C	2.54	2.54
D	0.00	2.54
E	0.00	0.00

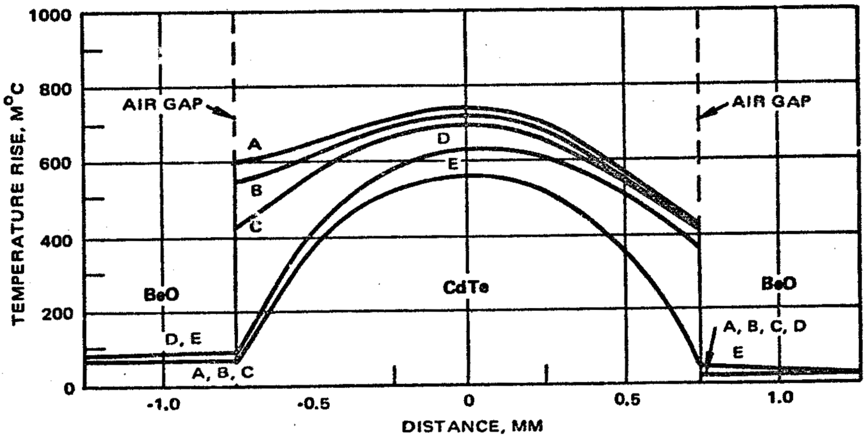

a) SECTION A-A OF FIGURE C-3

CURVE	TOP GAP, μm	BOTTOM GAP, μm
A	12.7	2.54
B	6.35	2.54
C	2.54	2.54
D	0.00	2.54
E	0.00	0.00

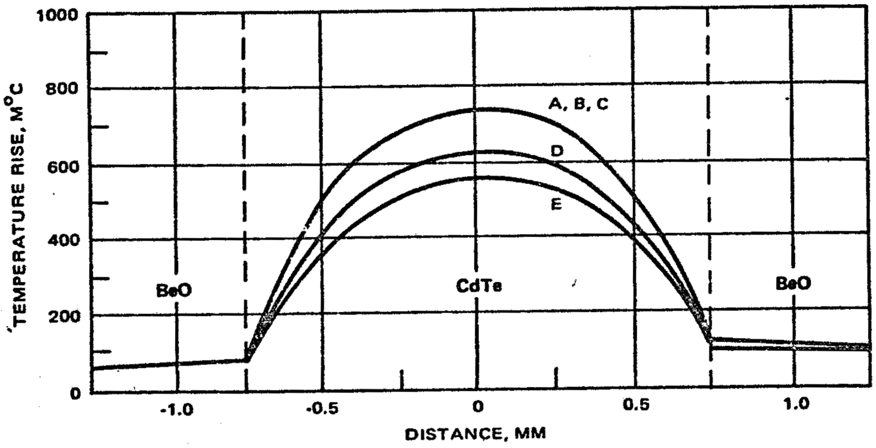

b) SECTION B-B OF FIGURE C-3

FIGURE C-5. CRYSTAL TEMPERATURE DISTRIBUTION FOR BeO SIDE PIECES

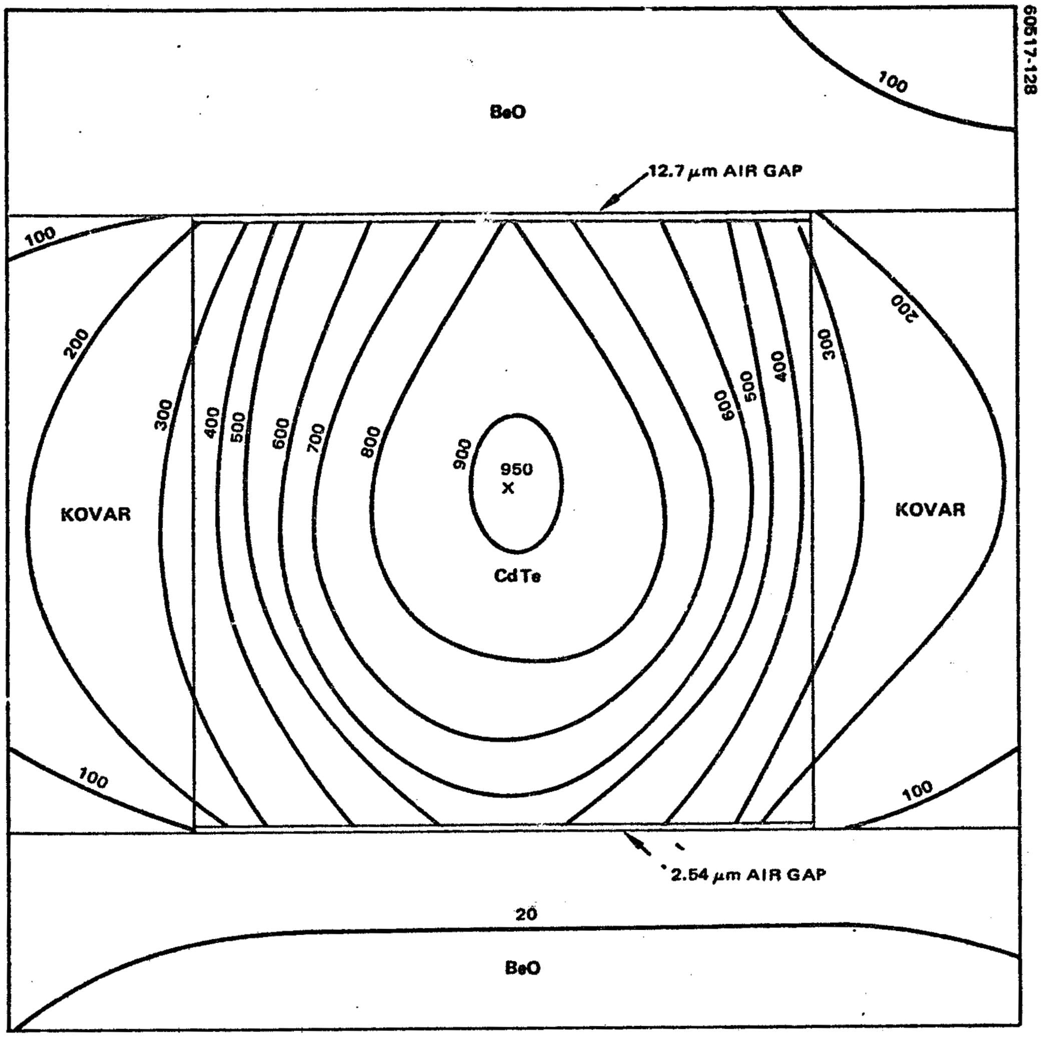

FIGURE C-6. MODULATOR CRYSTAL ISOTHERMAL CONTOUR MAP (REFER TO FIGURE C-3)

C.3 EFFECTS OF THERMAL GRADIENTS

Beam Deflection

Light traversing a distance, Z, in a medium possessing a linear index of refraction change will be deflected through an angle (measured in the material of index n_0)

$$\Delta = -\frac{Z}{n_0}\frac{dn}{dX} = -Z\frac{1}{n_0}\frac{dn}{dT}\frac{dT}{dX} \qquad (1)$$

For CdTe, $1/n\ (dn/dT)\ 4.4 \times 10^{-5}/°C = \beta$. The magnitude of this angular offset must be compared with the diffraction angle of the fundamental optical mode of the waveguiding modulator

$$\theta = \frac{k_x}{k_z} = \frac{\lambda_0}{4\,h\,n_0} \qquad (2)$$

where λ_o is the free space wavelength and 2h is the height (and width) of the square rod. Imposing the inequality $\Delta \ll \theta$, yields for an optical round trip ($Z = 2L = 12$ cm) through a rod with side 1.5 mm

$$\frac{dT}{dx} \ll \frac{\lambda_0}{8h\,L\,n_{0\beta}} = 2.4°C/cm \qquad (3)$$

Linear gradients of this magnitude are shown to exist in the preceding section at the 80 watt level when air gaps are inadvertently allowed in the housing. Consequently, extreme care must be taken with the thermal mounting at the top and bottom of the rod as well as the sides. In addition, the insulating compressive material around the BeO plate should be eliminated.

Beam Focusing

A perfect square law medium with retractive index distribution

$$n = n_0 - \frac{1}{2} n_1 (X^2 + Y^2) \tag{4}$$

supports guided waves. Neglecting any boundaries, the fundamental mode is Gaussian with beam waist, w

$$w^2 = \frac{2}{k_0 (n_0 n_1)^{1/2}} \tag{5}$$

Now, in CdTe with bulk index n_{ct}

$$n = n_{ct} + \frac{dn}{dT} \Delta T = n_{ct} (1 + \beta \Delta T) \tag{6}$$

If a true square law temperature distribution existed across the rod

$$\Delta T = T_1 \;\; 1 - \left[\frac{X^2 + Y^2}{h^2}\right], \tag{7}$$

then Equations 1 and 6 yield

$$\begin{aligned} n_0 &= n_{ct}(1 + \beta T_1) \simeq n_{ct} \\ n_1 &\simeq 2 \frac{n_0 \beta T_1}{h^2} \end{aligned} \tag{8}$$

The square law distribution is strictly true for uniform heating of the rod. This model is used here to demonstrate the qualitative effects of heating. It will not allow quantitative predictions.

For beam focusing to be unimportant, the beam waist given by Equation 5 must be larger than the rod width

$$w^2 = \frac{2h}{k_0 n_0} \frac{1}{(2 \beta T_1)^{1/2}} > h^2 \quad (9)$$

which imposes restriction on the peak temperature. Thus

$$T_1 < \frac{2}{\beta} \frac{1}{(k_0 n_0 h)^2} = 29 \text{ mC}^\circ \quad (10)$$

for the numerical values of the preceding subsection. Peak temperatures, an order of magnitude larger than Equation 10, were shown to exist at high power levels. This result indicates that beam focusing rather than the waveguide walls is the dominant guidance mechanism at high power.

Mode conversion resulting from propagation in the heated rod is now discussed. At the entrance to the modulator, the electric field distribution for the fundamental, EH_{11}, laser mode is assumed. This distribution is then expanded in the set of heated rod normal modes. These modes are allowed to propagate a distance, 2L, where their resulting superposition is used to calculate the coupling back into the laser fundamental mode. A similar procedure (Reference 10) has been used to calculate coupling loss from end mirrors. Therefore

$$\psi (X, Y, Z) = \sum_{mn} A_{mn} \Psi_{mn} (X, Y) e^{i\beta_{mn} Z} e^{-\alpha_{mn} Z} \quad (11)$$

where ψ is the amplitude distribution in the rod, Ψ_{mn} are the normal modes of the heated rod, β_{mn} is mode phase velocity, and α_{mn} is the mode attenuation. The expansion coefficients A_{mn} are determined at Z = 0 where ψ is usual cosine dependence of the EH_{11} mode.

It is possible to obtain a qualitative understanding of this mode conversion by again using the square law relationship. For $\Psi_{mn}(X, Y) = f(X)\, g(Y)$, the wave equation becomes

$$\frac{d^2 g}{dy^2} + \left(n_0^2 k_0^2 - \kappa^2 - \beta^2 - k_0^2 n_0 n_1 X^2 \right) f = 0$$

$$\frac{d^2 g}{dy^2} + \left({}^2 - k_0^2 n_0 n_1 Y^2 \right) g = 0 \qquad (12)$$

The values of K^2 and β^2 are determined by boundary conditions at the modulator walls. Let

$$\xi = \sqrt{2k_0}\, (n_0 n_1)^{1/4} X$$

$$a = \frac{n_0^2 k_0^2 - K^2 - \beta^2}{2k_0 (n_0 n_1)^{1/2}} \qquad (13)$$

$$b = \frac{K^2}{2k_0 (n_0 n_1)^{1/2}}$$

Both equations of Equation 12 can be put in the form

$$\frac{d^2 f}{d\xi^2} + \left(a - \frac{\xi^2}{4}\right) f = 0 \qquad (14)$$

For half-integer values of a, the expression gives the usual beam mode in terms of Hermite polynomials. As fields that vanish at the wall ($X = \pm h$) are required here, other than half-integral values of a are used. The solution to Equation 14 for symmetric modes is

$$f = \exp\left(- \frac{\xi^2}{4}\right) M\left(\frac{1}{2}\left[\frac{11}{2} - a\right], \frac{1}{2}, \frac{X^2}{2}\right) \qquad (15)$$

where M is a confluent hypergeometric function. A series solution

$$f = \exp\left(- \frac{\xi^2}{4}\right)\left\{1 + \left(\frac{1}{2} - a\right)\frac{\xi^2}{21} + \left(\frac{1}{2} - a\right)\left(\frac{5}{2} - a\right)\frac{\xi^4}{4^1} r \ldots\right\} \qquad (16)$$

$$\equiv \exp\left(- \frac{\xi^2}{4}\right) S(\xi, a)$$

is used to evaluate Equation 15. The amplitude distribution for the first two symmetric modes which vanish at the walls as shown in Figures C-7 and C-8 for two peak temperatures. It is seen that, at low temperature, the distribution is cosine in nature, while, at elevated temperature, a more Gaussian form results. Clearly, at the higher temperature, higher order modulator modes will be excited.

The expansion coefficients of Equation 11 can now be calculated. Multiplying both sides by Ψ_{mn} and integrating over the face of the rod yields,

$$A_{mn} = I_m I_n,$$

$$I_m = \frac{\left[\int_0^1 du \cos\left(\frac{\pi}{2} u\right) \exp - \left(\frac{\xi_0 u}{2}\right)^2 S_m(\xi_0 u)\right]^2}{\frac{1}{2}\int_0^1 du \left[\exp - \left(\frac{\xi_0 u}{2}\right)^2 S_m(\xi_0 u)\right]^2}. \qquad (17)$$

where

$$\xi_0 = (2 k_0)^{1/2} (n_0 n_1)^{1/4} h \qquad (18)$$

and S_m, given by Equation 16, has its mth zero crossing at X = ±h.

The propagation through the crystal is governed by Equation 11. A difficulty arises here as the loss coefficients for each mode are unknown. The higher order modes will suffer greater attenuation then the fundamental mode. In fact, for the first few lowest order modes, the bulk

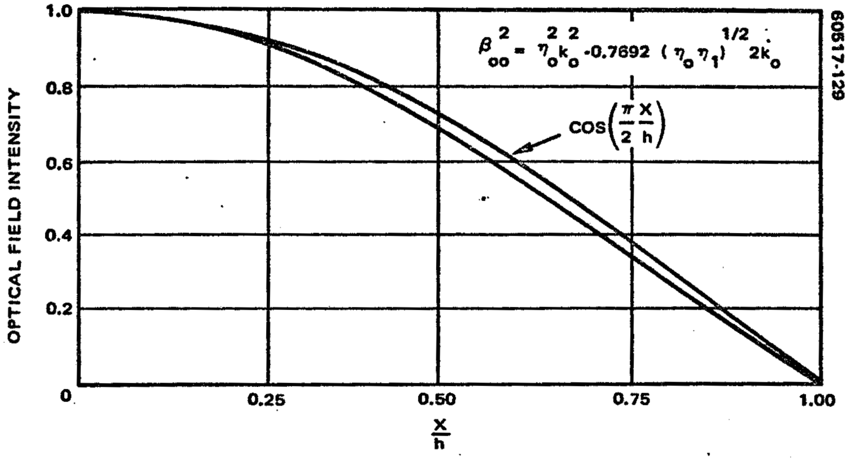

a) $T_1 = 26$ M°C

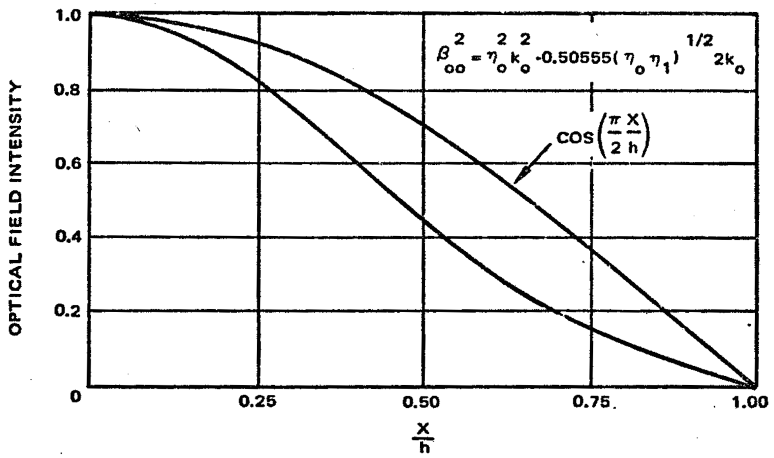

b) $T_1 = 270$ M°C

FIGURE C-7. FUNDAMENTAL MODE OF SQUARE LAW MOULATOR ROD

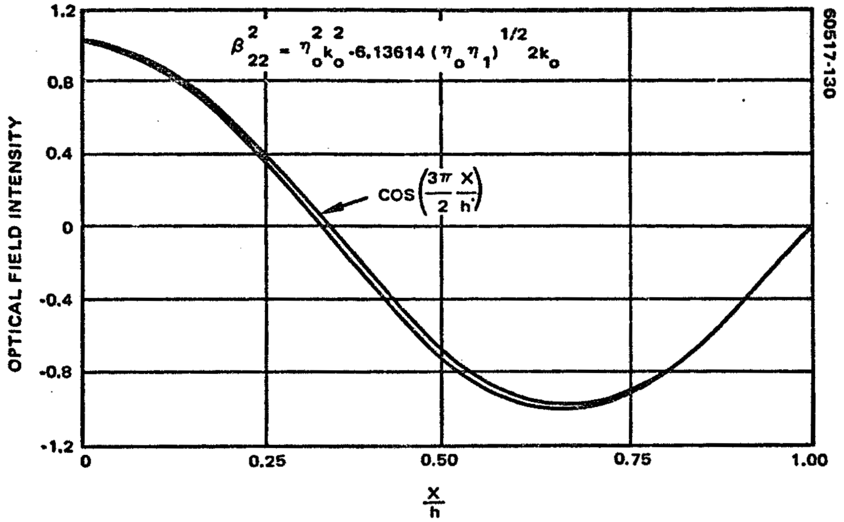

a) $T_1 = 26$ M°C

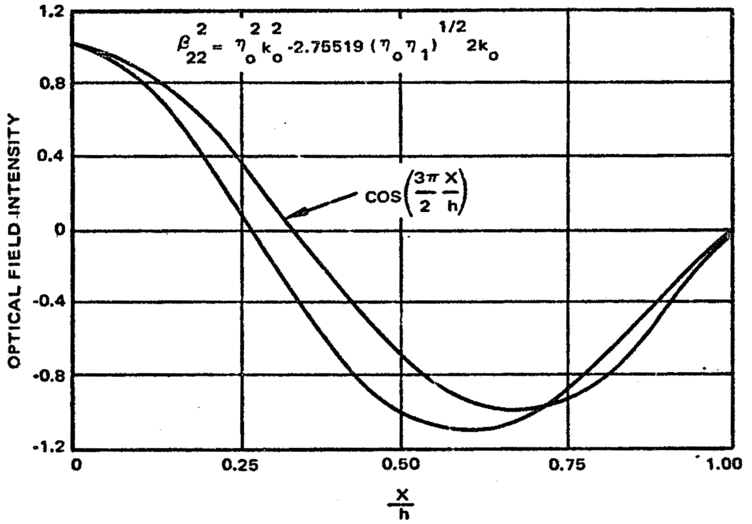

b) $T_1 = 270$ M°C

FIGURE C-8. SECOND MODE OF SQUARE LAW MODULATOR ROD loss in all likelihood will dominate. Therefore, equal attenuation is used for each mode of interest. Equation 11 becomes at Z = 2L

$$\psi(X, Y, Z) = e^{-\alpha L} \sum_{mn} I_m I_n \Psi_{mn}(X, Y)\, e^{2i\beta_{mn} L} \tag{19}$$

Decomposing Equation 17 into the EH_{11} laser mode gives the power coupling coefficient

$$C_t^2 = e^{-2\alpha L} \left| \sum_{mn} I_m^2 I_n^2\, e^{2i\beta_{mn} L} \right|^2 \tag{20}$$

It is seen that the coupling coefficient will posses oscillatory behavior with length due to mode interference effects analogous to the free space mirror loss (Reference 5). The phase velocities calculated from this approximate model are not well enough known to allow quantitative predictions of low loss regions. The magnitude of the effect can be estimated from the power coupling of the fundamental mode alone. This value represents a mean between the peaks and valleys of the oscillatory coupling. In terms of a single pass loss, $\mathscr{L} = 1 - C_t^2$

$$\mathscr{L} = e^{-\alpha L} I_0^4 \tag{21}$$

In Figure C-9, the mode conversion loss I_0^4 is shown as a function of temperature. Also shown is the product of modulator bulk absorption, α, and circulating power, P_{cir}, which generates the peak temperature. These values have been calculated by taking a 450 m°C peak for $\alpha = 0.002$ cm^{-1} and $P_{cir} = 80$ watts as shown in the thermal modeling. The dramatic increase in loss with temperature indicates that keeping the peak temperature low is essential for 50 watts circulating power and 0.001 cm^{-1} absorption. The estimated loss of 3 percent is acceptable.

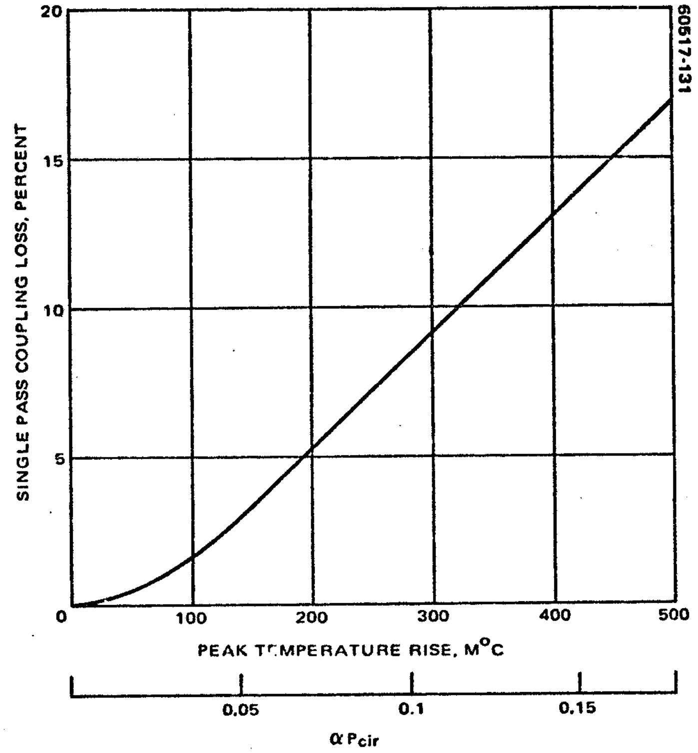

FIGURE C-9. ESTIMATE OF MODE CONVERSION LOSS

APPENDIX D

WAVEGUIDE LASERS WITH INTRACAVITY ELECTROOPTIC MODULATORS: MISALIGNMENT LOSS

Reprinted from APPLIED OPTICS, Vol. 15, page 1066, April 1976

Waveguide lasers with intracavity electrooptic modulators: misalignment loss

D. M. Henderson

Coupling from the EH_{11} fundamental mode of a square, hollow bore waveguide laser to a square electrooptic modulator is treated. The misalignment loss that results from coupling of the laser fundamental mode into higher order modulator modes is calculated. Results are presented for loss from transverse displacement, angular tilt, and axial separation of the two elements. From these results, the alignment tolerances required to minimize loss for an intracavity modulator are found.

Introduction

High data rate communication systems at 10.6 μm as presently conceived will employ intracavity electrooptic modulation. Since the coupling loss between laser and modulator adds directly to the cavity loss, it is an important consideration in the design of such a system. For laser resonators with bulk modulators, the conventional design follows the work of Kaminow and Turner.[1] In this configuration, the modulator transverse dimensions are chosen so the focused optical beam is not truncated by the modulator. A limiting length of the device is imposed by diffraction of the focused beam.

Waveguide lasers with intracavity waveguide modulators offer improved coupling over the above design. Here no limiting modulator length is imposed by open resonator diffraction as the light is guided. The safety factor in the size of the transverse dimension is also eliminated as identical modes propagate in both devices. Finally, the two elements can be directly coupled, thereby removing any loss introduced by a focusing lens in the cavity.

Hollow bore waveguide lasers at 10.6 μm are highly overmoded in order to minimize the effects of surface roughness.[2] The fundamental mode is low loss in this case. However, any mechanism that scatters light into higher order modes will introduce loss as these modes are more strongly attenuated. With an intracavity modulator, mode coupling can arise from misalignment, surface imperfections, and lack of parallelism of the surfaces. It is the purpose of this paper to point out the alignment tolerances needed to minimize cavity loss.

The problem entails the coupling between the EH_{11} modes of the laser and modulator through free space radiation fields. Earlier calculation[3,4] of resonator loss for waveguide lasers (with flat mirrors) is directly applicable here. References 3 and 4 indicate that the coupling loss is minimal for closely spaced components. However, they do not give an indication of the alignment tolerances that must be met to keep losses low. Just such a problem has been addressed in the coupling of Gaussian laser beams to multimode optical fibers.[5,6] The techniques outlined in Refs. 5 and 6 will be applied to the present coupling analysis.

Fundamental Mode Coupling

In computing power transmission from the laser to the modulator, the transmission coefficient τ is given by[5] $\tau = |c_t|^2$, where

$$c_t = \frac{(F_1F_2)^{1/2}}{2P}. \tag{1}$$

The parameters in Eq. (1) are

$$\begin{aligned} F_1 &= \int dx'dy'(E_xH_y'^* - E_yH_x'^*), \\ F_2 &= \int dx'dy'(E_x'^*H_y - E_y'^*H_x). \end{aligned} \tag{2}$$

The primed terms represent the complex conjugate of the electric and magnetic fields of the EH_{11} mode of the modulator in the misaligned x', y', z' coordinate system (see Fig. 1). In Eq. (2), the integrations are performed over the entrance face of the modulator. The unprimed quantities are the radiated laser fields that impinge on the modulator face. The power of the EH_{11} mode of the laser is denoted by P:

$$P = \frac{1}{2}\,\mathrm{Re}\int dxdy(E_xH_y^* - E_yH_x^*) \tag{3}$$

The author is with Hughes Aircraft Company, P.O. Box 92919, Airport Station, Los Angeles, California 90009.

Received 25 January 1975.

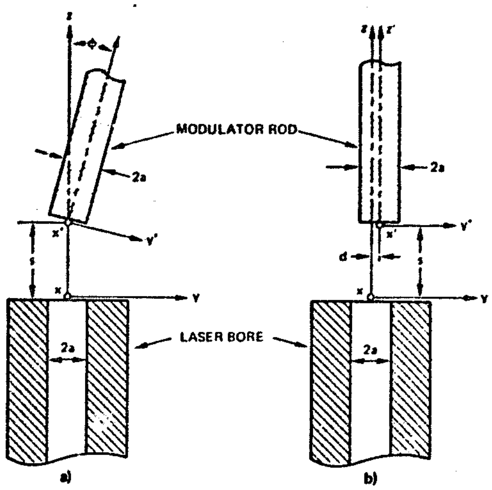

Fig. 1. Misaligned x',y',z' coordinate system.

EH_{11} Mode

This section describes the fields of the fundamental EH_{11} mode for a square modulator with sides $2a$. The propagation of waves on a square dielectric waveguide of index of refraction n_1 surrounded by material with index n_0 has been studied by Marcatili.[7] Within the dielectric, sinusoidal fields exist and outside, decaying fields. An intracavity waveguide modulator is generally a highly overmoded guide with a large differential index between the rod and the surrounding medium. Using typical numbers for a CdTe modulator ($n_1 = 2.6$, $n_0 = 1.0$, $\lambda = 10.6\ \mu$m, and $2a = 1.5$ mm), Ref. 7 shows that the penetration depth $K[\simeq 2\pi(n_1^2 - n_0^2)^{1/2}/\lambda]$ is ⅕ optical wavelength. The power flow in the surrounding medium is therefore negligible, and fields that vanish at the walls are used. A similar approximation has been used to describe the waveguide laser fields.[3,4] Within this approximation, the fundamental mode that propagates in the $+z$ direction and is polarized in the $+y$ direction is given by[7]

$$\begin{aligned} E_x &= 0, \\ E_y &= E_1 \cos(\pi x/2a)\cos(\pi y/2a)\exp[-i(k_1 z - \omega t)], \\ H_x &= -(n_1/Z_0)E_y, \\ H_y &= 0, \end{aligned} \tag{4}$$

where $k_1 = n_1 k_0$, k_0 is the free space wavenumber, and Z_0 is the free space wave impedance. From Eqs. (3) and (4), it is found that the power flow in such a guide is

$$P = (n_1 a^2 E_1^2)/2Z_0. \tag{5}$$

As indicated earlier, identical fields exist within the laser bore with the exceptions that n_1 is replaced by n_0, and the electric field amplitude E_0 is replaced by $(n_1/n_0)^{1/2}E_1$ for equal power flow in laser and modulator.

Radiated Fields

Following Abrams,[3] the electric field at the exit face ($z = 0$) of the laser is decomposed into a series of near field optical beam normal modes. The propagation of the radiated light to the modulator is then governed by the beam modes. As modulator locations in both the near and far field of the laser will be treated, this technique is used throughout this paper. For near field placement alone, Eq. (1) can be more directly evaluated from the waveguide modes.

Thus

$$E_y(x,y) = aE_0 \sum_{m,n} A_{mn}\psi_{mn}(x,y) \tag{6}$$

In Cartesian coordinates, the amplitude coefficients are given by[8]

$$\psi_{mn} = \frac{1}{(2^m m!)^{1/2}}\frac{1}{(2^n n!)^{1/2}}\left(\frac{2}{\pi}\right)^{1/2}\frac{1}{w_0} \cdot H_m[(2)^{1/2}x/w_0]H_n[(2)^{1/2}y/w_0]\cdot\exp[-(x^2+y^2)/w_0^2], \tag{7}$$

where w_0 describes the mode beam waist, and H_m is the Hermite polynomial of order m. The coefficients have been normalized to unity,

$$\int_{-\infty}^{+\infty} dx \int_{-\infty}^{+\infty} dy\,\psi_{mn}(x,y)\psi_{m'n'}(x,y) = \delta_{mm'}\delta_{nn'}. \tag{8}$$

It follows immediately from Eqs. (6) and (8) that

$$A_{mn} = \frac{1}{(2^m m!)^{1/2}}\frac{1}{(2^n n!)^{1/2}}\left(\frac{2}{\pi}\right)^{1/2}\frac{1}{aw_0} \cdot \int_{-a}^{+a} dx\cos\left(\frac{\pi x}{2a}\right)H_m\left[(2)^{1/2}\frac{x}{w_0}\right]\exp(-x^2/w_0^2) \cdot \int_{-a}^{+a} dy\cos\left(\frac{\pi y}{2a}\right)H_n\left[(2)^{1/2}\frac{y}{w_0}\right]\exp(-y^2/w_0^2). \tag{9}$$

From Eq. (9), it is seen that all odd order modes vanish as expected from symmetry.

Define

$$I_m = 2\int_0^1 du\cos(\pi u/2)H_m[(2)^{1/2}ru]\exp(-r^2u^2), \tag{10}$$

where $r = a/w_0$. Therefore Eq. (9) becomes

$$A_{mn} = \frac{1}{(2^m m!)^{1/2}}\frac{1}{(2^n n!)^{1/2}}\left(\frac{2}{\pi}\right)^{1/2} rI_m(r)I_n(r). \tag{11}$$

At present the optical beam waist w_0 is unspecified. Now it is shown that a value of w_0 maximizes the fundamental Gaussian mode coefficient A_{00}. Differentiating Eq. (11) yields

$$\frac{dA_{00}}{dr} \propto I_0\left(I_0 + 2r\frac{dI_0}{dr}\right) = \frac{-I_0 I_2}{2}. \tag{12}$$

Equating Eq. (12) to zero shows that at a value of r for which A_{00} is an extremum (maximum), all second order modes vanish. Numerical computation is simplified by selecting this value of r. In Table I, the first few expansion coefficients are shown for the near optimum value of $r = 1.422$. It is seen that the

Table I. First Few Expansion Coefficients for $r = 1.422$

A_{00}^2	0.9788
$A_{02}^2 = A_{20}^2$	0.2910×10^{-9}
$A_{04}^2 = A_{40}^2$	0.7849×10^{-2}
$A_{06}^2 = A_{60}^2$	0.1273×10^{-2}
$A_{08}^2 = A_{80}^2$	0.8156×10^{-4}
A_{22}^2	0.8654×10^{-19}
A_{44}^2	0.6294×10^{-4}
A_{66}^2	0.1657×10^{-5}
$A_{24}^2 = A_{42}^2$	0.2333×10^{-11}
$A_{26}^2 = A_{62}^2$	0.3786×10^{-12}
$A_{46}^2 = A_{64}^2$	0.1021×10^{-4}

decomposition of the EH_{11} mode is dominated by the Gaussian mode, all second order modes are negligible, and as a practical matter, only m,0 or 0,n modes contribute significantly to the radiated field. (This value of r is used throughout this paper.)

Equation (12) also implies

$$I_0 = -2r dI_0/dr \tag{13}$$

at the optimum beam waist.

Coupling with Offset

Tilt

The coupling efficiency from Eq. (1) for a misaligned laser and modulator is now calculated. In Fig 1(a), the geometry for a tilt (ϕ) in the yz plane is shown. The coordinate transformation is given by

$$\begin{aligned} x &= x', \\ y &= y' \cos\phi + z' \sin\phi, \\ z &= z' \cos\phi - y' \sin\phi + s. \end{aligned} \tag{14}$$

The modulator is considered to be in the near field of the laser. Consequently, propagation in the z direction is simply included by inserting the phase factor $\exp[-i(k_0 z - \omega t)]$ for all modes in Eq. 7.[8] The validity of this approximation will be examined later.

It is precisely this phase factor that dominates the coupling for low loss ($\phi \ll 1$). In the low loss limit, it is necessary to retain the tilt ϕ in the phase term but not the amplitude terms. This follows because the phase factor $k_0 a\phi$ greatly exceeds the amplitude factor $r\phi$ for the overmoded waveguide. In the $z' = 0$ plane of the modulator face, the coordinate transformation then becomes $x = x'$, $y = y'$, $z = -y'\phi + s$. Combining Eqs. (1), (4), and (6) with this transformation

$$\tau = \left| \sum_{m,n} A_{mn}{}^2 T_n \right|^2, \tag{15}$$

where

$$T_n(\Phi) = \frac{2}{I_n} \int_0^1 du \cos(u\Phi) \cos\left(\frac{\pi u}{2}\right) H_n[(2)^{1/2} r u] \exp(-r^2 u^2) \tag{16}$$

and $\Phi = k_0 a\phi$. Loss results from the $\cos(u\Phi)$ term of the integrand in a fashion closely related to heterodyne detection. Efficient coupling requires close matching of both amplitude and phase as does mixing.

The numerical evaluation of Eq. (15) has been performed and is shown in Fig. 2 as

$$\mathbf{L} = 1 - \tau(\Phi)/\tau(\Phi = 0). \tag{17}$$

For an intracavity modulator, $\mathbf{L}$ represents the single pass loss. The summation was carried out for all modes through $A_{12,12}$ which gives $\tau(\Phi = 0) = 0.9980$. The remaining 0.2% from the missing higher order modes does not contribute significantly to the offset loss. For low loss, the figure presents the full dependence on tilt for all modes.

To demonstrate this fact, consider the coupling of the Gaussian mode alone. From Eq. (16),

$$T_0 = \frac{2}{I_0} \int_0^1 du \cos(u\Phi) \cos\left(\frac{\pi u}{2}\right) \exp(-r^2 u^2). \tag{18}$$

For small offset ($\Phi \ll 1$), replace $\cos(u\Phi)$ by $1 - (u\Phi)^2/2$. Therefore, Eq. (18) can be written with the help of Eq. (13) as

$$T_0 = 1 + \frac{\Phi^2}{4rI_0} \frac{dI_0}{dr} = 1 - \frac{\Phi^2}{8r^2} + O(\Phi^4). \tag{19}$$

Denote by $\tau_0(\mathbf{L}_0)$, the transmission (loss) of the fundamental mode where $\tau_0 = |A_{00}{}^2 T_0|^2$. Therefore

$$\mathbf{L}_0 = 1 - \tau_0(\Phi)/\tau_0(\Phi = 0) = (k_0 a\phi/2r)^2. \tag{20}$$

This approximate solution is also shown in Fig. 2. Its comparison with the full solution indicates that the loss with tilt is determined at low loss by the fundamental mode alone. This behavior is expected because 98% of the radiated power is in the fundamental mode.

Displacement

The geometry for the transverse displacement (d) of laser and modulator is shown in Fig. 1(b). The coordinate transformation is

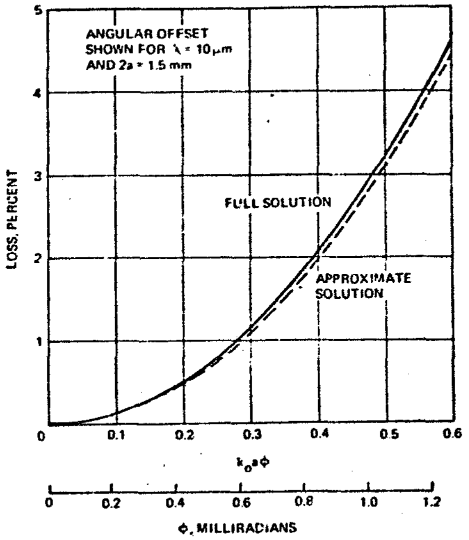

Fig. 2. Coupling loss from tilt.

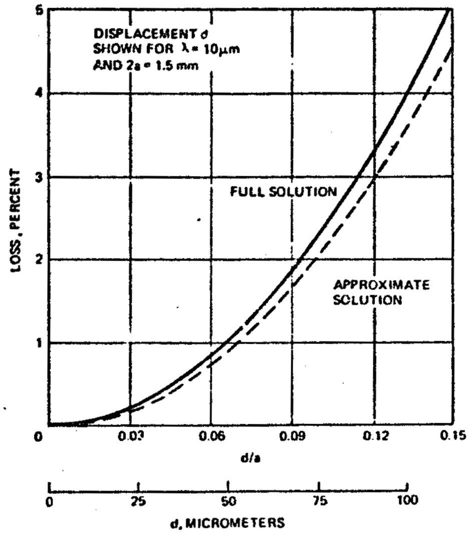

Fig. 3. Coupling loss from displacement.

$$
\begin{aligned}
x &= x', \\
y &= y' + d, \\
z &= z' + s.
\end{aligned} \qquad (21)
$$

For the near field approximation, the radiated fields and modulator fields are coplanar with this offset. Coupling loss results from amplitude mismatch alone. Combining Eqs. (1), (4), and (6) in the $z' = 0$ plane of the modulator gives

$$
\tau = \Big|\sum_{m,n} A_{mn}{}^2 D_n\Big|^2, \qquad (22)
$$

where

$$
D_n(\Delta) = \frac{1}{I_n}\int_{-1}^{+1} du \cos\left(\frac{\pi u}{2}\right) H_n[(2)^{1/2}(ru + \Delta)] \exp[-(ru + \Delta)^2] \qquad (23)
$$

with $\Delta = rd/a$.

Figure 3 presents the coupling loss using the same procedure of the preceding section and shows the approximate solution for the change in coupling for the Gaussian mode. This result is obtained as given below. From Eq. (23),

$$
D_0 = \frac{1}{I_0}\int_{-1}^{+1} du \cos\left(\frac{\pi u}{2}\right) \exp[-(ru + \Delta)^2]. \qquad (24)
$$

To second order in Δ; it can easily be shown

$$
D_0 = 1 - \Delta^2 - \frac{r\Delta^2}{I_0}\frac{dI_0}{dr} = 1 - \frac{\Delta^2}{2} + O(\Delta^4). \qquad (25)
$$

Consequently, the coupling loss is given approximately by $L_0 = (rd/a)^2$. It is seen that this result does not follow the full solution as closely as the case of angular offset but that again, for low loss, the fundamental mode dominates the dependence.

Separation

This concluding section describes the coupling loss resulting from axial separation(s) of laser and modulator. Here it is necessary to include the beam divergence and wavefront curvature neglected in the two previous cases. The full amplitude coefficients are given by[8]

$$
\begin{aligned}
\psi_{mn} = {}& \frac{1}{(2^m m!)^{1/2}}\frac{1}{(2^n n!)^{1/2}}\left(\frac{2}{\pi}\right)^{1/2}\frac{1}{w}H_m\left[(2)^{1/2}\frac{x}{w}\right] \\
&\times H_n\left[(2)^{1/2}\frac{y}{w}\right]\cdot\exp\left[-\left(\frac{x^2+y^2}{w^2}\right)(1 + iz/b)\right] \\
&\exp[-i(kz - \omega t - \Phi_{mn})],
\end{aligned} \qquad (26)
$$

where

$$
\begin{aligned}
w &= w_0[1 + (z/b)^2]^{1/2}, \\
\Phi_{mn} &= (m + n + 1)\tan^{-1}(z/b), \\
b &= \pi w_0{}^2/\lambda.
\end{aligned}
$$

The coupling, again found in a straightforward manner, is given by

$$
C = \Big|\alpha \sum_{m,n} A_{mn}{}^2 \exp(i\Phi_{mn}) S_m S_n\Big|^2, \qquad (27)
$$

where

$$
S_m = \frac{2}{I_m}\int_0^1 du \cos\left(\frac{\pi u}{2}\right) H_m[(2)^{1/2}\alpha r u] \exp[(-\alpha^2 r^2 u^2(1 + is/b))],
$$

with $\alpha = 1/[1 + (s/b)^2]^{1/2}$. In Fig. 4, the loss is presented. This result shows that, for $s/b \approx 0.05$, the near field approximation used previously is well met as the loss from axial separation is negligible. In practice, this condition is satisfied for components separated by a distance of three or less diameters for the numerical values indicated in the figure. Note

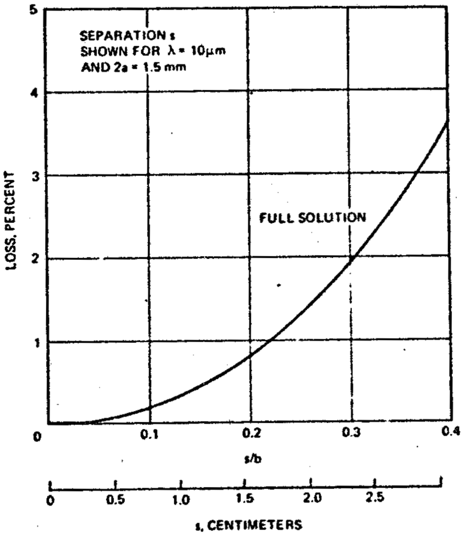

Fig. 4. Coupling loss from separation.

that the coupling will follow a square law dependence here as in the other two cases. In Fig. 4, the loss (in percent) is given by 20 $(s/b)^2$ over the range shown to within 10% of the full solution. For cylindrical bore lasers,[4] the loss varies as $(s/b)^{3/2}$.

Summary

The coupling loss resulting from misalignment of a square bore waveguide laser and electrooptic modulator has been derived. Alignment tolerances are given for a 10-μm intracavity modulator. It is found that (1) angular alignment of 200 μrad or better must be met, (2) a transverse displacement of 25 μm or better must be held, and (3) the axial separation of laser and modulator must be no more than a distance of three diameters to keep losses low. Approximate analytical solutions have been found for the coupling loss. A further result of the calculation is of interest for coupling a Gaussian laser beam into the fundamental EH_{11} mode of the modulator. It is found that the optimum match occurs for a $a/w_0 = 1.422$ for which 97.9% of the incident Guassian is coupled into the fundamental mode of the rod.

This work was supported by NASA Goddard Space Flight Center under contract NAS5-20623.

References

1. I. P. Kaminow and E. H. Turner, Appl. Opt. 5, 1612 (1966).
2. R. L. Abrams and W. B. Bridges, IEEE J. Quantum Electron. QE-9, 940 (1973).
3. R. L. Abrams, IEEE J. Quantum Electron. QE-8, 838 (1972).
4. J. J. Degnan and D. R. Hall, IEEE J. Quantum Electron. QE-9, 901 (1973).
5. D. Marcuse, Bell Syst. Tech. J. 49, 1695 (1970).
6. M. Imai and E. H. Hara, Appl. Opt. 13, 1893 (1974).
7. E. A. J. Marcatili, Bell Syst. Tech. J. 48, 2071 (1969).
8. H. Kogelnik and T. Li, Appl. Opt. 5, 1550 (1966).

APPENDIX E. COMPONENT SPECIFICATION FOR CADMIUM-TELLURIDE MODULATOR ROD

Summarized in this appendix are the optical, electrical, and physical requirements for a CdTe electro-optical crystal rod to be used in a wide bandwidth, intracavity modulator for a CO_2 laser. The CdTe rod will be the optically active element of a modulator structure designed for polarization (amplitude) modulation of the 10.6 μm laser beam. The laser transmitter, for which the modulator is required, will function in a space application.

E.1 OPTICAL CHARACTERISTICS

This subsection itemizes the optical performance requirements needed to assure compatibility with the laser transmitter. Optical characteristics of the modulator rod are as follows:

1)	Absorption loss, α_a	0.001 cm^{-1} (maximum)
2)	AR coating loss, α_c	0.2 percent/surface
3)	Alignment of crystal axis	+/- 1 minute
4)	End surface wedge angle	+/- 1 minute
5)	End surface polish*	60/40*
6)	Side surfaces E and P*	80/50*
7)	Crystal orientation	Figure E-1

---

*The first two digits are the apparent width of a tolerable scratch in micrometers, and the second two digits are the diameter of a permissible dig, pit, or bubble in hundredths of a millimeter.

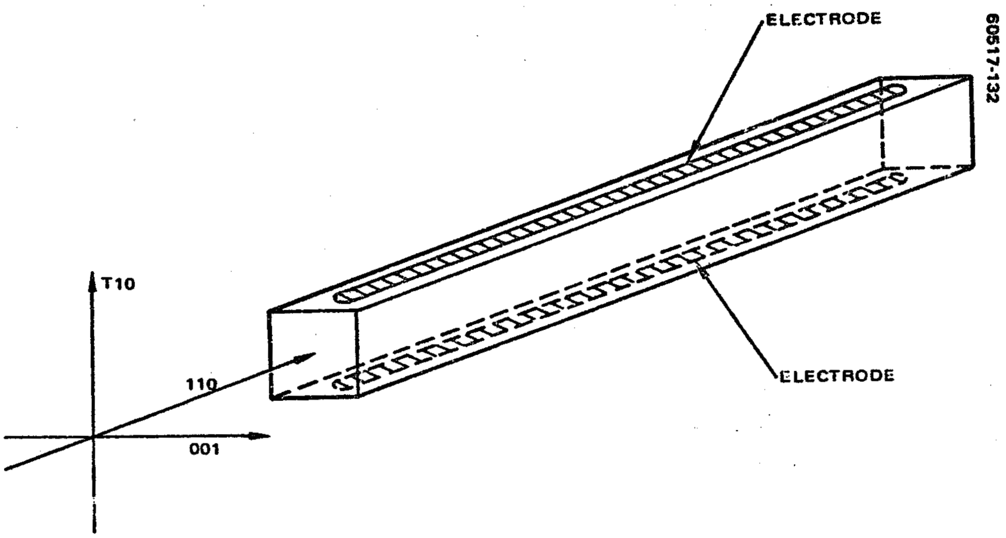

FIGURE E-1. ORIENTATION SKETCH OF CdTe ROD

E.2 ELECTRICAL PROPERTIES

The electrical and semiconducting parameters for the CdTe rod are as follows:

1)	Resistivity at 30°C, ρ	10^8 Ω-cm (minimum)
2)	Dielectric strength	6 kv/cm (CW) 12 kv/cm (pulse)
3)	Electrode surface preparation	Nitric acid etch
4)	Electrode dimensions	Figure E-2
5)	Electrode metalization	Evaporated silver
6)	Electrode/crystal boundary	Ohmic contact

E.3 MECHANICAL CHARACTERISTICS

The crystal and electrode dimensions required for mechanical compatibility with the modulator rod housing are as follows:

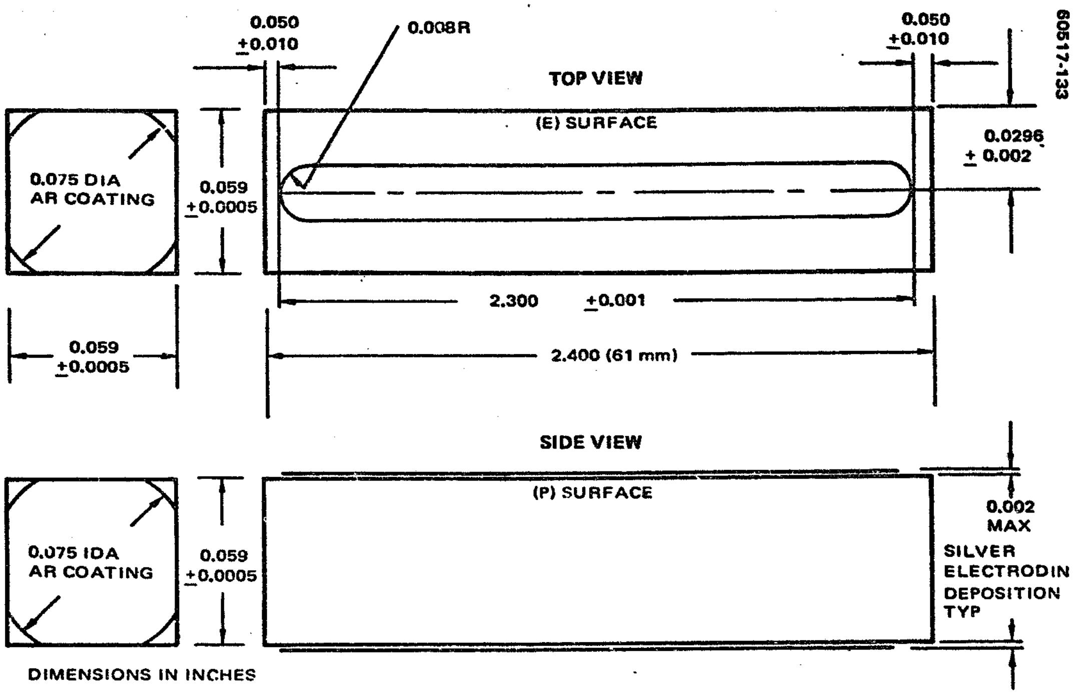

FIGURE E-2. CdTe CRYSTAL PHYSICAL DIMENSIONS

1) Surface dimensions		
End surface, in^2	0.059	±0.0005
Length (61 mm nominal), in.	2.400	±0.020
2) Perpendicularity of end faces to long axis of crystal	90°	±3 minutes
3) End surface corner angles (squareness of 4 angle)	90°	±6 minutes
4) Electrode dimensions, in.		
Width	0.019	±0.0005
Thickness	0.0002 (maximum)	
Length	2.300	±0.001
Centering from long edge	0.0295	±0.002
Centering from ends	0.050	±0.010

APPENDIX F. PARTS STRESS DERATING - MSC 80041 DRIVER TRANSISTORS

F.1 DETAILED DERATING POLICY

Preferred Region

Maximum use shall be made of electronic parts whose intersection of electrical stress and temperature is within the "preferred" region of Figure F-1. It is necessary to operate most parts in this region to assure meeting system reliability requirements and long life demonstrated in space operation. However, trades between operating outside the preferred region and adding complexity to maintain preferred level stresses should be performed to enhance system reliability in terms of low failure rates and long life.

Acceptable Region

Selection of electronic parts whose intersection of electrical stress and temperature is within the "acceptable" region of Figure F-1 shall be satisfactory when constraints make it unfeasible or it is uneconomical to use electronic parts whose intersection of electrical stress and temperature is within the "preferred" region.

Approval - Required Region

Operation in the "approval-required" region for extended periods could compromise reliability and life. Specific written approval must be obtained from the SCG Product Effectiveness Manager or the assigned Program Product Effectiveness Manager for the use of electronic parts whose intersection of electrical stress and temperature is within the approval-required region of Figure F-1. The approval request must provide justification (including availability, cost, weight, size, performance, etc.) to enable evaluation. Such approval shall be requested in sufficient time to permit the evaluation to be completed prior to the using item's critical design review (design freeze). The primary purpose of the written approval is to assure that special attention is given to those parts whose operational stress could compromise reliability.

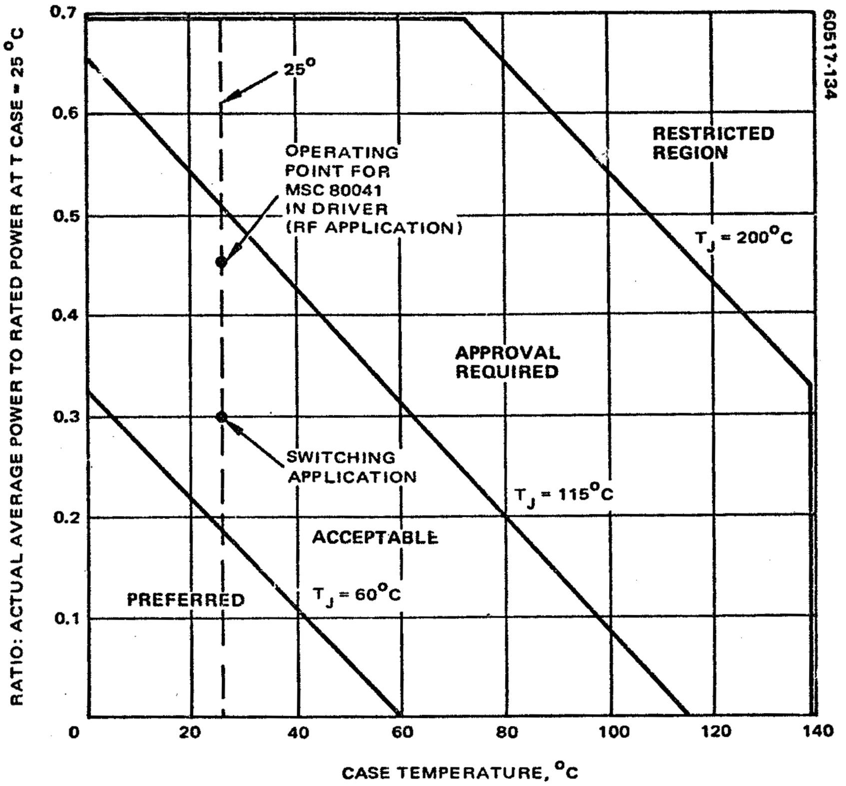

FIGURE F-1. POWER STRESS VERSUS TEMPERATURE SEMICONDUCTORS: 200°C MAXIMUM OPERATING JUNCTION TEMPERATURE

Restricted Region

Parts should not be applied in the "restricted" region. Operation at stresses in this region could seriously compromise reliability and life.

The restricted region is the region extending beyond the operating specification limits. Wherever feasible this region has been delineated on the derating curves. However, it is to be recognized that the restricted region always exists even if not shown on the curves. Except for highly specialized operations (i.e., squib circuits), no part shall be operated in the restricted region.

Exceptions shall require written approval from the SCG Product Effectiveness Manager or the assigned Program Product Effectiveness Manager.

AC voltage must be carefully evaluated for each application. Capacitor heating will depend on the temperature, frequency, and dissipation factor as well as the ac voltage level. Certain capacitors (such as high-K ceramic) will show a noticeable change with applied voltage and will exhibit dielectric absorption which may become a critical factor in pulse circuitry. Multipactor action in space must be considered for air dielectric capacitors. Individual capacitor specifications and supplier application notes must be consulted to determine the amount of permissible ac. The permissible ac peak may be derated by 50 percent; the sum of the ac and dc voltage, if any, shall be within the acceptable or preferred boundary of the derating curve. The peak voltage applied across the capacitor shall not exceed the rating in the detailed Hughes specification.

In view of the inherent unreliability of wet tantalum capacitors, it is recommended that they not be used. Approval shall be required in all cases.

F.2 SEMICONDUCTORS (Figure F-1)

This subsection presents the derating curves relative to semiconductors.

Failure rate data for various types of semiconductors require different mathematical models, and stresses on any parameters of semiconductors affect failure rates. However, temperature is the major factor in semiconductor reliability, and failure rates are commonly related to the junction temperature.

This junction temperature consists of the heat rise within the device caused by power dissipated in the junction plus the case temperature. In turn, the case temperature is related to the attached heat sink temperature. Transistors are normally rated at maximum power dissipation and diodes at maximum permissible current. Usually each device is given two rating points: one for maximum permissible junction temperature and the other for the maximum case temperature (derating point, T_S) at which 100 percent of the rated load can be dissipated without causing the sum of the case plus internal temperature rise to exceed the specified maximum junction temperature (T_J). As case temperature rises above the T_S value, the internal temperature rise and power load must be decreased if the combined temperature is not to exceed T_J.

The derating curves are therefore based on case temperature versus ratio of actual average power to rated power for fixed junction temperatures.

When derating curves are used for current rated devices (i.e., some diodes), the ordinate should be replaced by the ratio

Actual average current to rated current at T case = 25°C

Semiconductor parameters not included in the derating curves are listed below. In addition to junction temperature derating, design limits have been established for certain parameters of specific types of semiconductors.

1) Diodes

- Forward current shall not exceed 75 percent of maximum rated.
- Peak inverse voltage shall not exceed 80 percent of maximum rated.

2) Transistors

- Collector current shall not exceed 80 percent of maximum rated.
- No voltage shall exceed 90 percent of maximum rated breakdown voltage.

Characteristics of the MSC 80041 stud package and grounded base flange package are listed in Table F-1.

TABLE F-1. CHARACTERISTICS OF MSC 80041 STUD PACKAGE AND GROUNDED BASE FLANGE PACKAGE

DC Electrical Characteristics Case Temperature = 25°C	Symbol	Test Conditions						Limits		Units
		DC Collector, V		DC Base, V	DC Current, mA					
		V_{cb}	V_{ce}	V_{be}	I_e	I_b	I_c	Minimum	Maximum	
Collector-to-base breakdown voltage	BV_{cbo}				0		1	50		V
Collector-to-emitter breakdown voltage (with Rbe = 10)	BV_{cer}						10	50		V
Emitter-to-base breakdown voltage	BV_{ebo}				1		0	3.5		V
Collector cutoff current	I_{cbo}	28			0				500	A
Continuous collector current	I_c	2			0				1.0	A
Forward-current transfer ratio	HFE		15				50	20	120	–
Thermal resistance (junction-to-flange)	J-F								15	°C/W
Storage								-65		°C

RF Electrical Characteristics Case Temperature =25°C	Symbol	Test Conditions			Limits					
		DC Collector, V		Frequency,	Power Output, W		Power Gain, dB		Efficiency, %	
		V_{cb}	V_{ce}	GHz	Minimum	Typical	Minimum	Typical	Minimum	Typical
Amplifier power output	P_{out}	28		2.0	2.5	3.0	7	–	30	35
Oscillator power output	P_{out}	20		2.0	–	2.0	–	–	–	25
Amplifier power output	P_{out}	28		1.0	–	6.0	–	11	–	55
Oscillator power output	P_{out}	20		1.0	–	3.7	–	–	–	50
Gain-bandwidth product (at Ic = 200 mA)	f_T		10		1500 MHz (typical)					
Collector-to-base capacitance	C_{ob}	28		0.001	5 pF (maximum)					

ORIGINAL PAGE IS
OF POOR QUALITY

APPENDIX G. SPECIFICATIONS FOR HYBRID ASSEMBLY, VARI-L SA-167

G. 1 SPECIFICATIONS*

1)	-1 dB bandwidth	5 to 500 MHz minimum
2)	Insertion loss, 10 to 300 MHz	1 dB maximum; 0.8 dB, design goal
3)	Isolation	20 dB minimum
4)	Impedance, all signal ports	50Ω minimum
5)	VSWR, 10 to 300 MHz	1.5:1 maximum
6)	Size (see Figure G-1)	4 by 6 by 1-5/8 in., excluding connectors
7)	Connectors (see Figure G-1)	All signal ports, SMA-female; bias ports, feedthrough filter (Erie 1216-001 or equivalent)
8)	Weight	Approximately 350 grams

9) Input/output designations (see Figure G-1):

J1	Input A (0°),	J5	Output
J2	Input $\overline{A}$ (180°)	J6	Isolated port
J3	Input B (0°)	P1	DC bias, J1/J2
J4	Input $\overline{B}$ (180°)	P2	DC bias, J3/J4

10) Operating temperature -55°C to +100°C

---

*Specifications 1 through 5 must be satisfied under the condition of 0.7 ampere bias current into each dc bias port and up to 5 watts (rms) into each input port simultaneously. See Figures G-2 and G-3.

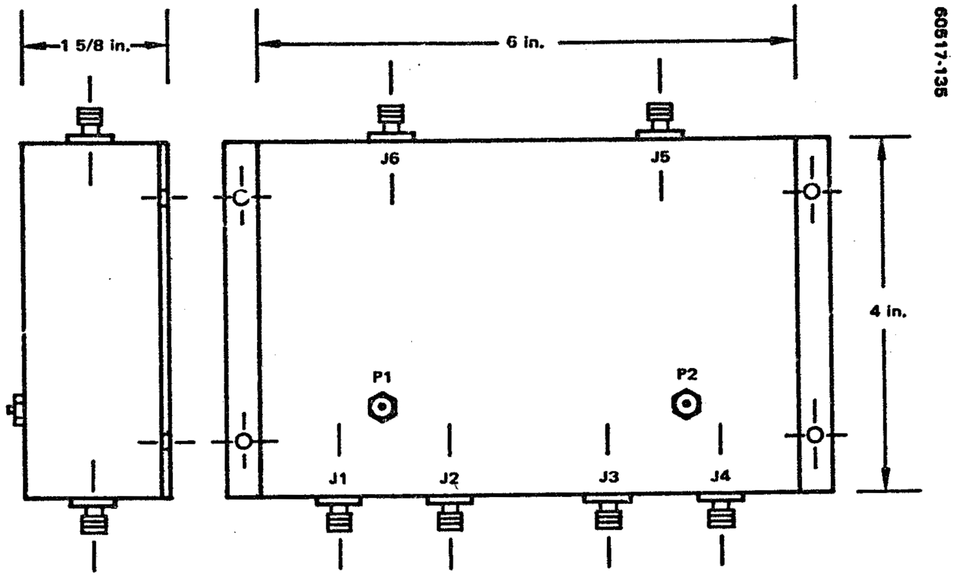

FIGURE G-1. SA-167 HYBRID ASSEMBLY OUTLINE DRAWING

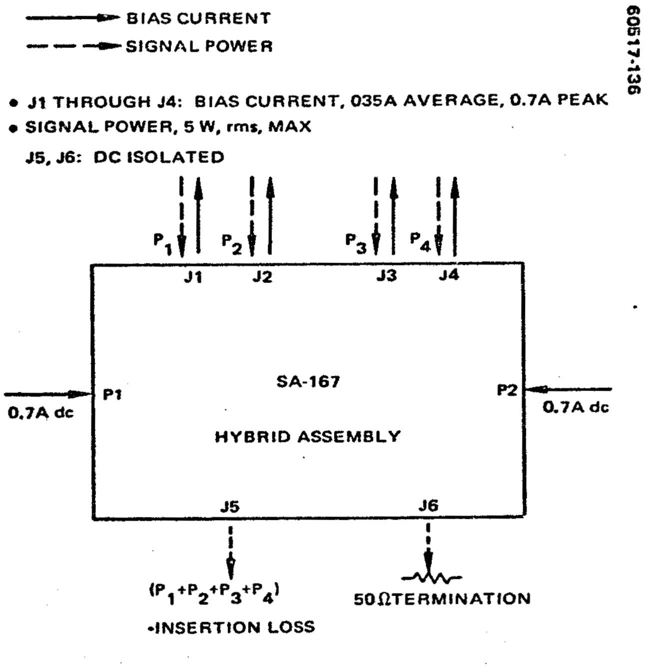

FIGURE G-2. BIAS/SIGNAL OPERATING CONDITIONS

ORIGINAL PAGE IS
OF POOR QUALITY

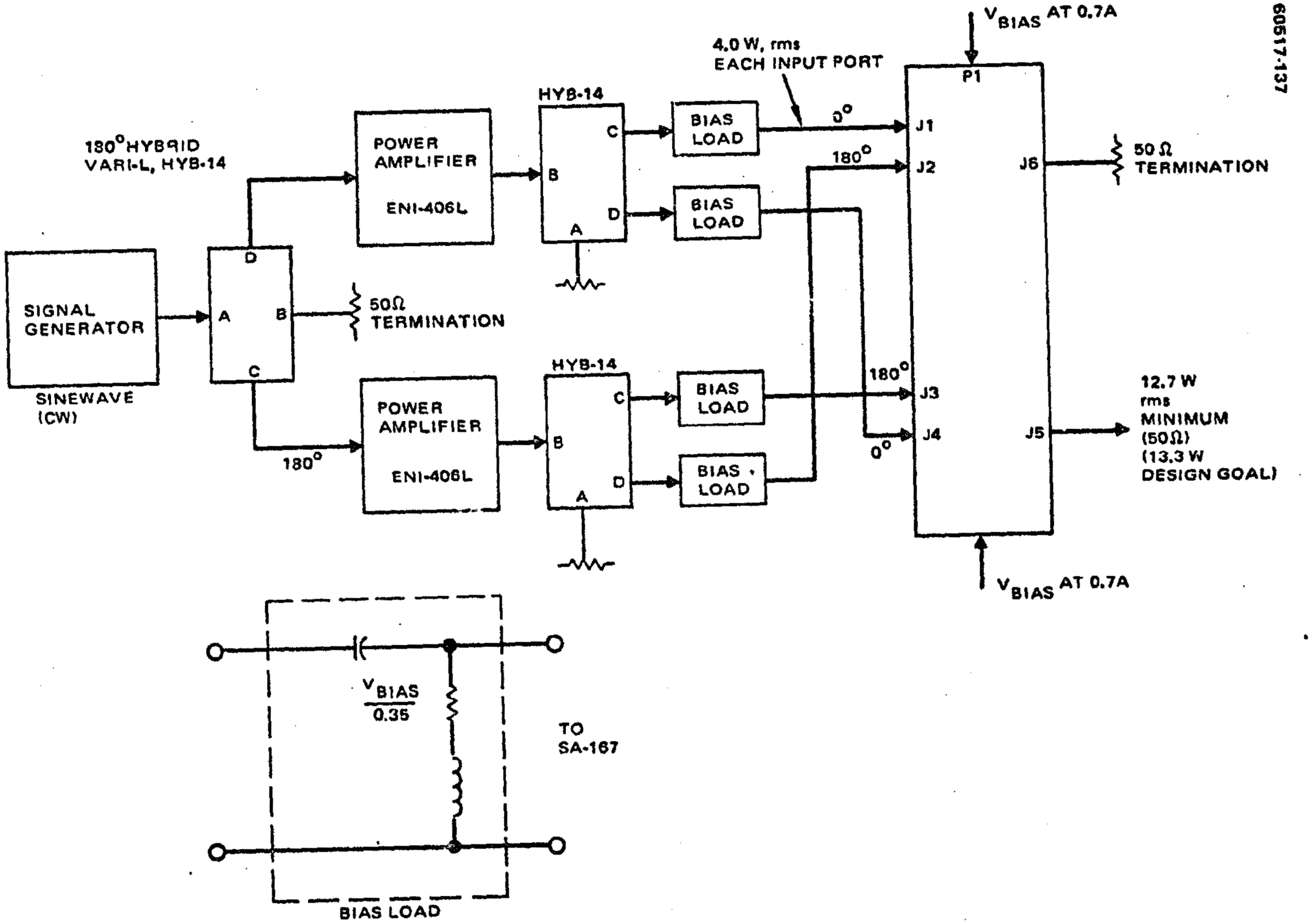

FIGURE G-3. TEST SETUP

APPENDIX H. CALCULATION OF AVERAGE OUTPUT POWER

From Equation 2 of Section 7 and of Section 3 the time average output power is

$$<P_{\perp}> = \eta_g <\Gamma_m^2> \frac{P_s}{2} \frac{g_0 L - \mathscr{L}}{\mathscr{L}}, \; \mathscr{L} = 1 - \sqrt{r_1 r_2'} \tag{1}$$

where

$$r_1 = 1 - a_1$$

$$r_2 = 1 - a_2$$

$$r_2' = r_2 \; 1 - <\Gamma_m^2>$$

The quantities a_1 and a_2 are the effective optical losses and end 1 and end 2 of the laser cavity. Note that output coupling loss is included. Assuming low loss, a_1, $a_2 \ll 1$, Equation 1 can be written

$$<P_{\perp}> = \eta_g \; P_s \frac{<\Gamma_m^2>}{2} \frac{\left[g_0 L - \frac{1}{2}(a_1 + a_2 + <\Gamma_m^2>)\right]}{\frac{1}{2}(a_1 + a_2 + <\Gamma_m^2>)} \tag{2}$$

Define

$$<\Gamma_m^2> = \pi^2 \frac{P_T}{P_\pi}\left(\frac{P_M}{P_T}\right) \equiv 2 \; a(\beta) \tag{3}$$

$$L = \frac{\eta_{nv}}{D_{sec}} \; P_T \left(\frac{P_L}{P_T}\right) \equiv b \; (1 - \beta) \tag{4}$$

and

$$\mathscr{L} = (a_1 + a_2)/2 \tag{5}$$

Therefore equation 2 can be written

$$<P_\perp> = \eta_g P_s \frac{(h - \mathscr{L})(c - dh)}{h} \tag{6}$$

where

$$\begin{aligned} h &= \mathscr{L} + a\beta \\ c &= g_0 b\,(1 + \mathscr{L}(a)) \\ d &= 1 + g_0 b/a \end{aligned} \tag{7}$$

Differentiating Equation 6 gives the conditions for maximum output power,

$$h = \sqrt{\mathscr{L}\, c/d} \tag{8}$$

and

$$<P_\perp> = \eta_g P_s (\sqrt{c} - \sqrt{\mathscr{L} d})^2 \tag{9}$$

In the limit of low level modulation, $a \ll \mathscr{L}$, $g_0 b$, Equation 9 reduces to the result contained in Section 5 of this report.

APPENDIX I. HYSTERESIS IN CAVITY LENGTH TUNING OF COUPLING MODULATED CO_2 LASERS

I. 1 INTRODUCTION

Coupling modulation is a commonly used technique at 10 μm for achieving a large depth of modulation of CO_2 laser light with practical modulator driver power levels (References 1, 2, 3). In this scheme an electro-optic crystal is placed within the laser cavity where the circulating power exceeds the output power by about an order of magnitude. An electric field applied to the crystal causes rotation of the laser polarization in the cavity. The cross polarized, modulated component is coupled out of the cavity with a Brewster angle window or blazed grating.

Because the commonly used electro-optic materials at 10 μm possess a significant temperature dependence in refractive index (Reference 4), the static and dynamic tuning of such a device differs significantly from a laser without the intracavity crystal. The cavity length is controlled by the voltage applied to a bender bimorph translator on which a laser mirror is mounted. Hysteresis in the laser output power is readily noted when manually tuning the cavity. With the conventional dither stabilization of the cavity length, this hysteresis results in locking the laser off-line center. Without the modulator in the cavity, no such problems occur.

A simple thermal relaxation model of modulator heating based on uniform absorption of the laser energy is shown to yield good qualitative agreement between the measured line shapes and those calculated in this paper. Other thermal effects such as self-focusing, which arise from thermal gradients (Reference 5) apparently do not play a significant role in the cavity operation.

I. 2 EXPERIMENTAL MEASUREMENTS

Figure I-1 shows the typical swept cavity output power from a single mode CO_2 laser oscillating on the P(20) vibrational line. A single crystal CdTe electro-optic modulator, 1.5 m x 1.5 m x 40 mm, is located in the cavity. The upper trace displays the voltage ramp (100 volts/div) applied to the PZT translator. The lower trace contains the output power. Each power peak occurs when the cavity has been swept through a half-wavelength

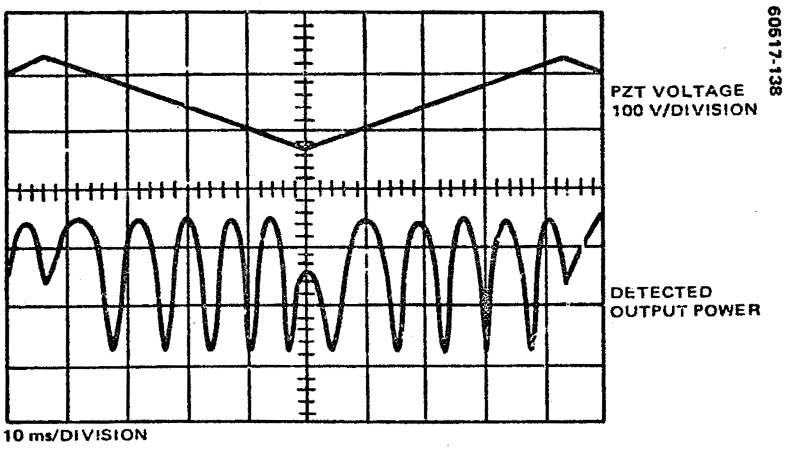

FIGURE I-1. TYPICAL SWEPT CAVITY LENGTH OUTPUT POWER RESPONSE OF SINGLE MODE CO_2 LASER

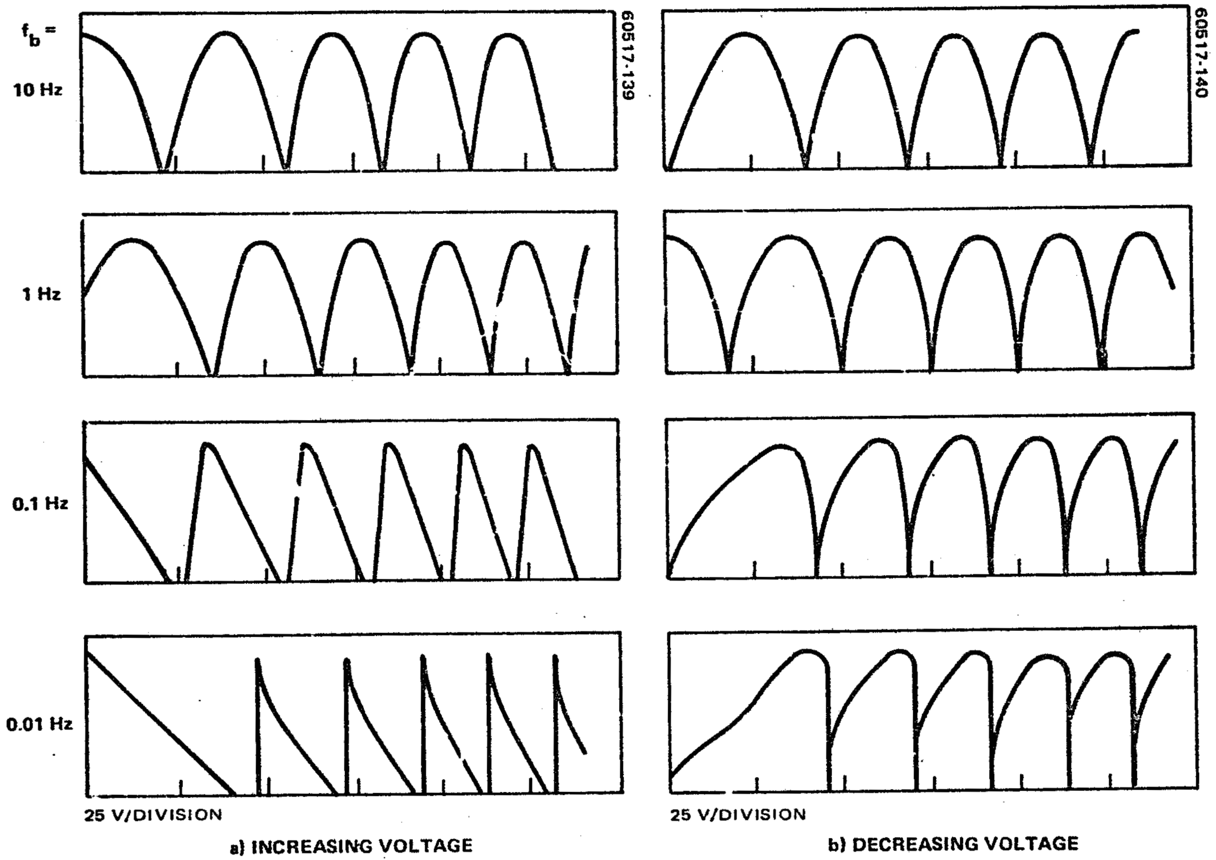

a) INCREASING VOLTAGE

b) DECREASING VOLTAGE

FIGURE I-2. MEASURED SWEPT CAVITY OUTPUT POWER VERSUS PZT VOLTAGE FOR FOUR SWEEP FREQUENCIES

(~5 μm). A small displacement hysteresis in the PZT is evident in the changing period of the peaks, especially near the point where the translator changes direction. This hysteresis is not the subject of this appendix. Rather, a thermal hysteresis is discussed which becomes apparent as the sweep speed is lowered.

In Figure I-2, the line shapes are shown at four different sweep speeds. The conditions of decreasing cavity length (decreasing voltage) and increasing cavity length (increasing voltage) have been separated in Figures I-2a and I-2b. In both cases, striking asymmetries appear. At the slowest sweep speed, the output actually shows unstable behavior as indicated by the large slopes. Such performance makes manual tuning most difficult. This behavior is theoretically investigated in the next subsection.

I. 3 THEORY

Consider an optical cavity in which a crystal of refractive index η_o and length ℓ_m has been placed. Let ℓ_c represent the change in cavity length from line center. Length change can be treated from two sources. First, the bimorph translator can be used to vary the mirror location. Secondly, the optical path length of the crystal changes with temperature. Thus

$$\ell_c(t) = \ell_b(t) + \ell_m \frac{d\eta_o}{dT} (T - T_o) \tag{1}$$

where ℓ_b is the change in mirror location due to translation, $d\eta_o/dT \equiv \eta_o\beta$ is the refractive index temperature coefficient, and T_o is the ambient temperature. Differentiating Equation 1 gives

$$\frac{d\ell_c}{dt} = \frac{d\ell_b}{dt} + \eta_o\beta\ell_m \frac{dT}{dt} \tag{2}$$

A simple relaxation model is used to describe the modulator heating,

$$\frac{dT}{dt} = \frac{\alpha\ell_m P}{CV} - \frac{(T - T_o)}{\tau_H} \tag{3}$$

In this result, α is the crystal absorption coefficient, C the specific heat per volume, V the modulator volume, and P the laser power circulating in the cavity. Absorption has been treated as uniform both along and across the modulator. Heat loss from the crystal is included in Equation 3 by the relaxation term with time constant τ_H. Combining Equations 1 through 3 give

$$\frac{d\ell_c}{dt} = \frac{d\ell_b}{dt} + \frac{\alpha \ell_m^2 \eta_o \beta P(\ell_c)}{CV} - \frac{(\ell_c - \ell_b)}{\tau_H} \tag{4}$$

The circulating power is itself a function of cavity length as shown in Equation 4. We use a square law profile to describe this dependence,

$$P(\ell_c) = P_o [1 - (\ell_c/a)^2] \tag{5}$$

in which a is the point at which the small signal gain equals the cavity loss and oscillation ceases. It can be shown that such dependence is exact for a pressure broadened transition (Reference 6). The data of Figures I-1 and I-2 were taken with a low pressure CO_2 laser filled to 30 Torr. In this case, both pressure broadening and doppler broadening play a role.* Because of the mathematical convenience offered by Equation 5, it is used exclusively.

Equation 4 has been numerically solved for the linear PZT drive used in the measurements. Let

$$\ell_b(t) = 2a \frac{t}{\tau_b} - a \tag{6}$$

According to Equation 6, the cavity length is tuned to the threshold of oscillation at time t = 0. The nominal line width is swept out in a time τ_b. Combining Equations 4 through 6, the following differential equation is obtained.

$$\frac{dy}{dx} = 2 - Ry + \mathscr{L}R (1 - y^2) + 2 (Rx - 1) \tag{7}$$

where

$y = \ell_c/a,\ x = t/\tau_b,\ R = \tau_b/\tau_n$ and $\mathscr{L} = \Delta\ell/a$.

---

*The calculated pressure broadening linewidth is 135 MHz while the calculated doppler linewidth is 50 MHz for this laser.

The parameter $\Delta\ell$ is the steady state change in optical path length due to heating,

$$\Delta\ell = \alpha\ell_m^2 \eta_o \beta \tau_H P_o / CV$$

Equation 7 describes the case in which the cavity length is increasing. The opposite case of decreasing cavity length is obtained by letting $\mathscr{L} = -\mathscr{L}$. It has been found that the best qualitative agreement between theory and measurement is obtained for $|\mathscr{L}| = 1.5$. The computed line shapes are shown in Figure I-3 for four sweep speeds. The first three cycles upon startup from a cold cavity are presented. Essentially all the key features seen in the measurements are contained in the computed traces.

The observed traces are easily understood by recognizing that the optical path length of the modulator increases due to heating by the circulating power. This change works in cooperation with the PZT drive in one case (increasing cavity length), but in opposition to the drive in the other (decreasing cavity length). Consider the case of increasing cavity length. Starting from the cold cavity, the total cavity length change is larger than the PZT displacement because of the absorbed laser light. Thus, the output power peaks at a PZT location that is less than the nominal line center. The unstable behavior seen in the figures for slow sweep speeds results when the steady state optical path length change due to heating is greater than the distance to line center. Heating of the crystal in this situation increases the path length which, in turn, increases the laser power causing further heating. This process takes place on the time scale of τ_H until the total cavity length is past line center. The line shapes for the case of opposite direction of PZT drive can be similarly interpreted.

I.4 DISCUSSION

The calculated line shapes have indicated that the steady state thermal path length change is $\mathscr{L} = \Delta\ell/a = 1.5$. The crystal absorption coefficient from Equation 7 is therefore

$$\alpha = \frac{a\, CV\mathscr{L}}{\ell_m^2 \eta_o \beta \tau_H P_o} \tag{8}$$

The following numerical values are appropriate to the measurements:

$a = 2.5\ \mu m$

$C = 1.2\ J/cm^3/^\circ C$

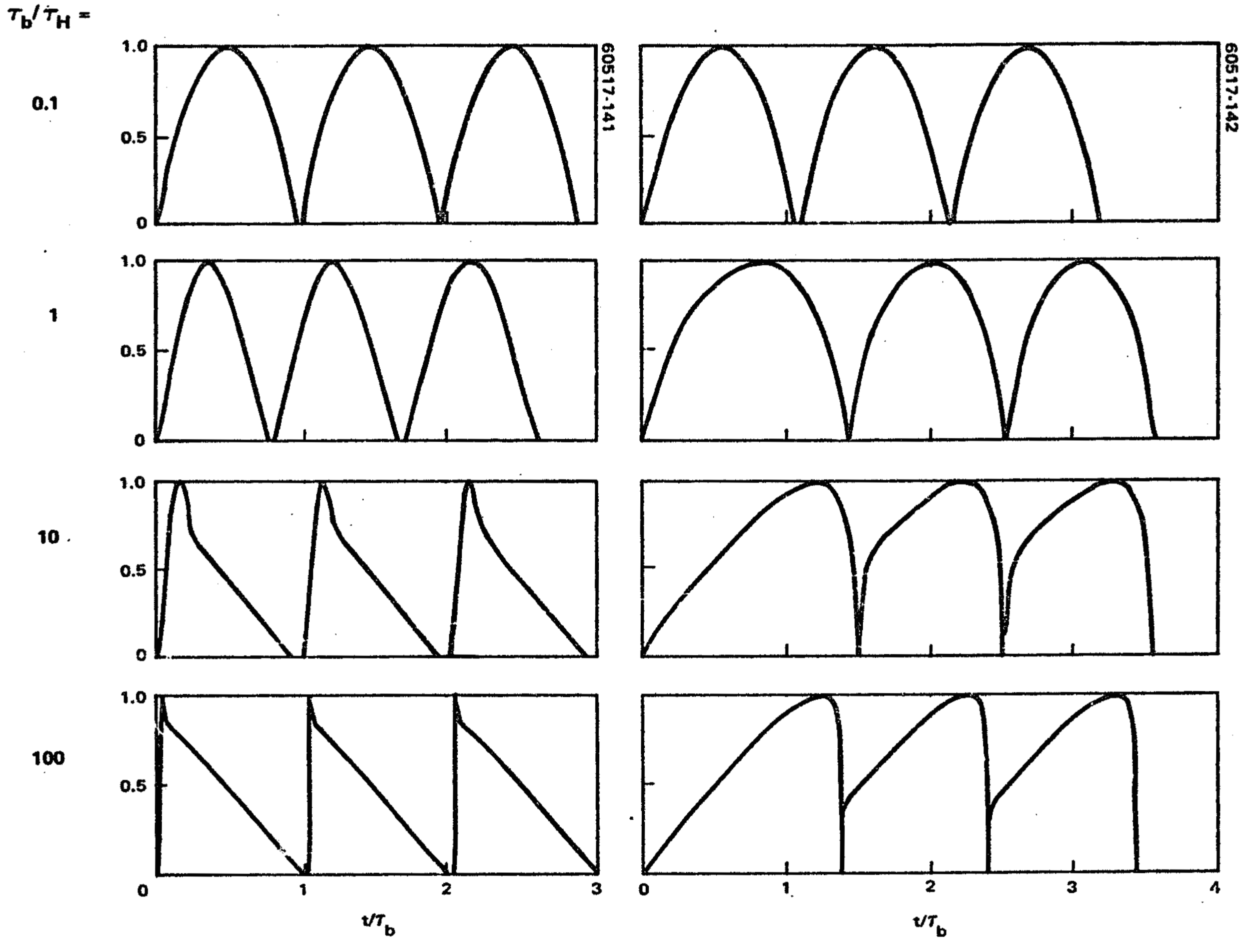

a) INCREASING CAVITY LENGTH

b) DECREASING CAVITY LENGTH

FIGURE I-3. CALCULATED OUTPUT POWER VERSUS PZT VOLTAGE FOR FOUR SWEEP SPEEDS

$V = 0.09\ cm^3$

$\ell_m = 4.0\ cm$

$\eta_o = 2.7$

$\beta = 4.4 \times 10^{-5}/°C$

$\tau_H = 0.15$ second

$P_o = 50$ watts

The value of the thermal time constant was obtained from a separate computer modeling of the modulator housing. This result is consistent with the interpretation of the observed line shapes. For example, the case calculated for $\tau_b/\tau_H = 1$ corresponds to a sweep speed of $f_o = 0.67$ second. Evaluating Equation 8 yields $\alpha = 0.0028\ cm^{-1}$. The crystal absorption coefficients of these CdTe modulator crystals typically fall in the range $0.002\ cm^{-1} \lesssim \alpha \lesssim 0.004\ cm^{-1}$. The agreement of the calculated value with the expected range therefore substantiates the heating interpretation of the observed hysteresis. Consequently, the use of the technique for estimating crystal absorption should be noted.

Dither stabilization of the laser results in locking of the cavity off-line center. *In some cases the accompanying frequency offset is not acceptable.* The source of the offset is the nonlinear contribution to the path length change in Equation 7 that results from heating. By using a high enough frequency dither signal this offset can be small, since the magnitude of the nonlinear contribution scales as τ_b/τ_h. A preferred method of stabilizing the coupling modulated laser is by Stark stabilization (Reference 7) in which no dither is applied to the laser. Here the cavity length is varied in accordance to the frequency of the laser and not its amplitude.

Self-focusing effects have been neglected. Their strength can now be estimated. For a parabolic index profile

$$\eta = \eta_o [1 + \delta(r^2/\omega^2)] \tag{9}$$

the focal length is given by (Reference 5)

$$F = -\frac{1}{2\delta} \frac{h_m^2}{\ell_m} \tag{10}$$

where $2h_m$ is the height of the crystal. The parabolic profile approximates the temperature gradient which exists across the crystal.* Here $\delta = -\eta_o \beta \Delta T$ where ΔT is the temperature difference between the center and the edge of the crystal. Thus

$$F = \frac{h_m^2}{2\eta_o \beta \ell_m \Delta T} \tag{11}$$

The previously mentioned computer modeling of the modulator housing indicates $\Delta T \sim 1/2°C$. Evaluating Equation 11 gives $F \sim 12$ cm. One would expect self-focusing effects in the cavity as this value is about one-third of the resonator length. That the observed behavior can be explained on the basis of uniform heating and not temperature gradients is related most likely to the cavity design. An intracavity lens of ~5 cm focal length focuses the light into the crystal. The cavity then contains two focusing elements. The resonator has been shown to be stable both in the presence and absence of the self-focusing lens (Reference 8). The output from this stable resonator is then determined by the total cavity length, which includes the uniform heating effects.

I. 5 REFERENCES

1. F.R. Nash and P.W. Smith, "Broad-band Optical Coupling Modulation," IEEE J. Quantum Electron., Vol. QE-4, pp.26-34, January 1968.

2. J.E. Kiefer, T.A. Nussmeier, and F.E. Goodwin, "Intracavity CdTe Modulators for CO_2 Lasers," IEEE J. Quantum Electron., Vol. QE-8, pp.173-179, February 1972.

3. J.J. Degnan, "Minimization of the Prime Power Consumption of a Coupling-Modulated Gas Laser Transmitter," Appl. Opt., Vol. 13, pp. 2489-2498, November 1974.

4. C.-C. Huang, Y.-H. Pao, P.C. Claspy, and F.W. Phelps, Jr., "Comparison of GaAs and CdTe Crystals for High-Frequency Intracavity Modulation of CO_2 Lasers," IEEE J. Quantum Electron., Vol. QE-10, pp. 186-191, February 1974.

5. J.P. Gordon, R.C.C. Leite, R.S. Moore, S.P.S. Porto, and J.R. Whinnery, "Long-Transient Effects in Lasers with Inserted Liquid Samples," J. Appl. Phys., Vol. 36, pp. 3-8, January 1965.

---

*This dependence is valid for uniform absorption across the crystal. It is used for convenience.

6. J. J. Degnan, "Phenomenological Approach to the Design of Highly Tunable Pressure-Broadended Gas Lasers," J. Appl. Phys., Vol. 45, pp. 257-262, January 1974.

7. T. A. Nussmeier and R. L. Abrams, "Stark Cell Stabilization of CO_2 Laser," Appl. Phys. Lett., Vol. 25, pp. 615-617, November 1974.

8. F. E. Goodwin, private communication.

APPENDIX J

OPTICAL COUPLING MODULATION IN TRAVELING WAVE CAVITIES

Optical Coupling Modulation in Traveling Wave Cavities

D. M. Henderson and V. A. Vilnrotter

Hughes Aircraft Company, Space and Communications Group
P.O. Box 92919, Los Angeles, CA 90009

ABSTRACT

Efficient, very wideband, coupling modulation of the CO_2 laser has been achieved in a traveling wave cavity configuration termed "ring modulator" that avoids the usual transit time-limited bandwidth of conventional coupling modulation. A 10.6 μm modulation experiment demonstrates flat frequency response from 10 MHz to 1 GHz.

Optical Coupling Modulation in Traveling Wave Cavities

D.M. Henderson, and V.A. Vilnrotter

Hughes Aircraft Company, Space and Communications Group
P.O. Box 92919, Los Angeles, CA 90009

Modulation of laser light, especially the CO_2 laser, by the coupling modulation technique has been extensively used to obtain high level optical modulation at practical values of prime electrical power.[1,2,3] In this scheme, an electro-optic crystal is placed within the laser cavity, where the circulating optical power exceeds the output power by about an order of magnitude. As a result, the modulated or sideband optical power exceeds by an order of magnitude the performance the same device would offer as an external cavity modulator. This double pass configuration has a limited bandwidth, however, due to the time of optical transit through the crystal. For conventional systems at 10.6 μm, the bandwidth is about 300 MHz. Wideband, traveling wave, electro-optic modulators have been built in which the electric field is imposed on the crystal by a stripline whose phase velocity is matched to the optical velocity.[4] These have been external cavity designs and therefore do not offer the performance of intra-cavity systems. One can easily envision placing such a stripline structure in a traveling wave, ring laser cavity to achieve the unidirectional optical propagation required. The bi-stable operation of such a cavity requires in addition some mechanism such as an optical isolator to assure propagation in the direction of the stripline signal. This added complexity diminishes the attractiveness of this approach.

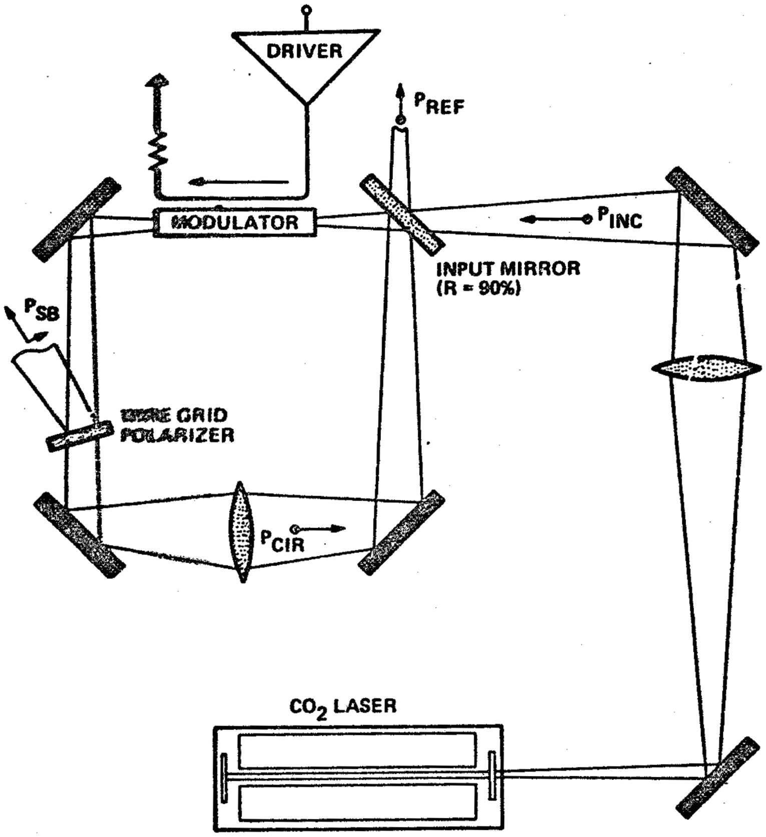

ALL SOLID BLACK ELEMENTS ARE TOTAL REFLECTORS
DOTTED ELEMENTS ARE TRANSMITTING

FIGURE 1. RING MODULATOR EXPERIMENT

This paper presents a novel approach suggested by Abrams[5] that combines the advantages of intra-cavity coupling modulation with the wideband performance of traveling wave modulators. This approach, which we term "ring modulator," can be seen in the experimental configuration of Figure 1. The modulator is placed in a traveling wave cavity pumped by an external laser. This geometry provides the necessary undirectionality (light can travel in only one direction through the modulator). We will show here that the ring structure forms a traveling wave Fabry-Perot cavity. The effective reflectivity of the input mirror can accordingly vary from about 100 percent to a near-zero value. When the reflectivity of the input mirror is minimized, the input laser power goes to build up the circulating power in the cavity. With proper design, the circulating power exceeds the input power. In practice, this enhancement can be as great as ten times. The modulator crystal is cut for amplitude modulation.[6] A voltage imposed across the crystal rotates slightly the polarization of the circulating field. Output coupling of the cross-polarized, modulated component is accomplished with a wire grid polarizer or Brewster angle window.

The performance of the cavity is easily determined by summing the components of the electric field which have traversed the ring repeated times. As the cavity has loss, we denote the single pass cavity transmissivity by T_c^2. In addition, let the input mirror power reflectivity (transmissivity) be represented by R_m^2 (T_m^2). After N optical traversals of the cavity, the electric field of the circulating light, E_{cir}, is given in terms of the incident field, E_{inc}, by

$$\frac{E_{cir}}{E_{inc}} = T_m \sum_{n=o}^{N} \left(T_c R_m e^{i\phi}\right)^n . \tag{1}$$

The optical phase shift encountered in going around the cavity is indicated by ϕ. In Equation 1, the series is easily summed as $N \rightarrow \infty$. In this case the optical power is found to be

$$\frac{P_{cir}}{P_{inc}} = \frac{1 - R_m^2}{1 - 2\,T_c R_m \cos\phi + \left(T_c R_m\right)^2} . \tag{2}$$

Similarly, the light reflected off the input mirror is

$$\frac{P_{ref}}{P_{inc}} = \frac{R_m^2 - 2\,T_c R_m \cos\phi + T_c^2}{1 - 2\,T_c R_m \cos\phi + \left(T_c R_m\right)^2} . \tag{3}$$

Note that $P_{inc} = P_{ref} + (1 - T_c^2)\,P_{cir}$, which assures energy is conserved On cavity resonance, $\phi = 2\pi\ell$, the reflected power becomes $P_{ref}/P_{inc} = (R_m - T_c)^2/(1 - T_c R_m)^2$. The cavity transmissivity has a fixed value, set by the quality of the optical components used. However, the reflectivity of the input mirror can be arbitrarily chosen. Taking $R_m = T_c$, the cavity is critically coupled. No light is reflected under this condition, and all the incident power goes to pump the cavity. The circulating power under the same conditions is $P_{cir}/P_{inc} = 1/(1 - T_c^2)$. In other words, the optical enhancement that the ring modulator offers is simply the inverse of the single pass cavity loss. An enhancement of ten times requires a loss ≤10 percent. It can be easily shown that the finesse of the resonances is

$$\mathcal{F} = \pi\left(R_m T_c\right)^{1/2} / \left(1 - R_m T_c\right) \tag{4}$$

Under critical coupling, Equation 4 reduces to the usual two-mirror Fabry-Perot result.[7]

The experiment shown in Figure 1 has been used to verify the ring modulator performance. A single crystal CdTe modulator rod, 1.5 x 1.5 x 40 mm, is placed in the four-mirror cavity. The crystal has narrow electrodes (~0.5 mm) deposited on the $(\bar{1}10)$ surfaces. When the crystal is assembled in its BeO housing, the electrodes form a 100Ω balanced stripline which is driven in a push-pull fashion by 50Ω unbalanced lines. The light propagates along the 110 crystal axis in the same direction as the stripline driver signal. Exact velocity matching is not achieved with the BeO housing. However, because the velocities are substantially matched, the structure has a 5 GHz calculated bandwidth. One of the total reflecting cavity mirrors is mounted on a bender bimorph translator to allow cavity length tuning.

Figure 2 shows the cavity response when a linear voltage ramp is applied to the mirror translator. In Figure 2(b) the light reflected from the input mirror is presented. The reference line marked "cavity blocked" indicates a power level which is 90 percent of the input power as the cavity is prevented from resonating. The reference line marked "detector blocked" gives the zero power level. When the cavity is allowed to resonate, the

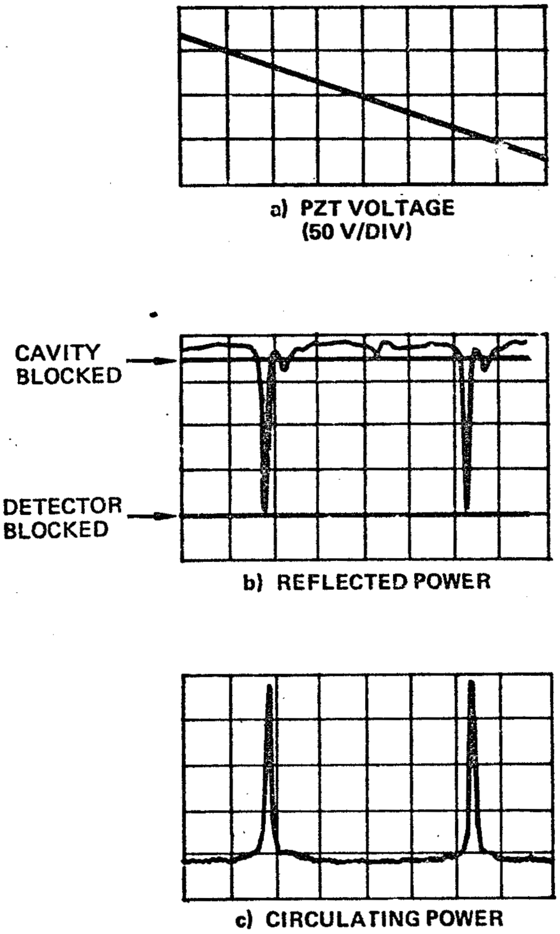

HORIZONTAL SCALE: 10 ms/DIVISION

FIGURE 2. MEASURED RING MODULATOR CAVITY

effective reflectivity varies from ~100 percent to near-zero. At low reflectivity, the circulating power, sampled with the wire grid polarizer, builds up as seen in Figure 2(c). These results demonstrate near-critical coupling of the ring modulator and thereby indicate a round trip cavity transmissivity (loss) of ~90 percent (10 percent). A cavity finesse of 30 has been measured for the data of Figure 2. Using Equation 4, a transmissivity value of 90 percent is again obtained. Finally, the enhancement of the optical signal was found directly by measuring the amplitude of the modulated light coupled from the polarizer both on resonance and with the cavity blocked beyond the polarizer. This ratio measurement gave an enhancement factor of ten times, again consistent with 90 percent transmissivity.

Wideband modulation tests on the enhanced light have been performed from 10 MHz to 1 GHz. A leveled, swept frequency source was applied to the stripline modulator and the resulting modulated light detected with a HgCdTe photo-voltaic detector. Figure 3 shows the driver electrical response along with the optical spectra for two different polarizers. Careful examination of Figure 2(b) has shown that the detected ring modulator response is determined totally by the modulator driver and the detector. No rolloff due to the modulator has been observed up to 1 GHz. The notch near 470 MHz results from a resonance in the detector housing, while the slightly reduced signal level at 1 GHz comes from the detector rolloff. The necessity of coupling out all of the modulated light is seen in Figure 3(c), where a ZnSe Brewster window is used instead of the wire grid. Here only

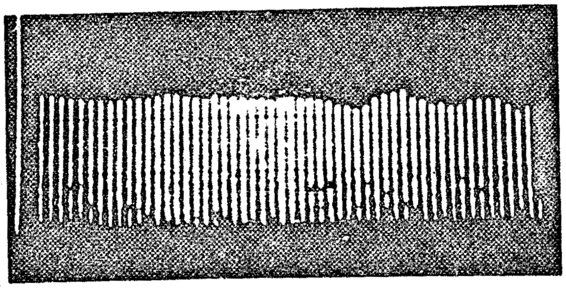

a) MODULATOR DRIVER INPUT

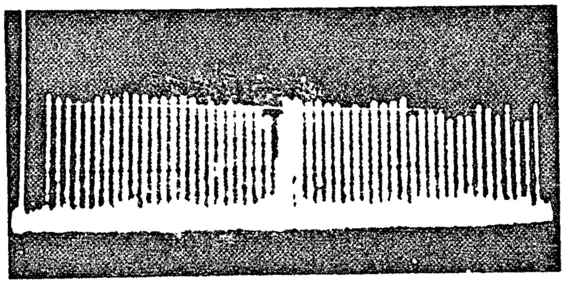

b) RING MODULATOR OUTPUT
(WITH WIRE GRID POLARIZER)

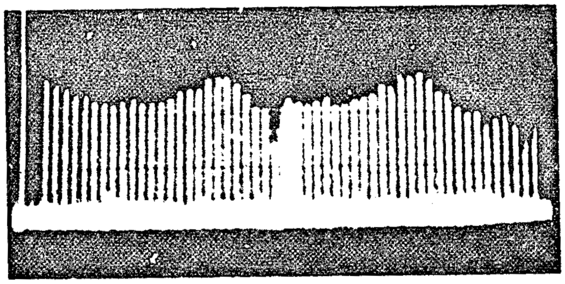

c) RING MODULATOR OUTPUT
(WITH BREWSTER WINDOW)

VERTICAL SCALE: 10 dB/DIVISION ?

"PICKET FENCE" APPEARANCE RESULTS FROM TIMING ASYNCHRONISM BETWEEN SWEPT FREQUENCY SOURCE AND SPECTRUM ANALYSIS

CALCULATED c/L FREQUENCIES OCCUR AT MULTIPLES OF 370 MHz IN AGREEMENT WITH RESONANCES OF FIGURE 3c

FIGURE 3. RING MODULATOR FREQUENCY RESPONSE FROM 0 TO 1 GHZ

about 75 percent of the cross-polarized, modulated light is extracted from the cavity. The remaining modulated portion can itself resonate in the cavity at multiples of the c /L frequencies (1/transit time) and thereby spoil the flat response. The wire grid polarizer, on the other hand, extracts all but about 1 percent of the cross-polarized signal.

This work has shown that the ring modulator attractively combines the benefits of coupling modulation and traveling wave modulation in a single design. Other benefits of the configuration should be noted. First, the performance of the laser itself is not spoiled by putting a crystal in the laser cavity. Secondly, there are no reflections from the modulator which go back into the laser cavity and thereby create instability. Finally, the cavity length can be actively stabilized by sensing the light reflected off the input mirror. The translatable cavity mirror position can be incorporated in a closed loop feedback circuit to minimize this reflection.

These present tests were not continued beyond 1 GHz because the modulator housing was not originally designed to be a microwave structure. Beyond this frequency, the VSWR of the housing becomes excessive. Work is presently under way to improve this structure and thereby extend the modulation to the 5 GHz calculated bandwidth.

REFERENCES

1. F.R. Nash and P.W. Smith IEEE J. Quantum Electron. QE-4, 26 (1968).

2. J.E. Kiefer, T.A. Nussmeier, and F.E. Goodwin, IEEE J. Quantum Electron. QE-8, 173 (1971).

3. J.J. Degnan, Appl. Opt. 11, 2489 (1974).

4. I.P. Kaminow and E.H. Turner, Appl. Opt. 10, 1612 (1966).

5. R.L. Abrams, private communication.

6. A. Yariv, Introduction to Optical Electronics (Holt, Rinehart and Winston, New York, 1971), Chap. 9.

7. M. Born and E. Wolf, Principles of Optics (Pergaman Press, London, 1970), Chap. 7.